



Design of coatings and adhesives inspired by natural mussel glue

Qie, Runtian

Publication date:
2022

Document Version
Publisher's PDF, also known as Version of record

[Link back to DTU Orbit](#)

Citation (APA):
Qie, R. (2022). *Design of coatings and adhesives inspired by natural mussel glue*. DTU Chemistry.

General rights

Copyright and moral rights for the publications made accessible in the public portal are retained by the authors and/or other copyright owners and it is a condition of accessing publications that users recognise and abide by the legal requirements associated with these rights.

- Users may download and print one copy of any publication from the public portal for the purpose of private study or research.
- You may not further distribute the material or use it for any profit-making activity or commercial gain
- You may freely distribute the URL identifying the publication in the public portal

If you believe that this document breaches copyright please contact us providing details, and we will remove access to the work immediately and investigate your claim.



Design of coatings and adhesives inspired by natural mussel glue

Runtian Qie

PhD Thesis

Supervisors:

Prof. Esben Thormann

Dr. Saeed Zajforoushan Moghaddam

Assoc. Prof. René Wugt Larsen

Technical University of Denmark

Department of Chemistry

Abstract

Nature is a treasure for material engineers, and learning from nature can play a key role in the design of novel materials for the future. Mussels, marine organisms that have been extensively studied in recent years, have evolved a set of adhesion mechanisms that enable them to form robust attachments to various surfaces underwater. This PhD study aims to mimic natural mussel adhesion to design practical coatings and adhesives with novel functionalities. This work can be divided into two sections: (i) coatings based on dopamine and (ii) adhesives for wet environments. There are two studies on coatings. The first study is mainly focused on characterising the optical properties of polydopamine (PDA) coatings and developing a proper modelling approach for the ellipsometry analysis of PDA coatings. The second study is focused on adjusting the properties of PDA coatings with a combined approach of dopamine co-deposition and layer-by-layer assembly; this approach is then applied to construct coatings with tuneable functionalities. The adhesive research also comprises two studies. The first study is dedicated to developing water-resistant bio-based adhesives by mimicking mussel adhesion mechanisms. The second study is focused on developing a novel adhesive inspired by mussel glue; the developed adhesive can bond various surfaces underwater as well as covalently cure to produce more durable adhesion.

Résumé

Naturen er et skattekammer for materialeingeniører, og at lære af naturen kan spille en nøglerolle i udformningen af nye materialer til fremtiden. Muslinger, marine organismer, der er blevet grundigt undersøgt i de senere år, har udviklet et sæt adhæsionsmekanismer, der gør dem i stand til at danne robuste vedhæftninger til forskellige overflader under vandet. Dette ph.d.-studie har til formål at efterligne naturlig muslingeadhæsion for at designe praktiske coatinger og klæbemidler med nye funktioner. Dette arbejde kan opdeles i to sektioner: (i) coatinger baseret på dopamin og (ii) klæbemidler til våde miljøer. Der er to studier om belægninger. Det første studie er hovedsageligt fokuseret på at karakterisere de optiske egenskaber af polydopamin (PDA) coatinger og udvikle en ordentlig modelleringstilgang til ellipsometrianalyse af PDA-coatinger. Det andet studie er fokuseret på at justere egenskaberne af PDA-coatinger med en kombineret tilgang af dopamin co-deposition og lag-for-lag samling; denne fremgangsmåde anvendes derefter til at konstruere coatinger med justerbare funktionaliteter. Klæbemiddelforskningen omfatter også to studier. Det første studie er dedikeret til at udvikle vandafvisende biobaserede klæbemidler ved at efterligne muslingevedhæftningsmekanismer. Det andet studie er fokuseret på at udvikle et nyt klæbemiddel inspireret af muslingelim; det udviklede klæbemiddel kan binde forskellige overflader under vandet samt kovalent hærde for at producere mere holdbar vedhæftning.

Acknowledgement

First of all, I thank my principal supervisor, Professor Esben Thormann, for providing me with the opportunity to pursue my PhD at DTU. I would like to express my sincere gratitude to him for the tremendous encouragement, discussion, constructive advice, and support, which are invaluable for my project and personal life. Besides my current study, he was also concerned about my future study and gave me lots of suggestions for my career planning. It has been a great pleasure to have him as my supervisor during this most important period of my life.

I am also grateful to my co-supervisor Dr. Saeed Zajforoushan Moghaddam for his patient instructions concerning laboratory instruments, insightful discussions regarding my project, and constructive comments on academic writing. I am fortunate to have Saeed as my supervisor, who is very kind, smart, and professional. In addition, I would like to thank my other co-supervisor, Associate Professor René Wugt Larsen for his discussion and help.

Furthermore, I would like to express my appreciation to all my colleagues, especially my friends (Koosha Ehtiati, Frederik Hegaard, Johannes Eiler, Robert Andrew Biro, Junhao Huang, Tao Jiang, Junjie Kang, Fatemeh Keshavarzi, Daniel Hansen, Achebe Niels Olesen Nzulumike, Palanisamy Anand Raj, and Mariusz Kubus) from the Group of Polymers and Functional Interfaces (GPFI). Thank you for making GPFI into a family with a warm atmosphere, where I always feel at home. The experience with all of you is enjoyable, which is the kind of memory worth cherishing for a lifetime. I also thanks my other friends Ping Zhu, Faliu Yang, Kai Gao, and Runwei Yao.

Finally, a great thanks to my family for their love, trust, and support throughout my education. I also acknowledge the financial support from the China Scholarship Council (CSC) and DTU Chemistry.

List of abbreviations

A	Area
AFM	Atomic force microscopy
aminePPO	Triamine terminated poly(propylene oxide)
CPS	Colloidal probe atomic force spectroscopy
Cu ²⁺	Copper ion
DA	Dopamine
DBA	3,4-dihydroxybenzaldehyde
Dopa	L-3,4-dihydroxyphenylalanine
epPPO	Poly(propylene oxide) diglycidyl ether
F	Force
FT-IR	Fourier-transform infrared spectroscopy
LBL	Layer-by-layer
MADQUAT	Poly(2-(trimethylamino) ethyl methacrylate)
Mfps	Mussel foot proteins
MSE	Mean squared error
Mw	Weight-average molecular weight
PDA	Polydopamine
PDMS	Poly(dimethylsiloxane)
PEI	Polyethyleneimine
PMMA	Poly(methyl methacrylate)
PPO	poly(propylene oxide)

PS	Polystyrene
PSAs	Pressure-sensitive adhesives
PVA	Polyvinyl alcohol
PVC	Polyvinyl chloride
QCM-D	Quartz crystal microbalance with dissipation monitoring
SFA	Surface forces apparatus
SMFS	Single-molecule force microscopy
TA	Tannic acid
TEOS	Tetraethyl orthosilicate
XPS	X-ray photoelectron spectroscopy

List of publications

1. Parameterization of the optical constants of polydopamine films for spectroscopic ellipsometry studies
Runtian Qie, Saeed Zajforoushan Moghaddam, and Esben Thormann*
Phys. Chem. Chem. Phys., 2021, 23, 5516–5526
2. DA-assisted layer-by-layer deposition provides coatings with controlled microstructure and physicochemical properties
Runtian Qie, Saeed Zajforoushan Moghaddam, and Esben Thormann*
(Submitted to Langmuir)
3. Making protein-based adhesives water resistant: role of protein water solubility, galloyl modification, and complexation
Saeed Zajforoushan Moghaddam*, Runtian Qie, and Esben Thormann*
ACS Appl. Polym. Mater. 2022, 4, 18–23
4. A self-curable underwater glue based on poly(propylene oxide) and tannic acid coacervate
Runtian Qie, Saeed Zajforoushan Moghaddam, and Esben Thormann*
(Submitted to ChemComm)

Not included manuscripts

1. Water-resistant adhesive
Saeed Zajforoushan Moghaddam, Esben Thormann, and Runtian Qie
(Under patenting)
2. A water-resistant bio-based adhesive
Runtian Qie, Saeed Zajforoushan Moghaddam, and Esben Thormann*
Unpublished manuscript (awaiting patent)

Contents

Abstract.....	i
Résumé.....	ii
Acknowledgement.....	iii
List of abbreviations	iv
List of publications.....	vi
1. Introduction.....	1
2. Background	4
2.1 Mussel adhesion	4
2.2 Mussel adhesion mechanisms	6
2.2.1 Composition of the plaque: mussel foot proteins (Mfps).....	6
2.2.2 How do mussels produce and apply their adhesive?	8
2.3 Engineered materials inspired by the mussel adhesive	19
2.3.1 Polydopamine (PDA) coatings	21
2.3.2 Mussel-inspired adhesives.....	33
3. Methods.....	38
3.1 PDA-based coatings	38
3.1.1 Substrate (silicon wafer) preparation.....	38
3.1.2 Preparation of PDA coatings	39
3.1.3 Preparation of PDA/dextran and PDA/PEI coatings	40
3.1.4 Preparation of PDA-based hierarchical coatings.....	41
3.2 Preparation of adhesives.....	41
3.3 Characterisation.....	42
3.3.1 Ellipsometry.....	42
3.3.2 Atomic force microscopy (AFM)	46
3.3.3 Adhesive lap shear testing	48

3.3.4 Underwater adhesion testing	49
3.3.5 Other characterisation techniques (water contact angle, zeta potential, XPS, FT-IR) .	50
4. Summary of results	52
5. Perspectives	69
6. References	70
Appendices	81

1. Introduction

Nature has long been a source of inspiration for the development of novel materials. In recent decades, there has been ongoing interest in designing functional materials inspired by mussel adhesives owing to their robust adhesion in wet environments. In this PhD study, I developed (i) coatings and (ii) adhesives with novel functionalities by mimicking the mussel adhesive mechanism. My PhD study contains four projects and four associated papers (published and submitted manuscripts), which form the backbone of this dissertation and are attached as appendices.

The thickness of polydopamine (PDA) as a thin film is generally estimated using ellipsometry, which is an optical characterisation technique. However, the complex optical behaviour of PDA makes this estimation approach difficult. Thus, in the *first* study, I focused on developing appropriate models to provide an accurate estimation of the optical properties and thickness of the PDA coatings using ellipsometry. Because the optical constants and microstructure vary with the reaction conditions, I prepared different samples by controlling the deposition time and then developed an optimised model for each case. The thickness estimated by ellipsometry was verified based on atomic force microscopy (AFM) measurements.

In the *second* study, a new coating approach was designed by combining dopamine (DA) co-deposition and layer-by-layer (LBL) assembly. Using this combined approach, I prepared PDA and PDA hybrid coatings and investigated the efficiency of the method in controlling the growth rate and surface morphology of the films. In addition, to demonstrate the potential of this method in developing functionality-controlled coatings, a hierarchical PDA-based coating was constructed, and its properties were systemically characterised.

Aside from the development of coatings, researchers have also derived inspiration from mussels to design adhesives for applications in wet environments. Bio-based adhesives as “green” substitutes for synthetic adhesives have attracted ongoing interest. However, the poor water resistance of bio-based adhesives, which is a major deficiency, has limited their application in wet conditions. To improve the water resistance, in my *third* study, bio-based adhesives were optimised at three levels: (i) the water solubility was reduced by choosing water-insoluble protein, (ii) polyphenol was added to mimic the catechol of mussel adhesive, and (iii) a protein-polyphenol complex coacervate was formed to mimic the coacervation of mussel adhesive. Combining these three parameters—catechol, coacervation, and protein water solubility—can yield protein-based adhesives with commercial-level water resistance.

Underwater adhesives are considered useful for many future applications such as biomedical adhesives and underwater operations. Such adhesives should be inexpensive, and easy to produce on a large scale. More importantly, these adhesives should be curable to ensure durability. Thus, in the *fourth* study, I designed a novel underwater adhesive based on a simple coacervation approach with poly(propylene oxide) and tannic acid. This adhesive provides strong tackiness underwater; however, more importantly, it cures underwater and provides durable water-proof bonding.

After briefly introducing the outline and outcome of my PhD research, I discuss the theoretical and experimental aspects in the following chapters. In Chapter 2, I provide an overview of mussel adhesion, which has inspired two systems: (i) PDA-based coatings and (ii) functional adhesives in wet environments. This chapter encompasses the underlying knowledge regarding mussel adhesive proteins, adhesion mechanisms, PDA-based coatings, and the design philosophy of adhesives (water-resistant adhesives and self-curable underwater adhesives). These topics are not

introduced in detail in the attached papers; thus, the second chapter can be used as a basis for understanding the findings and discussions presented in my papers. The Chapter 3 describes the experimental methods used in my PhD research. This chapter provides a basic introduction to each method and describes how the experiments were conducted and analysed. In Chapter 4, I discuss the research questions, aims, hypotheses, methodologies, main findings, and conclusions of my studies. Combining all of these parts can provide a better understanding of the acquired knowledge and connections between my studies.

2. Background

2.1 Mussel adhesion

Marine organisms have evolved a set of complex and effective wet adhesion mechanisms to adapt to their environments.[1,2] As a well-known example, mussels can firmly attach themselves to rocks or to each other underwater.[3,4] To do so, mussels use a collection of bio-polymeric fibres, also known as a byssus (Figure 2.1). These threads are produced by the mussel “foot” and comprise distinctive regions with specific functionalities: (i) the core (tensile tether), (ii) the cuticle (protective coating), and (iii) the plaque (adhesive/binder).[5] The adhesive plaque acts as a holdfast, firmly adhering to slimy, wet, and salt-crusts surfaces.[6–9]

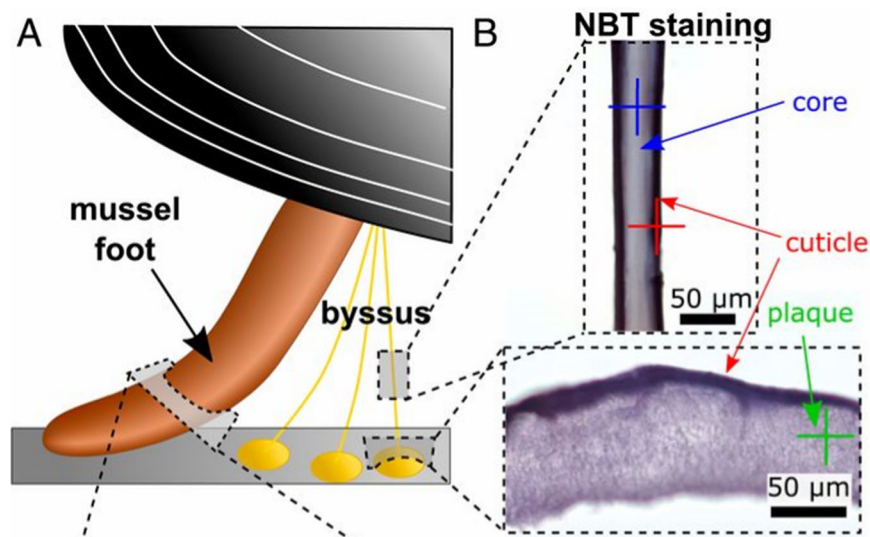


Figure 2.1 Structure of the mussel byssus thread. Reprinted with permission from [5].

Several studies have estimated the strength of mussel adhesives. For instance, Bell et al. measured the adhesion strength of mussel plaque on a rock surface (in seawater) using a handheld force gauge.[10,11] Accordingly, the tenacity of a solitary mussel containing 50 threads was found to be approximately 300 N and 180 N in the normal mode (lift) and parallel displacement mode

(drag), respectively (Figure 2.2).[4] In the normal mode, where all threads contribute to load bearing, the average adhesion strength of each thread was found to be ~ 6 N. Assuming a plaque diameter of 2 mm, the average adhesive strength of the plaque was then estimated to be ~ 6 MPa.[4] Aside from rocks, mussels can strongly adhere to various other substrates, such as metals and plastics, in both dry and wet conditions.[12–14] For instance, Burkett et al. estimated the wet adhesion strength (in normal-load mode) of an individual byssus to polyvinyl chloride (PVC), polymethyl methacrylate (PMMA), silicone, aluminium, and glass substrates to be ~ 100 – 300 kPa.[13] This means that a single byssus can withstand loads ranging from ~ 1 – 3 kg cm^{-2} in wet conditions.

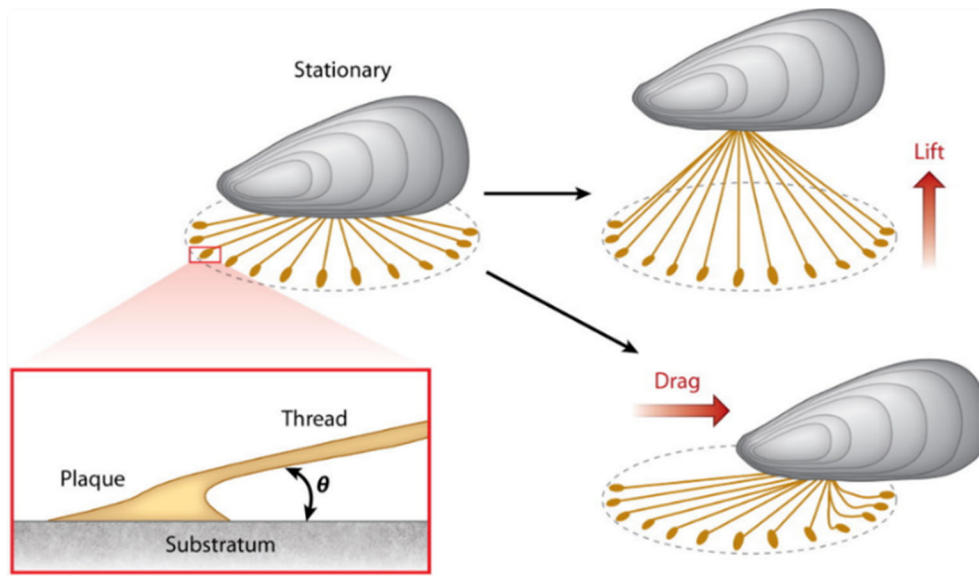


Figure 2.2. Mussel under lift and drag loads. Reprinted with permission from [4].

These remarkable adhesive properties of mussels have led to extensive research dedicated to (i) understanding the mechanisms of mussel adhesion and (ii) using this knowledge to develop novel engineered materials with enhanced adhesion in wet environments. Thus, this chapter of my PhD

thesis is dedicated to reviewing mussel adhesion mechanisms and discussing engineered materials inspired by mussel adhesives.

2.2 Mussel adhesion mechanisms

2.2.1 Composition of the plaque: mussel foot proteins (Mfps)

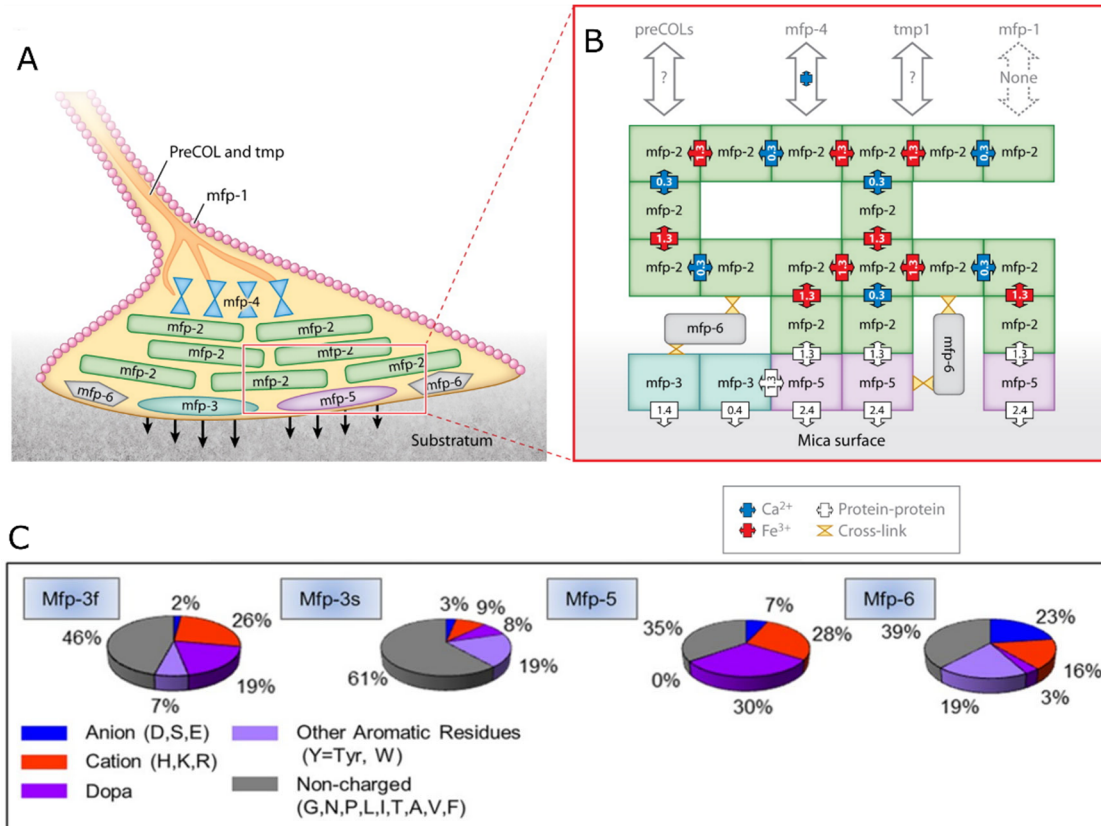


Figure 2.3. Mussel adhesive from a molecular perspective. (A) Schematic of Mfps distribution in the byssal plaque. (B) Schematic of Mfps interactions. (C) Pie charts illustrating the composition of Mfps in the plaque-substrate interface. Reprinted with permission from [4,15].

Extensive research has focused on investigating the molecular mechanisms of mussel adhesion.[14,15] It is believed that the byssus contains at least 20 different known protein components.[3] Among them, six major proteins, commonly known as the Mfps 1–6, are localised in the plaque (adhesive) region (Figure 2.3A). As a common characteristic, all Mfps contain

variable contents of L-3,4-dihydroxyphenylalanine (Dopa). The catechol moiety of Dopa is believed to play a key role in regulating the adhesion of the mussel adhesive to various substrates, as well as in the curing of the mussel adhesive, thus improving its cohesive properties.[15,16]

Mfps, each with unique molecular characteristics such as size and amino acid composition, synergistically contribute to the interfacial adhesive and bulk cohesive properties of the mussel adhesive.[14,15] Mfp-1, containing 10–15 mol% Dopa, is mainly found in the cuticle region of the byssus. It can form complexes with Fe^{3+} ions and mainly serves as a protective varnish layer (Figure 2.3A).[15,17,18] Mfp-2 contains a high level of cysteine (6 mol%), which can form disulphide bonds between the proteins and improve the cohesive properties of the network.[15,18] Mfp-4, which is rich in histidine, is located between the distal portions of the byssal threads and plaques.[4,15] It is believed that Mfp-4 can effectively link plaque proteins with PreCOL proteins in byssal threads (Figure 2.3A).[15] Mfp-3, 5, and 6 are predominantly located at the interface between the adhesive plaque and the substrate (Figure 2.3A, B), contributing to strong and durable wet adhesion. Mfp-3 is a Dopa-rich protein (Figure 2.3C) that is suggested to serve as an adhesive primer. The adhesion of Mfp-3 (to inorganic surfaces such as silica and metal oxides) is closely correlated with pH, becoming weaker at higher pH owing to catechol oxidation (this will be further discussed in Section 2.2.2.1).[19] As the smallest protein among the plaque proteins, it is the most polymorphic and contains approximately 30 different variants. These variants can be subdivided into two main groups: Mfp-3 fast (Mfp-3f) and Mfp-3 slow (Mfp-3s).[14,20] Both Mfp-3f and Mfp-3s contain high contents of asparagine (~10–18 mol%) and glycine (~25–29 mol%), which can provide the amine group for the amine-catechol synergistic effect (discussed further in Section 2.2.2.2).[15,21] In addition, Mfp-3f is rich in Dopa (~20 mol%) and positively charged residues (~26 mol%) (Figure 2.3C).[15] In contrast, Mfp-3s has a lower ratio of Dopa (5–10 mol%) and

charge density (3 mol% and 9 mol% of negatively and positively charged residues, respectively).[15] Additionally, Mfp-3s is the first known adhesive protein to exhibit self-coacervation (discussed further in Section 2.2.2.3).[14] Compared to other Mfps, Mfp-5 is the least polymorphic and has the largest content of Dopa (30 mol%) (Figure 2.3C).[15,20] Meanwhile, it also contains high amounts of lysine (17 mol%) and glycine (15 mol%). The combination of catechol chemistry with the cationic nature of the protein has been suggested that is crucial in both interfacial adhesion and plaque cohesion (discussed further in Section 2.2.2.2). Similar to Mfp-3, it has also been shown that Mfp-5 exhibits stronger adhesion in acidic pH conditions.[22] Mfp-6 is a tyrosine-rich (20 mol%) protein that exhibits a lower ratio of Dopa (3 mol%) than the other Mfps (Figure 2.3C).[15,21] Moreover, Mfp-6 contains a large amount of cysteine residues (11 mol%), resulting in a high level of thiols, which can effectively prevent the oxidation of catechol groups to maintain byssal adhesion (discussed further in Section 2.2.2).[21,23]

In summary, Mfps together contribute to the ability of mussels to firmly adhere to various substrates in wet environments. Some have a protective functionality, preserving the other Mfps from exposure to the seawater environment (such as Mfp-1). Some can improve the cohesive properties of the plaque by forming strong protein–protein interactions (such as Mfp-2 and Mfp-4). Some, by forming strong molecular interactions with the substrate, ensure firm interfacial adhesion (such as Mfp-3 and Mfp-5), while others mediate the redox chemistry of Dopa to regulate adhesion and cohesion (such as Mfp-6).

2.2.2 How do mussels produce and apply their adhesive?

In addition to knowing the protein composition of the mussel adhesive, it is important to understand how mussels secrete these proteins and apply them to surfaces as an adhesive material. Herein, I briefly discuss this process.[3]

are that it can (i) etch and clean the surface, (ii) kill the microbes on the surface, (iii) control the redox environment, and (iv) regulate the protein fluidity, phase inversion, and precipitation.[3] Next, the surface-targeted proteins, Mfp-3, 5, and 6, are secreted into the cavity. Dopa-rich Mfp-3 and Mfp-5 can be adsorbed onto the substrate through diverse interactions between their catechol groups and the substrate (as discussed in Section 2.2.2.1).[3] In addition to adhering to the substrate, Dopa can also be oxidised to Dopa-quinone in the cavity by introduced O_2 or Fe^{3+} , which can enhance the cohesion of the adhesive (Figure 2.4F).[3,25] To avoid over-oxidation, Mfp-6 can reduce either O_2 or Dopa-quinones, which is essential for regulating the adhesion and cohesion (Figure 2.4D, F).[3,26] In addition to adsorbing on the surface, these proteins can also undergo condensation in the form of a liquid–liquid phase separation, also known as coacervation (Figure 2.4G).[3] Next, the formed coacervate undergoes phase inversion with water and is solidified by protein cross-linking (Figure 2.4H).[3] Subsequently, the assembly of the plaque is completed, and a protective cuticle is formed over the plaque (Figure 2.4I).[3] Finally, the mussel foot is retracted, resulting in solidification of the plaque through cross-linking triggered by seawater (Figure 2.4J).[3]

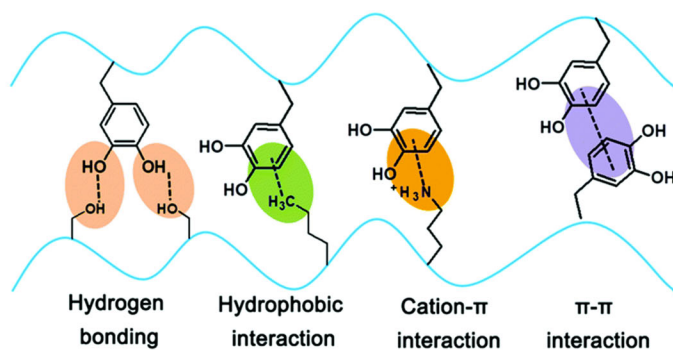
Clearly, the process is quite complex both in terms of the chemistry of the proteins involved and the number of steps through which the proteins are secreted and mixed to form the adhesive plaque. Given this overall picture, I next discuss the main factors that are currently believed to play key roles in the wet adhesion of mussels.

2.2.2.1 Catechol groups

Catechol is capable of forming various non-covalent (hydrogen bonding,[27] hydrophobic,[28] cation- π , [8] and π - π interactions [29]) and covalent (metal coordination,[30] boronate-catechol complexation,[31] Michael addition, Schiff base reaction, and other coupling reactions [32])

interactions, depending on the nature of the surface to which it will be attached (Figure 2.5). On inorganic surfaces, e.g. mica and metal oxides, catechol can form hydrogen and coordination bonds. On the other hand, the benzene ring allows the formation of π - π interactions with organic surfaces such as polystyrene.[33] Moreover, catechol in the oxidised form, i.e. quinone, can bind to nucleophilic molecules (amine- or thiol-containing molecules) via the Schiff base and Michael addition reactions.[34,35] The versatile chemistry of the catechol residue is suggested to contribute strongly to the adhesion (protein–substrate) properties of Mfp-3 and Mfp-5 as well as the cohesion (protein–protein) properties through cross-linking (covalent and coordination) of Dopa-quinones and Dopa-metal residues.[34]

(a) Typical non-covalent interactions in mussel-inspired chemistry



(b) Typical covalent bonds in mussel-inspired chemistry

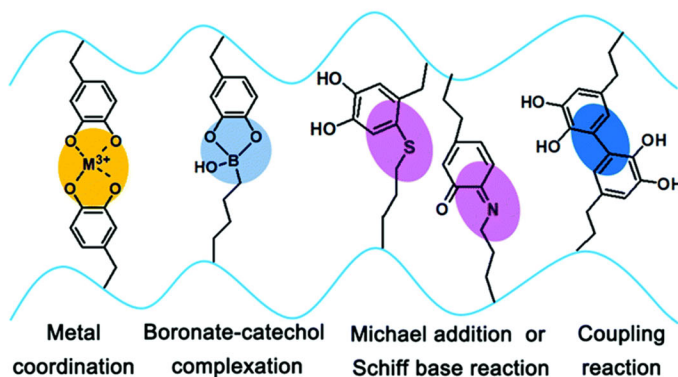


Figure 2.5 Schematic showing the typical interactions involved in mussel-inspired chemistry. Reprinted with permission from [34].

For the same reason, the pH is believed to have a notable effect on the adhesion properties of Mfps. Using a surface forces apparatus (SFA), Yu et al. measured the adhesion of Mfp-3 to mica at three different pHs (3, 5.5, and 7) (Figure 2.6).[3,19] They showed that Mfp-3 exhibited the strongest adhesion force of $\sim 12 \text{ mN m}^{-1}$ (equivalent to an adhesion energy of $\sim 2 \text{ mJ m}^{-2}$, $E = F/2\pi R$) at pH 3.[19] The adhesion force at pH 5.5 was found to be $\sim 4.5 \text{ mN m}^{-1}$, less than 40% of that at pH 3. Additionally, at pH 7.5, the adhesion force decreased to 0.7 mN m^{-1} , or only $\sim 5\%$ of that measured at pH 3.[19] It was suggested that the observed pH dependency could be attributed to Dopa oxidation. Oxidised Dopa cannot form hydrogen or coordination bonds with mica, resulting in weaker adhesion than occurs with Dopa.[19]

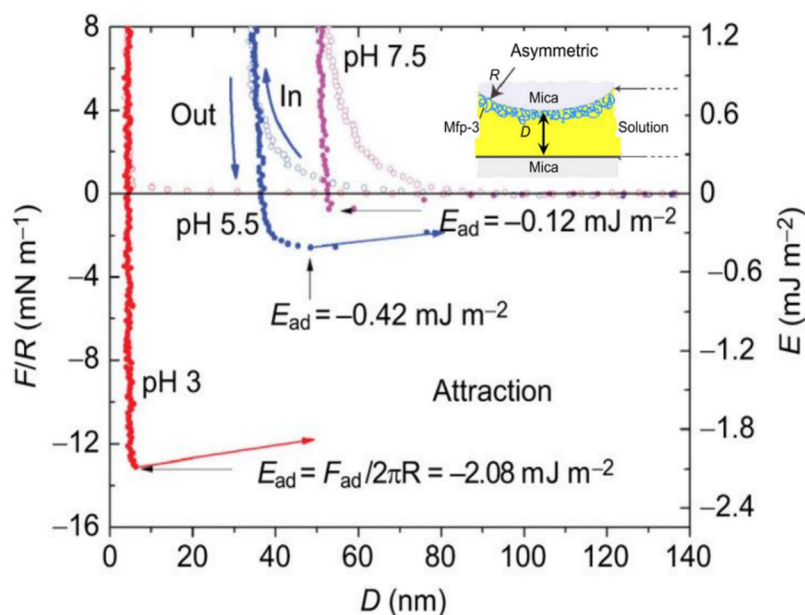


Figure 2.6 Adhesion of Mfp-3 to mica using SFA (asymmetric model) at different pHs. “In” and “out” denote the approach and separation of two surfaces, respectively. Reprinted with permission from [3].

2.2.2.2 Lysine-Dopa synergistic effects on adhesion and cohesion

Studies on mussel adhesion have primarily focused on the role of the catechol moiety and its versatile chemistry. However, more recent studies suggest that such complex adhesion behaviour

cannot be explained solely by the presence of Dopa; instead, it is a result of the synergetic interplay between different proteins and different amino acids. In particular, several recent studies suggest that lysine-Dopa (amine-catechol) interactions synergistically contribute to both the interfacial adhesion and cohesion of the mussel adhesive.[7,8,36–39] This means that not just Dopa, but also the amount and position of lysine, control the mussel adhesive performance.

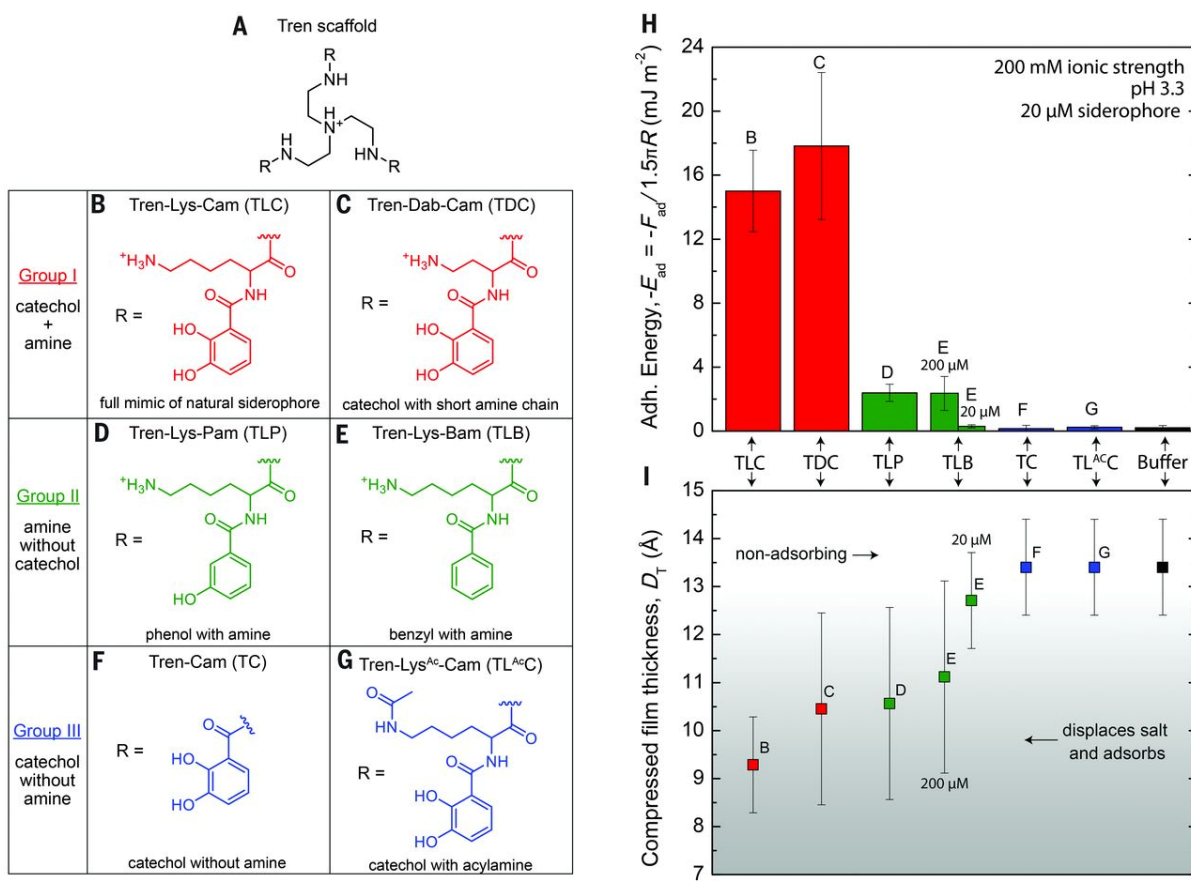


Figure 2.7. Synergy of amine and catechol groups in wet adhesion. (A) Structure of the Tren scaffold. (B–G) R groups grafted to Tren. (H) Average adhesion energy required with SFA to separate two mica surfaces with 20 μM adsorbed Tren, or 200 μM Tren where indicated, in pH 3.3 buffer. (I) DT of the Tren monolayer between two mica surfaces. The thickness of the film corresponds to the adhesion energy shown in (H). A film thickness of less than 12 Å suggests that B, C, D, and E (200 μM) displace hydrated salt and adsorb on the mica surface. Reprinted with permission from [37].

To investigate this concept, Maier et al. synthesised three groups of molecules: catechol with amine, only amine, and only catechol (Figure 2.7A–G).[37] Next, using SFA, they examined the adhesion of these molecules to mica at pH ~3. It was found that the molecules containing both catechol and amine (TLC and TDC) exhibited considerably stronger adhesion than molecules with only catechol or only amine (Figure 2.7H). They suggested that the stronger adhesion of the TLC and TDC molecules could be attributed to the synergistic interaction of amine and catechol, in which the amines displace hydrated salt ions, allowing catechols to bind to the mineral surface.[37]

Tiu et al. synthesised pressure-sensitive adhesives (PSAs) with different structures (catechol adjacent to amine or not) and chemical compositions (both amine and catechol present or not) (Figure 2.8A) to study the amine-catechol synergistic effect.[40] They examined the adhesion of PSAs (using single-molecule force microscopy (SMFS), colloidal probe atomic force spectroscopy (CPS), and static shear adhesion testing) (Figure 2.8B–D). It was found that PSAs containing amine and catechol exhibited much higher rupture forces, separation work, and failure times than the others, indicating that the presence of both amine and catechol could significantly enhance the adhesion of PSAs. Moreover, they observed that adhesion not only depended on the presence of amine-catechol, but also on their locations.[40] In addition to the key role of the amine-catechol synergistic effect in the regulation of adhesion, Gebbie et al. suggested that the cation- π interaction between lysine and Dopa could also enhance the cohesion of Mfps.[8]

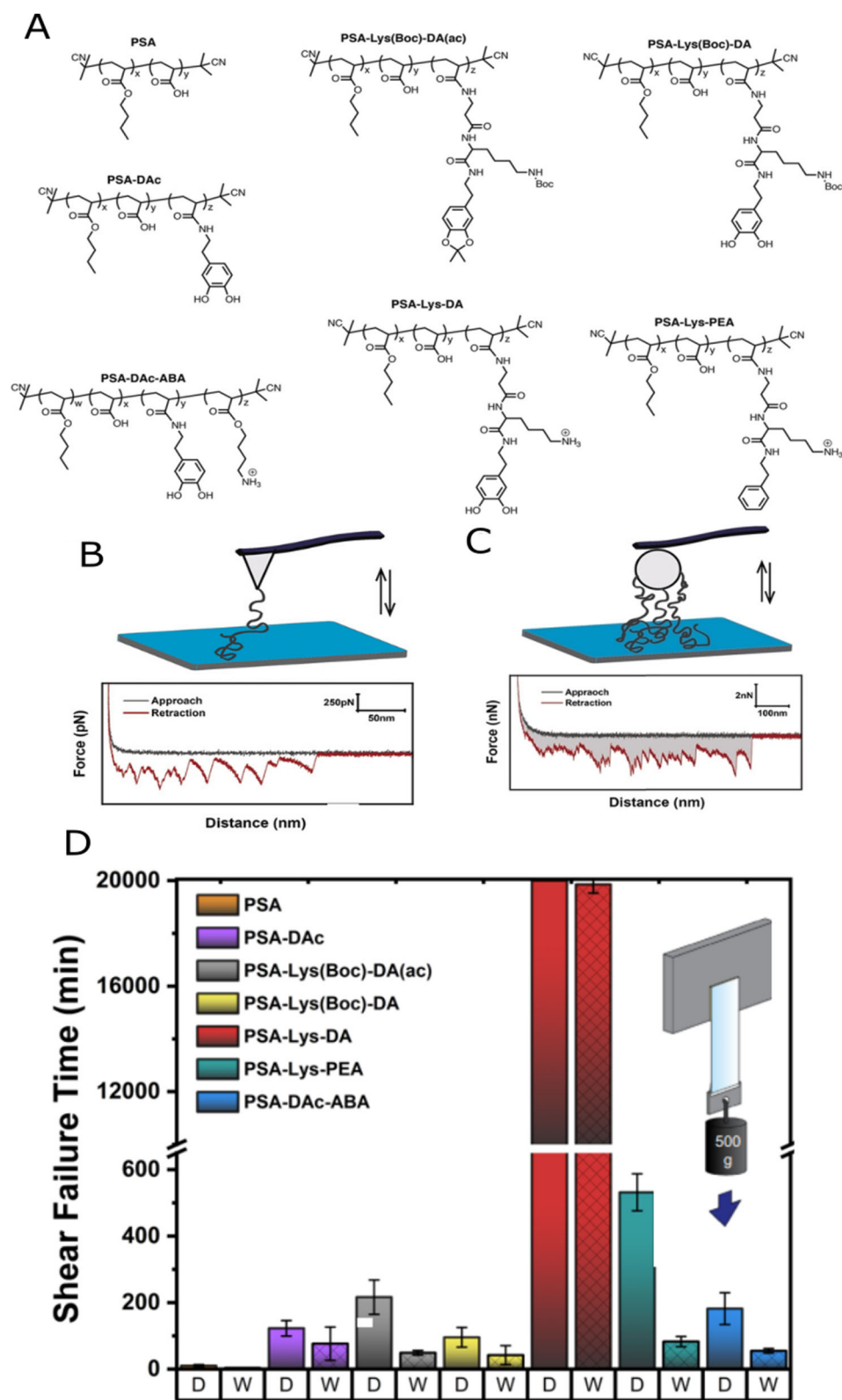


Figure 2.8 (A) Structure of PSAs (PSA and PSA homolog). (B) (C) Schematics of SMFS and CPS characterisation of PSAs. (D) Shear failure test of PSAs in ambient (D) and wet (W) conditions. Reprinted with permission from [40].

2.2.2.3 Coacervation

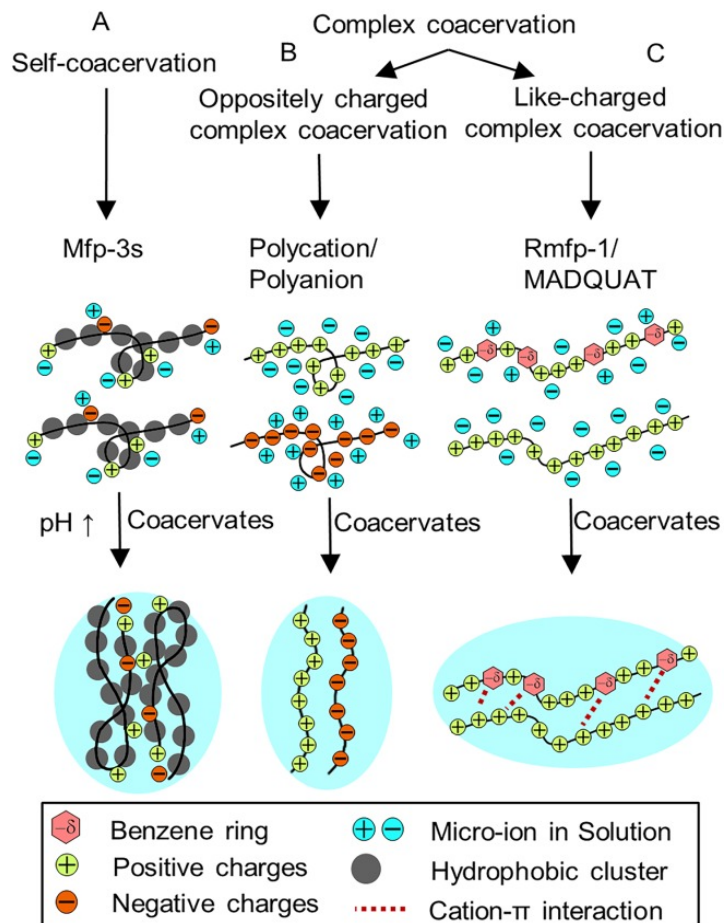


Figure 2.9 Schematic representation of coacervation. (A) self-coacervation of Mfp-3s with increasing pH. (B) Complex coacervation with oppositely charged polyelectrolytes through electrostatic interactions. (C) Complex coacervation with like-charged polyelectrolytes through cation- π interactions. Reprinted with permission from [15,41].

Coacervation is a liquid–liquid phase separation that can occur in aqueous solutions of macromolecules.[15,42] Coacervation can originate from various intermolecular interactions, such as hydrogen bonding, electrostatic attraction, cation- π , π - π , and hydrophobic interactions.[14] The coacervation process can be further divided into complex coacervation and self-coacervation (Figure 2.9).[15] The former refers to coacervation in which at least two molecules are involved,

whereas the latter refers to single-component systems. Complex coacervation is primarily observed with oppositely charged polyelectrolytes, where a polycation and a polyanion are attracted to one another through electrostatic interactions (Figure 2.9B). However, it can also occur for like-charged molecules; for example, Kim et al. suggested that the cation in poly(2-(trimethylamino)ethyl methacrylate) (MADQUAT) can form a cation- π interaction with the benzene ring of recombinant Mfp-1 (RMfp-1), driving these two components to produce coacervation (Figure 2.9C).[43]

In contrast to complex coacervation, self-coacervation occurs with a single macromolecule, e.g. zein, gelatin, or carboxymethyl chitosan, where the driving force is the charge balance resulting from the variation in the reaction conditions.[44,45] In the case of mussels, Mfp-3s can also undergo self-coacervation (Figure 2.9A).[16,41,46] Wei et al. reported that the coacervation process of Mfp-3s was affected by multiple parameters, including the concentration of Mfp-3s, type and pH of the solvent, ionic strength, and temperature. For instance, a higher ionic strength could screen the electric double-layer repulsion of Mfp-3 to trigger coacervation through non-electrostatic interactions such as coulombic interactions.[41] In addition, they measured the interfacial energy of the Mfp-3s coacervate using SFA, which was found to vary between 0.5 to 3.7 mJ m⁻². [41] With such low interfacial energies, the coacervate can adhere easily to a wet surface and readily spread over it. Subsequently, they examined the adsorption of Mfp-3s coacervate on hydroxyapatite surfaces using quartz crystal microbalance dissipation (QCM-D) (Figure 2.10A, B). QCM-D showed that the formed coacervate exhibited greater adsorption than the Mfp-3s solution (Figure 2.10A, in which the mass change is proportional to the frequency change ΔF), indicating that the formation of a coacervate can improve adhesion. Meanwhile, the coacervate exhibited a higher dissipative change, ΔD , which means that it was more fluid than the

Mfp-3 solution (Figure 2.10B). They suggested that the fluidic coacervate would be a suitable means of dissipating energy associated with the deformation of the byssus plaque as a result of drag and lift. Using a recombinant protein (drfp-3), Yang et al. found that coacervation could significantly enhance adhesion. In that study, they used SFA to measure the underwater adhesion force of a drfp-3 film and drfp-3 coacervate on mica (Figure 2.10C, D) and found that the coacervate provided superior adhesion ($\sim 46.5 \text{ mJ m}^{-2}$) to that of the film ($\sim 7.4 \text{ mJ m}^{-2}$).

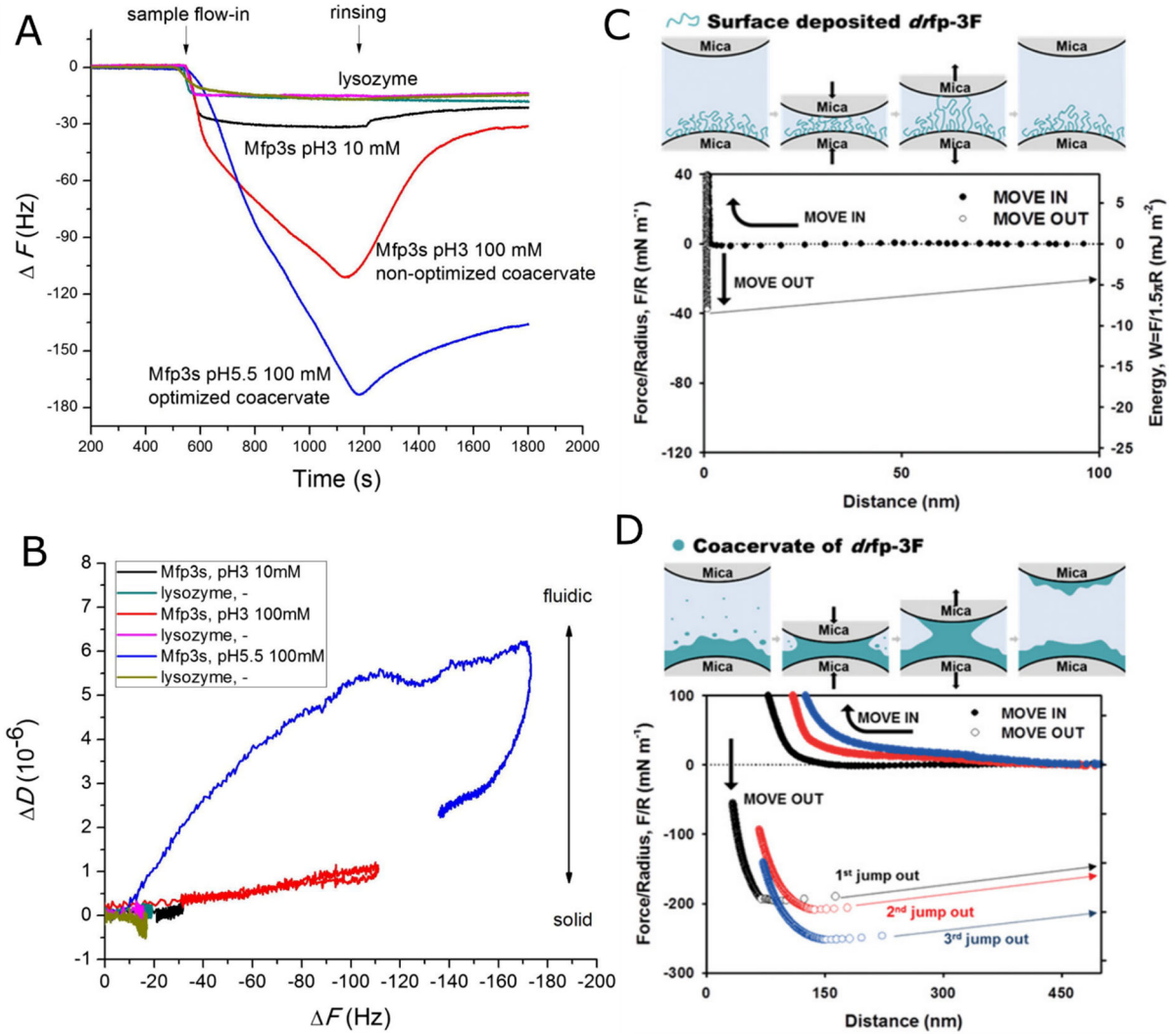


Figure 2.10. (A), (B) QCM-D measurements of Mfp-3s solution, Mfp-3s coacervate, and lysozyme deposition on a hydroxyapatite surface. (C), (D) Underwater adhesion test of drfp-3F film and its coacervate using SFA under asymmetric conditions. Reprinted with permission from [41,46].

Overall, the coacervate is an adhesive phase that exhibits excellent properties for underwater adhesion: (i) polymer-rich, (ii) insoluble, (iii) low interfacial energy, and (iv) shear-thinning viscosity.[3] Inspired by this, various favourable adhesives that function in wet environments can be produced by the coacervation of diverse chemical components.

2.3 Engineered materials inspired by the mussel adhesive

In the previous sections, I briefly discussed the essential understanding of mussel adhesion. Inspired by this natural system, extensive research has been dedicated to developing novel engineered materials, particularly coatings [47–50] and adhesives (Figure 2.11).[14,51,52]

Mussel-inspired coatings made of dopamine and other catecholamines have attracted considerable interest in various fields.[47] Controlled oxidation of these compounds can result in self-polymerisation reactions that form particles in the bulk solution and coatings on the surface of an immersed substrate.[47] The benefits of these mussel-inspired coatings are their versatility and simplicity (discussed further in Section 2.3.1).

Numerous studies have also focused on the development of new adhesive systems with enhanced performance in wet environments.[14,15] By learning from mussels and mimicking certain aspects of mussel adhesion, such as catechol and coacervation, these studies have aimed to develop adhesives for use in wet environments (Section 2.3.2).

2.3.1 Polydopamine (PDA) coatings

Catecholamines (e.g. norepinephrine, Dopa, and dopamine) are molecules that contain both catechol and amine groups. These molecules, through the controlled oxidation of their catechol moiety, can undergo a complex self-polymerisation reaction, which can form coatings with tuneable properties on various substrates.[47] The first half of my PhD research was devoted to investigations of PDA coatings; thus, I will discuss them first here.

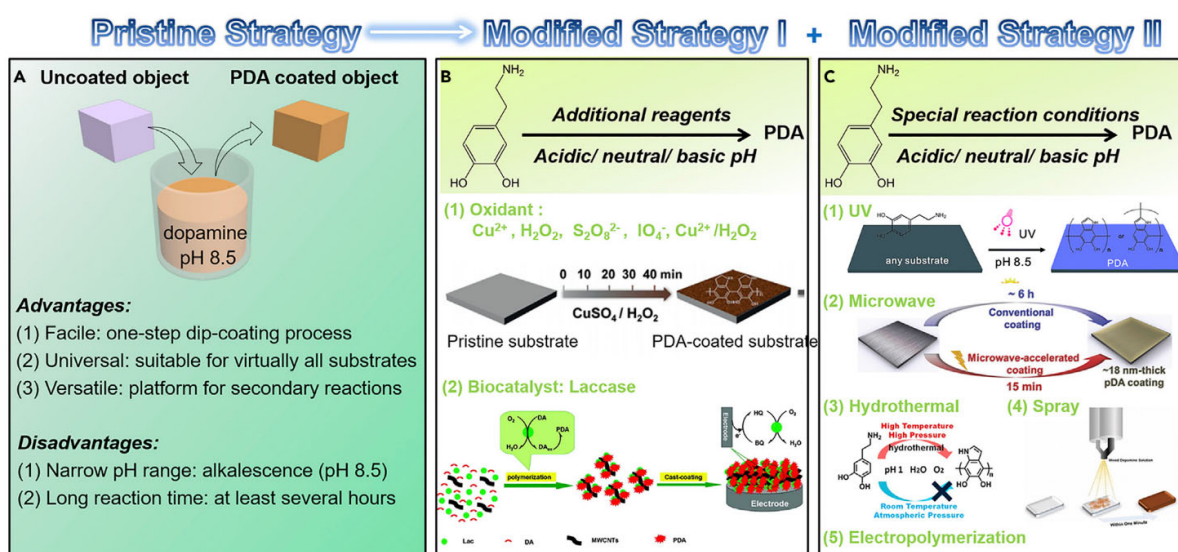


Figure 2.12 Different strategies for the preparation of PDA coatings. Reprinted with permission from [55].

2.3.1.1 Self-polymerisation of dopamine (DA)

In 2007, Lee et al. described a simple method for preparing mussel-inspired coatings through the spontaneous polymerisation of DA.[56] The inspiration behind this pioneering study was the adhesive property of Dopa and its synergistic effects with lysine in Mfp-5. DA, as a catecholamine, can self-polymerise with the assistance of additional reagents or under special reaction conditions to form PDA films on the surfaces of various materials (Figure 2.12).[55] Among these systems, oxygen-induced self-polymerisation of DA in Tris buffer (pH = 8.5) is the most common

procedure. DA polymerisation is a complex reaction involving many intermediate species. The exact reaction process and structures vary from system to system, but the common belief is that DA is first oxidised to dopaminequinone by dissolved oxygen in Tris buffer (Figure 2.13A).[47] Then, dopaminequinone undergoes intramolecular cyclisation and is transformed into leukodopaminechrome, which is further oxidised to dopaminechrome and converted into 5,6-dihydroxyindole through a rearrangement reaction. Subsequently, these intermediate components and unreacted DA molecules can undergo oligomerisation to form oligomers.[47] These oligomers then self-assemble into supramolecular aggregates via non-covalent interactions, including π - π stacking, hydrogen bonding, cation- π interactions, and electrostatic interactions.[47] The formed aggregates are further stabilised through covalent bonding formed via the Michael addition and Schiff base reactions.[47]

Similar to polymerisation in solution, PDA film deposition begins with the adsorption of monomeric species and small oligomers on the target surface (Figure 2.13B).[57] The adsorbed radicals then initiate the polymerisation process to form oligomers, nanoaggregates, and supramolecular structures. All of these components self-assemble to form a continuous PDA film on the substrate. In addition, monomers, nanoaggregates, and small particles can also be incorporated into the deposited PDA films by covalent bonds and non-covalent interactions.[57]

During the PDA deposition process, both catechol and quinone groups (the oxidised form of catechol) are required for film growth. For interface attachment, catechol and quinone groups have different interactions based on the properties of the substrate. For inorganic substrates such as mica, silica, and metal oxides, catechol can form hydrogen and coordination bonds with the surface to facilitate adhesion to the substrate.[47,58] In contrast, on organic surfaces containing amine or thiol groups, quinone contributes to adhesion by forming covalent bonds.[47]

2.3.1.2 Co-deposition of DA with other molecules

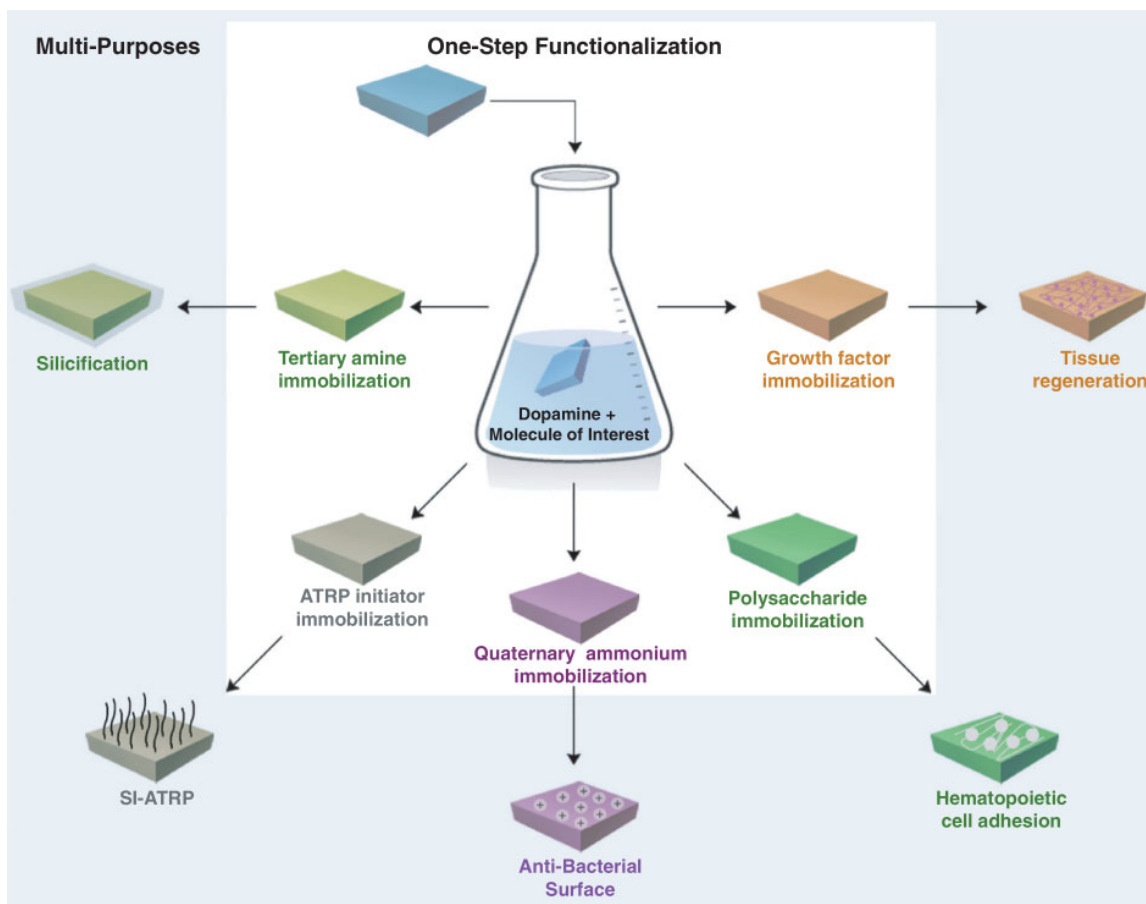


Figure 2.14 Schematic of the co-deposition of DA with various chemicals. Reprinted with permission from [60].

DA-assisted co-deposition is an effective surface modification method that was first proposed by Lee et al. in 2012.[60,61] In this method, a substrate is immersed in a mixed solution of DA and other chemical components, allowing PDA to trap other compounds within the deposited film (Figure 2.14). Based on the interactions between DA and these components, covalent and non-covalent co-deposition methods can occur. Molecules containing reactive functional groups such as aldehydes, amines, and thiols can form covalent bonds with DA and other intermediate structures. In the absence of covalent reactions, molecules can also be co-deposited through non-covalent bonds such as hydrogen bonding and electrostatic interactions.[61] By changing the types

of co-deposited components and their ratios to DA, the resulting coating properties, such as the hydrophilicity, roughness, and zeta potential, can be easily adjusted, as these are largely determined by the interactions and reactions between DA and the components, as well as the features of the components (Table 2.1).

Table 2.1 Summary of the dopamine-assisted co-deposition method for surface functionalisation. Reprinted with permission from [61].

Co-component	Suggested interaction	Co-deposition time/h	Characteristics	Potential application
PEG/PVA	Hydrogen bonding	1	Enhanced hydrophilicity	Antifouling
Dextran	Hydrogen bonding	18	Enhanced hydrophilicity	Antifouling
HA	Hydrogen bonding	1–3	Ultralow adsorption to proteins	Antifouling
Heparin	Hydrogen bonding	4	Enhanced hydrophilicity, blood biocompatibility	Antifouling, blood purification
PAM	Hydrogen bonding	24	Enhanced hydrophilicity	Antifouling, CE
TEOS	Hydrogen bonding	6–12	One-step silicification, superhydrophilicity	Oil/water separation, bone regeneration
PSBMA	Electrostatic interactions	18	Underwater superoleophobicity	Antifouling, oil/water separation
PMPC	Hydrogen bonding, cation- π interaction	0.5–12	Underwater superoleophobicity	Antifouling
HAuCl ₄	Chelation	4	Electron-transporting property	Biosensor
Fe ₃ O ₄ NPs	Chelation	12	Magnetism	Oil/water separation
PEI	Catechol-amino reactions	2–24	Excellent hydrophilicity, high positive charge, enhanced acid-alkali stability, enhance fluorescence	Water treatment, bio-imaging, antifouling for implants, CE, nanofiltration
PEPA	Catechol-amino reactions	40	Superhydrophilicity, high positive charge	Water treatment
P(MOXA-co-EI)	Catechol-amino reactions	65	Cytocompatibility	Antifouling for biomedical implants
PEI-g-RGD	Catechol-amino reactions	1	Osteoconduction	Bone regeneration
PEGDA	Michael addition	0.5	Chlorine resistance	Antifouling, water treatment
DMAET	Catechol-amino reactions	5	Enhanced wettability, initiator for silicification	Li-Ion battery separator
n-dodecylthiol	Catechol-thiol reaction	10	Superhydrophobicity	Oil/water separation
KH560	Hydrogen bonding, hydroxyl condensation	6	One-step silicification, superhydrophilicity	Antifouling, oil/water separation
DA-BiBB	Hydrogen bonding, catechol-amino reactions, hydrophobic interaction	24	Colorless coating	Polymer capsule

2.3.1.2.1. Non-covalent co-deposition

During the polymerisation of DA, a series of oligomers and supramolecular structures are formed, which contain aromatic rings, catechols, and amine functional groups. These compounds can interact with the mixed components via non-covalent interactions, including hydrophobic forces,[62] hydrogen bonding,[63–65] and electrostatic attraction (Table 2.1).[66,67] For example, Liu et al. co-deposited DA with dextran, a water-soluble and anti-fouling polysaccharide.[64] Dextran contains a large number of hydroxyl groups that can form hydrogen bonds with PDA

(including dopamine-quinone and other intermediates). With this method, PDA/dextran coatings were produced on various substrates, such as glass, silicon, polystyrene (PS), and poly(dimethylsiloxane) (PDMS). The inclusion of dextran inhibits the non-covalent self-assembly of PDA-PDA, thereby affecting the film thickness and roughness. In addition, the properties of the film were also tuned by the inclusion of dextran. For instance, the film became more hydrophilic (Figure 2.15A) and obtained anti-fouling performance (Figure 2.15B, in which a smaller frequency change, ΔF , corresponds to a smaller amount of protein adsorbed on the film).[64] Overall, co-deposited components can form non-covalent bonds with PDA, thus affecting the layer properties and providing new functionalities to the hybrid films. As part of my second study (paper II), I investigated the PDA/dextran film as a model non-covalent co-deposition system.

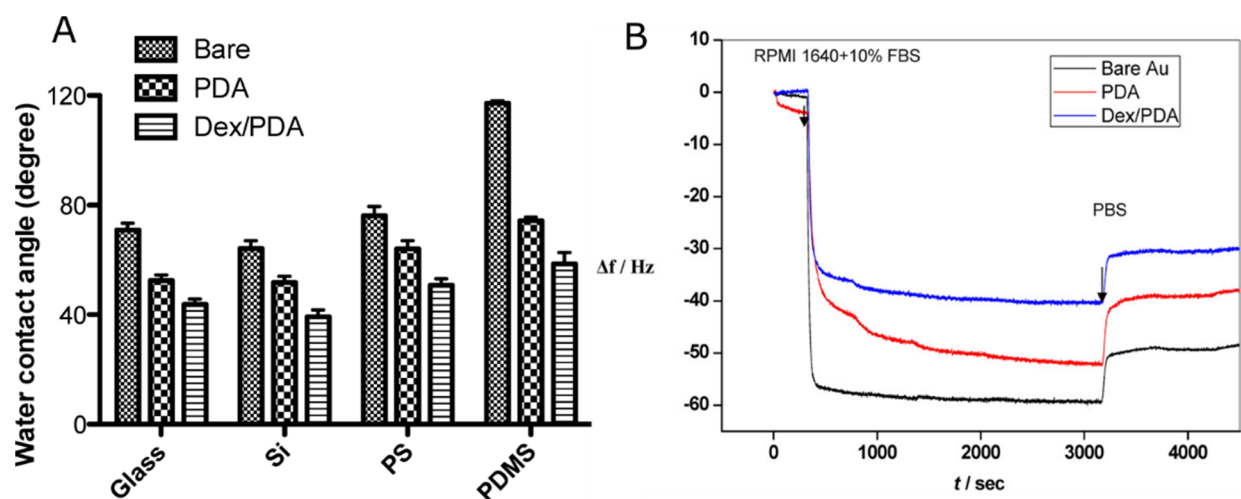


Figure 2.15 (A) Water contact angles of bare, PDA-coated, and PDA/dextran-coated substrates. (B) QCM-D measurements (frequency change vs. time) obtained for protein adsorption on bare, PDA-coated, and PDA/dextran-coated Au sensors. Reprinted with permission from [64].

2.3.1.2.2 Covalent co-deposition

DA can react with molecules that contain aldehyde, amine, or thiol groups through Schiff base or Michael addition reactions to form covalent bonds. The advantage of covalent co-deposition is that

it can provide a robust network to enhance the stability of films.[61] For instance, Lv et al. co-deposited DA with polyethyleneimine (PEI), an amine-rich polymer. PEI formed covalent bonds with PDA via Michael addition and Schiff base reactions, which improved the stability of the hybrid film in HCl, NaOH, and NaClO solutions.[68] Nevertheless, the inclusion of PEI inhibited the non-covalent assembly of PDA, resulting in decreased thickness and roughness. In addition, coating properties, such as the hydrophilicity, were also affected. The results showed that many factors, such as the Mw and concentration, could affect the coating properties (Figure 2.16). In some cases, no coating occurred, which indicates that a balance is needed when preparing the PDA/PEI coating. As part of my second study (paper II), I also investigated the PDA/PEI film as a model covalent co-deposition system.

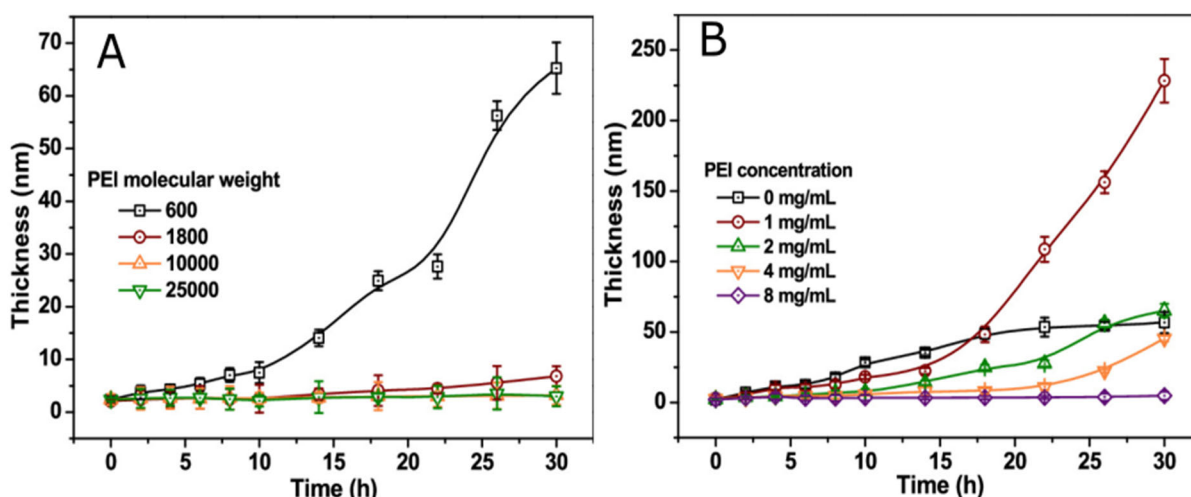


Figure 2.16 Ellipsometry thickness of PDA/PEI films obtained with different (A) PEI molecular weights (PEI concentration is 2 mg mL⁻¹) and (B) PEI concentrations (PEI molecular weight is 600 Da). DA concentration is 2 mg mL⁻¹. Reprinted with permission from [68].

In addition to polymers, ions and nanoparticles can also be co-deposited with DA. The catechol of PDA can form coordination bonds with metal ions.[47,61] For instance, Andersen showed that catechol and Fe³⁺ can form mono-catechol-Fe³⁺ complexes at pH <5.6. As the pH increased, bis-

catechol- Fe^{3+} formed at pHs below 9.1. Further increasing the pH resulted in transformation of the catechol complex with Fe^{3+} to tris-catechol- Fe^{3+} (Figure 2.17).[69] Bernsmann et al. co-deposited DA with Cu^{2+} and successfully obtained a PDA/ Cu^{2+} hybrid film. Compared with pure PDA films, it exhibited different optical properties. They suggested that the difference was due to Cu^{2+} changing the local environment of the adjacent 5,6-dihydroxyindole units. They also observed that coating growth properties such as the roughness and thickness were affected (Figure 2.18B). Overall, the ion species and pH of the solution are crucial factors in coordination and can be used to control the properties of the formed films.

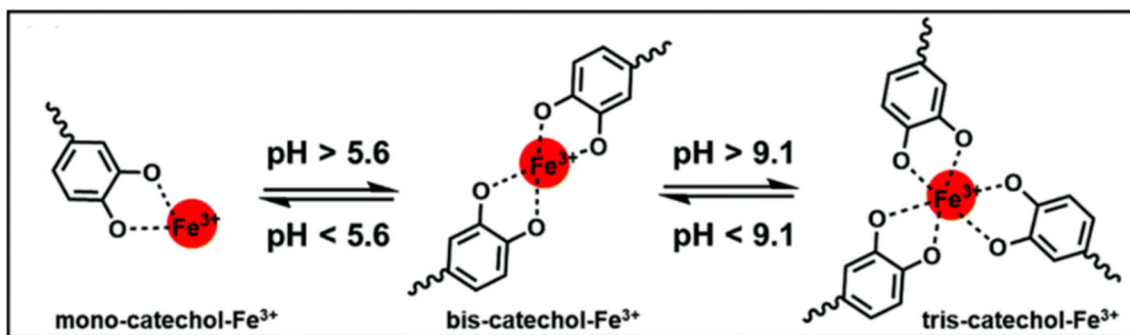


Figure 2.17 Coordination between catechol and Fe^{3+} ions at different pHs. Reprinted with permission from [69].

2.3.1.3 Properties of PDA films

The properties of PDA films, such as the thickness, roughness, refractive index, and chemical composition, can vary depending on numerous factors, including the deposition time,[56,70] concentration of DA,[71,72] reaction temperature,[59,73] substrate chemistry,[74] type of oxidant,[75] and buffer.[76] In my studies on PDA coatings, I mainly investigated the thickness, roughness, and optical properties of such coatings and their correlation with the coating deposition method.

2.3.1.3.1 Thickness and roughness

As discussed in Section 2.3.1.1, DA polymerisation occurs simultaneously in the solution and on the target surface. With time, the components on the surface can grow into larger parts owing to polymerisation. Meanwhile, the enlarged-size components from the solution can be incorporated into the PDA film. Both of these factors can lead to film growth with increasing deposition time.

Generally, the thickness of the PDA coating increases with the deposition time until it reaches a plateau (traditional one-step deposition method, Figure 2.18A–C).[72,77] Trzcinska et al. suggested that this plateau can be explained by the consumption of DA and oxygen, which can induce the eventual termination of the deposition.[78] Bernsmann et al. suggested that DA consumption was the key factor based on several experiments. For a fixed DA concentration, regardless of whether more oxygen was provided, the thickness of the coatings reached constant and similar values (Figure 2.18B).[77] An interesting study was reported by Bernsmann et al., in which layer-by-layer deposition through changing the fresh DA solution in the deposition process could successfully overcome the limitation of the PDA thickness plateau and provide continuous film growth (Figure 2.18A).[77,79] These results suggest that the observed plateau at long deposition times can be attributed to DA consumption, as well as excessive aggregation, which means only small aggregates and no further coating can be deposited onto the existing coating. In contrast to the traditional method, supplying fresh DA throughout the deposition process can provide continued growth of the PDA film.

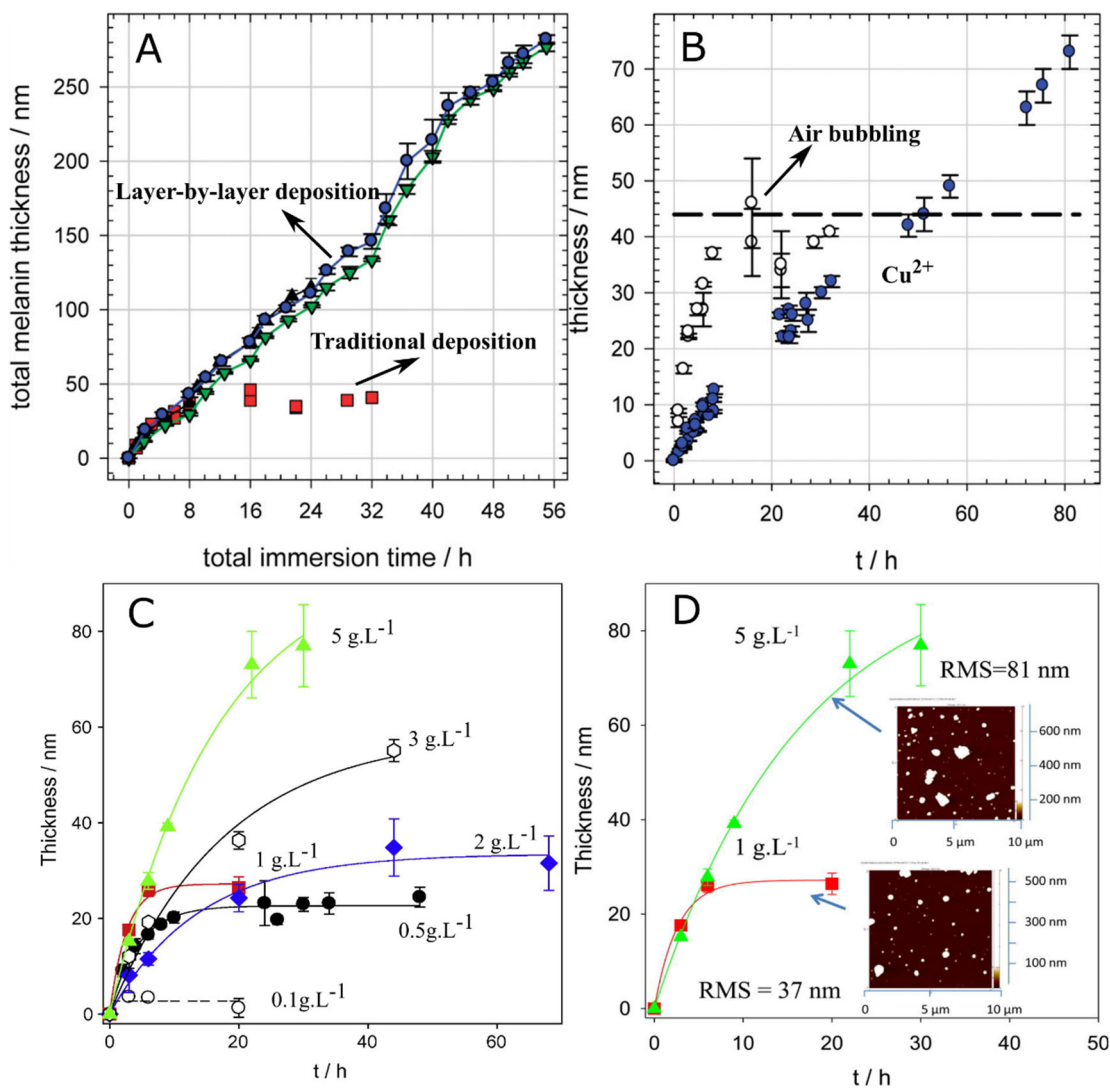


Figure 2.18 PDA film deposition versus time. (A) Traditional one-step deposition and layer-by-layer deposition. (B) Continuous air supply and co-deposition with CuSO_4 . (C) Variation in the thickness with concentration. (D) Thickness and roughness in concentrations of 2 and 5 mg mL^{-1} . Reprinted with permission from [72,77].

Surface roughness is another important factor that can affect PDA film performance.[80–82] PDA coatings generally possess rough and heterogeneous surfaces owing to the structures formed during the deposition process. It has been shown that the roughness increases considerably with the deposition time and DA concentration (Figure 2.18D).[70,72] As time passes, the sizes of both the components on the surface and aggregates in the solution increase. These aggregates can then

attach to the surface, resulting in a rough surface. In addition, a high DA concentration can also exert a stronger attraction between the nanoaggregates in solution and those on the PDA film, which allows more nanoaggregates to deposit on the PDA film and results in an increase in the surface roughness.[72] Such excessive uncontrolled roughness is normally unfavourable when fabricating thin films. For instance, Chen et al. claimed that the surface roughness of PDA-coated scaffolds could negatively affect cell adhesion and proliferation.[82] To optimise the performance of PDA films, several studies have focused on controlling the surface roughness of PDA to tune the roughness of PDA films.[72,80] For instance, Kim et al. prepared highly homogeneous PDA films through polymerisation at high oxygen concentrations.[80] They postulated that excess oxygen leads to a much higher amount of the final oxidation products, 5,6-dihydroxyindole and 5,6-indolequinone. These two molecules can fully conjugate to form homogenous PDA films through regular stacking, instead of random stacking, during air oxidation. Although this method can decrease the roughness of PDA films to some extent, the reaction rate is relatively high and difficult to control. Ball et al. suggested that low DA concentrations may help decrease the roughness of PDA films.[72] However, even when PDA films were prepared with a low concentration (1 mg mL^{-1}) and short deposition time (1 h), the surface roughness was still relatively high ($R_q > 10 \text{ nm}$).

These considerations inspired my second study (paper II), in which I focused on supplying fresh DA and observing the effects on the morphology of the PDA film. The hypothesis was that the replacement of an “aged” solution with “fresh” DA can produce continuously growing PDA films with low roughness.

2.3.1.3.3 Optical properties of PDA coatings

The thickness of a PDA coating is generally estimated using spectroscopic ellipsometry. This method measures the variation in the polarisation state of light reflected from a film on the substrate.[83] Therefore, an accurate optical model must be constructed, which includes the optical dispersions of the materials and their thicknesses. Generally, similar to any modelling approach, it is desirable to reduce the number of unknown parameters in the model; thus, it is preferable to use known optical constants as inputs to the model. Therefore, ellipsometry studies of PDA coatings can be challenging. As discussed earlier, PDA coatings consist of a complex mixture of aromatic compounds and possess a highly heterogeneous chemical composition. As a result, PDA exhibits a complex optical behaviour ranging from ultraviolet to near-infrared regions.[77,79,84] In addition, the optical properties of PDA films are not constant because of the diverse chemical compositions and structures obtained under different reaction conditions. For instance, Kawamura et al. reported the index of refraction (n) of PDA particles to be approximately 1.7–1.8 in the region of 400–800 nm.[85] Repenko et al. reported a relatively constant n of ~ 1.55 in the wavelength range of 400–800 nm, which increased to ~ 1.8 in the ultraviolet range.[86] However, most ellipsometry studies on PDA have ignored the light absorption and variability of the optical constants (n and k). For instance, several studies have used the Cauchy equation to model the optical properties of PDA and estimate the coating thickness. However, this model is only valid for transparent materials with no or negligible light absorption. Considering that PDA is a strong light-absorbing material, the Cauchy equation is expected to provide inaccurate estimates of the film thickness.[48,68,87,88] Some studies have used more complex models, but an overall investigation on the modelling of different PDA films is lacking.[64,89,90] Therefore, my first study (paper I) focused on a detailed modelling approach for various PDA coatings; the coatings

were obtained with different deposition times and chemistries and modelled with different modelling approaches. The aim was to compare the outputs of different models and determine which one was correct. There are two studies in my research where such considerations are important: (i) pure PDA (paper I) and (ii) PDA hybrid films (paper II). In both cases, the models were carefully developed from simple to complex, and the estimated thickness was double-checked using AFM.

2.3.2 Mussel-inspired adhesives

Mussels have also been a source of inspiration for the design of novel adhesives with improved performance in wet environments.[33] One direction is to develop adhesives mainly from bio-based materials that exhibit enhanced water resistance. Water resistance is the ability to maintain the functionality and strength of adhesives when they are exposed to weathering conditions such as humidity and rain. Despite their favourable environmental effects, bio-based adhesives normally exhibit poor water resistance, which can negatively affect their use in outdoor applications. Thus, one of the new trends in bio-based adhesives is to make them water resistant by learning from mussels. The other direction is to design underwater adhesives that can bond materials directly under wet conditions. Most man-made adhesives cannot be applied underwater; thus, developing underwater adhesives similar to those used by mussels is a new application direction for the future.

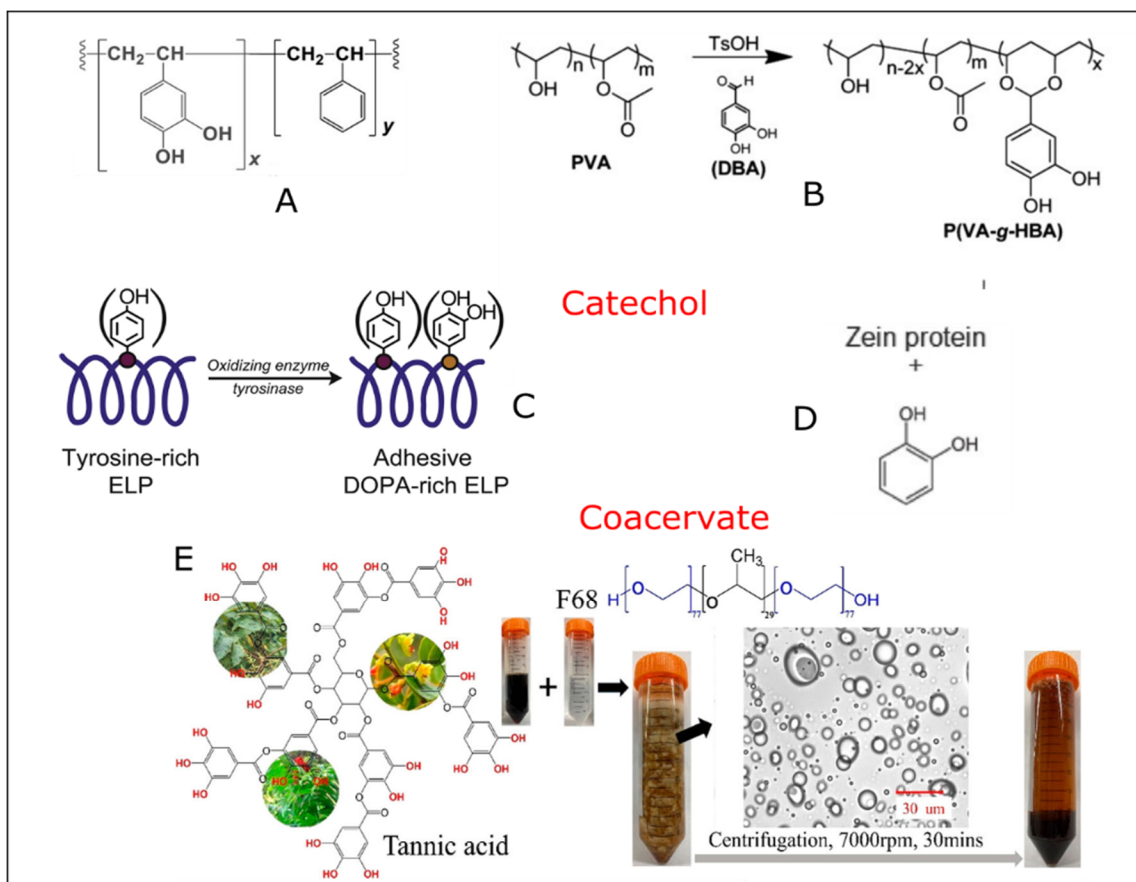


Figure 2.19 Diverse approaches to developing mussel-inspired adhesives. (A–D) Incorporation of catechol or catechol-mimetic functional groups. (E) Formation of a coacervate. Reprinted with permission from [91–95].

As previously discussed, catechol is an important factor for mussel wet adhesion. Thus, many studies focused on developing adhesives with enhanced wet adhesion have incorporated catechol or catechol-mimetic functional groups into adhesives to mimic mussel adhesive.[91,92,94,96–103] Various approaches have been used. (i) Catechol-containing polymers have been synthesised,[91,97] such as the poly[(3,4-dihydroxystyrene)-co-styrene] adhesive developed by Meredith et al., which showed a lap shear strength of up to 11 MPa on an aluminium substrate (Figure 2.19A).[91] (ii) Catechol groups have been grafted onto a polymeric backbone (synthetic or natural in origin).[92,98–103] For instance, Mu et al. conjugated 3,4-dihydroxybenzaldehyde (DBA) onto a polyvinyl alcohol (PVA) backbone, which exhibited strong adhesion to stainless

steel (>17 MPa) (Figure 2.19B).[92] (iii) Tyrosine on proteins has been converted to Dopa.[93,96] For instance, Brennan et al. developed an adhesive precursor comprising a tyrosine-rich elastin-like polypeptide, which could be converted to an adhesive by modifying the tyrosinase enzyme. The formed adhesive exhibited cytocompatibility, strong dry adhesion (>2 MPa), and moderate wet adhesion (~240 kPa) on glass (Figure 2.19C).[93] (iv) Polymers have been mixed with catechol or catechol-mimetic functional groups. For instance, Schmidt et al. mixed zein with a series of phenolics and obtained a group of water-resistant adhesives (Figure 2.19D).[94] Overall, the catechol and catechol-mimetic groups involved in these systems mimic the role of catechol in Mfps, which improves the performance of adhesives in wet environments.

Table 2.2 Main components, test conditions, and adhesion performance of adhesives based on coacervates.

Components	Substrates	Adhesion strength	Test condition	Ref.
PVA + TA	Glass, metal, plastics	50-70 kPa	Tack test (Wet)	[104]
PAE + TA	Glass, metal, plastics, wood	80-450 kPa	Lap shear (Wet)	[105]
PVP + TA	Glass, metal, plastics	150-3700 kPa	Lap shear (Dry)	[106]
PEOX + TA	Glass, metal, plastics	420-1100 kPa	Lap shear (Dry)	[107]
PolyAspAm(EA/EDA) + TA	Glass, metal, plastics	50-1150kPa	Lap shear (Dry)	[108]
PHEAA + TA	Ceramic, glass, metal	150-750kPa	Lap shear (Dry)	[109]
(P(HEA-co-AA) + TA	Wood, metal	750-4100 kPa	Lap shear (Dry and wet)	[110]
soy protein + TA + metal ion/particle	Wood	400-2000 kPa	Lap shear (Dry and wet)	[52]
Gelatin + TA	Bovine leather	≈36.3 kPa	Tensile test (Dry)	[111]
SF + TA	Glass	6-12.6 kPa	Lap shear (Dry)	[112]
PEG ₇₇ -PPG ₂₉ -PEG ₇₇ + TA	Glass, wood, plastic	160 kPa	Tack test (Wet)	[95]

In addition to mimicking the role of catechol, novel adhesives have been developed through coacervation of polymers and molecules bearing catechol-mimetic groups (Figure 2.19E).[95,104,109,110] These coacervate adhesives are typically easy to prepare and often no synthesis process is involved. In many of these studies, tannic acid (TA) was used as a molecule with similar chemistry to catechol to form complexes with various polymers (Table 2.2).

TA is a naturally derived plant polyphenol rich in catechol and pyrogallol groups, which can mimic the role of catechol in Dopa to interact with macromolecules and substrates via various interactions.[113] Compared with catechol, pyrogallol has one more hydroxyl group and exhibits improved antioxidant properties.[114] Pyrogallol has been shown to exhibit better adhesive properties than catechol in synthesised polymers.[115] In addition, TA exhibits high solubility and can be easily dissolved up to concentrations of 50 wt% in water. TA is also a safe material approved by the US Food and Drug Administration.[116] Based on these features, many studies have focused on TA-based coacervate adhesives. For the preparation of such adhesives, two aqueous solutions of the polymer and TA are used. When these two solutions are mixed, strong interactions cause phase separation and coacervation, providing polymer-rich and water-rich phases. Then, through a centrifuge step, the coacervate phase can be collected, which has been found to have good adhesive properties in different aspects. For instance, Peng et al. mixed two aqueous solutions of poly(ethylene glycol)₇₇-b-poly(propylene glycol)₂₉-b-poly(ethylene glycol)₇₇ and TA, centrifuged the mixture, and the coacervate adhesive was collected at the bottom. The collected material exhibited instant and robust underwater adhesion on different substrates (600 kPa on PMMA and 1.1 MPa on porcine skin).[95]

On this basis, the second part of my research (papers III and IV) focused on developing novel adhesives that mimicked some aspects of mussel glue to provide enhanced wet adhesion properties,

including water resistance and underwater adhesion. In the third study (paper III), I aimed to enhance the water resistance of protein-based adhesives through a systematic investigation of three parameters (water solubility of the protein, addition of polyphenol, and protein-polyphenol coacervation). Finally, the synergetic effects of these factors could yield protein-based adhesives with commercial-level water resistance. In addition to developing the water-resistant adhesive, my fourth study (paper IV) aimed to develop a self-curable underwater adhesive. In this study, I designed an underwater adhesive based on TA, poly(propylene oxide) (PPO), and PPO derivatives. The adhesive exhibited strong tackiness underwater, but more importantly, the epoxide and amine-terminated PPO could render the adhesive curable and provide durable water-proof bonding.

3. Methods

In this chapter, the experimental procedures and characterisation methods used in my PhD studies are described in detail in three sections:

- Preparation of the PDA-based coatings,
- Preparation of the mussel-inspired adhesives,
- Characterisation methods for coatings and adhesives.

3.1 PDA-based coatings

In papers I and II, pure PDA (DA only) and hybrid PDA films (DA co-deposited with PEI, tetraethyl orthosilicate (TEOS), $\text{CuSO}_4 \cdot 5\text{H}_2\text{O}$, and dextran) were obtained using two approaches: one-step (traditional method for the deposition of PDA-based coatings) and LBL deposition (the method explored in this PhD thesis).

3.1.1 Substrate (silicon wafer) preparation

In my studies, the PDA-based coatings were prepared on silicon wafers (100 mm 1KA thermal oxide, WaferNet Inc.). The silicon wafers ($2.5 \text{ cm} \times 1.5 \text{ cm}$) were first rinsed with acetone, ethanol, and ultrapure water, and then dried using compressed air. Next, the wafers were cleaned using plasma (PDC-32G plasma cleaner, Harrick Plasma) with high power under a constant water vapour pressure (500 mTorr) for 30 s. The silicon dioxide (SiO_2) layer thickness was estimated by spectroscopic ellipsometry.

3.1.2 Preparation of PDA coatings

DA was first dissolved in Tris buffer (pH 8.5, IS 50 mM) and the wafers were immediately immersed in the DA solution (2 mg mL^{-1}) while stirring at 250 rpm. To keep all of the specimens still and vertically aligned, the substrates were mounted into a custom-made Teflon holder (Figure 3.1). The total volume of the solution was (always) fixed at 300 mL. The distance between the wafer centre and the air–solution interface was maintained at $\sim 4 \text{ cm}$ (to maintain the oxygen content at the same level). After a given deposition time (0.5, 2, 4, 6, 12, 18, 24, and 48 h), the wafers were removed from the reaction solution and rinsed with Tris buffer. They were then sonicated using an ultrasonic cleaner (USC 600 TH, VWR) in fresh Tris buffer for 1 min at room temperature and was repeated three times to ensure removal of the attached aggregates (Figure 3.2), then dried with compressed dry air.

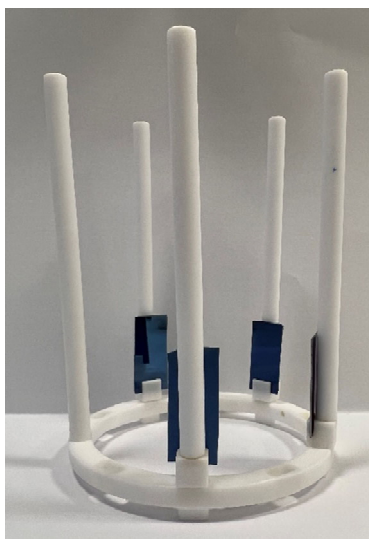


Figure 3.1 Silicon wafers mounted into a Teflon holder.

A similar procedure was employed to prepare PDA coatings using the LBL method; however, the DA solution was regularly exchanged with fresh DA solution (Figure 3.3). To produce coatings with the LBL method, the samples were immersed for 2 h (a sufficiently short time), and the

process was repeated a certain number of times. Therefore, coatings could be produced through steps of 2×2 h, 3×2 h, 6×2 h, 9×2 h, and 12×2 h. Three replicates were prepared for each sample.

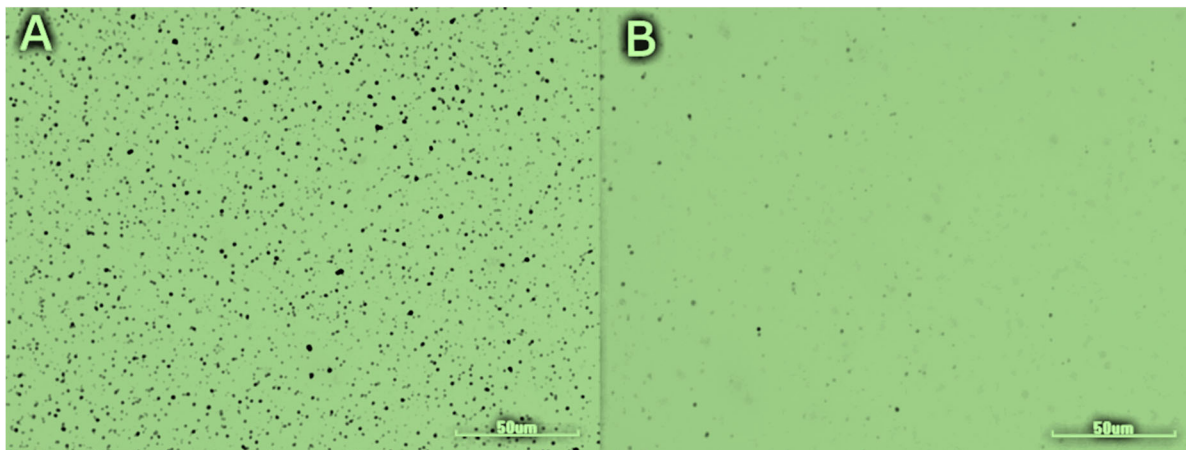


Figure 3.2 Optical micrographs of PDA coatings obtained after 6 h with one-step deposition: (A) before and (B) after sonication.

3.1.3 Preparation of PDA/dextran and PDA/PEI coatings

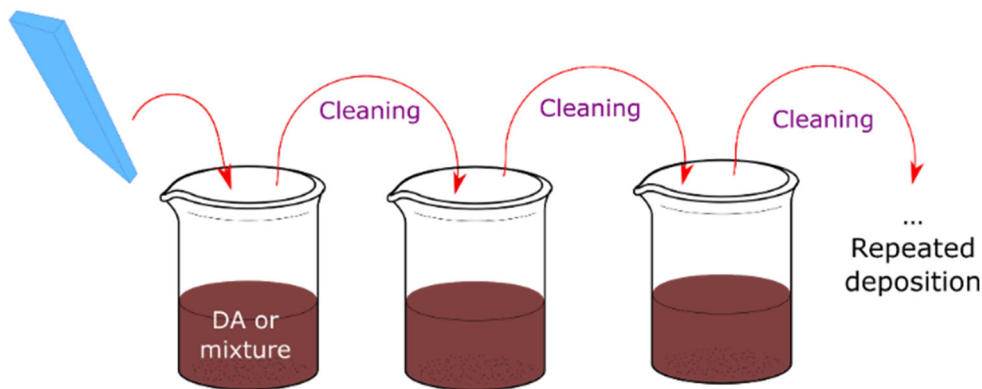


Figure 3.3 Schematic of the layer-by-layer construction of PDA, PDA/dextran, PDA/PEI, and hierarchical films.

PDA/dextran films were prepared using the above procedure; however, a mixture of DA (2 mg mL^{-1}) and dextran (10 mg mL^{-1}) was used in the solution.[64] Dextran powder ($M_w \sim 150,000$, from *Leuconostoc mesenteroides*) was first dissolved in Tris buffer, and then DA was added to the

solution. The samples were prepared using both one-step and LBL methods. PDA/PEI films were deposited similarly using a solution mixture of PEI (0.2 mg mL^{-1}) and DA (2 mg mL^{-1}).[68]

3.1.4 Preparation of PDA-based hierarchical coatings

A hierarchical film consisting of five different layers was constructed by the sequential LBL deposition of PDA, PDA/PEI, PDA/TEOS, PDA/ $\text{CuSO}_4 \cdot 5\text{H}_2\text{O}$, and PDA/dextran. The deposition time was identical for each layer (2 h). The concentrations of PDA, PEI, and dextran were the same as previously, while TEOS (precursor of SiO_2) and $\text{CuSO}_4 \cdot 5\text{H}_2\text{O}$ were added at concentrations of 42 [117] and 0.3 mg mL^{-1} , respectively.[118]

3.2 Preparation of adhesives

Two types of adhesives were prepared in my studies: (i) protein-based adhesives and (ii) PPO-based adhesives.

In paper III, two types of proteins (gelatine from porcine skin and zein from maize) were used in combination with TA, either by making a solution of the components or by forming a coacervate. To create gelatine-TA solution adhesives, gelatine was dissolved in warm water (20 wt.% dry content), and then TA aqueous solutions with different concentrations were added drop-wise. The gelatine-TA coacervate was produced by mixing aqueous solutions of gelatine and TA and then centrifuging the mixture. For zein-TA solution adhesives, zein was dissolved in an aqueous ethanol solution (90 v/v% ethanol), and various amounts of TA powder were added to the zein solution and mixed for 2 h (45 wt.% dry content). In addition, zein-TA coacervate adhesives were obtained by mixing the zein ethanol solution with the TA aqueous solution and centrifuging the mixture (Figure 3.4).

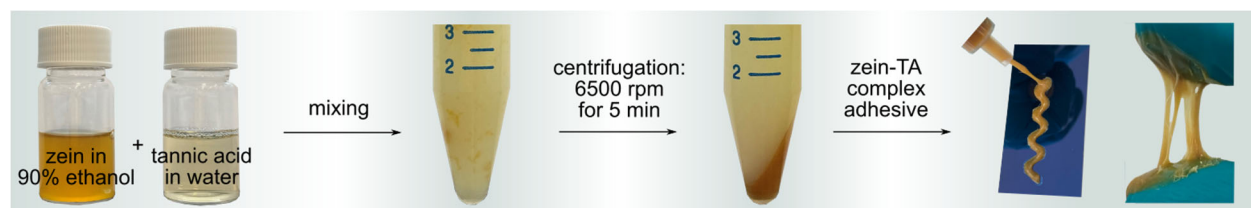


Figure 3.4 Preparation procedure for zein–tannic acid complex coacervate adhesives. Reprinted with permission from [119].

In paper IV, PPO-TA coacervate adhesives were prepared by mixing PPO (5 wt.%, 4 °C) and TA (5 wt.%, 4 °C) aqueous solutions at a 1:1 weight ratio; after centrifuging, the PPO-TA coacervate phase was collected at the bottom. Diepoxide-terminated PPO (epPPO) and triamine-terminated PPO (aminePPO) were also mixed with TA and centrifuged under identical conditions. To make a curable adhesive, epPPO-TA coacervate and aminePPO were mixed in a series of weight ratios.

3.3 Characterisation

3.3.1 Ellipsometry

In the first two studies (papers I and II), ellipsometry measurements were conducted to estimate the thickness of the PDA-based films.

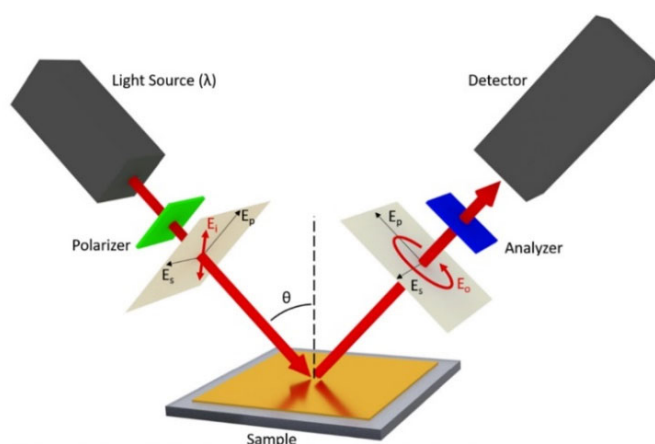


Figure 3.5 Schematic illustration of spectroscopic ellipsometry. Reprinted with permission from [120] © The Optical Society.

Figure 3.5 shows a schematic illustration of the spectroscopic ellipsometry setup. An ellipsometer measures the changes in the polarisation state of light reflected from a flat sample. The incident light passes through a polariser to generate elliptically polarised light that irradiates the sample. The polarised light is composed of two components: s-polarised light (perpendicular to the plane of incidence) and p-polarised light (parallel to the plane of incidence). The interaction between the incident light and the sample alters the polarisation state of the reflected light, which is detected by the analyser and quantified in terms of the ellipsometric parameters Δ and Ψ . The former represents the phase difference between the p- and s-polarisations, and the latter represents the amplitude ratio. The correlation between the measured values of Δ and Ψ and the sample properties is described by the following equation:[121]

$$\tan \Psi e^{i\Delta} = \rho(\theta_0, N_a, N_s, N_1, \dots, N_j, d_1, \dots, d_j).$$

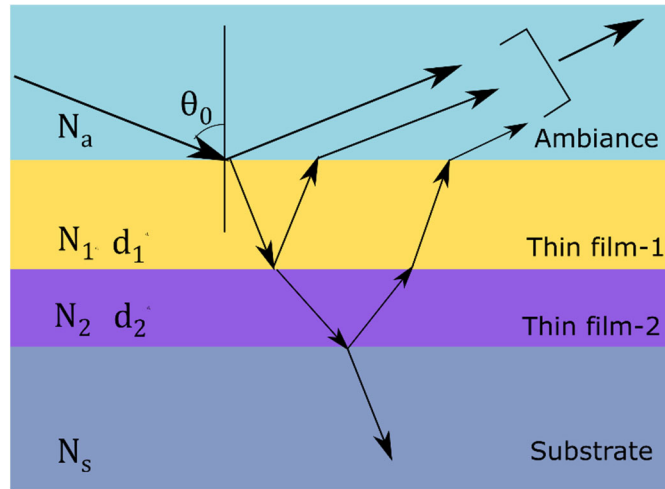


Figure 3.6 Optical model consisting of ambiance, thin films, and substrate.

Here, four layers are considered as an example; ρ is a complex reflectance function of the angle of incidence (θ_0); optical constants of the ambiance (N_a), substrate (N_s), layers (N_1 and N_2); and the thickness (d) of the film (Figure 3.6). After determining Δ and Ψ , an appropriate optical model

should be constructed to describe the nominal structure of the multilayer sample, including the optical constants and thickness information for all constituents. Then, Fresnel equations are applied to calculate Δ and Ψ for the constructed optical model, and the best fit (with the smallest mean squared error (MSE)) between the characterised and modelled values is obtained through regression.

The PDA-coated silicon wafer in my studies is represented by a three-layer optical model consisting of (i) a silicon (c-Si) substrate, (ii) an oxide layer (SiO_2), and (iii) a PDA coating. Because the optical constants of PDA are unknown, an appropriate model is required to describe its dielectric function and optical behaviour. To do so, the optical constants of PDA coatings were modelled, and the detailed modelling description is provided in the attached papers I and II. Here, I briefly describe the models used in my studies to estimate the PDA coatings. The modelling procedure should always start from the simple Cauchy model and proceed to the complex B-spline model. The Cauchy equation is an empirical relation between the refractive index of the material and the wavelength.[122]

$$n(\lambda) = A + \frac{B}{\lambda^2} + \frac{C}{\lambda^4},$$

where A adjusts the amplitude of the index of refraction and B and C account for the curvature of the dispersion. Considering the light absorption property of the PDA coating, the Urbach absorption term is added to modify the Cauchy relation.

$$k(E) = A_k e^{B_k(E-E_b)},$$

$$E_b = \frac{1024}{\lambda_b},$$

where the extinction coefficient (k) is characterised by the “offset” for all wavelengths (A_k), exponent factor (B_k), photon energy (E), and band-edge energy (E_b). In the model, λ_b is fixed, and A_k and B_k are free parameters. The Urbach absorption term is only appropriate for materials with weak light absorption; thus, for PDA coatings with strong absorption, a complex model, the B-spline function, was applied. This model is a mathematical function and is defined as a recursive set of single polynomial splines.[122,123]

$$B_i^0(x) = \begin{cases} 1 & t_i \ll x \ll t_{i+1} \\ 0 & \text{otherwise} \end{cases},$$

$$B_i^0(x) = \left(\frac{x-t_i}{t_{i+k}-t_i} \right) B_i^{k-1}(x) + \left(\frac{t_{i+k+1}-x}{t_{i+k+1}-t_{i+1}} \right) B_{i+1}^{k-1}(x),$$

where k is the degree of the spline (a third-degree polynomial function used in my study), and i is the index for the nodes (t_i) across which the polynomial functions connect. The multiple basis functions are then summed to produce the over-shape, $S(x)$, of the dielectric function.

$$S(x) = \sum_{i=1}^n C_i B_i^k(x),$$

where C_i denotes the coefficient of the basis function. The number of nodes is a crucial parameter that is directly related to the description of the optical dispersion and number of free parameters. Moreover, to avoid the appearance of non-physical solutions with negative ε_2 values and ensure the correlation between ε_1 and ε_2 , Kramers–Kronig (KK) relations are applied together with the B-spline function[122,123]

$$\varepsilon_1(E) = 1 + \frac{2}{\pi} P \int_0^{\infty} \frac{E' \varepsilon_2(E')}{E'^2 - E^2} dE$$

Furthermore, for a rough PDA film, a roughness layer, defined as a PDA–air mixture, is added on top of the B-spline. The optical dispersions of the PDA–air roughness layer are described using the Bruggeman effective medium approximation (EMA) equation.[122,124,125]

$$f_{\text{PDA}} \frac{\epsilon_{\text{PDA}} - \epsilon_{\text{EMA}}}{\epsilon_{\text{PDA}} + 2\epsilon_{\text{EMA}}} + f_{\text{air}} \frac{\epsilon_{\text{air}} - \epsilon_{\text{EMA}}}{\epsilon_{\text{air}} + 2\epsilon_{\text{EMA}}} = 0$$

where ϵ_{EMA} is the complex dielectric function of the PDA–air layer and f_{PDA} and f_{air} are the volume fractions of PDA and air, respectively. In my study, the roughness layer was treated as a homogenous layer comprising a 50:50 mixture of PDA: air; thus, f_{PDA} and f_{air} were both 0.5.

3.3.2 Atomic force microscopy (AFM)

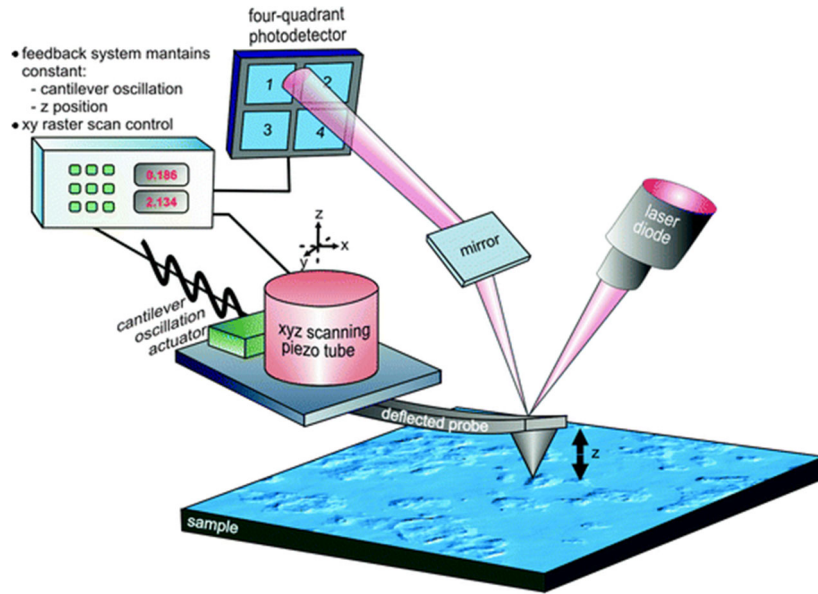


Figure 3.7 Schematic illustration of atomic force microscopy. Reprinted with permission from [126].

AFM is a scanning probe microscopy technique based on the interaction between a probe and the sample surface.[127] AFM comprises four major parts: a cantilever with a probe, laser source, piezoelectric scanner, and photodiode detector (Figure 3.7). The piezoelectric scanner drives the cantilever mounted with a tip to scan the sample surface in three directions (x, y, and z). The forces

between the tip and sample cause deflection of the cantilever, which can be detected and utilised to obtain topographical images. To monitor the deflection, a laser beam is reflected from the back of the cantilever onto the photodiode detector. When the cantilever deflects, the angle of the reflected laser beam changes, and the spot falls on a new position of the photodetector, which can be converted into lateral and vertical deflections of the cantilever.

In my studies (papers I and II), AFM (NanoWizard 3, JPK Instruments AG, Berlin, Germany) operating in tapping mode in air was employed to obtain topographical images and estimate the thickness of the coatings. In tapping mode (Figure 3.8), the cantilever oscillates vertically close to its resonant frequency. When the distance between the tip and the sample decreases, phase and amplitude shifts occur; to keep the amplitude constant, the piezo then withdraws the tip away from the sample surface, and vice versa. This is the feedback movement of the piezo, which is used to generate the topographic image of the surface.

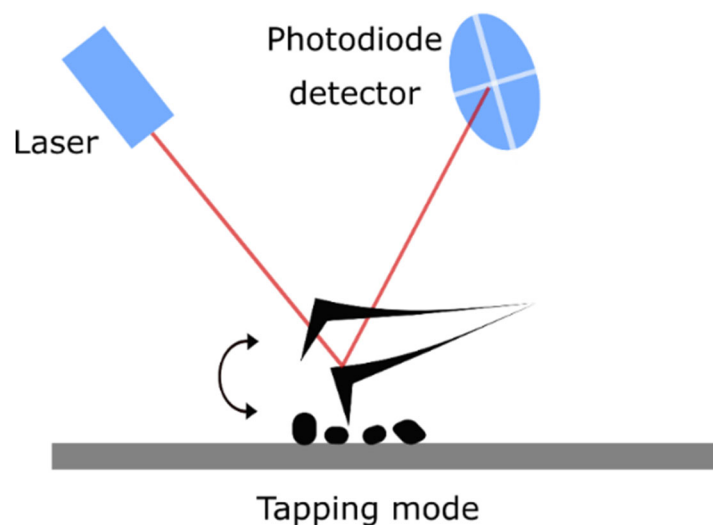


Figure 3.8 Tapping mode of atomic force microscopy.

3.3.3 Adhesive lap shear testing

Lap shear tests (papers III and IV) were conducted using a Universal Testing System (Instron 345c, USA) to examine the adhesion strength of the adhesives.

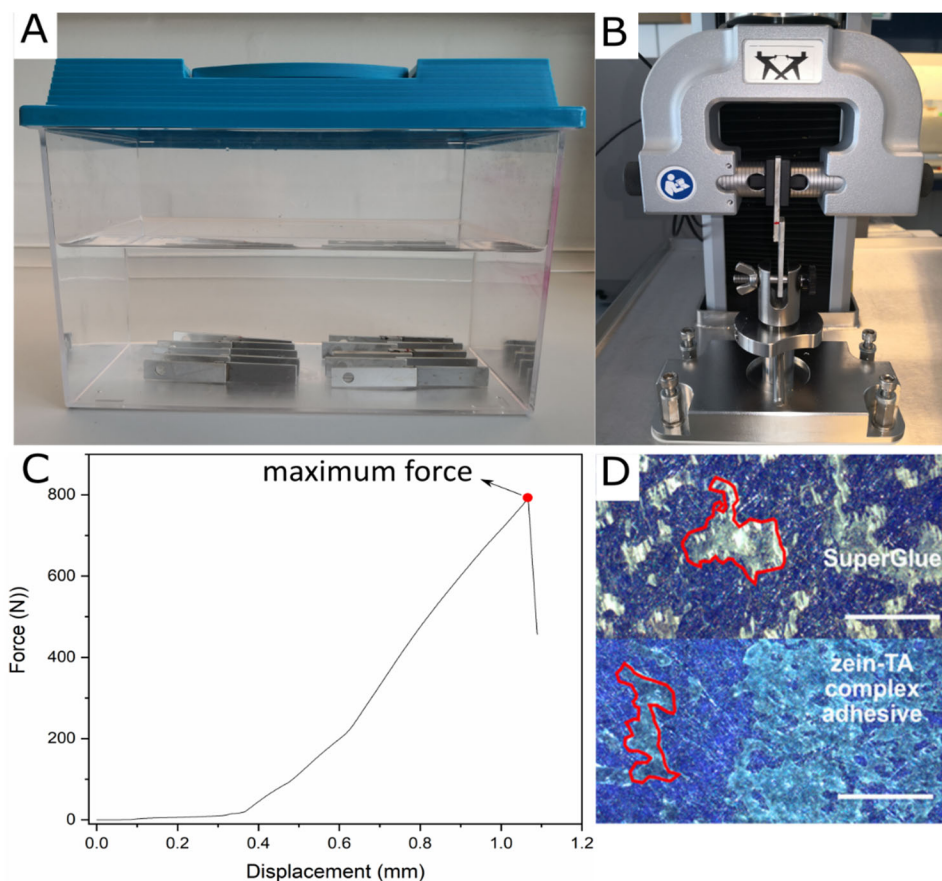


Figure 3.9 (A) and (B) Summary of immersion tests. (C) Representative force curve obtained from the lap shear test of the zein-TA coacervate. (D) Mode failure (adhesive, cohesive, or both) was assessed using light microscopy. Reprinted with permission from [119].

For preparation of the specimens, pre-cut aluminium substrates (50 mm \times 12 mm) were polished, degreased, and rinsed with demineralised water, ethanol, and acetone before use. The adhesives were then evenly applied to the substrates (overlap area 12 mm \times 12 mm), clamped, and cured under the following conditions. (i) The adhesive joints of pure gelatine and gelatine-TA were dried at ambient temperature for 48 h and then stored in a desiccator for 12 h before testing. (ii) The

zein-TA formulation and zein-TA coacervate adhesive joints were dried at ambient temperature for 1 h, cured at 120 °C for 24 h, and stored in a desiccator for 12 h prior to testing. (iii) The PPO, PPO-TA, epPPO-TA, and epPPO-TA + aminePPO adhesive joints were cured under two conditions: at ambient temperature and underwater for 48 h. (iv) The commercial adhesive (Loctite Superglue) joints, as the positive control, were cured following the instructions provided by the supplier (24 h at an ambient humidity of ~50%). After curing, the adhesive joints (five samples for each adhesive) were evaluated through lap shear testing according to a modified ASTM D1002 procedure (cross-head speed of 1.5 mm min⁻¹) (Figure 3.9B).

In addition to evaluating the dry adhesion of the adhesives, the water resistance was also examined by immersing the adhesive samples in demineralised water for different durations. After a certain immersion time, the samples were removed from the water, and the lap shear strength was immediately measured (Figure 3.9A, B). Based on the force curves of the lap shear tests, the maximum breaking force can be obtained (790 N, Figure 3.9C), which can be converted into the adhesion strength ($P = F/S = 790 \text{ N}/(12 \text{ mm} \times 12 \text{ mm}) = 5.49 \text{ MPa}$). The failure mechanism (adhesive failure, cohesive failure, or both) can be distinguished by assessing the performance of the failed joints (Figure 3.9D).

3.3.4 Underwater adhesion testing

Underwater adhesion testing (paper IV) was conducted using the Universal Testing System (Instron 345c, USA) to estimate the underwater adhesion of the underwater coacervate adhesives (Figure 3.10).

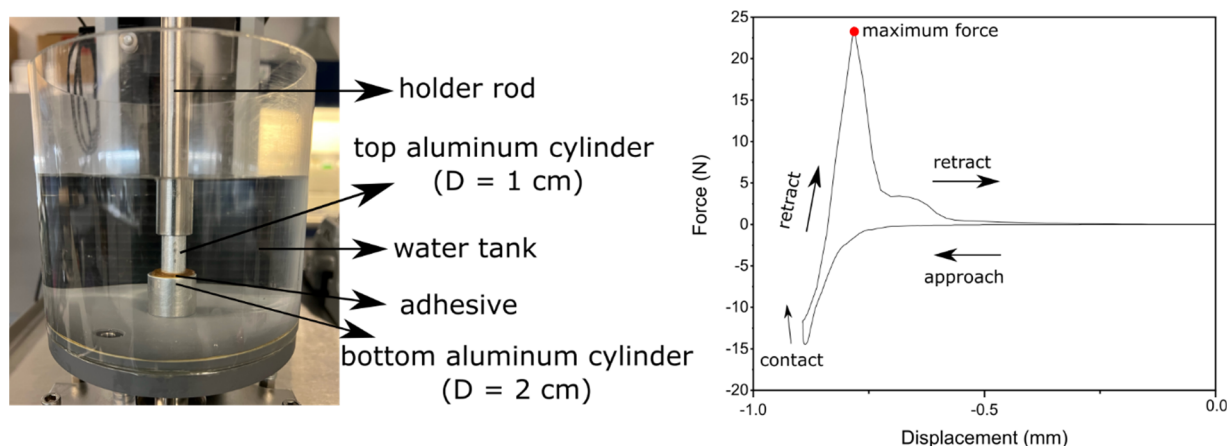


Figure 3.10 Setup of underwater adhesion testing and representative force curve of PPO-TA (5 wt.%-5 wt.%).

The setup of underwater adhesion testing is shown in Figure 3.10 (left); two aluminium cylinders were mounted on a tensile testing machine with a 50 N load cell and immersed in deionised water. To test the underwater adhesion, freshly prepared coacervate adhesive was applied using a syringe onto the bottom cylinder (diameter = 2 cm) underwater and compressed by the top cylinder (diameter = 1 cm) with a certain force (10 N) and time (1 min). The underwater adhesion strength was then obtained by pulling the top cylinder at a speed of 1 mm s^{-1} . Ten measurements were performed for each adhesive and the average adhesion strength was determined. The underwater adhesion strength and dissipation energy of the adhesives were estimated based on the force curves (Figure 3.10, right).

3.3.5 Other characterisation techniques (water contact angle, zeta potential, XPS, FT-IR)

In addition to the aforementioned techniques, other characterisation methods were also employed in my studies. Because these methods were only used as surface analytical tools and were performed following the standard procedures, the detailed theoretical principles are not given here. Water contact angle measurements were conducted using a Theta Lite optical tensiometer (Biolin Scientific, Sweden) to assess the hydrophilic/hydrophobic performance of PDA and PDA hybrid

films (papers I and II). Surface zeta potential (SurPASS3, Anton Paar GmbH, Austria) measurements were conducted at different pH (3 and 9) to examine the charging behaviour of the hierarchical PDA hybrid films (paper II). In other words, the change in zeta potential of different hybrid films could also be used to examine the construction of PDA hybrid films. Elemental analyses of the samples were performed using X-ray photoelectron spectroscopy (XPS). This technique was used to investigate the different deposition processes of PDA-based films (papers I and II) and to examine the formulation of zein-TA and AP coacervate adhesives (paper III). Finally, Fourier-transform infrared spectroscopy (FTIR) was used to characterise the functional groups to determine the interaction types in the zein-TA coacervate adhesive.

4. Summary of results

In this section, I briefly discuss the aims and main findings of my studies on coatings (*first* and *second* studies) and adhesives (*third* and *fourth* studies) inspired by mussel glue. The full content of these studies can be found in papers I–IV (appendices).

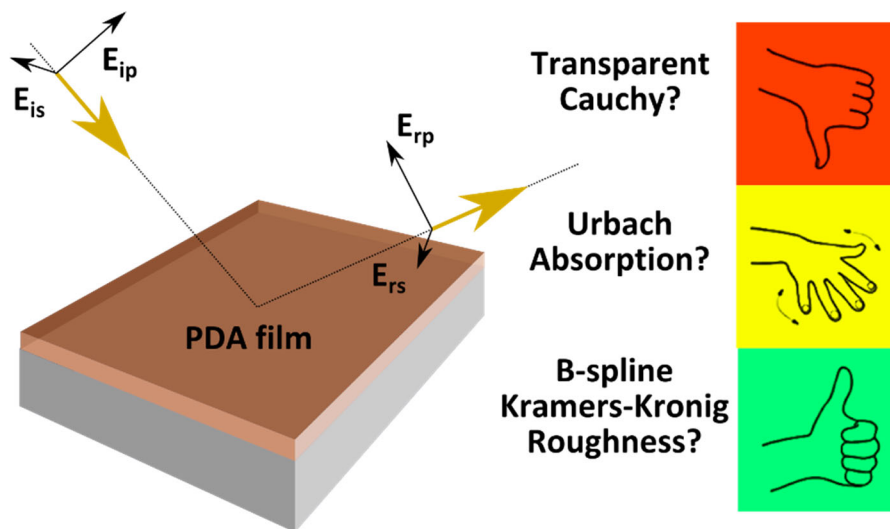


Figure 4.1 Schematic summary of the first study, ellipsometry analysis of PDA films. Reprinted with permission from [83].

The *first* study (paper I) was an ellipsometry study of PDA films, with an emphasis on developing appropriate optical models (Figure 4.1). PDA possesses complex optical behaviour that requires a careful modelling approach when analysing ellipsometric data; otherwise, inaccurate estimations of the thickness of the PDA film may be obtained. However, there are two issues in previously reported studies: (i) some studies completely ignored the light absorption of PDA films and thus used simple models such as the Cauchy model,[48,68,87,88] and (ii) a few studies considered the light absorption, yet these did not discuss the general considerations of analysing such data, such as the roughness and variable optical constants.[64,89,90] In this study, three sets of PDA coatings

were obtained using (i) short, (ii) intermediate, and (iii) long deposition times (Figure 4.2). With increasing deposition time, increased thickness and roughness of the coatings are expected, as well as variations in their optical properties (as discussed in Section 2.3.1.3.3). Based on the previously reported studies, PDA is also expected to exhibit increased light absorption with deposition time.[84,128] Thus, these three PDA coatings corresponded to

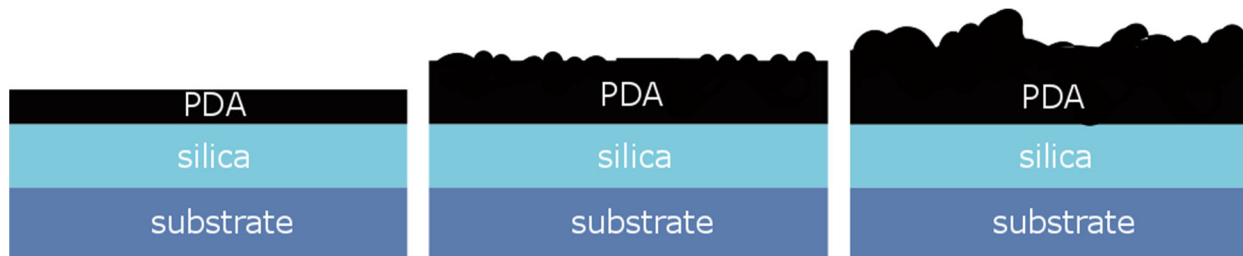


Figure 4.2 Three PDA coatings: (A) thin with weak light absorption obtained with a short deposition time (B) thick and fairly smooth with strong light absorption obtained with an intermediate deposition time, and (C) thick and rough with strong light absorption obtained with a long deposition time on the silicon wafer. Reprinted with permission from [83].

(i) A thin and smooth coating with weak light absorption (Figure 4.2, left).

(ii) A thick and fairly smooth coating with strong light absorption (Figure 4.2, middle).

(iii) A thick and rough coating with strong light absorption (Figure 4.2, right).

In each case, a step-by-step modelling approach was conducted starting from the Cauchy model, after which more model parameters were added to account for light absorption and roughness. As an example, I will here describe the step-by-step modelling for the coating obtained by the long deposition. First, the Cauchy model was used; however, the modelled Δ and Ψ spectra failed to match the experimental data (Figure 4.3, MSE = 150.7). Here, A (amplitude parameter) and the coating thickness were the free parameters. B and C were fixed at 0.01 and 0 (typical for organic transparent materials), respectively, as including them as free parameters did not significantly

improve the fitting quality. Thus, the Cauchy model was not a suitable model for describing the optical properties of PDA. To account for the light-absorbing properties of PDA, an Urbach absorption term was added to the Cauchy model. Urbach decreased the MSE (Figure 4.4, MSE = 99.7), so there was a need for including light absorption, but Urbach alone was not good enough. This is because the Urbach is for weak light absorption mainly in the UV range, and with a simple exponential dispersion shape. In contrast, PDA exhibits strong light absorption over the entire wavelength range and a complex dispersion shape rather than an exponential one. Thus, more complex models should be used to describe a thick PDA film with strong absorption.

<p>Fit Results</p> <p>MSE = 150.754 (Out-Of-Spec)</p> <p>Thickness # 3 = 35.26 ± 0.221 nm</p> <p>A = 1.965 ± 0.005662</p> <p>Total Thickness = 137.69 ± 0.221 nm</p>	<p>Optical Model</p> <table border="1"> <tr> <td colspan="2">- Layer # 3 = <u>Cauchy</u> Thickness # 3 = <u>35.26 nm</u> (fit)</td></tr> <tr> <td colspan="2">A = <u>1.965</u> (fit) B = <u>0.01000</u> C = <u>0.0000</u></td></tr> <tr> <td colspan="2">+ Urbach Absorption Parameters</td></tr> <tr> <td>Layer # 2 = <u>SIO2_JAW</u></td><td>Thickness # 2 = <u>101.43 nm</u></td></tr> <tr> <td>Layer # 1 = <u>INTR_JAW</u></td><td>Thickness # 1 = <u>1.00 nm</u></td></tr> <tr> <td colspan="2">Substrate = <u>SI_JAW</u></td></tr> </table>	- Layer # 3 = <u>Cauchy</u> Thickness # 3 = <u>35.26 nm</u> (fit)		A = <u>1.965</u> (fit) B = <u>0.01000</u> C = <u>0.0000</u>		+ Urbach Absorption Parameters		Layer # 2 = <u>SIO2_JAW</u>	Thickness # 2 = <u>101.43 nm</u>	Layer # 1 = <u>INTR_JAW</u>	Thickness # 1 = <u>1.00 nm</u>	Substrate = <u>SI_JAW</u>	
- Layer # 3 = <u>Cauchy</u> Thickness # 3 = <u>35.26 nm</u> (fit)													
A = <u>1.965</u> (fit) B = <u>0.01000</u> C = <u>0.0000</u>													
+ Urbach Absorption Parameters													
Layer # 2 = <u>SIO2_JAW</u>	Thickness # 2 = <u>101.43 nm</u>												
Layer # 1 = <u>INTR_JAW</u>	Thickness # 1 = <u>1.00 nm</u>												
Substrate = <u>SI_JAW</u>													

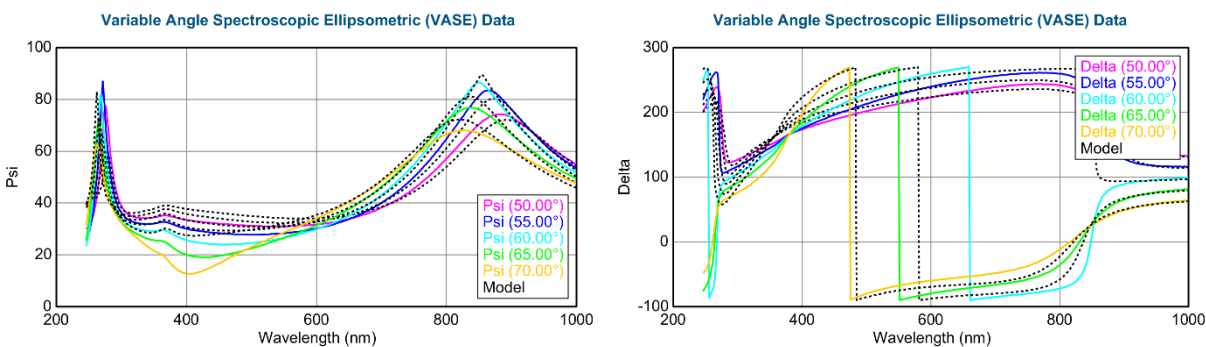


Figure 4.3 Thick and rough PDA coating with strong light absorption modelled using the Cauchy model.

Fit Results

MSE = 99.780

Thickness # 3 = 38.47 ± 0.158 nm

A = 1.887 ± 0.003577

k Amplitude = 0.09741 ± 0.001566

Exponent = 0.460 ± 0.0101

Total Thickness = 140.91 ± 0.158 nm

Optical Model

- Layer # 3 = <u>Cauchy</u> Thickness # 3 = <u>38.47 nm</u> (fit)	
A = <u>1.887</u> (fit) B = <u>0.01000</u> C = <u>0.0000</u>	
- Urbach Absorption Parameters	
k Amplitude = <u>0.09741</u> (fit) Exponent = <u>0.460</u> (fit)	
Band Edge = <u>400.0 nm</u>	
Layer # 2 = <u>SiO2_JAW</u>	Thickness # 2 = <u>101.43 nm</u>
Layer # 1 = <u>INTR_JAW</u>	Thickness # 1 = <u>1.00 nm</u>
Substrate = <u>SI_JAW</u>	

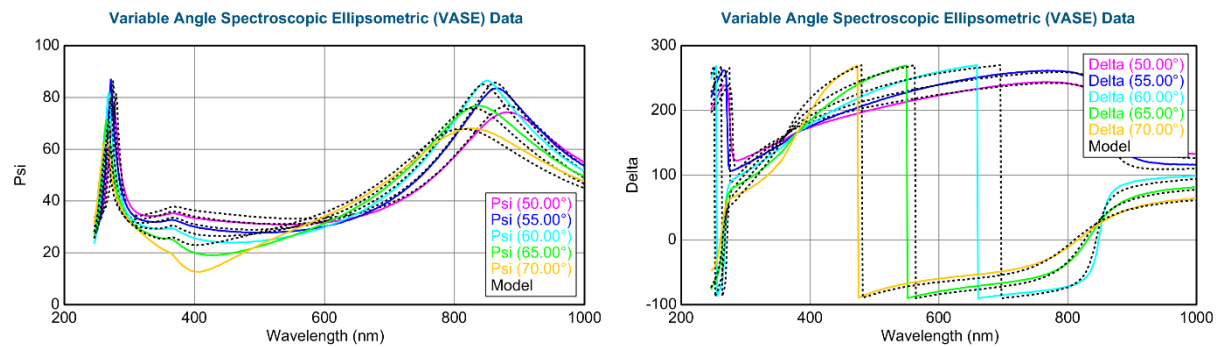


Figure 4.4 Thick and rough PDA coating with strong light absorption modelled using the Cauchy model with Urbach absorption.

When having materials with unknown optical constants, one approach is to use B-spline, which is a simple mathematical model that can provide a continuous dispersion curve with adjustable free parameters. The B-spline is not a “physical” model, and thus the Kramers–Kronig relation should be included to maintain the physical results. In addition, the number of nodes, as the free fitting parameters, needs to be minimised to avoid over-parameterisation; the optimised number of nodes was six in this study. Compared to the Cauchy and Cauchy with Urbach term models, the B-spline function afforded a better match between the model and ellipsometric data (Figure 4.5, MSE = 15.0), yet the fitting was still not perfect for short wavelengths.

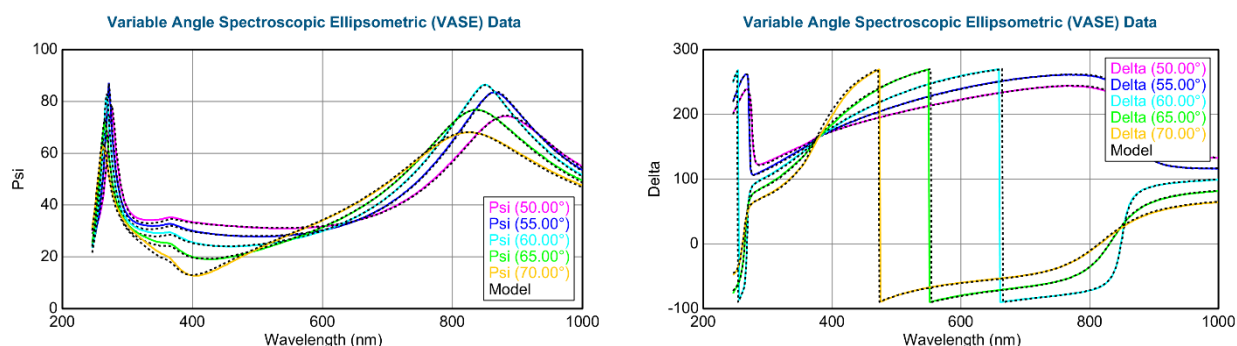
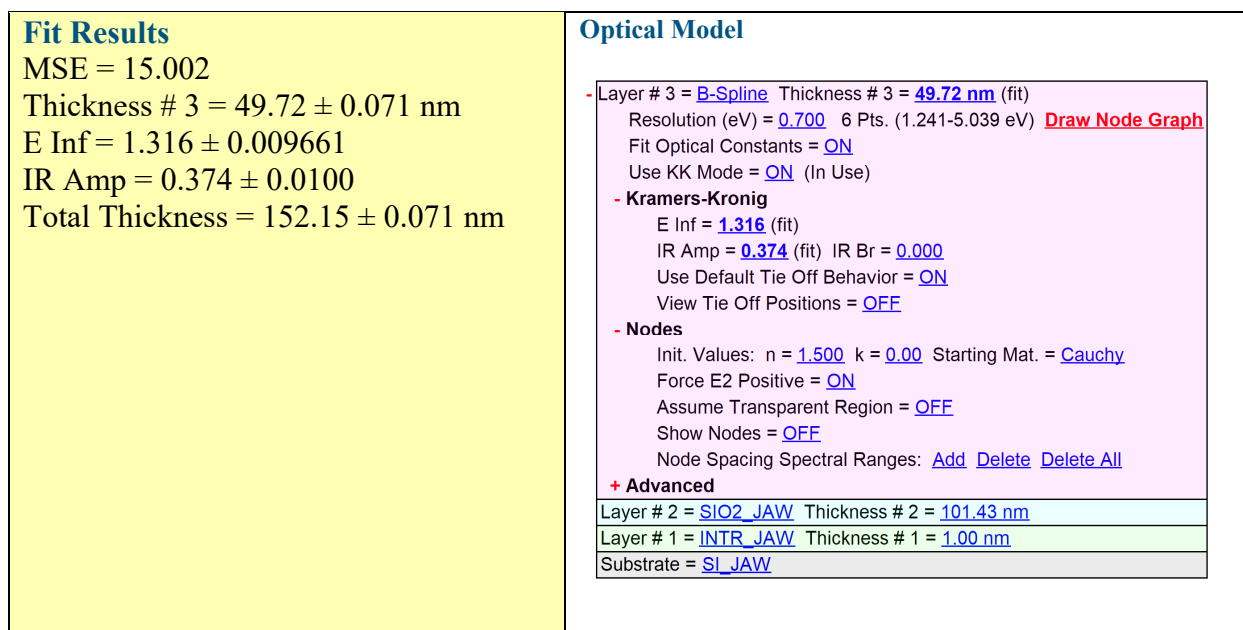


Figure 4.5 Thick and rough PDA coating with strong light absorption modelled using the KK-consistent B-spline model.

Considering that the PDA coating was prepared with a long deposition time, the surface is expected rough. In this case, a roughness layer, treated as a homogenous mixture of PDA/air, was added to the B-spline layer, which provided a perfect match across the entire range of wavelengths (Figure 4.6, MSE = 6.9). To confirm the uniqueness of the modelling outcome, the correlation between the film thickness and roughness was investigated (Figure 4.7A). Various combinations of thickness and roughness values were estimated based on their MSE values. Accordingly, the unique combination of the thickness (~ 46 nm) and roughness (~ 9 nm) providing the smallest MSE

(red region) confirmed that the modelling outcome was unique. The thicknesses estimated based on ellipsometry using different models for the PDA coating produced with a long deposition time are summarised in Figure 4.7B, which shows the values depending on the type of model. To verify the correctness of the results, three methods were used:

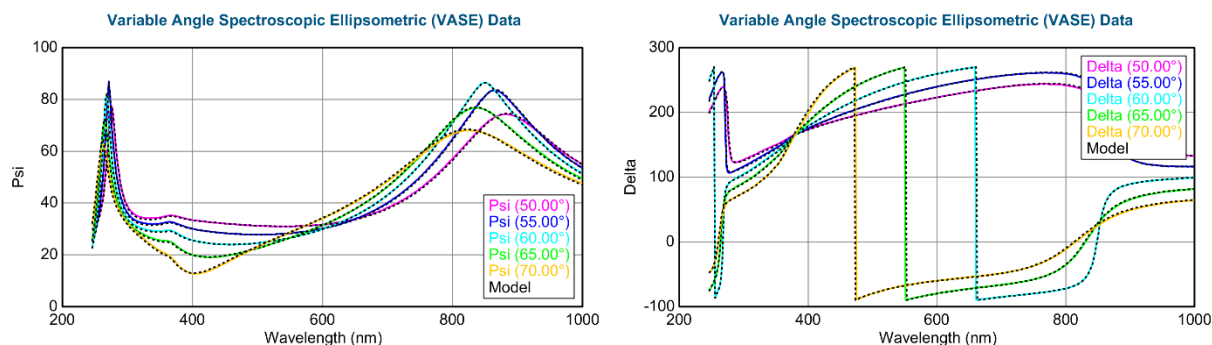
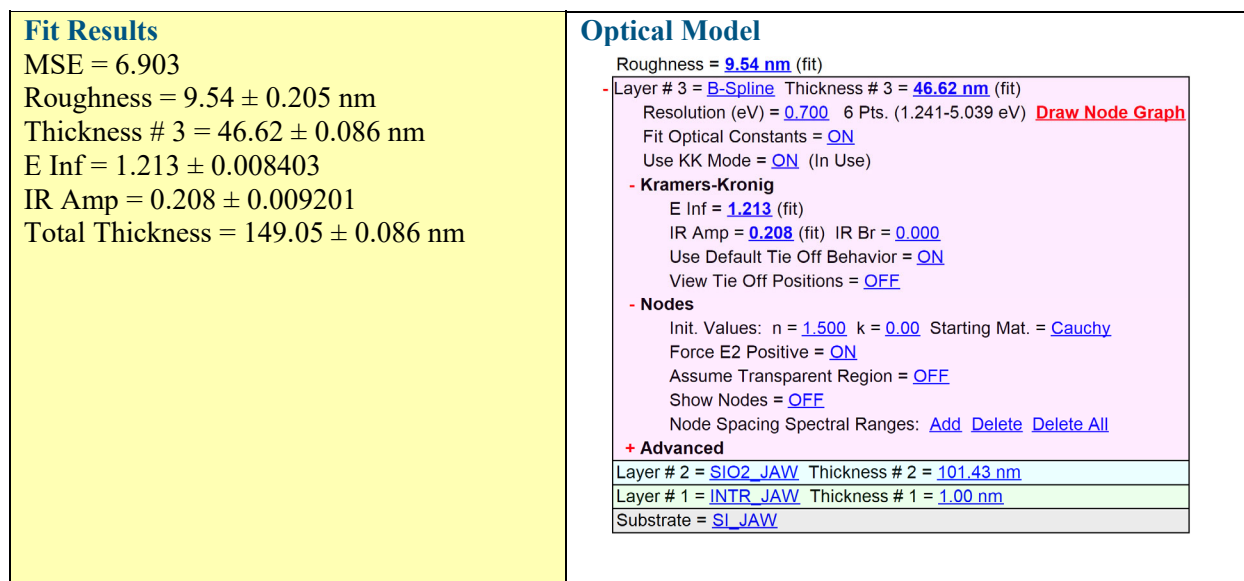


Figure 4.6 Thick and rough PDA coating with strong light absorption modelled using the KK-consistent B-spline model with roughness.

- (i) The estimated thickness from ellipsometry was compared with that estimated by AFM (Figure 4.7C, scratch test), and both values were in agreement (Figure 4.7D).
- (ii) The estimated thickness from AFM was used as an input to the model, and thus only the optical constants were unknown free parameters.

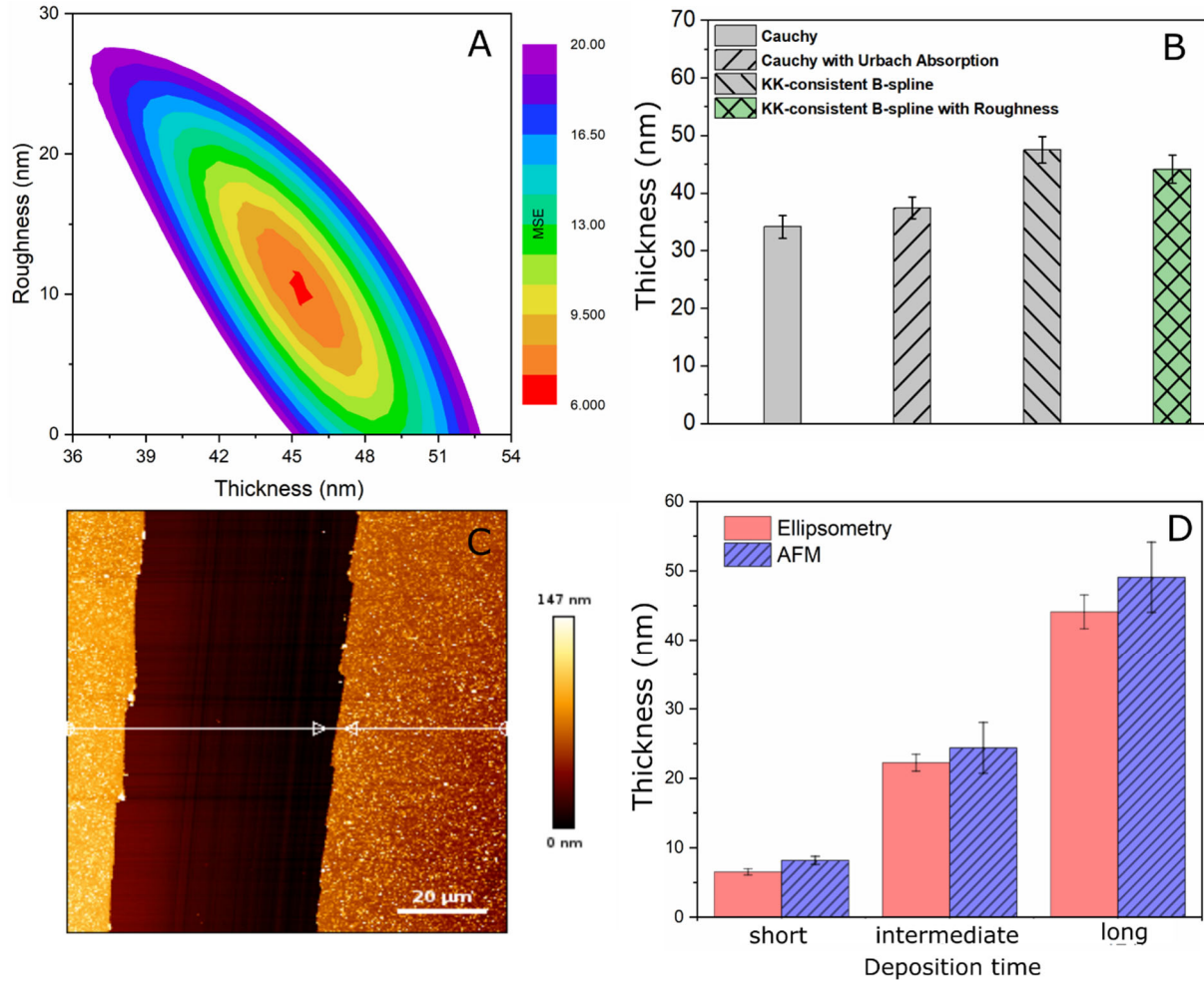


Figure 4.7 (A) Thickness–roughness uniqueness graph and (B) thickness estimations with different models for the PDA coating produced using a long deposition time. (C) Representative AFM image for the scratch test. (D) Ellipsometry and AFM thicknesses of PDA coatings. Reprinted with permission from [83].

(iii) Optical constants of thick coatings were estimated from methods (i) and (ii) and then used as inputs to analyse thin layers (with only thickness as a free parameter).

Overall, this study demonstrated several points:

(i) For materials with unknown optical constants (such as PDA), modelling the optical properties requires extra attention, because erroneously chosen models and parameters can result in inaccurate estimations (Figure 4.7B).

(ii) The chemistry and microstructure of PDA vary depending on preparation conditions. This means that PDA does not have "fixed" optical constants; therefore, a thorough modelling procedure is required for each case.

(iii) For materials with unknown n and k (such as PDA), the modelling outcome should be verified using other methods such as AFM.

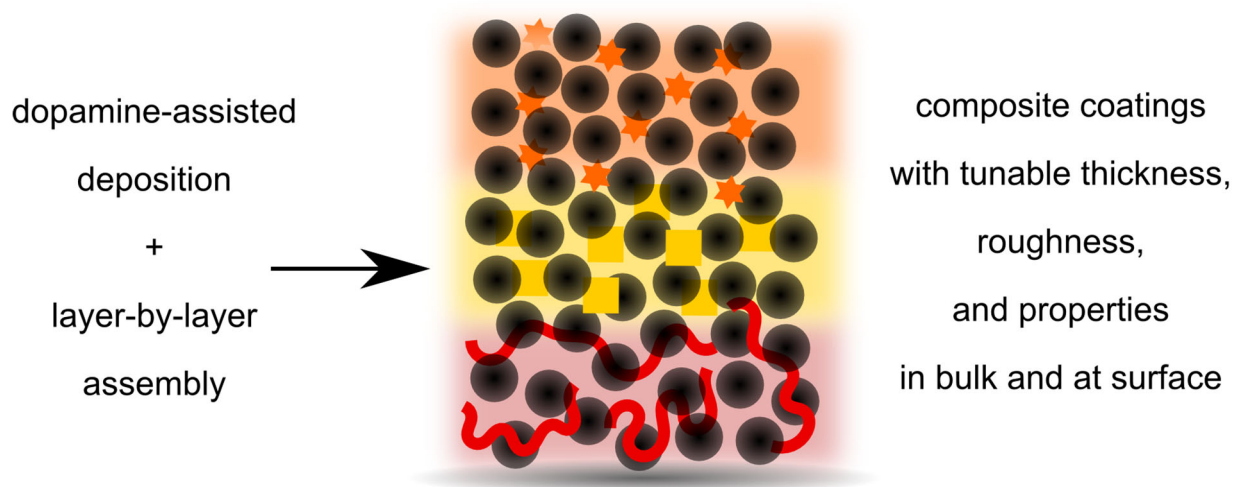


Figure 4.8 Schematic illustration of dopamine-assisted layer-by-layer deposition, yielding coatings with controlled microstructure and physicochemical properties (Cover figure for paper II). Reprinted from the submitted paper with permission from the American Chemical Society.

The **second** study (paper II) proposed a novel method for constructing coatings with controlled microstructures and physicochemical properties. DA-assisted deposition, based on catechol chemistry and inspired by mussel adhesion, allows covalent and non-covalent incorporation of various materials within a coating. Despite its versatile chemistry, this method has issues in controlling the thickness growth and excessive surface roughness/aggregation of the coating. LBL assembly has been widely used to prepare polyelectrolyte multilayer coatings. Despite its ease and practicality, this method is generally limited to charged molecules and particles. In this study, I demonstrated that combining these two approaches (DA-assisted deposition and LBL deposition)

allowed the construction of complex coatings with efficient control of the microstructure (thickness and surface morphology) and chemical composition (Figure 4.8). Two sets of experiments were conducted to investigate the benefits of this combined method.

(i) PDA, PDA/PEI (covalent deposition), and PEI/dextran (non-covalent deposition) coatings were prepared as representative cases. All of these cases showed that the combined method could improve the growth and surface morphology of the coatings. For instance, as shown in Figure 4.9, the PDA/PEI hybrid coating obtained with one-step deposition (traditional method) exhibited a decaying growth rate and reached a plateau after 10 h with a thickness of ~12 nm. In contrast, the coating obtained with the LBL deposition exhibited linear growth, and the thickness reached ~50 nm after 6×2 h depositions. Similarly, the AFM results also showed that the LBL deposition could provide a smoother morphology.

(ii) Hierarchal layers consisting of a synthetic polyelectrolyte, uncharged biopolymer, copper ions (coordination deposition), and nanoparticles were constructed. The results demonstrated that this combined method could easily adjust the coating properties (compositions, thickness, surface charge, wettability, refractive index, and others) (Figure 4.9B, C, D). For example, as shown in figure 4.9 D, by depositing each individual layer, we were able to control the surface wettability, i.e., making it more hydrophilic or hydrophobic.

Overall, the combined approach of DA-assisted deposition with LBL assembly enabled an increased coating thickness, smoother surface morphology, and varied coating properties in the Z-direction as required. Such "Lego-like" constructions open up an infinite number of possibilities for designing composite coatings, where the physicochemical properties can be adjusted both within the bulk and at the surface of the coating.

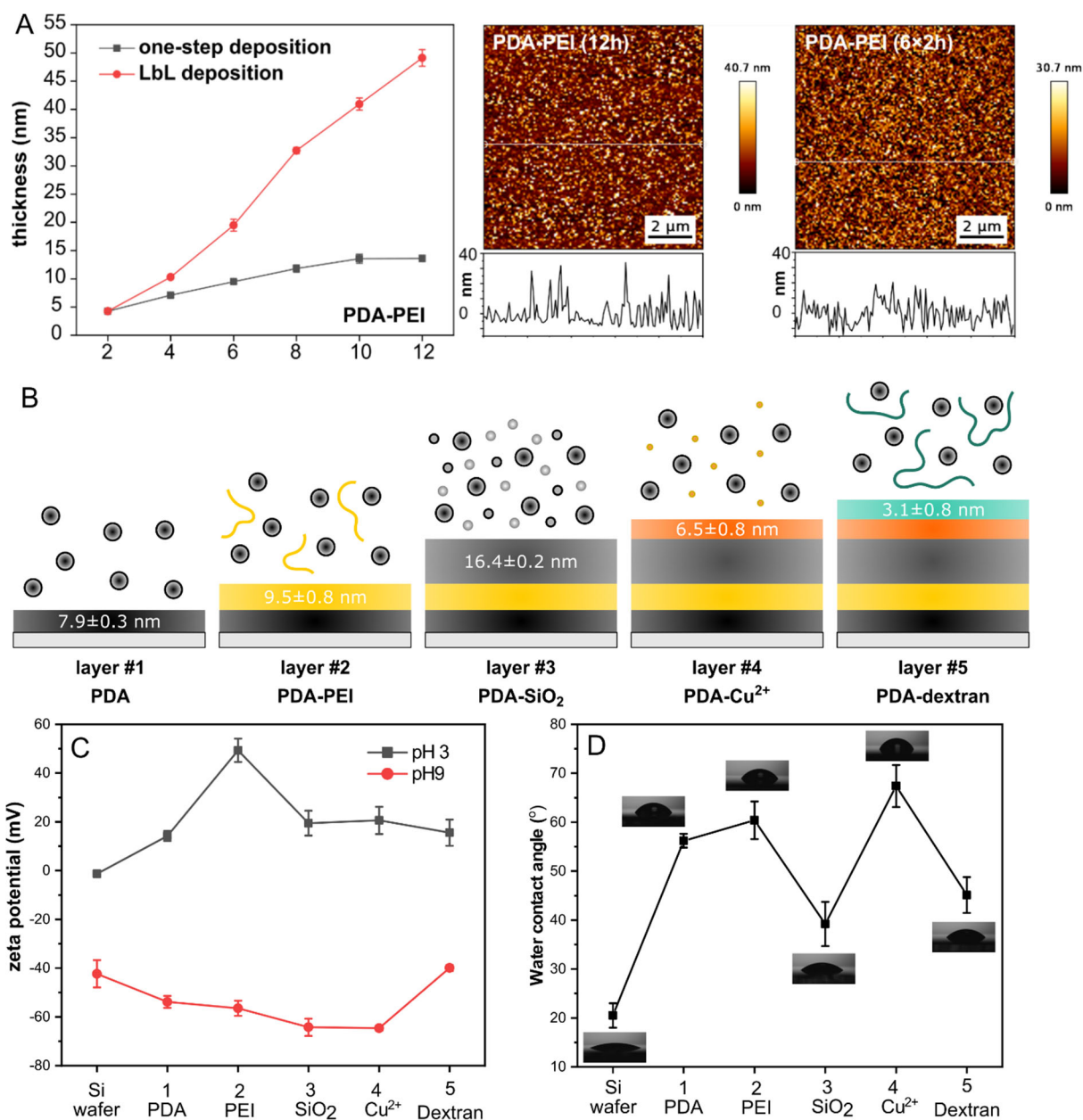


Figure 4.9 Characterisation of hybrid films. (A) PDA/PEI films obtained with one-step deposition and LBL deposition. (B–D) Hierarchical hybrid films obtained through the LBL deposition of DA, DA/PEI, DA/TEOS (precursor of SiO₂), DA/CuSO₄, and DA/dextran on a silicon wafer. (B) Schematic of the multiple layers and ellipsometry thickness of each layer. (C) Surface zeta potential and (D) water contact angle of each layer after deposition. Reprinted from the submitted paper with permission from the American Chemical Society.

Following the coating studies, adhesives for wet environments, including water-resistant adhesives (paper III) and underwater adhesives (paper IV), were also designed, inspired by mussel glue.

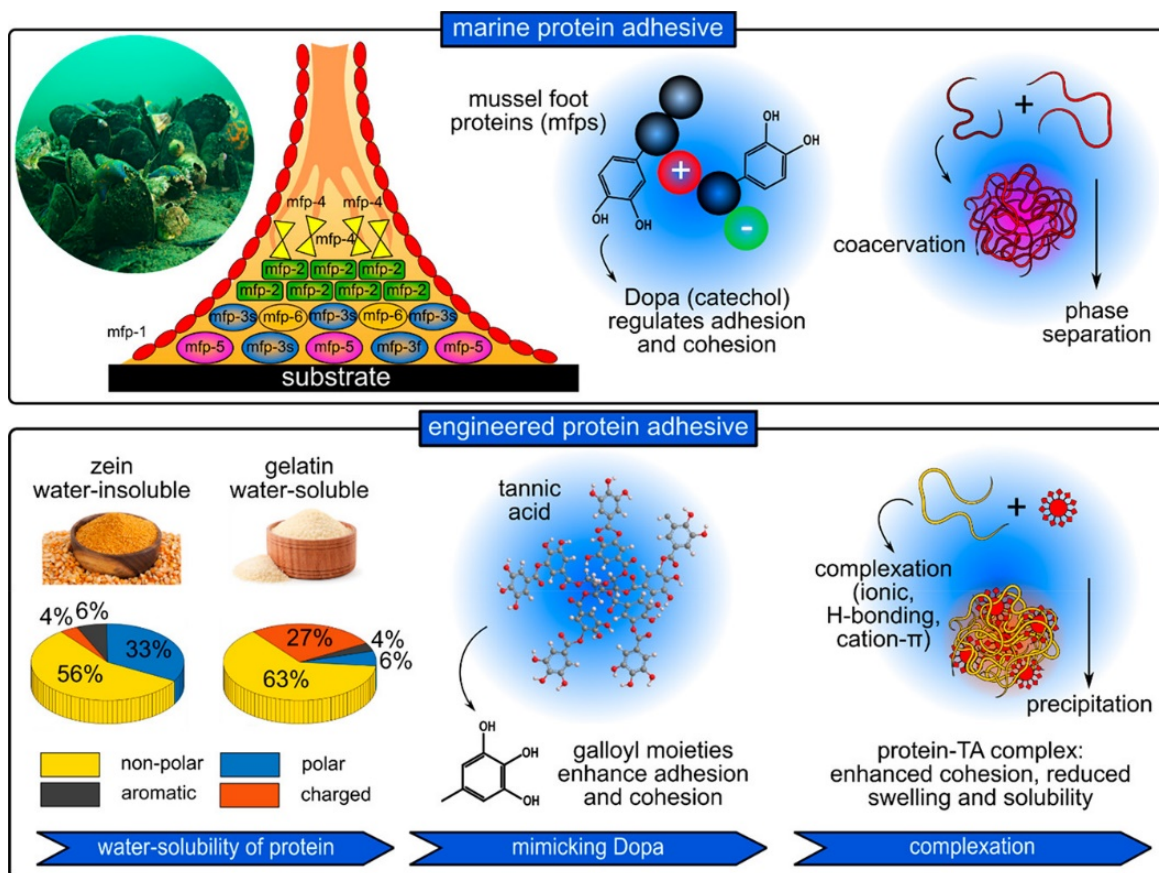


Figure 4.10 Summary of mussel protein adhesive (top) and engineered protein adhesive (bottom). Mussel adhesive contains several foot proteins (Mfps). Dopa-rich Mfp-3 and Mfp-5 can regulate adhesion and cohesion. Mfp-3s also undergoes coacervation and phase separation to form an adhesive plaque. The water solubility of the protein, addition of tannic acid, and protein-TA complex coacervation were studied to improve the water resistance of protein adhesives. Reprinted with permission from [119].

The *third* study (paper III) focused on developing bio-based adhesives with improved water resistance by enhancing the cohesive properties in the wet state. As mentioned in the background section, bio-based materials such as proteins have been investigated as potential substitutes for synthetic adhesives. Nevertheless, protein-based adhesives often exhibit poor water resistance

owing to water absorption, which limits their outdoor applications. This study aimed to inhibit water penetration and uptake in protein-based adhesives to enhance their water resistance. To achieve this, we systemically studied three factors (Figure 4.10):

- Water solubility of the protein: water-soluble (gelatine) and water-insoluble (zein) proteins were compared.
- Polyphenol: tannic acid (TA) was added to zein and gelatine solutions to mimic the catechol moiety of Dopa.
- Coacervation: proteins and TA undergo complex coacervation.

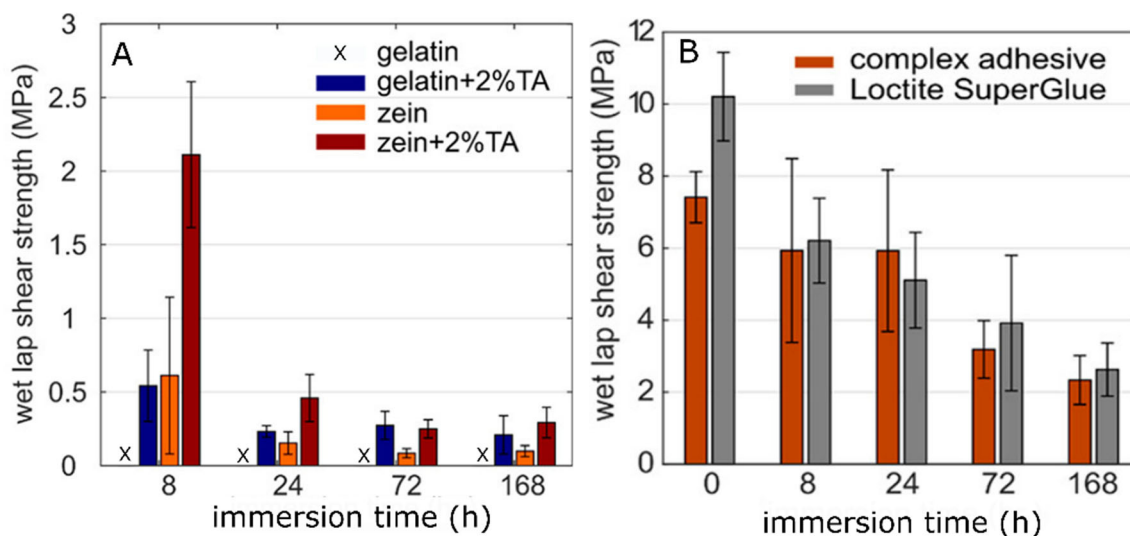


Figure 4.11 Wet lap shear strength of the adhesives with increasing immersion time. (A) Gelatine- and zein-based adhesives (obtained by solution mixing) with and without tannic acid. (B) Zein-tannic acid complex coacervate adhesive and commercial adhesive (Loctite SuperGlue). Reprinted with permission from [119].

The effects of these factors on the water resistance were estimated using wet lap shear tests (short- and long term immersion in water). The results indicated that water solubility was an important parameter, and zein exhibited stronger water resistance than gelatine (Figure 4.11A) after a short immersion time. However, zein also exhibited poor long-term water resistance. Thus, although

water insolubility of the protein can prevent water penetration to enhance water resistance, it cannot ensure prolonged durability.

TA was then added, which is a common approach reported in the literature (as discussed in Section 2.3.2) to enhance the performance of adhesives under wet conditions. It was found that TA could improve the water resistance of zein and gelatine in the short term through cross-linking of the proteins; nevertheless, it could not ensure longer durability (Figure 4.11A).

The third step was coacervation driven by the different interactions between the protein and TA, which formed insoluble protein-TA complex coacervate adhesives. It was found that the zein-TA complex coacervate exhibited significantly improved water resistance and even emulated commercial glue.

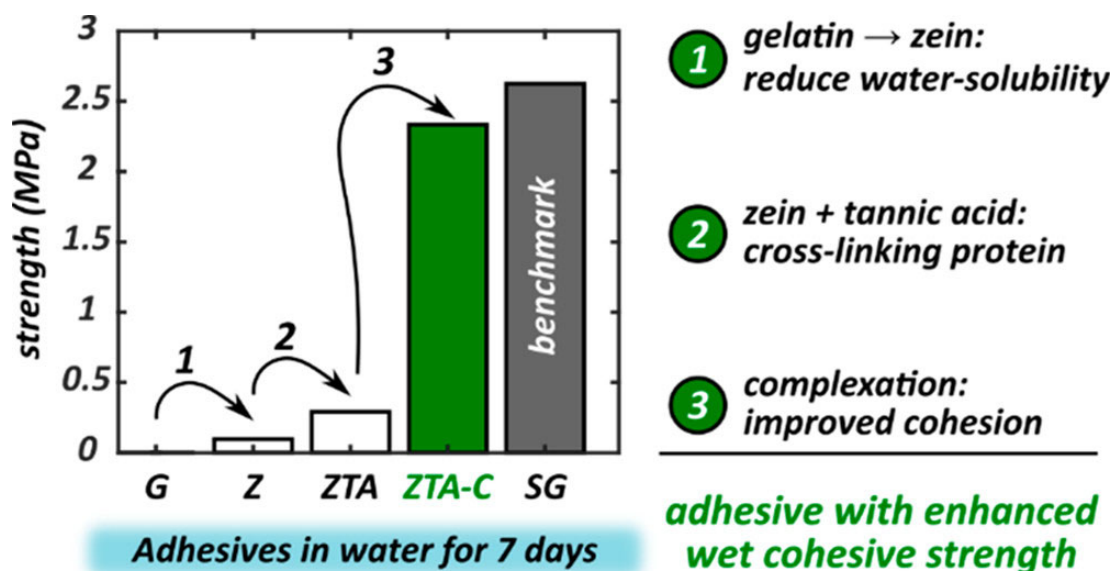


Figure 4.12 Summary of the water resistance (lap shear strength) evaluation of adhesives for gelatine (G), zein (Z), zein with tannic acid (ZTA), zein-tannic acid complex coacervation (ZTA-C), and Loctite SuperGlue (SG) adhesive joints immersed in water for 7 days. Reprinted with permission from [119].

Overall, this study suggests that by combining mechanisms that can reduce water uptake within the biopolymer adhesive (reducing water-solubility, cross-linking, coacervation, etc.), one can improve the wet cohesive properties and thus improve the water resistance (Figure 4.12). Based on our short study, coacervation appears to be an efficient mechanism that requires further investigation.

In the *fourth* study (paper IV), I designed a novel underwater adhesive based on the coacervation of poly(propylene oxide) (PPO and TA, which provided strong tackiness and could cure underwater (Figure 4.13). Polymer-TA coacervation is a promising approach for designing underwater adhesives (as discussed in Section 2.3.2), where the galloyl structure of TA mimics catechol in mussel glue. More importantly, the formed coacervate adhesive provides reduced water solubility and improves wetting properties. However, because these coacervate adhesives are normally formed via non-covalent bonding (hydrogen bonding and ionic interactions), one issue is that they cannot be cured to form a permanent bond. Thus, two systems were designed in this study: (i) a PPO-TA underwater adhesive and (ii) a curable underwater adhesive based on PPO derivatives and TA.

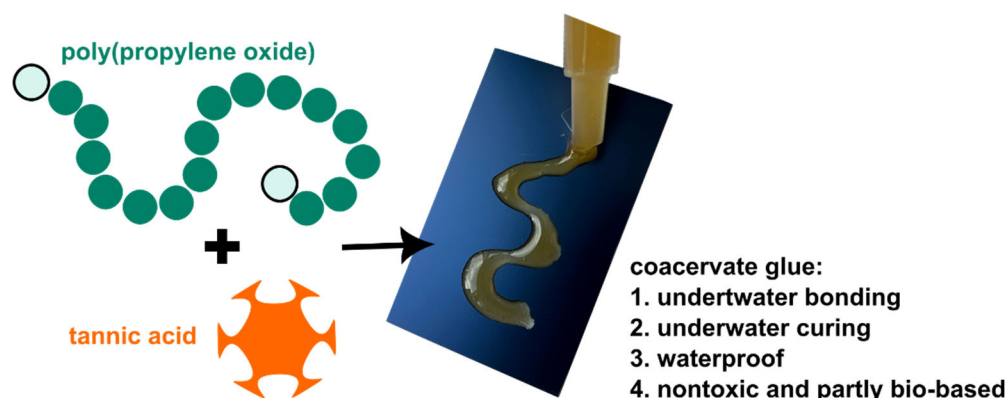


Figure 4.13 Schematic of the self-curable underwater adhesive obtained with poly(propylene oxide) and tannic acid (Cover figure for paper IV). Reprinted from the submitted paper with permission from the Royal Society of Chemistry.

PPO is a suitable material for producing underwater adhesive because it has several benefits:

- (i) It is non-toxic;
- (ii) Relatively easy to solubilize in water;
- (iii) It is commercially available with different end group functionalities.

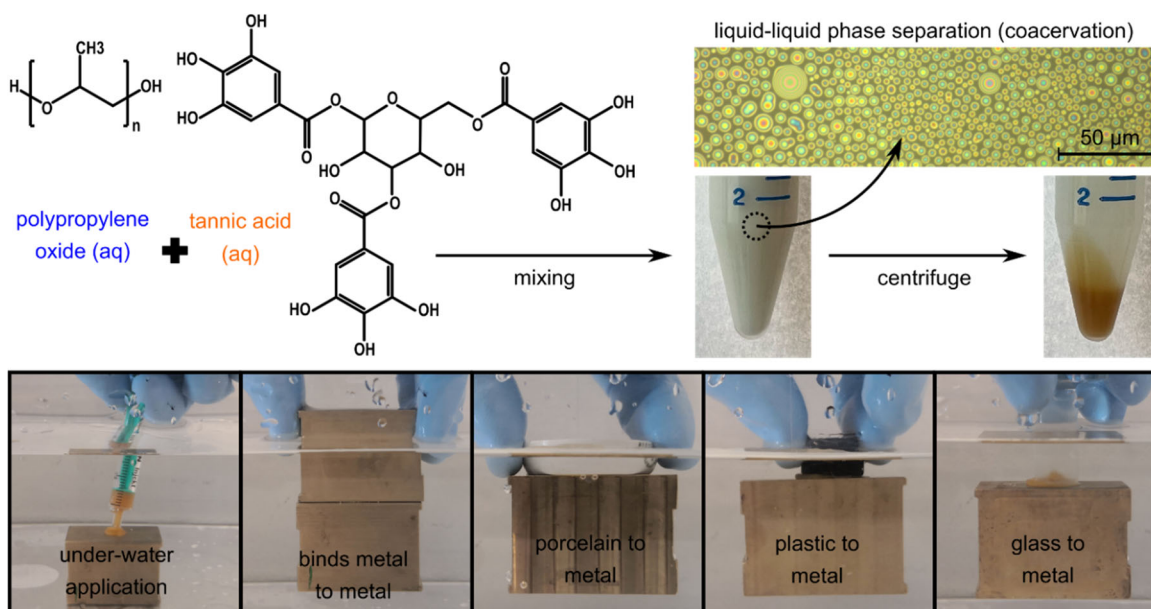


Figure 4.14 Characterisation of PPO-TA coacervate formation and underwater bonding tests on different materials. Reprinted from the submitted paper with permission from the Royal Society of Chemistry.

The PPO-TA adhesive was readily produced by mixing PPO with hydroxyl end groups and TA aqueous solutions. After mixing, the solution became milky immediately because of the coacervation, where the polymer-rich droplets were dispersed in the water-rich phase (Figure 4.14). Upon centrifugation, the PPO-TA coacervate adhesive (light orange in colour) was obtained at the bottom. It was found that the PPO-TA adhesive not only provided strong underwater adhesion to aluminium (Figure 4.15A, ~350 kPa) but also exhibited instant underwater bonding ability to different materials, such as metal, porcelain, plastic, and glass (Figure 4.14). However,

because there is no covalent bonding between PPO and TA, the PPO-TA coacervate cannot cure. Therefore, the adhesive after 2 days in water showed a lap shear strength of zero (Figure 4.15 B).

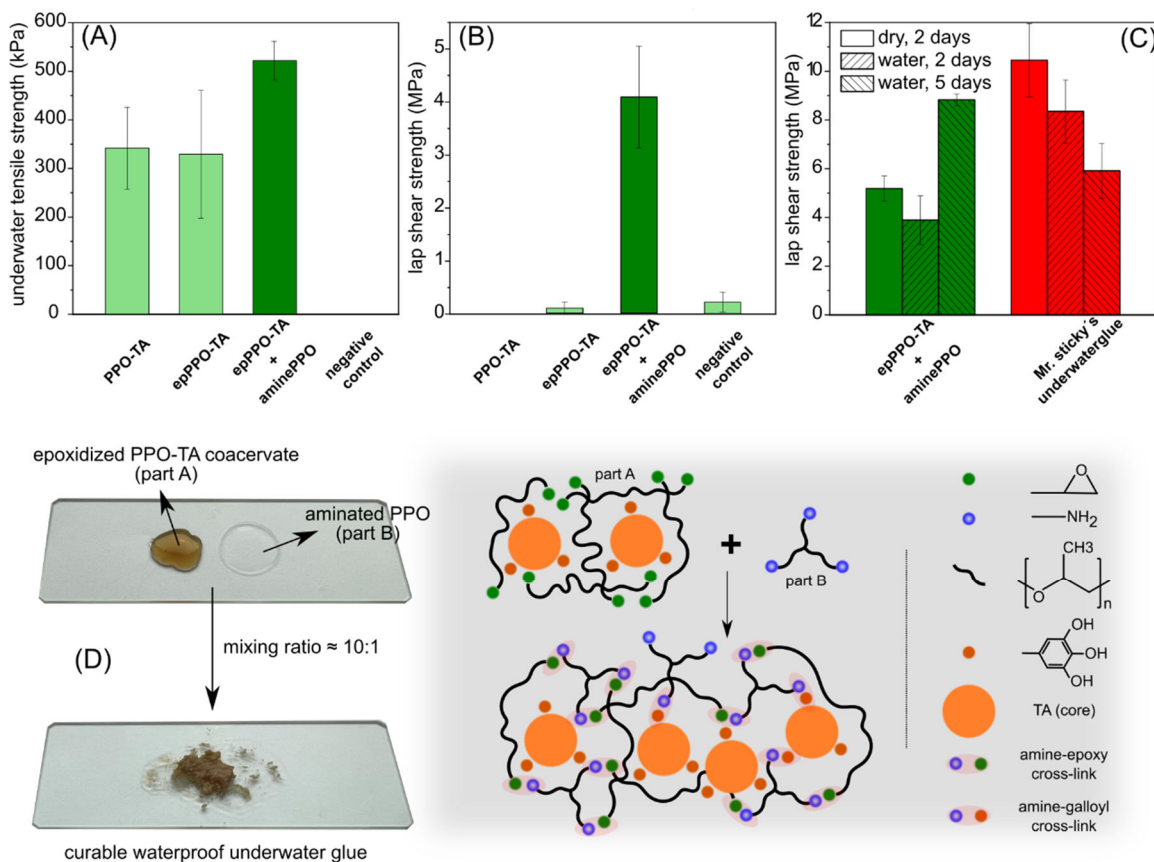


Figure 4.15 Evaluation of (A) underwater adhesion, (B) curing performance after 2 days in water, and (C) curing performance of the two-component adhesive in air and water along with the commercial benchmark. (D) Schematic illustration of the two-component adhesive. Reprinted from the submitted paper with permission from the Royal Society of Chemistry.

To make the adhesive curable, I designed a two-part adhesive based on the epoxide-phenol-amine chemistry. Part I (epPPO-TA) was prepared by the coacervation of diepoxide-terminated PPO (epPPO) and TA, as described earlier. The collected coacervate shows underwater adhesion, but it cannot cure itself underwater. Part I required a hardener (cross-linker, curing agent), so it can undergo covalent cross-linking and form a curable adhesive underwater. Herein, triamine-

terminated PPO (aminePPO) was mixed with Part I as a hardener in an optimised ratio. The epoxide and amine groups are expected to react at room temperature. Also, the amine groups should form both covalent (Schiff base and Michael addition) and non-covalent interactions with TA (Figure 4.15D). Thus, these reactions are expected to provide a curable underwater adhesive. The two-part adhesive was found to exhibit improved underwater adhesion strength (Figure 4.15A, ~500 kPa), which was attributed to the stronger cohesiveness of this system. More importantly, this two-part adhesive could cure underwater and realised a significantly enhanced lap shear strength of ~9 MPa after immersion in water for 5 days, which was more favourable waterproofing than that of the Mr. Sticky's adhesive (commercial underwater glue) (Figure 4.15C).

In summary, PPO-TA coacervation provides a viscous material with underwater bonding property. More importantly, a curing functionality is obtained by designing a two-part system: epoxidized PPO-TA coacervate as part I and aminated PPO as part II.

5. Perspectives

Nature provides a wealth of inspiration for the creation of functional materials for various applications. My PhD studies were inspired by mussel glue that works on functional coatings and adhesives. Following my research on these two parts, several further studies can be conducted.

For the ellipsometry studies of thick PDA films, it was suggested that an upper roughness layer may be required in the optical model. However, in the typical ellipsometry analysis, the roughness layer is generally assumed as a homogenous 50:50 mixture of PDA and air, which might not be the “real” roughness profile. Therefore, one possible direction would be to examine the roughness of the film using AFM and use that as an input to the optical model for ellipsometric analysis.

In addition to PDA film characterisation, the concept of DA-assisted LBL deposition in my second study provides a concept for building layers in a universal manner. One future direction is conducting the LBL deposition process in a flow cell, where the parameters can be easily adjusted. Another possible direction is to focus on applications where coatings with Cu^{2+} or dextran can be made for high-refractive index or anti-fouling materials.

For the adhesive part, the zein-TA complex coacervate adhesive exhibits promising water resistance. A further investigation of how different factors such as the solvent composition and mixing ratios can affect coacervate properties such as microstructure, followed by research on how these properties relate to the adhesive properties including bonding strength and water resistance, is beneficial for designing commercially competitive zein-based adhesives. In the case of the PPO-based underwater adhesive system, in the future, it would be beneficial to study using PPO derivatives produced with natural materials and replacing the short-chain amine hardener with other natural polyamine components to remove the environmental footprints.

6. References

- [1] H. Fan, J.P. Gong, Bioinspired Underwater Adhesives, *Adv. Mater.* (2021). <https://doi.org/10.1002/adma.202102983>.
- [2] C. Cai, Z. Chen, Y. Chen, H. Li, Z. Yang, H. Liu, Mechanisms and applications of bioinspired underwater/wet adhesives, *J. Polym. Sci.* (2021). <https://doi.org/10.1002/pol.20210521>.
- [3] J.H. Waite, Mussel adhesion – essential footwork, *J. Exp. Biol.* 220 (2017) 517–530. <https://doi.org/10.1242/jeb.134056>.
- [4] B.P. Lee, P.B. Messersmith, J.N. Israelachvili, J.H. Waite, Mussel-inspired adhesives and coatings, *Annu. Rev. Mater. Res.* 41 (2011) 99–132. <https://doi.org/10.1146/annurev-matsci-062910-100429>.
- [5] T. Priemel, R. Palia, M. Babych, C.J. Thibodeaux, S. Bourgault, M.J. Harrington, Compartmentalized processing of catechols during mussel byssus fabrication determines the destiny of DOPA, *Proc. Natl. Acad. Sci. U. S. A.* 117 (2020) 7613–7621. <https://doi.org/10.1073/pnas.1919712117>.
- [6] B.K. Ahn, S. Das, R. Linstadt, Y. Kaufman, N.R. Martinez-Rodriguez, R. Mirshafian, E. Kesselman, Y. Talmon, B.H. Lipshutz, J.N. Israelachvili, J.H. Waite, High-performance mussel-inspired adhesives of reduced complexity, *Nat. Commun.* 6 (2015) 4–10. <https://doi.org/10.1038/ncomms9663>.
- [7] Y. Li, J. Cheng, P. Delparastan, H. Wang, S.J. Sigg, K.G. DeFrates, Y. Cao, P.B. Messersmith, Molecular design principles of Lysine-DOPA wet adhesion, *Nat. Commun.* 11 (2020). <https://doi.org/10.1038/s41467-020-17597-4>.
- [8] M.A. Gebbie, W. Wei, A.M. Schrader, T.R. Cristiani, H.A. Dobbs, M. Idso, B.F. Chmelka, J. Herbert Waite, J.N. Israelachvili, Tuning underwater adhesion with cation- π interactions, *Nat. Chem.* 9 (2017) 473–479. <https://doi.org/10.1038/nchem.2720>.
- [9] B.K. Ahn, Perspectives on Mussel-Inspired Wet Adhesion, *J. Am. Chem. Soc.* 139 (2017) 10166–10171. <https://doi.org/10.1021/jacs.6b13149>.
- [10] E.C. Bell, J.M. Gosline, Strategies for life in flow: Tenacity, morphometry, and probability of dislodgment of two *Mytilus* species, *Mar. Ecol. Prog. Ser.* 159 (1997) 197–208. <https://doi.org/10.3354/meps159197>.
- [11] E.C. Bell, J.M. Gosline, Mechanical design of mussel byssus: Material yield enhances attachment strength, *J. Exp. Biol.* 199 (1996) 1005–1017. <https://doi.org/10.1242/jeb.199.4.1005>.
- [12] H.G. Silverman, F.F. Roberto, Understanding marine mussel adhesion, *Mar. Biotechnol.* 9 (2007) 661–681. <https://doi.org/10.1007/s10126-007-9053-x>.
- [13] J.R. Burkett, J.L. Wojtas, J.L. Cloud, J.J. Wilker, A method for measuring the adhesion strength of marine mussels, *J. Adhes.* 85 (2009) 601–615.

<https://doi.org/10.1080/00218460902996903>.

- [14] Q. Guo, J. Chen, J. Wang, H. Zeng, J. Yu, Recent progress in synthesis and application of mussel-inspired adhesives, *Nanoscale*. 12 (2020) 1307–1324.
<https://doi.org/10.1039/c9nr09780e>.
- [15] P. Kord Forooshani, B.P. Lee, Recent approaches in designing bioadhesive materials inspired by mussel adhesive protein, *J. Polym. Sci. Part A Polym. Chem.* 55 (2017) 9–33.
<https://doi.org/10.1002/pola.28368>.
- [16] W. Wei, J. Yu, C. Broomell, J.N. Israelachvili, J.H. Waite, Hydrophobic enhancement of dopa-mediated adhesion in a mussel foot protein, *J. Am. Chem. Soc.* 135 (2013) 377–383.
<https://doi.org/10.1021/ja309590f>.
- [17] M.J. Harrington, A. Masic, N. Holten-Andersen, J.H. Waite, P. Fratzl, Iron-Clad Fibers: A Metal-Based Biological Strategy for Hard Flexible Coatings, *Science*. 328 (2010) 216–220. <https://doi.org/10.1126/science.1181044>.
- [18] D.S. Hwang, H. Zeng, A. Masic, M.J. Harrington, J.N. Israelachvili, J.H. Waite, Protein- and metal-dependent interactions of a prominent protein in mussel adhesive plaques, *J. Biol. Chem.* 285 (2010) 25850–25858. <https://doi.org/10.1074/jbc.M110.133157>.
- [19] J. Yu, W. Wei, E. Danner, J.N. Israelachvili, J.H. Waite, Effects of interfacial redox in mussel adhesive protein films on mica, *Adv. Mater.* 23 (2011) 2362–2366.
<https://doi.org/10.1002/adma.201003580>.
- [20] H. Zhao, J.H. Waite, Proteins in Load-Bearing Junctions: The Histidine-Rich Metal-Binding Protein of Mussel Byssus, *Biochemistry*. 45 (2006) 14223–14231.
<https://doi.org/10.1021/bi061677n>.
- [21] H. Zhao, J.H. Waite, Linking adhesive and structural proteins in the attachment plaque of *Mytilus californianus*, *J. Biol. Chem.* 281 (2006) 26150–26158.
<https://doi.org/10.1074/jbc.M604357200>.
- [22] E.W. Danner, Y. Kan, M.U. Hammer, J.N. Israelachvili, J.H. Waite, Adhesion of mussel foot protein Mefp-5 to mica: An underwater superglue, *Biochemistry*. 51 (2012) 6511–6518. <https://doi.org/10.1021/bi3002538>.
- [23] J. Yu, *Adhesive Interactions of Mussel Foot Proteins*, Springer International Publishing, Cham, 2014. <https://doi.org/10.1007/978-3-319-06031-6>.
- [24] N.R.M. Rodriguez, S. Das, Y. Kaufman, J.N. Israelachvili, J.H. Waite, Interfacial pH during mussel adhesive plaque formation, *Biofouling*. 31 (2015) 221–227.
<https://doi.org/10.1080/08927014.2015.1026337>.
- [25] D.G. Barrett, D.E. Fullenkamp, L. He, N. Holten-Andersen, K.Y.C. Lee, P.B. Messersmith, PH-based regulation of hydrogel mechanical properties through mussel-inspired chemistry and processing, *Adv. Funct. Mater.* 23 (2013) 1111–1119.
<https://doi.org/10.1002/adfm.201201922>.
- [26] R. Mirshafian, W. Wei, J.N. Israelachvili, J.H. Waite, α,β -Dehydro-Dopa: A Hidden Participant in Mussel Adhesion, *Biochemistry*. 55 (2016) 743–750.

<https://doi.org/10.1021/acs.biochem.5b01177>.

- [27] S. Chen, B. Shen, F. Zhang, H. Hong, J. Pan, Mussel-Inspired Graphene Film with Enhanced Durability as a Macroscale Solid Lubricant, *ACS Appl Mater Interfaces*. (2019). <https://doi.org/10.1021/acsami.9b10404>.
- [28] J. Yu, Y. Kan, M. Rapp, E. Danner, W. Wei, S. Das, D.R. Miller, Y. Chen, J.H. Waite, J.N. Israelachvili, Adaptive hydrophobic and hydrophilic interactions of mussel foot proteins with organic thin films, *Proc. Natl. Acad. Sci. U. S. A.* 110 (2013) 15680–15685. <https://doi.org/10.1073/pnas.1315015110>.
- [29] Y. Li, M. Liao, J. Zhou, Catechol and Its Derivatives Adhesion on Graphene: Insights from Molecular Dynamics Simulations, *J. Phys. Chem. C*. 122 (2018) 22965–22974. <https://doi.org/10.1021/acs.jpcc.8b06392>.
- [30] Z. Wang, Y. Zou, Y. Li, Y. Cheng, Metal-Containing Polydopamine Nanomaterials: Catalysis, Energy, and Theranostics, *Small*. 16 (2020) 1–21. <https://doi.org/10.1002/smll.201907042>.
- [31] A.R. Narkar, B. Barker, M. Clisch, J. Jiang, B.P. Lee, pH Responsive and Oxidation Resistant Wet Adhesive based on Reversible Catechol-Boronate Complexation, *Chem. Mater.* 28 (2016) 5432–5439. <https://doi.org/10.1021/acs.chemmater.6b01851>.
- [32] H.-C. Yang, K.-J. Liao, H. Huang, Q.-Y. Wu, L.-S. Wan, Z.-K. Xu, Mussel-inspired modification of a polymer membrane for ultra-high water permeability and oil-in-water emulsion separation, *J. Mater. Chem. A*. 2 (2014) 10225–10230. <https://doi.org/10.1039/C4TA00143E>.
- [33] Q. Lu, E. Danner, J.H. Waite, J.N. Israelachvili, H. Zeng, D.S. Hwang, Adhesion of mussel foot proteins to different substrate surfaces, *J. R. Soc. Interface*. 10 (2013). <https://doi.org/10.1098/rsif.2012.0759>.
- [34] C. Zhang, B. Wu, Y. Zhou, F. Zhou, W. Liu, Z. Wang, Mussel-inspired hydrogels: From design principles to promising applications, *Chem. Soc. Rev.* 49 (2020) 3605–3637. <https://doi.org/10.1039/c9cs00849g>.
- [35] Y. Tian, Y. Cao, Y. Wang, W. Yang, J. Feng, Realizing ultrahigh modulus and high strength of macroscopic graphene oxide papers through crosslinking of mussel-inspired polymers, *Adv. Mater.* 25 (2013) 2980–2983. <https://doi.org/10.1002/adma.201300118>.
- [36] M. V. Rapp, G.P. Maier, H.A. Dobbs, N.J. Higdon, J.H. Waite, A. Butler, J.N. Israelachvili, Defining the Catechol–Cation Synergy for Enhanced Wet Adhesion to Mineral Surfaces, *J. Am. Chem. Soc.* 138 (2016) 9013–9016. <https://doi.org/10.1021/jacs.6b03453>.
- [37] G.P. Maier, M. V. Rapp, J.H. Waite, J.N. Israelachvili, A. Butler, Adaptive synergy between catechol and lysine promotes wet adhesion by surface salt displacement, *Science*. 349 (2015) 628–632. <https://doi.org/10.1126/science.aab0556>.
- [38] M. Shin, J.Y. Shin, K. Kim, B. Yang, J.W. Han, N.K. Kim, H.J. Cha, The position of lysine controls the catechol-mediated surface adhesion and cohesion in underwater mussel adhesion, *J. Colloid Interface Sci.* 563 (2020) 168–176.

<https://doi.org/10.1016/j.jcis.2019.12.082>.

- [39] Y. Li, T. Wang, L. Xia, L. Wang, M. Qin, Y. Li, W. Wang, Y. Cao, Single-molecule study of the synergistic effects of positive charges and Dopa for wet adhesion, *J. Mater. Chem. B*. 5 (2017) 4416–4420. <https://doi.org/10.1039/C7TB00131B>.
- [40] B.D.B. Tiu, P. Delparastan, M.R. Ney, M. Gerst, P.B. Messersmith, Cooperativity of Catechols and Amines in High-Performance Dry/Wet Adhesives, *Angew. Chemie - Int. Ed.* 59 (2020) 16616–16624. <https://doi.org/10.1002/anie.202005946>.
- [41] W. Wei, Y. Tan, N.R. Martinez Rodriguez, J. Yu, J.N. Israelachvili, J.H. Waite, A mussel-derived one component adhesive coacervate, *Acta Biomater.* 10 (2014) 1663–1670. <https://doi.org/10.1016/j.actbio.2013.09.007>.
- [42] C.E. Sing, S.L. Perry, Recent progress in the science of complex coacervation, *Soft Matter*. 16 (2020) 2885–2914. <https://doi.org/10.1039/d0sm00001a>.
- [43] S. Kim, J. Huang, Y. Lee, S. Dutta, H.Y. Yoo, Y.M. Jung, Y. Jho, H. Zeng, D.S. Hwang, Complexation and coacervation of like-charged polyelectrolytes inspired by mussels, *Proc. Natl. Acad. Sci. U. S. A.* 113 (2016) E847–53. <https://doi.org/10.1073/pnas.1521521113>.
- [44] A. Perro, L. Giraud, N. Coudon, S. Shanmugathan, V. Lapeyre, B. Goudeau, J.P. Douliez, V. Ravaine, Self-coacervation of ampholyte polymer chains as an efficient encapsulation strategy, *J. Colloid Interface Sci.* 548 (2019) 275–283. <https://doi.org/10.1016/j.jcis.2019.04.033>.
- [45] H. Jing, X. Du, L. Mo, H. Wang, Self-coacervation of carboxymethyl chitosan as a pH-responsive encapsulation and delivery strategy, *Int. J. Biol. Macromol.* 192 (2021) 1169–1177. <https://doi.org/10.1016/j.ijbiomac.2021.10.072>.
- [46] B. Yang, S. Jin, Y. Park, Y.M. Jung, H.J. Cha, Coacervation of Interfacial Adhesive Proteins for Initial Mussel Adhesion to a Wet Surface, *Small*. 14 (2018) 1–12. <https://doi.org/10.1002/smll.201803377>.
- [47] T.G. Barclay, H.M. Hegab, S.R. Clarke, M. Ginic-Markovic, Versatile Surface Modification Using Polydopamine and Related Polycatecholamines: Chemistry, Structure, and Applications, *Adv. Mater. Interfaces*. 4 (2017) 1601192. <https://doi.org/doi:10.1002/admi.201601192>.
- [48] Y. Fang, S. Gonuguntla, S. Soh, Universal Nature-Inspired Coatings for Preparing Noncharging Surfaces, *ACS Appl. Mater. Interfaces*. 9 (2017) 32220–32226. <https://doi.org/10.1021/acsami.7b07711>.
- [49] C. Zhang, L. Gong, L. Xiang, Y. Du, W. Hu, H. Zeng, Z.K. Xu, Deposition and Adhesion of Polydopamine on the Surfaces of Varying Wettability, *ACS Appl Mater Interfaces*. 9 (2017) 30943–30950. <https://doi.org/10.1021/acsami.7b09774>.
- [50] Y. Yang, P. Qi, Y. Ding, M.F. Maitz, Z. Yang, Q. Tu, K. Xiong, Y. Leng, N. Huang, A biocompatible and functional adhesive amine-rich coating based on dopamine polymerization, *J. Mater. Chem. B*. 3 (2015) 72–81. <https://doi.org/10.1039/c4tb01236d>.

- [51] Z. Wang, S. Zhang, S. Zhao, H. Kang, Z. Wang, C. Xia, Y. Yu, J. Li, Facile biomimetic self-coacervation of tannic acid and polycation: Tough and wide pH range of underwater adhesives, *Chem. Eng. J.* 404 (2021) 127069. <https://doi.org/10.1016/j.cej.2020.127069>.
- [52] X. Zhu, C. Song, X. Sun, D. Wang, D. Cai, Z. Wang, Y. Chen, X. Chen, Improved water resistance of TA-modified soy adhesive: Effect of complexation, *Int. J. Adhes. Adhes.* 108 (2021) 102858. <https://doi.org/10.1016/j.ijadhadh.2021.102858>.
- [53] S. Li, J. Chen, J. Wang, H. Zeng, Anti-biofouling materials and surfaces based on mussel-inspired chemistry, *Mater. Adv.* 2 (2021) 2216–2230. <https://doi.org/10.1039/d1ma00053e>.
- [54] H. Wang, L. Wang, S. Zhang, W. Zhang, J. Li, Y. Han, Mussel-inspired polymer materials derived from nonphytogenic and phytogenic catechol derivatives and their applications, *Polym. Int.* 70 (2021) 1209–1224. <https://doi.org/10.1002/pi.6230>.
- [55] Z. Wang, H.C. Yang, F. He, S. Peng, Y. Li, L. Shao, S.B. Darling, Mussel-Inspired Surface Engineering for Water-Remediation Materials, *Matter.* 1 (2019) 115–155. <https://doi.org/10.1016/j.matt.2019.05.002>.
- [56] H. Lee, S.M. Dellatore, W.M. Miller, P.B. Messersmith, Mussel-inspired surface chemistry for multifunctional coatings, *Science.* 318 (2007) 426–430. <https://doi.org/10.1126/science.1147241>.
- [57] F. Bernsmann, A. Ponche, C. Ringwald, J. Hemmerlé, J. Raya, B. Bechinger, J.-C. Voegel, P. Schaaf, V. Ball, Characterization of Dopamine–Melanin Growth on Silicon Oxide, *J. Phys. Chem. C.* 113 (2009) 8234–8242. <https://doi.org/10.1021/jp901188h>.
- [58] C. Cui, W. Liu, Recent advances in wet adhesives: Adhesion mechanism, design principle and applications, *Prog. Polym. Sci.* 116 (2021) 101388. <https://doi.org/10.1016/j.progpolymsci.2021.101388>.
- [59] J. Jiang, L. Zhu, L. Zhu, B. Zhu, Y. Xu, Surface characteristics of a self-polymerized dopamine coating deposited on hydrophobic polymer films, *Langmuir.* 27 (2011) 14180–14187. <https://doi.org/10.1021/la202877k>.
- [60] S.M. Kang, N.S. Hwang, J. Yeom, S.Y. Park, P.B. Messersmith, I.S. Choi, R. Langer, D.G. Anderson, H. Lee, One-Step Multipurpose Surface Functionalization by Adhesive Catecholamine, *Adv. Funct. Mater.* 22 (2012) 2949–2955. <https://doi.org/10.1002/adfm.201200177>.
- [61] W.Z. Qiu, H.C. Yang, Z.K. Xu, Dopamine-assisted co-deposition: An emerging and promising strategy for surface modification, *Adv. Colloid Interface Sci.* 256 (2018) 111–125. <https://doi.org/10.1016/j.cis.2018.04.011>.
- [62] M. Kohri, H. Kohma, Y. Shinoda, M. Yamauchi, S. Yagai, T. Kojima, T. Taniguchi, K. Kishikawa, A colorless functional polydopamine thin layer as a basis for polymer capsules, *Polym. Chem.* 4 (2013) 2696–2702. <https://doi.org/10.1039/c3py00181d>.
- [63] Y. Zhang, B. Thingholm, K.N. Goldie, R. Ogaki, B. Stadler, Assembly of poly(dopamine) films mixed with a nonionic polymer, *Langmuir.* 28 (2012) 17585–17592. <https://doi.org/10.1021/la304080c>.

- [64] Y. Liu, C.P. Chang, T. Sun, Dopamine-assisted deposition of dextran for nonfouling applications, *Langmuir*. 30 (2014) 3118–3126. <https://doi.org/10.1021/la500006e>.
- [65] R. Huang, X. Liu, H. Ye, R. Su, W. Qi, L. Wang, Z. He, Conjugation of Hyaluronic Acid onto Surfaces via the Interfacial Polymerization of Dopamine to Prevent Protein Adsorption, *Langmuir*. 31 (2015) 12061–12070. <https://doi.org/10.1021/acs.langmuir.5b02320>.
- [66] P.-F. Ren, H.-C. Yang, Y.-N. Jin, H.-Q. Liang, L.-S. Wan, Z.-K. Xu, Underwater superoleophobic meshes fabricated by poly(sulfobetaine)/polydopamine co-deposition, *RSC Adv.* 5 (2015) 47592–47598. <https://doi.org/10.1039/c5ra05937b>.
- [67] R. Zhou, P.-F. Ren, H.-C. Yang, Z.-K. Xu, Fabrication of antifouling membrane surface by poly(sulfobetaine methacrylate)/polydopamine co-deposition, *J. Memb. Sci.* 466 (2014) 18–25. <https://doi.org/10.1016/j.memsci.2014.04.032>.
- [68] Y. Lv, S.J. Yang, Y. Du, H.C. Yang, Z.K. Xu, Co-deposition Kinetics of Polydopamine/Polyethyleneimine Coatings: Effects of Solution Composition and Substrate Surface, *Langmuir*. 34 (2018) 13123–13131. <https://doi.org/10.1021/acs.langmuir.8b02454>.
- [69] B. Yang, C. Lim, D.S. Hwang, H.J. Cha, Switch of Surface Adhesion to Cohesion by Dopa-Fe 3+ Complexation, in Response to Microenvironment at the Mussel Plaque/Substrate Interface, *Chem. Mater.* 28 (2016) 7982–7989. <https://doi.org/10.1021/acs.chemmater.6b03676>.
- [70] J.H. Cho, R. Katsumata, S.X. Zhou, C. Bin Kim, A.R. Dulaney, D.W. Janes, C.J. Ellison, Ultrasoother Polydopamine Modified Surfaces for Block Copolymer Nanopatterning on Flexible Substrates, *ACS Appl. Mater. Interfaces*. 8 (2016) 7456–7463. <https://doi.org/10.1021/acsami.6b00626>.
- [71] M. Alfieri, L. Panzella, S. Oscurato, M. Salvatore, R. Avolio, M. Errico, P. Maddalena, A. Napolitano, M. D’Ischia, The Chemistry of Polydopamine Film Formation: The Amine-Quinone Interplay, *Biomimetics*. 3 (2018) 26. <https://doi.org/10.3390/biomimetics3030026>.
- [72] V. Ball, D. Del Frari, V. Toniazio, D. Ruch, Kinetics of polydopamine film deposition as a function of pH and dopamine concentration: insights in the polydopamine deposition mechanism, *J. Colloid Interface Sci.* 386 (2012) 366–372. <https://doi.org/10.1016/j.jcis.2012.07.030>.
- [73] P. Zhou, Y. Deng, B. Lyu, R. Zhang, H. Zhang, H. Ma, Y. Lyu, S. Wei, Rapidly-Deposited Polydopamine Coating via High Temperature and Vigorous Stirring: Formation, Characterization and Biofunctional Evaluation, *PLoS One*. 9 (2014) e113087. <https://doi.org/10.1371/journal.pone.0113087>.
- [74] L. Klosterman, J.K. Riley, C.J. Bettinger, Control of heterogeneous nucleation and growth kinetics of dopamine-melanin by altering substrate chemistry, *Langmuir*. 31 (2015) 3451–3458. <https://doi.org/10.1021/acs.langmuir.5b00105>.
- [75] F. Ponzio, J. Barthès, J. Bour, M. Michel, P. Bertani, J. Hemmerlé, M. D’Ischia, V. Ball,

- Oxidant Control of Polydopamine Surface Chemistry in Acids: A Mechanism-Based Entry to Superhydrophilic-Superoleophobic Coatings, *Chem. Mater.* 28 (2016) 4697–4705. <https://doi.org/10.1021/acs.chemmater.6b01587>.
- [76] K. Patel, N. Singh, J. Yadav, J.M. Nayak, S.K. Sahoo, J. Lata, D. Chand, S. Kumar, R. Kumar, Polydopamine films change their physicochemical and antimicrobial properties with a change in reaction conditions, *Phys. Chem. Chem. Phys.* 20 (2018) 5744–5755. <https://doi.org/10.1039/c7cp08406d>.
- [77] F. Bernsmann, V. Ball, F. Addiego, A. Ponche, M. Michel, J.J. Gracio, V. Toniazzi, D. Ruch, Dopamine-melanin film deposition depends on the used oxidant and buffer solution, *Langmuir*. 27 (2011) 2819–2825. <https://doi.org/10.1021/la104981s>.
- [78] Z. Trzcińska, M. Bruggeman, H. Ijakipour, N.J. Hodges, J. Bowen, A. Stamboulis, Polydopamine linking substrate for AMPs: Characterisation and stability on Ti6Al4V, *Materials (Basel)*. 13 (2020) 1–19. <https://doi.org/10.3390/MA13173714>.
- [79] F. Bernsmann, O. Ersen, J.C. Voegel, E. Jan, N.A. Kotov, V. Ball, Melanin-Containing Films: Growth from Dopamine Solutions versus Layer-by-Layer Deposition, *ChemPhysChem*. 11 (2010) 3299–3305. <https://doi.org/10.1002/cphc.201000384>.
- [80] H.W. Kim, B.D. McCloskey, T.H. Choi, C. Lee, M.J. Kim, B.D. Freeman, H.B. Park, Oxygen concentration control of dopamine-induced high uniformity surface coating chemistry, *ACS Appl Mater Interfaces*. 5 (2013) 233–238. <https://doi.org/10.1021/am302439g>.
- [81] I.S. Kwon, G. Tang, P.J. Chiang, C.J. Bettinger, Texture-Dependent Adhesion in Polydopamine Nanomembranes, *ACS Appl Mater Interfaces*. 10 (2018) 7681–7687. <https://doi.org/10.1021/acsami.7b15608>.
- [82] X. Jiang, Y. Li, Y. Liu, C. Chen, M. Chen, Selective enhancement of human stem cell proliferation by mussel inspired surface coating, *RSC Adv.* 6 (2016) 60206–60214. <https://doi.org/10.1039/c6ra11173d>.
- [83] R. Qie, S. Zajforoushan Moghaddam, E. Thormann, Parameterization of the optical constants of polydopamine films for spectroscopic ellipsometry studies, *Phys. Chem. Chem. Phys.* 23 (2021) 5516–5526. <https://doi.org/10.1039/d0cp04796a>.
- [84] W. Sheng, B. Li, X. Wang, B. Dai, B. Yu, X. Jia, F. Zhou, Brushing up from “anywhere” under sunlight: a universal surface-initiated polymerization from polydopamine-coated surfaces, *Chem. Sci.* 6 (2015) 2068–2073. <https://doi.org/10.1039/C4SC03851G>.
- [85] A. Kawamura, M. Kohri, G. Morimoto, Y. Nannichi, T. Taniguchi, K. Kishikawa, Full-Color Biomimetic Photonic Materials with Iridescent and Non-Iridescent Structural Colors, *Sci. Rep.* 6 (2016) 33984. <https://doi.org/10.1038/srep33984>.
- [86] T. Repenko, A. Rix, A. Nedilko, J. Rose, A. Hermann, R. Vinokur, S. Moli, R. Cao-Milàn, M. Mayer, G. von Plessen, A. Fery, L. De Laporte, W. Lederle, D.N. Chigrin, A.J.C. Kuehne, Strong Photoacoustic Signal Enhancement by Coating Gold Nanoparticles with Melanin for Biomedical Imaging, *Adv. Funct. Mater.* 28 (2018) 1–8. <https://doi.org/10.1002/adfm.201705607>.

- [87] S. Nirasay, A. Badia, G. Leclair, J. Claverie, I. Marcotte, Polydopamine-Supported Lipid Bilayers, *Materials (Basel)*. 5 (2012) 2621–2636. <https://doi.org/10.3390/ma5122621>.
- [88] S.C. Goh, Y. Luan, X. Wang, H. Du, C. Chau, H.E. Schellhorn, J.L. Brash, H. Chen, Q. Fang, Polydopamine–polyethylene glycol–albumin antifouling coatings on multiple substrates, *J. Mater. Chem. B*. 6 (2018) 940–949. <https://doi.org/10.1039/C7TB02636F>.
- [89] A. Vaish, D.J. Vanderah, L.J. Richter, M. Dimitriou, K.L. Steffens, M.L. Walker, Dithiol-based modification of poly(dopamine): enabling protein resistance via short-chain ethylene oxide oligomers, *Chem. Commun.* 51 (2015) 6591–6594. <https://doi.org/10.1039/C5CC00299K>.
- [90] O.Y. Milyaeva, A.G. Bykov, R.A. Campbell, G. Loglio, R. Miller, B.A. Noskov, Polydopamine layer formation at the liquid–gas interface, *Colloids Surfaces A Physicochem. Eng. Asp.* 579 (2019) 123637. <https://doi.org/10.1016/j.colsurfa.2019.123637>.
- [91] H.J. Meredith, C.L. Jenkins, J.J. Wilker, Enhancing the Adhesion of a Biomimetic Polymer Yields Performance Rivaling Commercial Glues, *Adv. Funct. Mater.* 24 (2014) 3259–3267. <https://doi.org/10.1002/adfm.201303536>.
- [92] Y. Mu, X. Wan, Simple but Strong: A Mussel-Inspired Hot Curing Adhesive Based on Polyvinyl Alcohol Backbone, *Macromol. Rapid Commun.* 37 (2016) 545–550. <https://doi.org/10.1002/marc.201500723>.
- [93] M.J. Brennan, B.F. Kilbride, J.J. Wilker, J.C. Liu, A bioinspired elastin-based protein for a cytocompatible underwater adhesive, *Biomaterials*. 124 (2017) 116–125. <https://doi.org/10.1016/j.biomaterials.2017.01.034>.
- [94] G. Schmidt, B.R. Hamaker, J.J. Wilker, High Strength Adhesives from Catechol Cross-Linking of Zein Protein and Plant Phenolics, *Adv. Sustain. Syst.* 2 (2018) 1700159. <https://doi.org/10.1002/adsu.201700159>.
- [95] Q. Peng, Q. Wu, J. Chen, T. Wang, M. Wu, D. Yang, X. Peng, J. Liu, H. Zhang, H. Zeng, Coacervate-Based Instant and Repeatable Underwater Adhesive with Anticancer and Antibacterial Properties, *ACS Appl. Mater. Interfaces*. (2021) acsami.1c13744. <https://doi.org/10.1021/acsami.1c13744>.
- [96] Y. Chan Choi, J.S. Choi, Y.J. Jung, Y.W. Cho, Human gelatin tissue-adhesive hydrogels prepared by enzyme-mediated biosynthesis of DOPA and Fe³⁺ ion crosslinking, *J. Mater. Chem. B*. 2 (2014) 201–209. <https://doi.org/10.1039/c3tb20696c>.
- [97] C.R. Matos-Pérez, J.D. White, J.J. Wilker, Polymer composition and substrate influences on the adhesive bonding of a biomimetic, cross-linking polymer, *J. Am. Chem. Soc.* 134 (2012) 9498–9505. <https://doi.org/10.1021/ja303369p>.
- [98] D. Du, X. Chen, C. Shi, Z. Zhang, D. Shi, D. Kaneko, T. Kaneko, Z. Hua, Mussel-Inspired Epoxy Bioadhesive with Enhanced Interfacial Interactions for Wound Repair, *Acta Biomater.* (2021). <https://doi.org/10.1016/j.actbio.2021.09.054>.
- [99] D. Lee, H. Bae, J. Ahn, T. Kang, D.G. Seo, D.S. Hwang, Catechol-thiol-based dental adhesive inspired by underwater mussel adhesion, *Acta Biomater.* 103 (2020) 92–101.

- <https://doi.org/10.1016/j.actbio.2019.12.002>.
- [100] W.Y. Quan, Z. Hu, H.Z. Liu, Q.Q. Ouyang, D.Y. Zhang, S.D. Li, P.W. Li, Z.M. Yang, Mussel-inspired catechol-functionalized hydrogels and their medical applications, *Molecules*. 24 (2019) 1–27. <https://doi.org/10.3390/molecules24142586>.
 - [101] Y. He, J. Chen, I. Rafique, Z. Lu, Star-shaped polycaprolactone bearing mussel-inspired catechol end-groups as a promising bio-adhesive, *Eur. Polym. J.* 139 (2020) 110025. <https://doi.org/10.1016/j.eurpolymj.2020.110025>.
 - [102] M.A. North, C.A. Del Grosso, J.J. Wilker, High Strength Underwater Bonding with Polymer Mimics of Mussel Adhesive Proteins, *ACS Appl. Mater. Interfaces*. 9 (2017) 7866–7872. <https://doi.org/10.1021/acsami.7b00270>.
 - [103] I. You, S.M. Kang, Y. Byun, H. Lee, Enhancement of Blood Compatibility of Poly(urethane) Substrates by Mussel-Inspired Adhesive Heparin Coating, *Bioconjug. Chem.* 22 (2011) 1264–1269. <https://doi.org/10.1021/bc2000534>.
 - [104] D. Lee, H. Hwang, J.S. Kim, J. Park, D. Youn, D. Kim, J. Hahn, M. Seo, H. Lee, VATA: A Poly(vinyl alcohol)- And Tannic Acid-Based Nontoxic Underwater Adhesive, *ACS Appl. Mater. Interfaces*. 12 (2020) 20933–20941. <https://doi.org/10.1021/acsami.0c02037>.
 - [105] Z. Wang, S. Zhang, S. Zhao, H. Kang, Z. Wang, C. Xia, Y. Yu, J. Li, Facile biomimetic self-coacervation of tannic acid and polycation: Tough and wide pH range of underwater adhesives, *Chem. Eng. J.* 404 (2021) 127069. <https://doi.org/10.1016/j.cej.2020.127069>.
 - [106] H.G. Nam, M.G. Nam, P.J. Yoo, J.H. Kim, Hydrogen bonding-based strongly adhesive coacervate hydrogels synthesized using poly(N-vinylpyrrolidone) and tannic acid, *Soft Matter*. 15 (2019) 785–791. <https://doi.org/10.1039/c8sm02144a>.
 - [107] Q.D. Dang, J.R. Moon, Y.S. Jeon, J.H. Kim, Supramolecular adhesive gels based on biocompatible poly(2-ethyl-2-oxazoline) and tannic acid via hydrogen bonding complexation, *J. Appl. Polym. Sci.* 137 (2020) 48285. <https://doi.org/10.1002/app.48285>.
 - [108] H.L.N. Nguyen, J.-H. Kim, Stimuli-sensitive complexation and the strongly adhesive antibacterial gel from biocompatible PolyAspAm(EA/EDA) and tannic acid, *Int. J. Polym. Mater. Polym. Biomater.* (2020) 1–8. <https://doi.org/10.1080/00914037.2020.1848830>.
 - [109] D. Zhang, Z. Xu, H. Li, C. Fan, C. Cui, T. Wu, M. Xiao, Y. Yang, J. Yang, W. Liu, Fabrication of strong hydrogen-bonding induced coacervate adhesive hydrogels with antibacterial and hemostatic activities, *Biomater. Sci.* 8 (2020) 1455–1463. <https://doi.org/10.1039/c9bm02029b>.
 - [110] J. Sun, M. He, W. Zhao, Y. Dan, L. Jiang, Endowing water-based polyacrylics adhesives with enhanced water-resistant capability by integrating with tannic acid, *React. Funct. Polym.* 163 (2021) 104890. <https://doi.org/10.1016/j.reactfunctpolym.2021.104890>.
 - [111] Q. Zhao, S. Mu, Y. Long, J. Zhou, W. Chen, D. Astruc, C. Gaidau, H. Gu, Tannin-Tethered Gelatin Hydrogels with Considerable Self-Healing and Adhesive Performances, *Macromol. Mater. Eng.* 304 (2019) 1–8. <https://doi.org/10.1002/mame.201800664>.
 - [112] J. Jing, S. Liang, Y. Yan, X. Tian, X. Li, Fabrication of Hybrid Hydrogels from Silk

- Fibroin and Tannic Acid with Enhanced Gelation and Antibacterial Activities, *ACS Biomater. Sci. Eng.* 5 (2019) 4601–4611.
<https://doi.org/10.1021/acsbiomaterials.9b00604>.
- [113] M. Zhang, C. Cheng, C. Guo, L. Jin, L. Liu, M. Li, L. Shang, Y. Liu, Y. Ao, Co-depositing bio-inspired tannic acid-aminopropyltriethoxysilane coating onto carbon fiber for excellent interfacial adhesion of epoxy composites, *Compos. Sci. Technol.* 204 (2021) 108639. <https://doi.org/10.1016/j.compscitech.2020.108639>.
- [114] G. Choe, Y. Cho, S.M. Bae, S.H. Yoon, J. Lee, Is a pyrogallol group better than a catechol group for promoting adhesion between polymers and metals?, *J. Ind. Eng. Chem.* 73 (2019) 58–61. <https://doi.org/10.1016/j.jiec.2019.01.020>.
- [115] K. Zhan, C. Kim, K. Sung, H. Ejima, N. Yoshie, Tunicate-Inspired Gallol Polymers for Underwater Adhesive: A Comparative Study of Catechol and Gallol, *Biomacromolecules.* 18 (2017) 2959–2966. <https://doi.org/10.1021/acs.biomac.7b00921>.
- [116] Z. Le, Y. Chen, H. Han, H. Tian, P. Zhao, C. Yang, Z. He, L. Liu, K.W. Leong, H.Q. Mao, Z. Liu, Y. Chen, Hydrogen-Bonded Tannic Acid-Based Anticancer Nanoparticle for Enhancement of Oral Chemotherapy, *ACS Appl. Mater. Interfaces.* 10 (2018) 42186–42197. <https://doi.org/10.1021/acsami.8b18979>.
- [117] C.C. Ho, S.J. Ding, Novel SiO₂/PDA hybrid coatings to promote osteoblast-like cell expression on titanium implants, *J Mater Chem B.* 3 (2015) 2698–2707.
<https://doi.org/10.1039/c4tb01841a>.
- [118] R. Gao, L. Zhang, Y. Hao, X. Cui, D. Liu, M. Zhang, Y. Tang, One-step preparation of magnetic imprinted nanoparticles adopting dopamine-cupric ion as a co-monomer for the specific recognition of bovine hemoglobin, *J. Sep. Sci.* 38 (2015) 3568–3574.
<https://doi.org/10.1002/jssc.201500677>.
- [119] S. Zajforoushan Moghaddam, R. Qie, E. Thormann, Making Protein-Based Adhesives Water Resistant: Role of Protein Water Solubility, Galloyl Modification, and Complexation, *ACS Appl. Polym. Mater.* (2021).
<https://doi.org/10.1021/acsapm.1c01089>.
- [120] R. Secondo, D. Fomra, N. Izyumskaya, V. Avrutin, J.N. Hilfiker, A. Martin, Ü. Özgür, N. Kinsey, Reliable modeling of ultrathin alternative plasmonic materials using spectroscopic ellipsometry [Invited], *Opt. Mater. Express.* 9 (2019) 760.
<https://doi.org/10.1364/ome.9.000760>.
- [121] H. Fujiwara, *Spectroscopic Ellipsometry: Principles and Applications*, 2007.
<https://doi.org/10.1002/9780470060193>.
- [122] H.G. Tompkins, J.N. Hilfiker, *Spectroscopic Ellipsometry: Practical Application to Thin Film Characterization (Materials Characterization and Analysis Collection)*, Elsevier, 2016.
- [123] B. Johs, J.S. Hale, Dielectric function representation by B-splines, *Phys. Status Solidi.* 205 (2008) 715–719. <https://doi.org/10.1002/pssa.200777754>.
- [124] D. Lehmann, F. Seidel, D.R.T. Zahn, Thin films with high surface roughness: Thickness

- and dielectric function analysis using spectroscopic ellipsometry, Springerplus. 3 (2014) 1–8. <https://doi.org/10.1186/2193-1801-3-82>.
- [125] D.E. Aspnes, J.B. Theeten, F. Hottier, Investigation of effective-medium models of microscopic surface roughness by spectroscopic ellipsometry, Phys. Rev. B. 20 (1979) 3292–3302. <https://doi.org/10.1103/PhysRevB.20.3292>.
- [126] B. Bharat, Scanning Probe Microscopy in Nanoscience and Nanotechnology 3, Springer Berlin Heidelberg, Berlin, Heidelberg, 2013. <https://doi.org/10.1007/978-3-642-25414-7>.
- [127] Y. Kim, W. Kim, J.W. Park, Principles and Applications of Force Spectroscopy Using Atomic Force Microscopy, Bull. Korean Chem. Soc. 37 (2016) 1895–1907. <https://doi.org/10.1002/bkcs.11022>.
- [128] H. Mei, Z. Gao, Q. Wang, H. Sun, K. Zhao, P. Zhang, J. Hao, M. Ashokkumar, J. Cui, Ultrasound expands the versatility of polydopamine coatings, Ultrason. Sonochem. 74 (2021) 105571. <https://doi.org/10.1016/j.ultsonch.2021.105571>.

Appendices

Paper I



Cite this: *Phys. Chem. Chem. Phys.*, 2021, **23**, 5516

Parameterization of the optical constants of polydopamine films for spectroscopic ellipsometry studies†

Runtian Qie,^{ID} Saeed Zajforoushan Moghaddam^{ID} and Esben Thormann^{ID}*

Bio-inspired polydopamine coatings offer vast possibilities for surface modification of materials. The thickness of such nanometric coatings is usually estimated based on ellipsometry measurements. However, the complex light-absorbing nature of polydopamine is often overlooked when analyzing such data, which can result in inaccurate estimations of the coating thickness as well as the optical properties. In this study, we prepared and characterized three polydopamine coatings where the film thickness and surface roughness are systematically varied. For each case, we developed suitable optical models and showed how an inappropriate optical model can provide inaccurate estimates of the coating properties. AFM height profiles were obtained from scratched areas of each sample to verify the thickness values estimated by ellipsometry. The results confirm that polydopamine coatings, depending on the oxidation conditions, can possess different structural and optical properties, and thus require unique optical models for the ellipsometry analysis.

Received 10th September 2020,
Accepted 22nd February 2021

DOI: 10.1039/d0cp04796a

rsc.li/pccp

1. Introduction

Polydopamine (PDA) has drawn enormous attention as a versatile coating material that can readily form nanometric thin films on different materials.^{1–3} Besides, PDA coatings can be co-deposited or post-functionalized with different molecules providing a wealth of surface modification possibilities.^{4–8} Owing to these advantages, there has been a growing research effort devoted to the fabrication and characterization of PDA coatings during the past decade. Spectroscopic ellipsometry, as a powerful tool to estimate the thickness of organic and inorganic thin-films, is often employed to characterize PDA coatings.^{9–18} Ellipsometry is a non-destructive optical method that measures the changes in the polarization state of the light reflected from a thin-film on a substrate.^{19,20} The film thickness is indirectly estimated from the experimental data by constructing a proper model, which represents the optical behavior of the material. For materials with known optical constants, the film thickness is simply obtained as the only “free” parameter in the model. Contrarily, materials with unknown optical constants are challenging because the thickness as well as the optical constants are free model parameters. This brings up two issues: (i) choosing the appropriate dispersion equation that

can describe the optical behavior of the material, (ii) the possibility of overparameterization and correlation between the free model parameters. Hence, samples with unknown optical constants should be subjected to rigorous analysis to ensure the reliability of the modeling outcome.

Polydopamine coatings comprise a complex mixture of different aromatic compounds.^{21,22} The covalent coupling of dopamine occurs through the oxidation of the catechol group to quinone, followed by a cyclization reaction generating indole, as well as other oxidation and reorganization reactions forming several monomeric and oligomeric products.²³ These compounds aggregate through various supramolecular interactions and produce polydopamine particles in the solution and thin-films on the immersed substrates. Given such chemical heterogeneity, polydopamine possesses a rather complex optical dispersion with multiple absorption features over a broad range of wavelength from UV to NIR regions.^{24–27} Besides, the oxidation conditions affect the chemical composition and structure of polydopamine films.²³ Therefore, the optical properties of PDA can also vary depending on the reaction conditions, meaning that obtaining “tabulated” optical constants for PDA is infeasible. Such complex optical behavior of PDA necessitates a careful modeling approach to analyse the ellipsometric data of PDA films. Moreover, the intrinsic granular, porous, and rough nature of PDA films is another complication that must be considered. Such careful analysis and report of the ellipsometric data of PDA films is often overlooked. Many studies still rely on the Cauchy model, which is only valid for transparent materials with

Department of Chemistry, Technical University of Denmark, 2800 Kgs. Lyngby, Denmark. E-mail: esth@kemi.dtu.dk

† Electronic supplementary information (ESI) available: Additional XPS data, water contact angle data, detailed ellipsometry modeling data and sensitivity analysis, optical functions estimated from modeling, ellipsometry data of 24 h deposition PDA. See DOI: 10.1039/d0cp04796a

no or negligible light absorption. Besides, many studies report merely the estimated thickness without unfolding the modeling procedure and assessing the quality of the modeling data.

In this study, we prepared and characterized three PDA samples through different deposition times, *i.e.*, 2 h, 6 h, and 12 h. By doing so, we obtained PDA films of systematically varied thickness and surface roughness; thus, we could optimize the modeling approach for each case. The estimated thickness for each sample was also verified by parallel AFM measurements on scratched films. It is shown that PDA samples obtained from different deposition times need unique optical models, depending on their structural and optical characteristics. Moreover, the misuse of the optical models provides significantly overestimated optical constants and underestimated thickness values. Hence, even if the optical constants of PDA are not of interest, the estimated film thickness will be inaccurate unless an appropriate optical model is utilized.

2. Methods

2.1. Experimental section

Dopamine hydrochloride (DA) and tris(hydroxymethyl) aminomethane (>99.9%) were purchased from Sigma-Aldrich. DA was dissolved in tris-buffer solution (pH = 8.5, 50 mM) and silicon wafers (WaferNet, San Jose, USA) were immersed into the DA solution (2 mg mL⁻¹) for 2, 6, and 12 h. The DA solution was exchanged with a fresh solution every 2 h. Between each exchange step, the wafers were sonicated in fresh tris-buffer, then dried with compressed air. This procedure ensures a smoother surface with less aggregates,^{9,28} which can improve the quality of the ellipsometric data. Similar samples were prepared on glass slides for transmission measurements.

To analyse the chemical composition of the PDA films, X-ray photoelectron spectroscopy (XPS) measurements were conducted using a Thermo Scientific K-Alpha X-ray photoelectron spectrometer equipped with a hemispherical analyser and an Al K α micro-focused monochromator. Peak analysis was conducted using Avantage software. Surface charging was corrected with carbon C 1s peak at 284.8 eV. The “smart” background and mixed Lorentzian (30%)/Gaussian (70%) functions were used. An initial value of 1.7 eV was used for full width at half maximum (FWHM) of all peaks, which could vary between 1.5–1.9 eV.²⁹ Spectroscopic ellipsometry measurements (M-2000U, J. A. Woollam Co., Inc.) were performed in the wavelength range of 245–1000 nm at 5 different angles of incidence (50, 55, 60, 65, 70°). Transmission measurements (90°) were conducted on bare and PDA-coated glass slides. For each PDA sample, a total number of 15 measuring points (five randomly selected areas on three specimens) were obtained and the median representative data are presented. The instrument software (CompleteEASE, J. A. Woollam Co., Inc.) was used for data modeling and analysis. Atomic force microscope (AFM, NanoWizard 3, JPK Instruments AG, Berlin, Germany) operating in tapping mode in air was used to estimate the thickness of the PDA coatings. The coatings were carefully scratched using a

tweezer and AFM images were collected over the scratched area. The images were collected using a standard tapping mode cantilever (HQ: NSC5/AL BS, tip radius ~ 8 nm, $k \sim 40$ N m⁻¹; Mikromasch, Germany) with a scan rate of 0.1 Hz and pixel resolution of 256 \times 256. The thickness was then estimated from the cross-section height profiles (three replicas) using the standard software of the instrument (JPK SPM Data Processing).

2.2. Theory and modeling procedure

In an ellipsometry experiment, p-polarized (parallel to the plane of incidence) and s-polarized (perpendicular to the plane of incidence) light waves are irradiated on a flat sample. The interaction of light with the material gives rise to a variation in the polarization state of the reflected light, which is quantified in terms of ellipsometric ψ and Δ . The former represents the amplitude ratio and the latter indicates the phase difference between p- and s-polarizations, respectively. The measured ψ and Δ values are related to the sample properties through the complex reflectance function (ρ).³⁰

$$\tan \Psi e^{i\Delta} = \rho(N_a, N_s, N_1, \dots, N_j, d_1, \dots, d_j, \theta_0)$$

The change in polarization state is then related to the angle of incidence (θ_0), the thicknesses (d_j) of the layers, as well as the complex optical constants of medium (N_a), substrate (N_s), and the layers (N_j). The optical constants of a material describe how it interacts with the light, which can be characterized using the complex refractive index (N) or the complex dielectric function (ϵ).³¹

$$N = n \pm ik$$

$$\epsilon = \epsilon_1 \pm i\epsilon_2$$

The complex refractive index specifies how light–matter interaction modifies the light properties in terms of phase velocity, direction of propagation, and intensity loss. Contrarily, the complex dielectric function characterizes how light–matter interaction affects the material in terms of dielectric polarization. These two parameters are then related to each other by:

$$\epsilon = N^2$$

$$\epsilon_1 = n^2 - k^2$$

$$\epsilon_2 = 2nk$$

Since the optical constants of the material depend on the light wavelength (λ), $N(\lambda)$ and $\epsilon(\lambda)$ are recognized as the optical dispersions of the material. Alternatively, the optical constants can be described as a function of photon energy, which is related to wavelength through:

$$E \text{ (eV)} = \frac{1240}{\lambda \text{ (nm)}}$$

After collecting the measured $\psi(\lambda)$ and $\Delta(\lambda)$, one must construct an appropriate optical model that represents the

nominal structure of the multilayer sample comprising information on thickness and optical constants of all the constituents. Next, the Fresnel's equations are used to calculate $\psi(\lambda)$ and $\Delta(\lambda)$ for the constructed optical model and the best match (with the smallest mean squared error (MSE)) between the measured and modelled values is obtained through regression.

The PDA-coated silica wafer is herein represented with a three-layered optical model. The bottom-most component is an optically thick silicon (c-Si) substrate, *i.e.*, characterized by its tabulated optical constants. A thermally grown oxide layer (SiO_2) is found on top of the substrate, which is characterized by its thickness and optical constants. The values of optical constants from the software library are used, while the thickness (~ 100 nm) of the oxide layer was measured prior to PDA deposition and then was fixed in the model. The topmost layer represents the PDA coating characterized by the thickness and optical constants. Since the optical constants of PDA are unknown, an appropriate model is then required to describe its dielectric function and optical behavior.^{32–36}

The Cauchy relation is an empirical equation that is commonly used to describe the optical dispersion of transparent dielectrics and organic materials.

$$n(E) = A + BE^2 + CE^4$$

$$k(E) = 0$$

where A adjusts the amplitude of the index of refraction, while B and C account for the curvature of the dispersion. The Cauchy relation can be used only if the material displays a “normal” dispersion, *i.e.*, ϵ_1 and n values increase towards larger photon energy values (or shorter wavelengths) and light absorption is negligible (ϵ_2 and $k \sim 0$) over the investigated wavelength range. Generally, there is a possibility of correlation between these parameters (specifically between B and C), so extra care is needed to avoid overparameterization and physically implausible dispersion shapes. In case of minor light absorption, one can modify the Cauchy relation by adding the Urbach absorption term:

$$k(E) = \alpha e^{\beta(E-E_b)}$$

The extinction coefficient is then characterized by the amplitude (α), the exponent factor (β), and the band-edge energy (E_b), which together produce a small exponentially-decaying extinction coefficient. This term is useful if the absorption is sufficiently small ($k < 0.01$) and the index of refraction still shows a normal dispersion, *e.g.*, weak light absorption in the UV range.

For samples with a strong light absorption over a broad range of wavelengths, the Urbach term cannot properly describe the optical behavior. Such materials are usually characterized by an “anomalous” dispersion, where ϵ_2 displays multiple peaks, at which ϵ_1 shows a negative slope (decreases with increasing photon energy). The alternative method is then to parameterize the optical dispersion using a mathematical

spline function, specifically when information on the optical constants of the material is limited. The spline function splits the entire spectrum into defined intervals, over which the optical dispersion curve is described using a simple polynomial function. The interval size can be tuned by the number of “nodes” defined along the energy (wavelength) axis. A basis-spline (B-spline) function sums all the individual basis functions to construct the final optical dispersion rather than joining the curves. Accordingly, a B-spline function is defined as a recursive set of single polynomial splines.^{37,38}

$$B_i^0(x) = \begin{cases} 1 & t_i \ll x \ll t_{i+1} \\ 0 & \text{otherwise} \end{cases}$$

$$B_i^k(x) = \left(\frac{x - t_i}{t_{i+k} - t_i} \right) B_i^{k-1}(x) + \left(\frac{t_{i+k+1} - x}{t_{i+k+1} - t_{i+1}} \right) B_{i+1}^{k-1}(x)$$

where k represents the degree of the spline (usually 3rd-degree polynomial function, including this study), i is the index (number) for the nodes (t_i) over which the polynomial functions connect. The multiple basis functions (spline components) are then summed at each node to produce the overall shape of the dielectric function.

$$S(x) = \sum_{i=1}^n c_i B_i^k(x)$$

where c_i are the coefficients that adjust the amplitude of each spline component. One can decrease the spacing (interval size) between the nodes to gain more control over the shape of the B-spline curve. Nevertheless, while increasing the number of nodes might seem to better describe the shape of the dispersion, it will usually lead to unrealistic dispersions in which only the noise is described better. On the other hand, the larger the number of free parameters the higher the chance of correlation between the parameters will be. Hence, generally one should begin with an estimated lowest number of nodes and systematically increase the number of nodes. The number of nodes is directly related to the number of free parameters; therefore, increasing the number of nodes is acceptable only if a marked improvement in the modeling quality is achieved, otherwise, the lower number of nodes would be desired.³⁹ Furthermore, B-spline curves render a “convex hull” property, *i.e.*, the summed function cannot exceed the highest or lowest node amplitudes, which allows the B-spline to remain positive if all spline coefficients are ≥ 0 , thus avoiding non-physical solutions with negative ϵ_2 values. However, since B-spline is a purely mathematical parameterization of the optical dispersion, it cannot ensure the physical correlation between ϵ_1 and ϵ_2 . To address this problem, Kramers–Kronig (KK) relations are used together with the B-spline function. Accordingly, the real and imaginary parts of the dielectric function are not independent, so ϵ_1 can be obtained by the KK-transform of ϵ_2 . Hence, the general approach is to parametrize ϵ_2 using the B-spline function and then ϵ_1 is calculated using the Kramers–Kronig causality relation:³⁷

$$\epsilon_1(E) = 1 + \frac{2}{\pi} P \int_0^\infty \frac{E' \epsilon_2(E')}{E'^2 - E^2} dE'$$

where P is the principal part of the integral. When parametrizing both ε_1 and ε_2 using B-splines, the number of free parameters is approximately twice the number of nodes. On the other hand, when parameterizing ε_2 only and then calculating ε_1 from the KK relation, the number of fitting parameters is reduced by almost half. In addition, it is ensured that the dielectric function adopts a physically plausible shape, *i.e.*, light absorption causes anomalous dispersion (absorption bumps/peaks in ε_2 produce wiggles in ε_1) and the larger the area under ε_2 , the larger the effect on ε_1 .

The surface roughness can be modelled as a mixed material–air layer, whose complex dielectric function is described by an effective medium approximation (EMA) such as the Bruggeman's EMA:^{40,41}

$$f_A \frac{\varepsilon_A - \varepsilon_{\text{EMA}}}{\varepsilon_A + 2\varepsilon_{\text{EMA}}} + f_B \frac{\varepsilon_B - \varepsilon_{\text{EMA}}}{\varepsilon_B + 2\varepsilon_{\text{EMA}}} = 0$$

3. Results

PDA films are prepared through different deposition times, *i.e.*, 2, 6, and 12 h. Fig. 1 (panel a) and Table 1 summarize the XPS chemical analysis and atomic composition of the coatings. The signals of C, N, and O atoms are found in all the samples,

implying successful deposition of PDA coatings. The signal of the silica substrate (Si 2p) is found for PDA 2 h sample, whereas it is undetected for PDA 6 h and 12 h due to the larger thickness of these samples. The calculated N/C ratio of the PDA 2, 6, and 12 h films is 0.131, 0.119 and 0.121, respectively. It can be seen that N/C ratio of PDA films obtained with different deposition times are ≈ 0.12 , which is comparable to the stoichiometric atomic composition of DA (N/C = 0.125). Next, deconvolution analysis of high-resolution C 1s, O 1s, and N 1s peaks was conducted.^{9,42,43} The representative high-resolution spectra of C 1s, O 1s and N 1s regions, obtained for 2 h sample, are presented in Fig. 1 (panel b–d). The corresponding data for 6 and 12 h samples are available in the ESI† (Section S1). The C 1s region comprises five peaks representing CH_x (284.8 eV), C–O/C–N (286.3 eV), C=O/C=N (287.8 eV), COOH (288.8 eV) and π – π^* (291.1 eV). The N 1s region includes three species representing tertiary/aromatic (=NH₂, 398.5 eV), secondary (R–NH–R, 399.9 eV), and primary (R–NH₂, 401.7 eV) amine groups. The O 1s region represents three main components, namely O–C (531.3 eV), O=C (532.8 eV) and O_{ads} (534.3 eV, adsorbed H₂O).

To investigate the effect of deposition time on the surface properties of the coatings, water contact angle measurements were also conducted (ESI†, Section S2). In general, the water contact angle increases with the deposition time for PDA

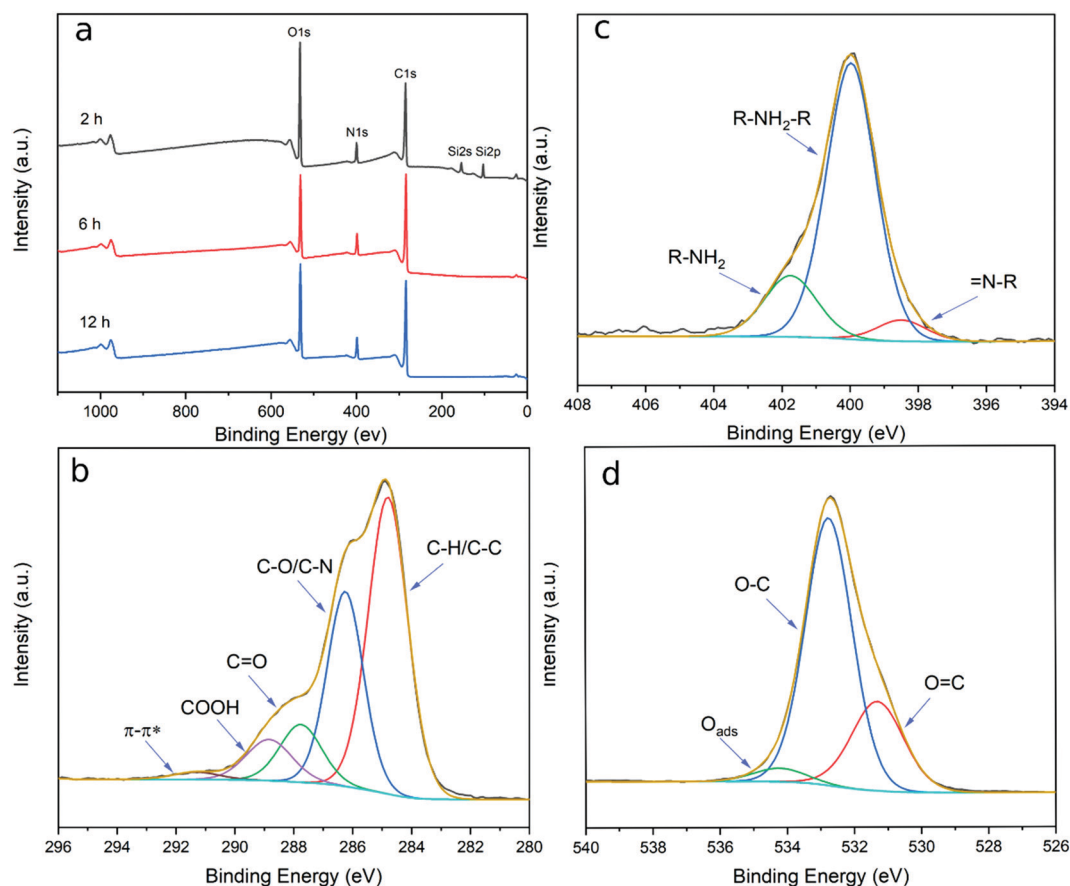


Fig. 1 Surface characteristics of PDA films. (a) XPS spectra of PDA films of varying deposition times; high-resolution XPS spectra of (b) C 1s, (c) N 1s and (d) O 1s regions of PDA 2 h deposition.

Table 1 Atomic composition of the PDA coatings determined by XPS

Deposition time	C 1s	O 1s	N 1s	Si 2p
2 h	57.8	28.1	7.7	6.4
6 h	69.3	22.1	8.6	—
12 h	67.3	24.2	8.5	—

coatings (roughly from 50 to 60°), which also suggests variations in the surface properties of the coatings.

To examine the light-absorbing behavior of the PDA films, transmission (straight-through) ellipsometry measurements were conducted. Fig. 2 displays the intensity of the light transmitted through bare and PDA-coated glass slides as a function of wavelength. It is evident that all the PDA films demonstrate a broad light absorption behavior (*i.e.*, reduce the transmission intensity) in the UV to NIR range, an effect that becomes stronger towards shorter wavelengths. This observation is consistent with the reported extinction coefficient of the polydopamine particles in solution using UV-Vis spectroscopy.^{24,25} Notably, these studies suggest that light-absorption by PDA particles enhances with time, meaning that the extinction coefficient spectrum evolves with the oxidative reaction. Thus, optical modeling of the PDA films requires two essential considerations. First, the optical model should account for the complex and broad light-absorbing nature of PDA. Second, depending on the deposition conditions, *i.e.*, deposition time herein, the optical properties of PDA can vary so each sample may require a unique optical model.

Fig. 3 demonstrates the ellipsometric ψ and Δ spectra collected from the PDA films on silica wafer together with the optimized modeling data. A step-by-step construction of the optical model is used to analyse the PDA samples of different deposition times (ESI†, Section S3). For 2 h deposition (Fig. 3, left column), the Cauchy model was first utilized to describe the

optical dispersion of PDA. Herein, the film thickness and A (amplitude parameter) were the free model parameters. It was found that including B and C as free parameters has no significant improvement in the quality of fitting, then constant values of 0.01 and 0 (typical for organic transparent materials) were used. However, the modelled ψ and Δ spectra poorly matched the experimental data over the entire range of wavelengths (Fig. S3 (ESI†), MSE = 37.7). The Cauchy relation is thus not an appropriate model to describe the optical behavior of PDA. Given the light-absorbing nature of PDA, an Urbach absorption term was included to add a small exponentially decaying extinction coefficient to the Cauchy model. Thus, in addition to thickness and A , amplitude (α) and exponent (β) parameters of the Urbach relation are also free model parameters (E_b was set to the highest photon energy in the spectrum, *i.e.*, 5 eV). By doing so, a notable improvement in the fitting quality was achieved (Fig. S4 (ESI†), MSE = 6.9 ± 0.6).

For 6 h deposition (Fig. 3, middle column), the Cauchy model, as expected, poorly described the optical properties (Fig. S5 (ESI†), MSE = 101.1). Including the Urbach absorption partly improved the fitting quality (Fig. S6 (ESI†), MSE = 39.6), yet the modelled data still could not sufficiently match the measured data, *e.g.*, in the 300–400 nm region. Hence, the Urbach absorption term cannot represent the strong light absorption by PDA obtained by 6 h deposition. As discussed earlier, the Urbach absorption term is often employed to address minor light absorption in the UV range, whereas it fails to represent large and complex light absorption over a broad range of wavelengths. Two common modeling approaches can be adopted when analysing the ellipsometric data of light-absorbing materials with unknown optical properties, *i.e.*, oscillator models and B-spline parametrization.³¹ The oscillator models are used to describe the light absorption at different resonance frequencies using mechanical resonance models, *e.g.* Gaussian or Tauc-Lorentz oscillators.^{44,45} While B-spline function is not a “physical” model, it can still afford a smooth and continuous dispersion curve with few free parameters.³⁷ Considering the complex chemical structure and light-absorbing nature of PDA, we employed B-spline to parametrize the optical constants of PDA and analyse the ellipsometric data. To eliminate the possible non-physical results, only the imaginary part of the dielectric function was parameterized by B-spline, while the real part was calculated using the Kramers–Kronig relation. An optimized resolution of 0.7 eV corresponding to 6 nodes was used. B-spline parametrization of the optical functions of PDA provided a nearly perfect match between the experimental and modelled data over the entire range of wavelengths (Fig. S7 (ESI†), MSE = 5.4 ± 1.3). Comparing the three modeling approaches, it is evident that the optical model not only affects the fitting quality and the estimated optical constants, but also greatly influences the estimated thickness value. Accordingly, the estimated film thicknesses are roughly 16, 19 and 22 nm from Cauchy, Cauchy with Urbach term, and B-spline models, respectively. Therefore, even if the optical dispersions of PDA are not of interest, a wrong dispersion equation can provide an inaccurate estimation of the coating thickness. The underestimated thickness from the Cauchy

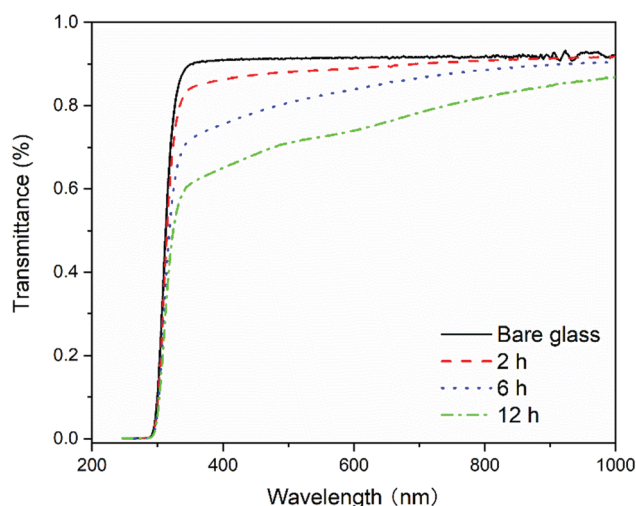


Fig. 2 Light transmittance as a function of wavelength for PDA film on glass slide prepared with different deposition times: 2 h, 6 h, and 12 h. The representative curve, out of 15 measurements, is provided for each sample.

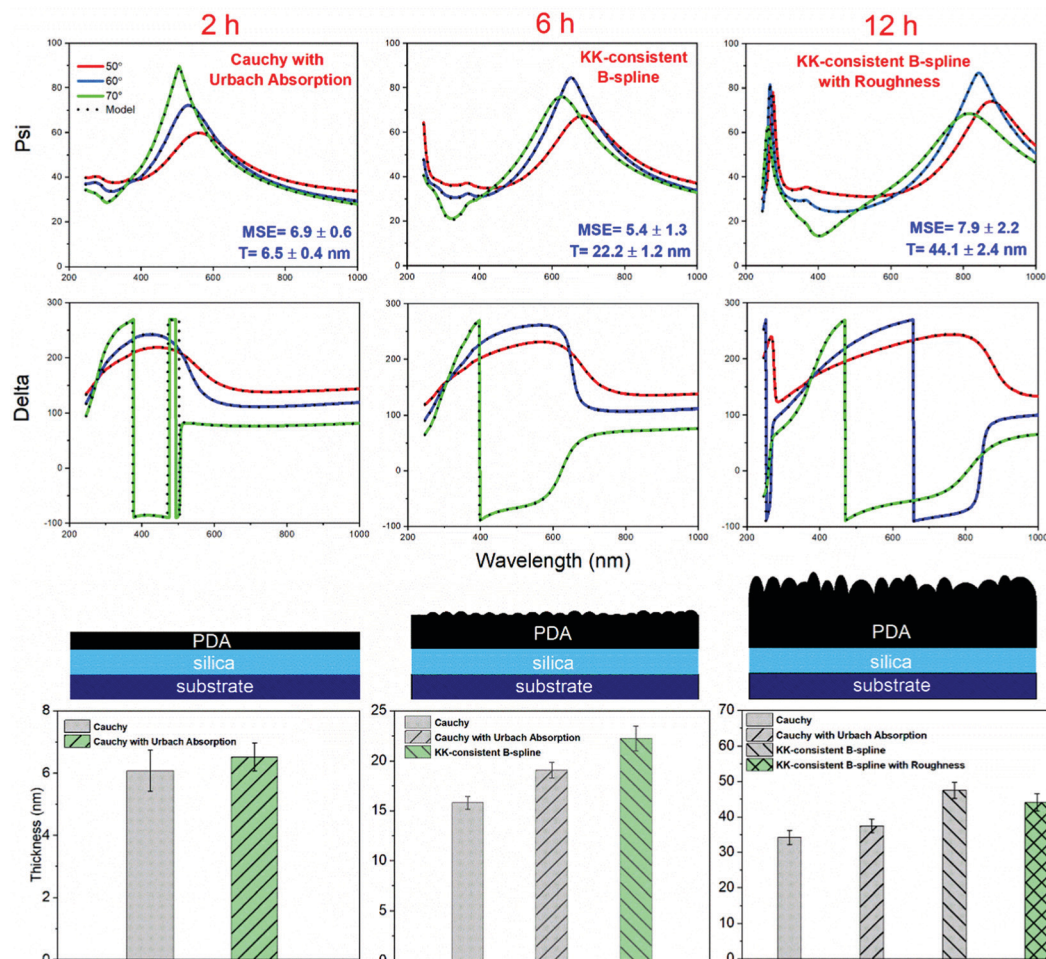


Fig. 3 The measured $\psi(\lambda)$ and $\Delta(\lambda)$ data together with the modelled $\psi(\lambda)$ and $\Delta(\lambda)$. Three different optical models are used to describe the optical dispersions of PDA, i.e., Cauchy with Urbach absorption term (2 h), Kramers–Kronig-consistent B-spline (6 h), and Kramers–Kronig-consistent B-spline with roughness layer (12 h). The values of mean squared error (MSE) and film thickness (T) are provided for each modeling procedure. Film thickness (bottom row) corresponds to the average of 15 ellipsometric measurements.

model can be explained based on the strong correlation between the thickness and optical constant (A from the Cauchy equation). This can be perceived more clearly from Fig. 4 (panel a and b) where the PDA optical dispersions obtained from the different modeling approaches are compared (6 h deposition). Regarding the Cauchy relation, the obtained dispersion for index of refraction is around 2, which is considerably larger than the typical values for organic materials (roughly between 1.4 to 1.75).⁴⁶ This suggests the thickness and optical constants are strongly correlated; hence, an overestimated index of refraction and underestimated optical thickness is found. Addition of the Urbach absorption term leads to a downward shift in the index of refraction dispersion and an extinction coefficient in the range of 0.1–0.25 (growing with a shift towards the UV range) is found. Regarding B-spline modeling, the index of refraction is shifted further down and a more complex dispersion curve for the extinction coefficient is obtained. In general, the extinction coefficient curve presents complex absorption features and increases when moving to shorter wavelengths reaching a value of around 0.15 to 0.25 in the UV range. The index of refraction shows an anomalous dispersion

(n decreases towards shorter wavelengths, e.g., in 300–400 nm) and varies roughly in the range of 1.6 to 1.7. Determination of the optical dispersions of PDA is a challenge as discussed earlier. A survey through the literature shows that the reported n and k for PDA, melanin, and other catecholamine derivatives notably depend on the material preparation and the measurement method.^{9,47–53} For instance, Xiao *et al.*,⁵¹ Kawamura *et al.*,⁵² and Stavenga *et al.*⁵³ reported $1.7 < n < 1.8$ for PDA and melanin particles in the 400–800 nm region. Vega *et al.* reported a rather constant value of ~ 1.5 for PDA films in the 300–900 nm region.⁴⁸ Li *et al.* reported $n \sim 1.7$ – 1.85 with a dispersion shape similar to our study in the 400–1000 nm region.⁴⁷ Repenko *et al.* reported a rather constant $n \sim 1.55$ in the 400–800 nm region, which increases to around 1.8 in the UV range. Akin *et al.* reported $n \sim 1.4$ – 1.6 in the 200–1000 nm region, which decreases towards shorter wavelengths.⁵⁰ In general, the refractive index of PDA seems to notably depend on its microstructure and particle shape/size and thus the preparation method. On the other hand, the k dispersion in this study and other literature reports are in good agreement both in terms of the shape and the range of values.

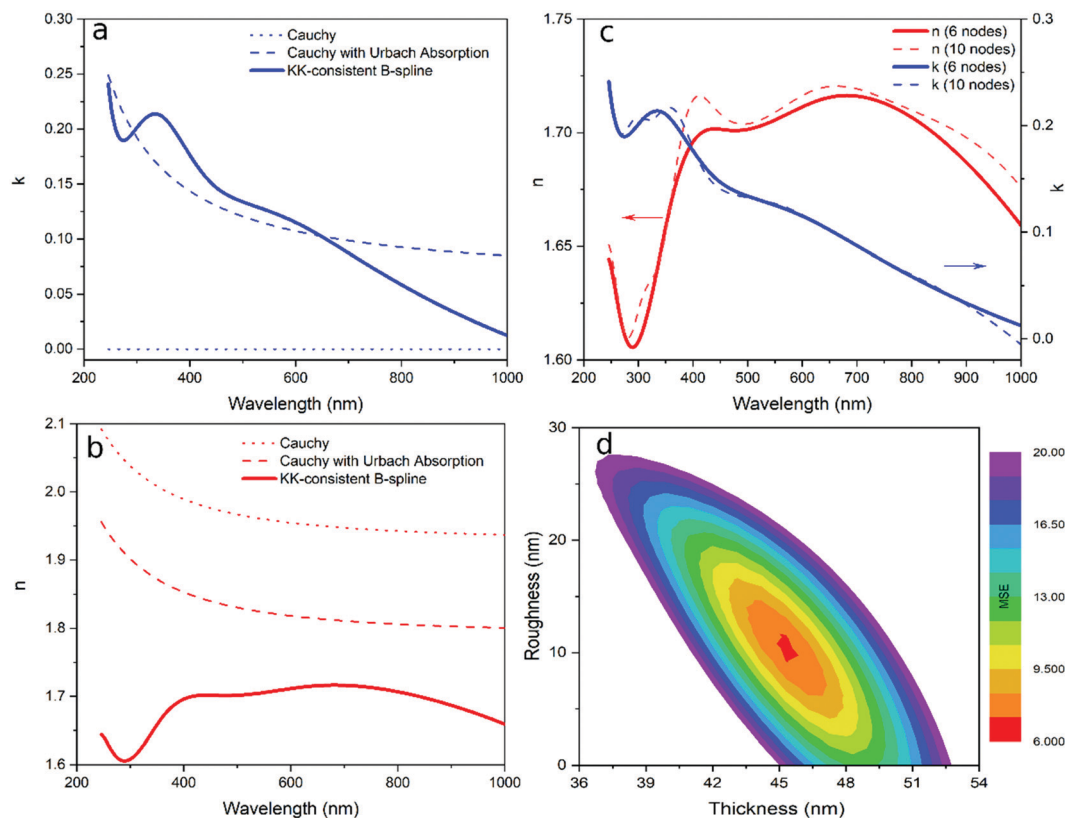


Fig. 4 (a) and (b) Optical dispersions of PDA 6 h deposition sample obtained from different modeling approaches, (c) effect of number of B-spline nodes on the modelled optical constants of PDA 6 h deposition sample, (d) two-parameter thickness–roughness uniqueness chart for PDA 12 h deposition sample.

As discussed regarding B-spline parameterization, one should always minimize the number of nodes (and thus free model parameters) to avoid overparameterization. We performed a thorough sensitivity analysis of the modelled thickness and optical dispersions against the number of nodes (ESI,† Section S4). Herein, we briefly discuss how overparameterization can affect the modeling outcome and highlight the importance of finding the minimum number of nodes. Fig. 4 (panel c) compares the modelled optical dispersions of the PDA film (6 h deposition) using two different numbers of nodes, *i.e.*, 6 and 10 nodes. Accordingly, the number of nodes does not affect the overall shape and values of the optical dispersions. However, using 10 nodes produces small features and peaks in the optical dispersions, which remain unknown to be the real optical behaviour of PDA or merely modeling artefact. For this reason, it is reasonable to choose only 6 nodes that can provide smooth optical dispersions without overfitting.

For 12 h deposition (Fig. 3, right column), both Cauchy (Fig. S8 (ESI†), MSE = 149.1) and Cauchy with Urbach term (Fig. S9 (ESI†), MSE = 98.5) completely fail to match the experimental data. B-spline parameterization provides a better agreement between the experimental and modeling data (Fig. S10 (ESI†), MSE = 12.6), yet the model cannot perfectly match the data for short wavelengths. Considering the rather long deposition time, the PDA film herein is expected to have a relatively rough surface. Hence, an upper roughness layer,

modelled as a uniform mixture of PDA–air, is added on top of the B-spline layer. The roughness layer improved the fitting of optical dispersion (Fig. S11 (ESI†), MSE = 7.9 ± 2.2). A roughness value of around 10 ± 2 nm is estimated from the model. We also conducted a thorough sensitivity analysis of the model parameters for this sample (ESI,† Section S4). Herein, we shortly discuss the importance of analysis of the parameters uniqueness, *i.e.*, only one particular combination of the parameters provides a good match between the model and the experimental data. Fig. 4 (panel d) depicts the two-parameter uniqueness chart for the PDA film (12 h deposition). Herein, different combinations of thickness–roughness values are characterized by their MSE value. Accordingly, all thickness–roughness combinations provide large MSE values, except a particular combination of thickness (~ 45 nm)–roughness (~ 10 nm) that provides the smallest MSE (red region in the chart). Hence, we can conclude that the modeling outcome is unique. In order to validate the thickness values estimated from ellipsometry, the thickness of the films was also examined using AFM imaging. Fig. 5 shows the AFM topography images together with the cross-section height profiles of the scratched area of each PDA film. Overall, the estimated thickness values from the two methods are in agreement (Fig. 6), suggesting that the optimized optical models for each PDA sample provided accurate estimates. The AFM data also confirms that the roughness of the coatings increases with the deposition time. It should be noted that the estimated roughness

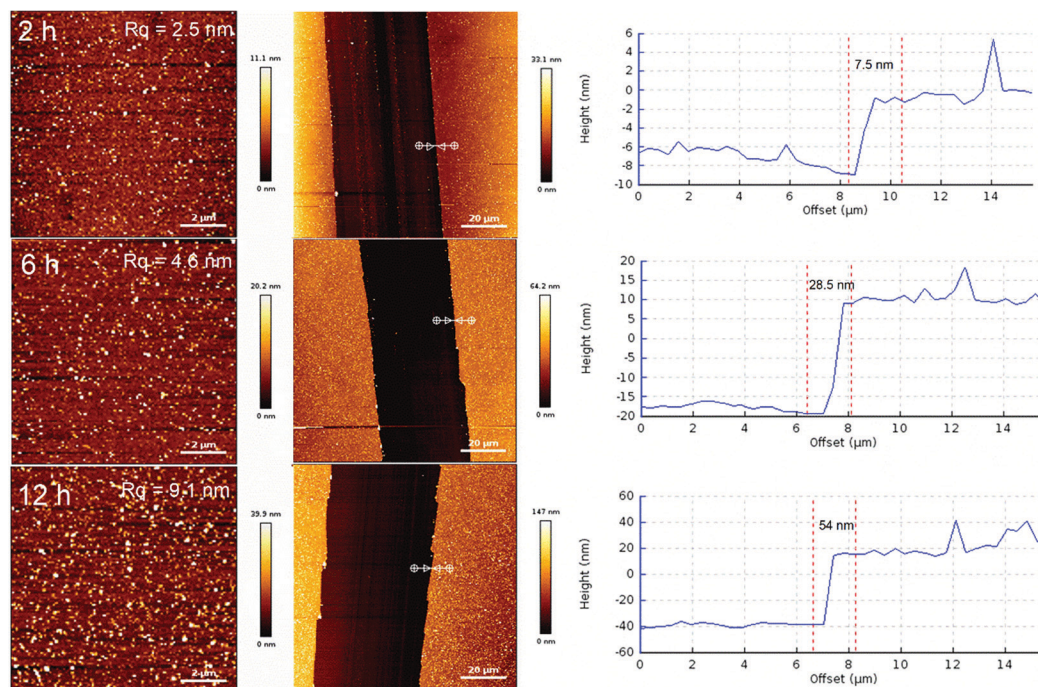


Fig. 5 Representative AFM images and corresponding height profiles of PDA films on silicon wafer for 2 h (top row), 6 h (middle row) and 12 h (bottom row) deposition times.

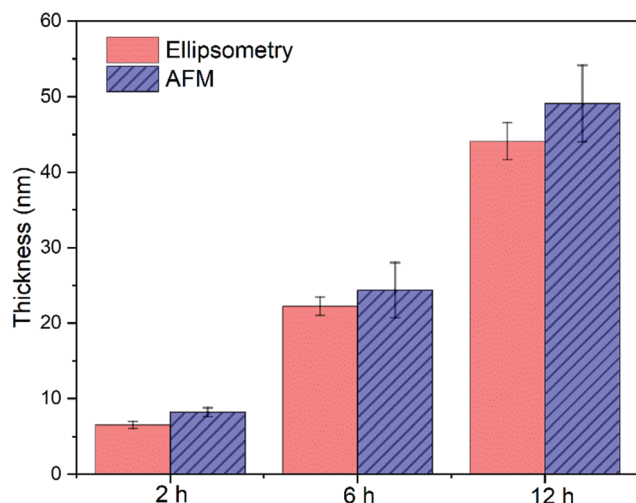


Fig. 6 Thickness of PDA films measured with AFM and ellipsometry. For AFM thickness, 30 height profiles (3 images, 10 height profiles in each) were examined. The ellipsometry thickness corresponds to 15 measurements.

(12 h deposition) from ellipsometry is comparable with the calculated R_q roughness value obtained by AFM. It should be considered, though, that while AFM measurements can supplement the ellipsometry data in terms of constructing appropriate optical models for relatively rough coatings, the roughness values from the two methods are calculated differently and have different mathematical meanings (ESI,† Section S5).

We have thus herein demonstrated that PDA films, depending on the preparation condition, can have different optical behavior

and microstructure, *e.g.*, surface roughness, which necessitate rigorous modeling analysis and construction of exclusive optical models for each PDA sample. The B-spline parameterization in general provided reliable modeling outcome in terms of the film thickness. In this regard, we also tested if fixing the optical constants (using the values for PDA 6 h) can provide accurate estimates of the film thickness (Fig. S12 and S13, ESI†). Regarding the optical properties, we observed that the modelled k dispersion remains almost the same for all the samples in terms of shape and the range. Contrarily, n dispersion showed dependence on the deposition time, *i.e.*, while the overall shape remains the same, n increases with deposition time. In this case, we cannot certainly verify if this is due to a variation in the physicochemical properties of PDA (*e.g.* variations in chemical composition and particle size) or merely modeling artefact. To further investigate this point (ESI,† Section S6), we used fixed PDA thickness in the models (using the estimated values from AFM), leaving the optical constants as the model variables. Similarly, it was found that the dispersion shapes are almost independent of deposition time, but n in particular increases with the deposition time. It should be also noted that the investigated samples herein all possessed relatively smooth surfaces (due to a rather short reaction time and multistep preparation method). However, for PDA samples with strong granular surface structure and (or) thickness nonuniformity (relatively long deposition times),^{10,11} one must consider the required nonideality corrections in the optical model. To verify if the step-by-step modeling approach also works for the standard PDA samples, we prepared a thicker and rougher PDA film obtained by 24 h one-step deposition (ESI,† Section S7). It was found that the modeling procedure is useful also for this sample;

however, extra consideration was needed to avoid correlation between the parameters due to the uneven surface structure. Last but not least, it should be noted that PDA coatings possess a rather porous and heterogeneous internal structure.¹¹ Accordingly, while an isotropic uniform box model is generally used to represent the film when modeling the ellipsometric data, a PDA coating is more like a non-uniform mixture of PDA particles and void, which can also demonstrate gradients of particle size, particle chemistry, and particle volume content in the vertical direction, all of which can affect the optical properties measured by ellipsometry (in particular n). Therefore, the optical dispersions obtained from the B-spline parameterization of the PDA ellipsometric data are more correctly the “pseudo” optical constants rather than the intrinsic properties of the material.

4. Summary and conclusion

In this study, we demonstrated that the light-absorbing nature of PDA is an essential factor that must be considered when assessing the ellipsometric data of such coatings. Accordingly, the commonly but erroneously used Cauchy equation cannot accurately describe the optical behavior of PDA. While addition of the Urbach absorption term to the Cauchy model led to an improved modeling quality, the more accurate representation of the optical dispersion was obtained by a KK-consistent B-spline model. Overall, a fallacious optical model not only provides inaccurate and possibly non-physical optical dispersions but also renders incorrect estimation of the film thickness. Besides, an appropriate optical model solely cannot guarantee a decent modeling quality and physically plausible solutions, but extra care is needed for optimizing the number of free parameters and assessing their cross-correlation. Finally, the rough and porous structure of PDA coatings is a factor that may be considered in the optical model.

Conflicts of interest

There are no conflicts to declare.

Acknowledgements

R. Q. acknowledges a stipend from the China Scholarship Council (CSC). The authors also kindly acknowledge Dr Thomas Wagner (Quantum Design Europe GmbH, Darmstadt, Germany) for the constructive comments on the data analysis.

Notes and references

- H. Lee, S. M. Dellatore, W. M. Miller and P. B. Messersmith, Mussel-Inspired Surface Chemistry for Multifunctional Coatings, *Science*, 2007, **318**, 426–430.
- D. R. Dreyer, D. J. Miller, B. D. Freeman, D. R. Paul and C. W. Bielawski, Perspectives on poly(dopamine), *Chem. Sci.*, 2013, **4**, 3796–3802.
- M. E. Lyng, R. Van Der Westen, A. Postma and B. Städler, Polydopamine – A nature-inspired polymer coating for biomedical science, *Nanoscale*, 2011, **3**, 4916–4928.
- K. Lim, R. R. Y. Chua, B. Ho, P. A. Tambyah, K. Hadinoto and S. S. J. Leong, Development of a catheter functionalized by a polydopamine peptide coating with antimicrobial and antibiofilm properties, *Acta Biomater.*, 2015, **15**, 127–138.
- H. Gao, Y. Sun, J. Zhou, R. Xu and H. Duan, Mussel-inspired synthesis of polydopamine-functionalized graphene hydrogel as reusable adsorbents for water purification, *ACS Appl. Mater. Interfaces*, 2013, **5**, 425–432.
- S. H. Ku, J. Ryu, S. K. Hong, H. Lee and C. B. Park, General functionalization route for cell adhesion on non-wetting surfaces, *Biomaterials*, 2010, **31**, 2535–2541.
- S. M. Kang, N. S. Hwang, J. Yeom, S. Y. Park, P. B. Messersmith, I. S. Choi, R. Langer, D. G. Anderson and H. Lee, One-step multipurpose surface functionalization by adhesive catecholamine, *Adv. Funct. Mater.*, 2012, **22**, 2949–2955.
- O. Pop-Georgievski, N. Neykova, V. Proks, J. Houdkova, E. Ukraintsev, J. Zemek, A. Kromka and F. Rypáček, Polydopamine-modified nanocrystalline diamond thin films as a platform for bio-sensing applications, *Thin Solid Films*, 2013, **543**, 180–186.
- F. Bernsmann, A. Ponche, C. Ringwald, J. Hemmerle, J. Raya, B. Bechinger, J. C. Voegel, P. Schaaf and V. Ball, Characterization of dopamine-melanin growth on silicon oxide, *J. Phys. Chem. C*, 2009, **113**, 8234–8242.
- F. Bernsmann, V. Ball, F. Addiego, A. Ponche, M. Michel, J. J. D. A. Gracio, V. Toniazio and D. Ruch, Dopamine-melanin film deposition depends on the used oxidant and buffer solution, *Langmuir*, 2011, **27**, 2819–2825.
- V. Ball, D. Del Frari, V. Toniazio and D. Ruch, Kinetics of polydopamine film deposition as a function of pH and dopamine concentration: insights in the polydopamine deposition mechanism, *J. Colloid Interface Sci.*, 2012, **386**, 366–372.
- Y. Liu, W. Z. Qiu, H. C. Yang, Y. C. Qian, X. J. Huang and Z. K. Xu, Polydopamine-assisted deposition of heparin for selective adsorption of low-density lipoprotein, *RSC Adv.*, 2015, **5**, 12922–12930.
- X. Du, L. Li, J. Li, C. Yang, N. Frenkel, A. Welle, S. Heissler, A. Nefedov, M. Grunze and P. A. Levkin, UV-triggered dopamine polymerization: control of polymerization, surface coating, and photopatterning, *Adv. Mater.*, 2014, **26**, 8029–8033.
- F. Ponzio, J. Barthès, J. Bour, M. Michel, P. Bertani, J. Hemmerlé, M. D'Ischia and V. Ball, Oxidant Control of Polydopamine Surface Chemistry in Acids: A Mechanism-Based Entry to Superhydrophilic-Superoleophobic Coatings, *Chem. Mater.*, 2016, **28**, 4697–4705.
- Y. Lv, S. J. Yang, Y. Du, H. C. Yang and Z. K. Xu, Co-deposition Kinetics of Polydopamine/Polyethyleneimine Coatings: Effects of Solution Composition and Substrate Surface, *Langmuir*, 2018, **34**, 13123–13131.
- S. Kasemset, L. Wang, Z. He, D. J. Miller, A. Kirschner, B. D. Freeman and M. M. Sharma, Influence of

- polydopamine deposition conditions on hydraulic permeability, sieving coefficients, pore size and pore size distribution for a polysulfone ultrafiltration membrane, *J. Membr. Sci.*, 2017, **522**, 100–115.
- 17 H. Coskun, A. Aljabour, L. Uiberlacker, M. Strobel, S. Hild, C. Cobet, D. Farka, P. Stadler and N. S. Sariciftci, Chemical vapor deposition – based synthesis of conductive polydopamine thin-films, *Thin Solid Films*, 2018, **645**, 320–325.
 - 18 G. Sun, F. Zu, N. Koch, J. Rappich and K. Hinrichs, In Situ Infrared Spectroscopic Monitoring and Characterization of the Growth of Polydopamine (PDA) Films, *Phys. Status Solidi B*, 2019, **256**, 1800308.
 - 19 W. Ogieglo, H. Wormeester, K. J. Eichhorn, M. Wessling and N. E. Benes, In situ ellipsometry studies on swelling of thin polymer films: a review, *Prog. Polym. Sci.*, 2015, **42**, 42–78.
 - 20 K. Vedam, Spectroscopic ellipsometry: a historical overview, *Thin Solid Films*, 1998, **313–314**, 1–9.
 - 21 D. R. Dreyer, D. J. Miller, B. D. Freeman, D. R. Paul and C. W. Bielawski, Elucidating the structure of poly(dopamine), *Langmuir*, 2012, **28**, 6428–6435.
 - 22 J. Liebscher, R. Mrówczyński, H. A. Scheidt, C. Filip, N. D. Haidade, R. Turcu, A. Bende and S. Beck, Structure of polydopamine: a never-ending story?, *Langmuir*, 2013, **29**, 10539–10548.
 - 23 T. G. Barclay, H. M. Hegab, S. R. Clarke and M. Ginic-Markovic, *Adv. Mater. Interfaces*, 2017, **4**, 1601192.
 - 24 W. Sheng, B. Li, X. Wang, B. Dai, B. Yu, X. Jia and F. Zhou, Brushing up from ‘anywhere’ under sunlight: a universal surface-initiated polymerization from polydopamine-coated surfaces, *Chem. Sci.*, 2015, **6**, 2068–2073.
 - 25 J. Cui, J. Iturri, J. Paez, Z. Shafiq, C. Serrano, M. d’Ischia and A. del Campo, Dopamine-Based Coatings and Hydrogels: Toward Substitution-Related Structure-Property Relationships, *Macromol. Chem. Phys.*, 2014, **215**, 2403–2413.
 - 26 V. Ball, Determination of the extinction coefficient of “polydopamine” films obtained by using NaIO₄ as the oxidant, *Mater. Chem. Phys.*, 2017, **186**, 546–551.
 - 27 F. Bernsmann, O. Ersen, J. C. Voegel, E. Jan, N. A. Kotov and V. Ball, Melanin-Containing Films: Growth from Dopamine Solutions versus Layer-by-Layer Deposition, *ChemPhysChem*, 2010, **11**, 3299–3305.
 - 28 J. H. Cho, R. Katsumata, S. X. Zhou, C. Bin Kim, A. R. Dulaney, D. W. Janes and C. J. Ellison, Ultrasmooth Polydopamine Modified Surfaces for Block Copolymer Nanopatterning on Flexible Substrates, *ACS Appl. Mater. Interfaces*, 2016, **8**, 7456–7463.
 - 29 N. Singh, F. Sallem, C. Mirjolet, T. Nury, S. K. Sahoo, N. Millot and R. Kumar, Polydopamine Modified Superparamagnetic Iron Oxide Nanoparticles as Multifunctional Nanocarrier for Targeted Prostate Cancer Treatment, *Nanomaterials*, 2019, **9**, 138.
 - 30 H. Fujiwara, *Spectroscopic Ellipsometry: Principles and Applications*, John Wiley & Sons, Ltd, 2007.
 - 31 H. G. Tompkins and J. N. Hilfiker, *Spectroscopic Ellipsometry: Practical Application to Thin Film Characterization*, Momentum Press, 2016.
 - 32 H. Fujiwara and R. W. Collins, *Spectroscopic Ellipsometry for Photovoltaics*, Springer, 2018, vol. 1.
 - 33 E. Agocs, B. Fodor, B. Pollakowski, B. Beckhoff, A. Nutsch, M. Jank and P. Petrik, Approaches to calculate the dielectric function of ZnO around the band gap, *Thin Solid Films*, 2014, **571**, 684–688.
 - 34 S. Schöche, N. Hong, M. Khorasaninejad, A. Ambrosio, E. Orabona, P. Maddalena and F. Capasso, Optical properties of graphene oxide and reduced graphene oxide determined by spectroscopic ellipsometry, *Appl. Surf. Sci.*, 2017, **421**, 778–782.
 - 35 J. W. Weber, V. E. Calado and M. C. M. Van De Sanden, Optical constants of graphene measured by spectroscopic ellipsometry, *Appl. Phys. Lett.*, 2010, **97**, 091904.
 - 36 J. W. Weber, T. A. R. Hansen, M. C. M. Van De Sanden and R. Engeln, B-spline parametrization of the dielectric function applied to spectroscopic ellipsometry on amorphous carbon, *J. Appl. Phys.*, 2009, **106**, 123503.
 - 37 B. Johs and J. S. Hale, Dielectric function representation by B-splines, *Phys. Status Solidi A*, 2008, **205**, 715–719.
 - 38 P. H. C. Eilers and B. D. Marx, Splines, knots, and penalties, *Wiley Interdiscip. Rev.: Comput. Mol. Sci.*, 2010, **2**, 637–653.
 - 39 D. V. Likhachev, Selecting the right number of knots for B-spline parameterization of the dielectric functions in spectroscopic ellipsometry data analysis, *Thin Solid Films*, 2017, **636**, 519–526.
 - 40 D. E. Aspnes, J. B. Theeten and F. Hottier, Investigation of effective-medium models of microscopic surface roughness by spectroscopic ellipsometry, *Phys. Rev. B: Condens. Matter Phys.*, 1979, **20**, 3292–3302.
 - 41 D. Lehmann, F. Seidel and D. R. T. Zahn, Thin films with high surface roughness: thickness and dielectric function analysis using spectroscopic ellipsometry, *SpringerPlus*, 2014, **3**, 82.
 - 42 S. Rella, E. Mazzotta, A. Caroli, M. De Luca, C. Bucci and C. Malitesta, Investigation of polydopamine coatings by X-ray Photoelectron Spectroscopy as an effective tool for improving biomolecule conjugation, *Appl. Surf. Sci.*, 2018, **447**, 31–39.
 - 43 R. A. Zangmeister, T. A. Morris and M. J. Tarlov, Characterization of polydopamine thin films deposited at short times by autoxidation of dopamine, *Langmuir*, 2013, **29**(27), 8619–8628.
 - 44 F. Wooten, *Optical properties of solids*, Academic Press, 2013.
 - 45 D. V. Likhachev, N. Malkova and L. Poslavsky, Modified Tauc-Lorentz dispersion model leading to a more accurate representation of absorption features below the bandgap, *Thin Solid Films*, 2015, **589**, 844–851.
 - 46 T. Higashihara and M. Ueda, Recent Progress in High Refractive Index Polymers, *Macromolecules*, 2015, **48**, 1915–1929.
 - 47 W. Li, A. Patil, X. Zhou, Z. Wang, M. Xiao, M. D. Shawkey, N. C. Gianneschi and A. Dhinojwala, Characterization of broadband complex refractive index of synthetic melanin coatings and their changes after ultraviolet irradiation, *Appl. Phys. Lett.*, 2020, **117**, 203701.

- 48 M. Vega, E. M. Martín del Valle, M. Pérez, C. Pecharromán and G. Marcelo, Color Engineering of Silicon Nitride Surfaces to Characterize the Polydopamine Refractive Index, *ChemPhysChem*, 2018, **19**, 3418–3424.
- 49 T. Repenko, A. Rix, A. Nedilko, J. Rose, A. Hermann, R. Vinokur, S. Moli, R. Cao-Milán, M. Mayer, G. von Plessen, A. Fery, L. De Laporte, W. Lederle, D. N. Chigrin and A. J. C. Kuehne, Strong Photoacoustic Signal Enhancement by Coating Gold Nanoparticles with Melanin for Biomedical Imaging, *Adv. Funct. Mater.*, 2018, **28**, 1705607.
- 50 Ü. Akın, İ. Çelik, Ç. Avcı, N. Tuğluoğlu and Ö. F. Yüksel, Some optical properties of melanin thick film, *Mater. Today: Proc.*, 2019, **18**, 1972–1977.
- 51 M. Xiao, Y. Li, M. C. Allen, D. D. Deheyn, X. Yue, J. Zhao, N. C. Gianneschi, M. D. Shawkey and A. Dhinojwala, Bio-Inspired Structural Colors Produced *via* Self-Assembly of Synthetic Melanin Nanoparticles, *ACS Nano*, 2015, **9**, 5454–5460.
- 52 A. Kawamura, M. Kohri, G. Morimoto, Y. Nannichi, T. Taniguchi and K. Kishikawa, Full-Color Biomimetic Photonic Materials with Iridescent and Non-Iridescent Structural Colors, *Sci. Rep.*, 2016, **6**, 33984.
- 53 D. G. Stavenga, H. L. Leertouwer, D. C. Osorio and B. D. Wilts, High refractive index of melanin in shiny occipital feathers of a bird of paradise, *Light: Sci. Appl.*, 2015, **4**, e243.

Supporting Information for

Parameterization of the Optical Constants of Polydopamine Films for Spectroscopic Ellipsometry Studies

*Runtian Qie, Saeed Zajforoushan Moghaddam, and Esben Thormann**

Department of Chemistry, Technical University of Denmark, 2800 Kgs. Lyngby, Denmark

Table of Contents

Section 1 XPS data of PDA films	S2
Section 2 Contact angle of PDA films	S3
Section 3 Step-by-step modeling of the ellipsometry data	S3
PDA 2 h deposition	S4
PDA 6 h deposition	S5
PDA 12 h deposition	S6
Modeling using fixed optical constants	S8
Section 4 Sensitivity analysis for the B-spline function	S9
PDA 6 h deposition	S10
PDA 12 h deposition	S13
Section 5 Roughness from ellipsometry	S14
Section 6 Optical dispersions of PDA films	S15
Modeling with unknown thickness and optical constants	S15
Modeling with unknown optical constants (known thickness from AFM)	S16
Section 7 Step-by-step modeling approach (PDA film one-step 24 h deposition)	S16
Step-by-step modeling	S17
Sensitivity analysis	S19
AFM data	S19
Optical dispersions	S21

S1. XPS data of PDA films: Figure S1 demonstrates the high resolution XPS spectra and peak deconvolution of C 1s, N 1s and O 1s of the PDA films (6 and 12 h). The estimated percentages of the functional groups of the PDA films (2, 6, and 12 h) are summarized in Table S1.

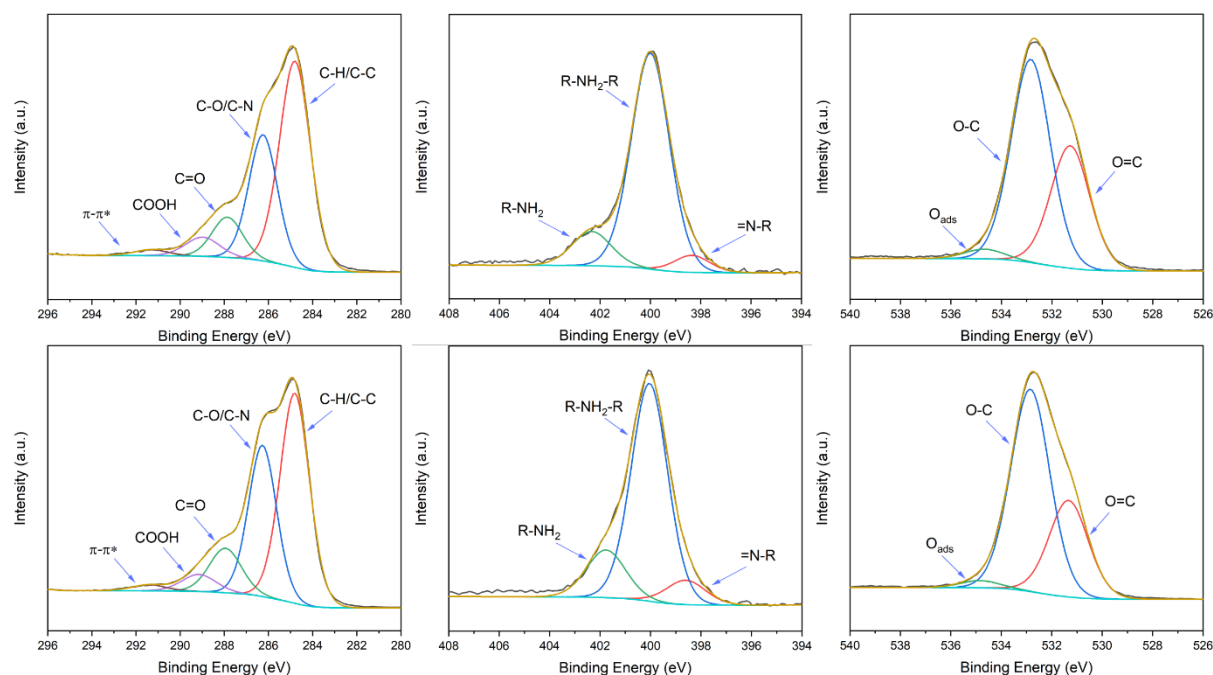


Figure S1 High-resolution XPS spectra of C 1s, N 1s and O 1s of PDA films; (top row) 6 h deposition, (bottom row) 12 h deposition

Table S1 XPS functional group percentages for PDA films of different deposition times

Deposition time	C 1s				O 1s			N 1s		
	CHx, C-NH ₂	C-O, C-N	C=O	COOH	O=C	O-C	Oads	=N-R	R-NH-R	R-NH ₂
2 h	50.6	31.8	9.2	8.4	25.8	70.5	3.7	7.1	74.6	18.3
6 h	53.6	30.9	9.3	6.2	36.5	60.6	2.9	6.3	80.5	13.2
12 h	51.0	32.1	11.7	5.2	31.5	66.2	2.3	8.4	74.6	17.0

S2. Water contact angle of PDA films: The water contact angles of bare and PDA-coated silicon wafers were measured using Theta Lite optical tensiometer (Biolin Scientific, Sweden). Measurements were conducted using a 1.5 μl water droplet at ambient temperature. **Figure S2** shows the representative contact angle (15 measurements: 5 randomly chosen areas on 3 specimens) of PDA samples of different deposition times.

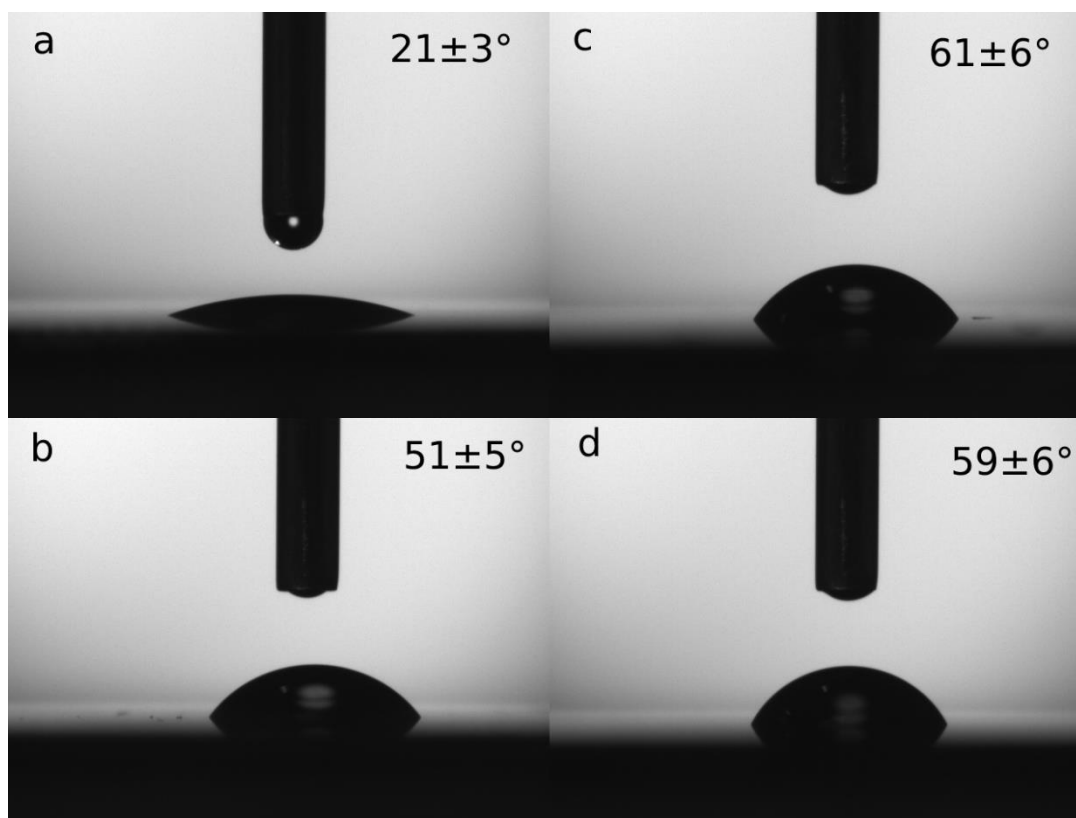


Figure S2 Water contact angle of bare and PDA-coated silicon wafers; (a) bare wafer, (b) PDA 2 h, (c) PDA 6 h, and (d) PDA 12 h deposition. The reported value represents the average of 15 data points.

S3 Step-by-step modeling of the ellipsometry data: as discussed in the main manuscript, a step-by-step construction of an appropriate optical model is required for the ellipsometry analysis of PDA films, depending on various aspects of the film such as thickness, roughness, and light absorption. When constructing the optical model, one should always consider that the minimum number of “free” parameters in the model is desired, and that adding further free parameters to the model should significantly improve the quality of the fitting (as a rule of thumb: at least 20% reduction in MSE when a free parameter is added to the model). In the following, the step-by-step construction of the appropriate optical models for the PDA films of this study (in each case, the representative median sample from 15 data measurements) is provided in **Figure S3-S11**.

We begin with the simplest optical model, i.e., Cauchy relation (2 free parameters: PDA film thickness (layer # 3) and A of Cauchy), then advance the optical model to Cauchy with an Urbach absorption term (4 free parameters: PDA film thickness (layer # 3), A of Cauchy, amplitude and exponent of the Urbach relation), KK-consistent B-spline (9 free parameters: PDA film thickness (layer # 3), 6 nodes, 2 KK-relation parameters), and ultimately KK-consistent B-spline with an EMA roughness layer (10 free parameters: PDA film thickness (layer # 3), 6 nodes, 2 KK-relation parameters, thickness of the roughness layer).

Fit Results

MSE = 37.783

Thickness # 3 = 5.88 ± 0.107 nm

A = 1.714 ± 0.0117

Total Thickness = 107.80 ± 0.107 nm

Optical Model

- Layer # 3 = Cauchy Thickness # 3 = 5.88 nm (fit)
A = 1.714 (fit) B = 0.01000 C = 0.0000

+ Urbach Absorption Parameters

Layer # 2 = SIO2_JAW Thickness # 2 = 100.93 nm

Layer # 1 = INTR_JAW Thickness # 1 = 1.00 nm

Substrate = SI_JAW

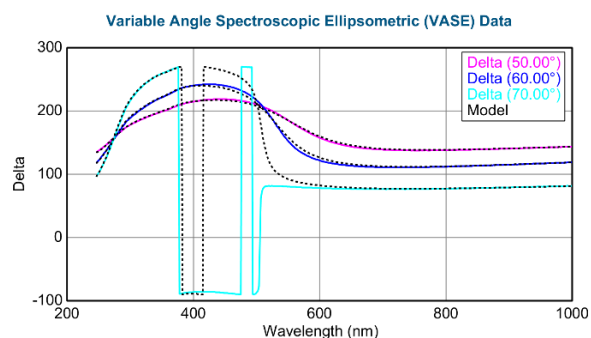
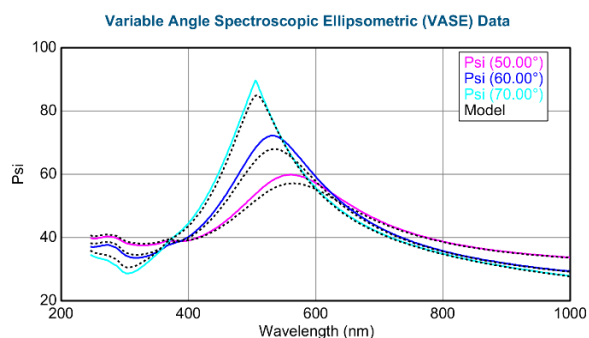


Figure S3 PDA 2 h deposition, Cauchy model

Fit Results

MSE = 7.041

Thickness # 3 = 6.50 ± 0.021 nm

A = 1.655 ± 0.001984

k Amplitude = 0.15071 ± 0.001020

Exponent = 0.319 ± 0.007785

Total Thickness = 108.43 ± 0.021 nm

Optical Model

- Layer # 3 = Cauchy Thickness # 3 = 6.50 nm (fit)
A = 1.655 (fit) B = 0.01000 C = 0.0000

- Urbach Absorption Parameters

k Amplitude = 0.15071 (fit) Exponent = 0.319 (fit)
Band Edge = 400.0 nm

Layer # 2 = SIO2_JAW Thickness # 2 = 100.93 nm

Layer # 1 = INTR_JAW Thickness # 1 = 1.00 nm

Substrate = SI_JAW

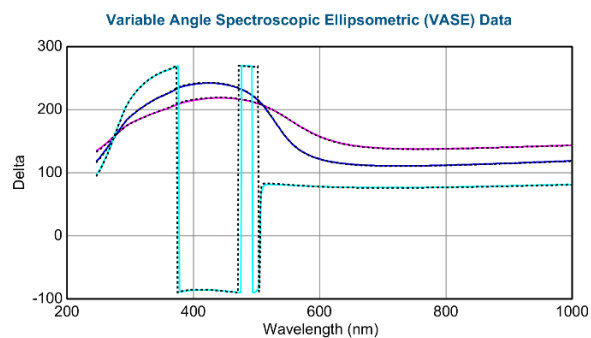
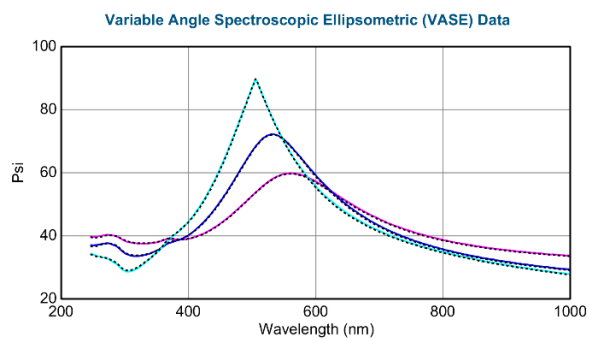


Figure S4 PDA 2 h deposition, Cauchy with Urbach absorption model

Fit Results

MSE = 101.135 (Out-Of-Spec)
Thickness # 3 = 15.70 ± 0.227 nm
A = 1.927 ± 0.0114
Total Thickness = 119.08 ± 0.227 nm

Optical Model

- Layer # 3 = [Cauchy](#) Thickness # 3 = [15.70 nm](#) (fit)
A = [1.927](#) (fit) B = [0.01000](#) C = [0.0000](#)
+ Urbach Absorption Parameters
Layer # 2 = [SIO2_JAW](#) Thickness # 2 = [102.38 nm](#)
Layer # 1 = [INTR_JAW](#) Thickness # 1 = [1.00 nm](#)
Substrate = [SI_JAW](#)

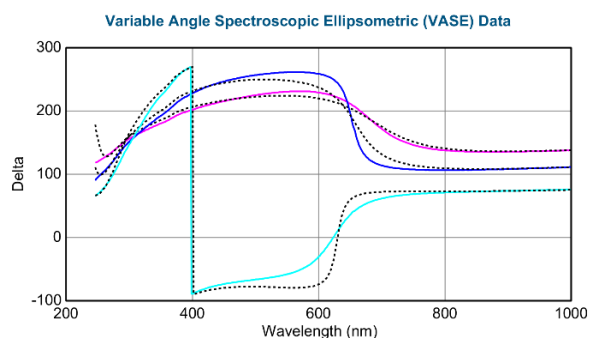
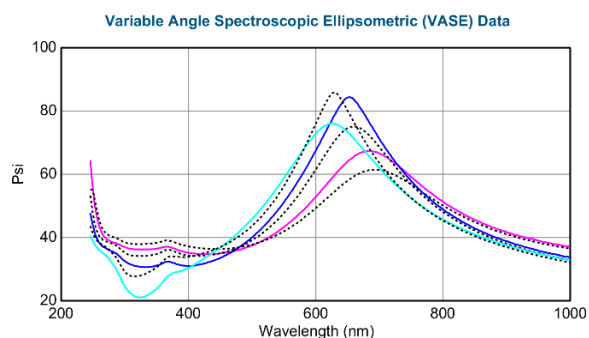


Figure S5 PDA 6 h deposition, Cauchy model

Fit Results

MSE = 39.641
Thickness # 3 = 18.75 ± 0.121 nm
A = 1.791 ± 0.004675
k Amplitude = 0.14243 ± 0.001384
Exponent = 0.273 ± 0.007101
Total Thickness = 122.13 ± 0.121 nm

Optical Model

- Layer # 3 = [Cauchy](#) Thickness # 3 = [18.75 nm](#) (fit)
A = [1.791](#) (fit) B = [0.01000](#) C = [0.0000](#)
- Urbach Absorption Parameters
k Amplitude = [0.14243](#) (fit) Exponent = [0.273](#) (fit)
Band Edge = [400.0 nm](#)
Layer # 2 = [SIO2_JAW](#) Thickness # 2 = [102.38 nm](#)
Layer # 1 = [INTR_JAW](#) Thickness # 1 = [1.00 nm](#)
Substrate = [SI_JAW](#)

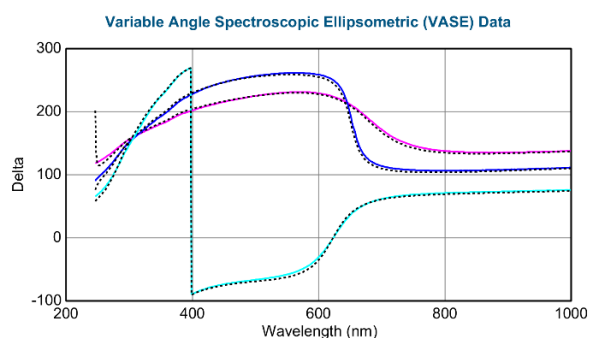
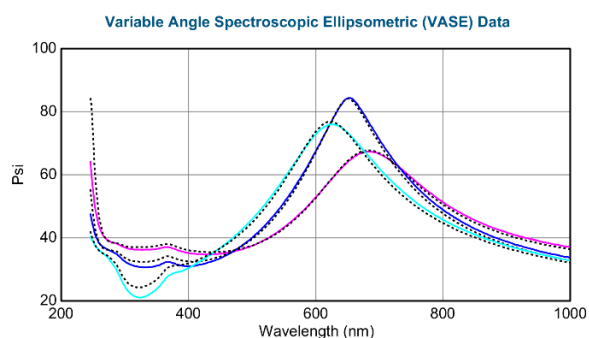


Figure S6 PDA 6 h deposition, Cauchy with Urbach absorption model

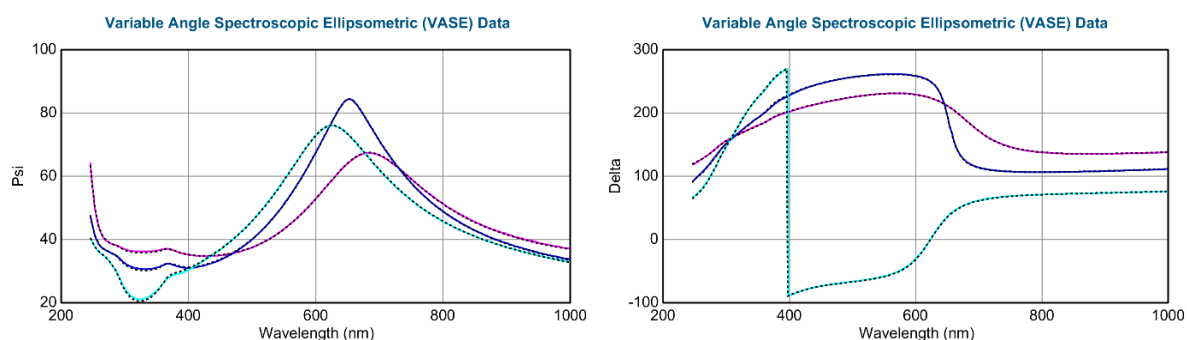
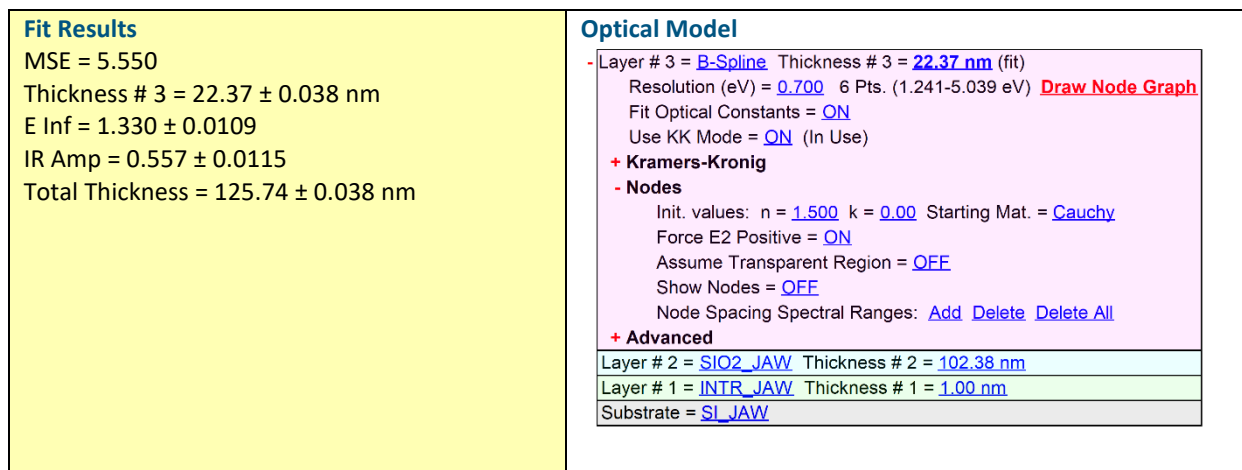


Figure S7 PDA 6 h deposition, KK-consistent B-spline model

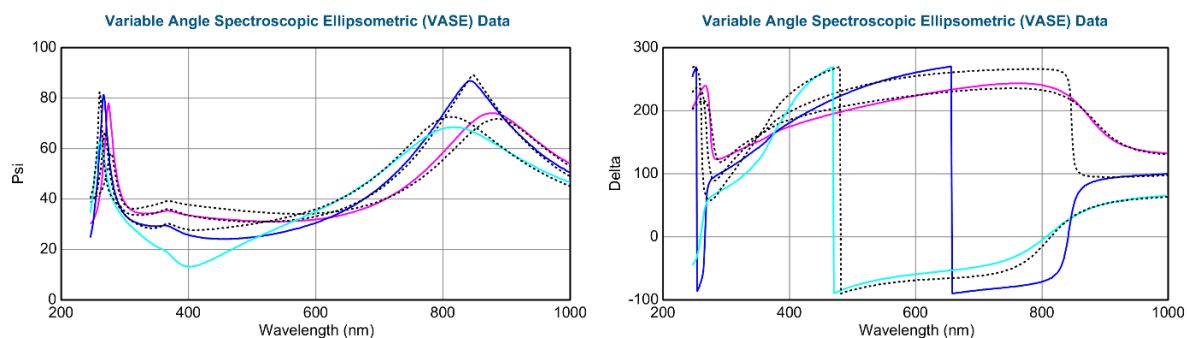
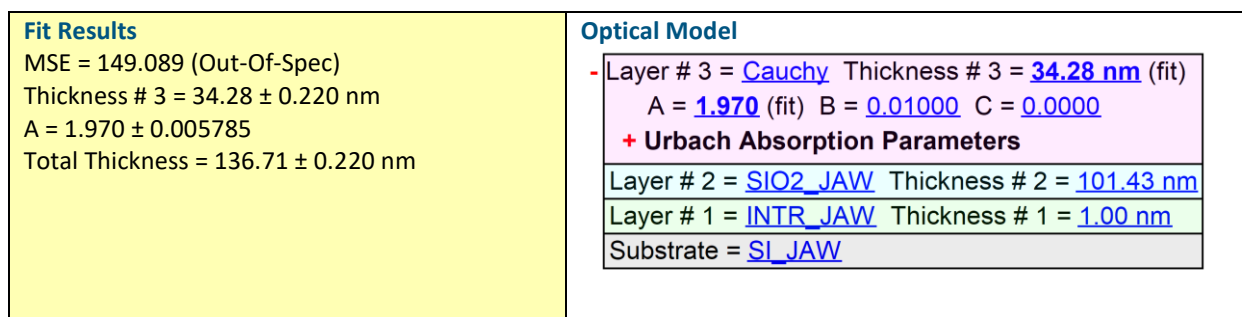


Figure S8 PDA 12 h deposition, Cauchy model

Fit Results

MSE = 98.520
 Thickness # 3 = 37.55 ± 0.158 nm
 A = 1.888 ± 0.003644
 k Amplitude = 0.09725 ± 0.001561
 Exponent = 0.457 ± 0.0100
 Total Thickness = 139.98 ± 0.158 nm

Optical Model

- Layer # 3 = [Cauchy](#) Thickness # 3 = [37.55 nm](#) (fit)
 A = [1.888](#) (fit) B = [0.01000](#) C = [0.0000](#)
 - Urbach Absorption Parameters
 k Amplitude = [0.09725](#) (fit) Exponent = [0.457](#) (fit)
 Band Edge = [400.0 nm](#)
 Layer # 2 = [SiO2_JAW](#) Thickness # 2 = [101.43 nm](#)
 Layer # 1 = [INTR_JAW](#) Thickness # 1 = [1.00 nm](#)
 Substrate = [SI_JAW](#)

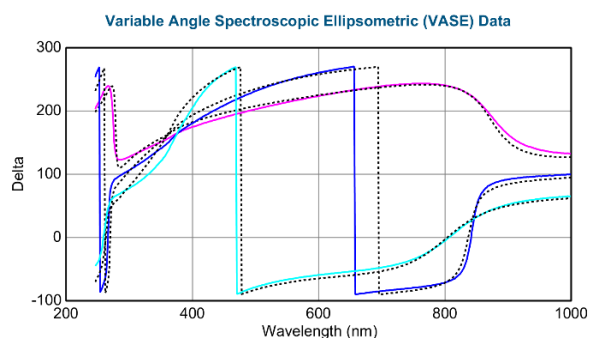
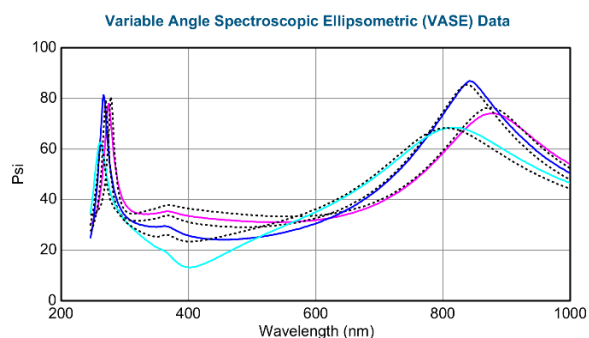


Figure S9 PDA 12 h deposition, Cauchy with Urbach absorption model

Fit Results

MSE = 12.619
 Thickness # 3 = 48.70 ± 0.060 nm
 E Inf = 1.289 ± 0.008047
 IR Amp = 0.350 ± 0.008563
 Total Thickness = 151.14 ± 0.060 nm

Optical Model

- Layer # 3 = [B-Spline](#) Thickness # 3 = [48.70 nm](#) (fit)
 Resolution (eV) = [0.700](#) 6 Pts. (1.241-5.039 eV) [Draw Node Graph](#)
 Fit Optical Constants = [ON](#)
 Use KK Mode = [ON](#) (In Use)
 + Kramers-Kronig
 - Nodes
 Init. values: n = [1.500](#) k = [0.00](#) Starting Mat. = [Cauchy](#)
 Force E2 Positive = [ON](#)
 Assume Transparent Region = [OFF](#)
 Show Nodes = [OFF](#)
 Node Spacing Spectral Ranges: [Add](#) [Delete](#) [Delete All](#)
 + Advanced
 Layer # 2 = [SiO2_JAW](#) Thickness # 2 = [101.43 nm](#)
 Layer # 1 = [INTR_JAW](#) Thickness # 1 = [1.00 nm](#)
 Substrate = [SI_JAW](#)

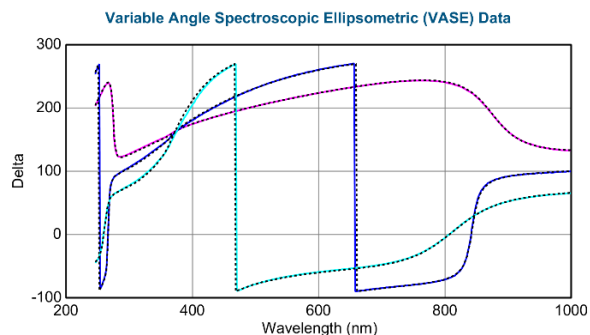
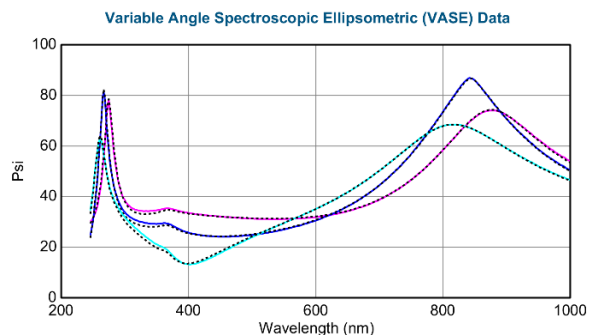


Figure S10 PDA 12 h deposition, KK-consistent B-spline model

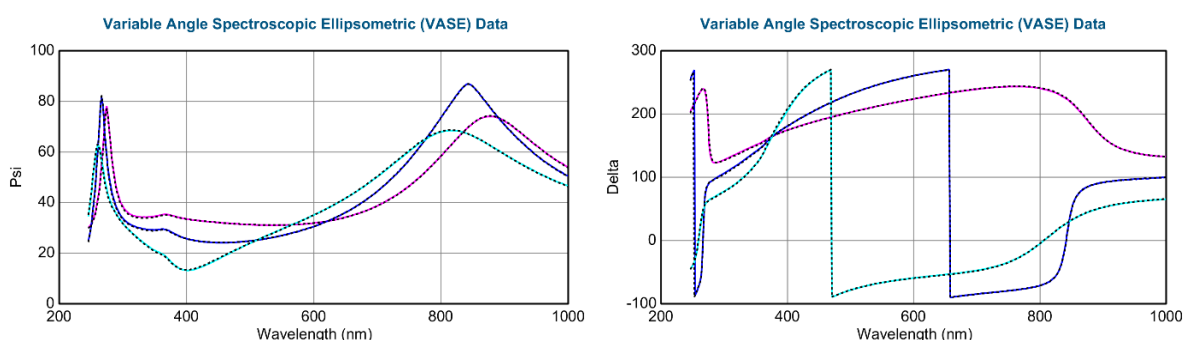
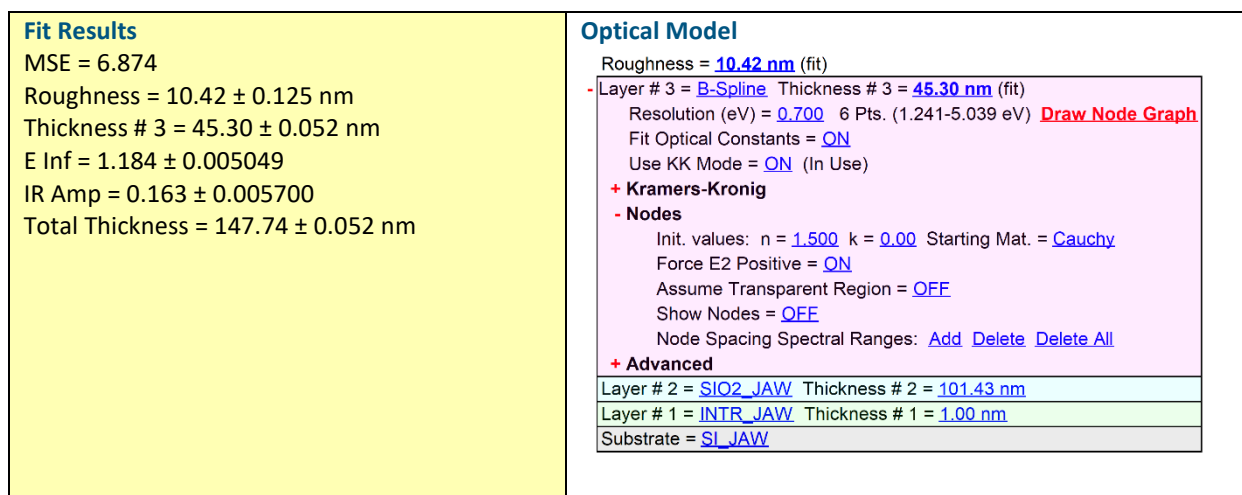


Figure S11 PDA 12 h deposition, KK-consistent B-spline with roughness model

In addition, we tested an alternative approach to estimate the thickness of the films. Herein, the optical constants (from B-spline parametrization) of PDA 6 h sample were used to analyse the data for PDA 2 h and 12 h samples. In this approach, the optical constants of the material are obtained from a “reference” sample that not only is relatively thick (i.e., not 2 h sample) but also is not too rough (i.e., not 12 h sample). Thus, one can argue that the modelled optical constants for the reference sample are the most trustable. Assuming that the optical constants of the material are the same for all the samples, one can use the “reference” optical constants to estimate the thickness of the other samples. **Figure S12** summarizes the modeling data for PDA 2 h sample using this approach. An acceptable MSE value is found, also the estimated thickness agrees with **Figure S4** (when using Cauchy with Urbach absorption, i.e., modeling both thickness and optical constants). **Figure S13** shows the modeling data for PDA 12 h sample using the fixed optical constants. Herein, the modelled data doesn’t match the experimental data completely, i.e., MSE is notably large, compared with **Figure S11** (when modeling both thickness and optical constants). Overall, while this approach is commonly used in the literature, the variable chemistry and microstructure of PDA films (depending on the deposition conditions) could contradict the assumption of having fixed optical constants for samples of varying thicknesses.

Fit Results MSE = 7.379 Thickness # 3 = 6.41 ± 0.005 nm Total Thickness = 108.34 ± 0.005 nm	Optical Model Layer # 3 = <u>6h PDA (Tabulated B-spline)</u> Thickness # 3 = <u>6.41 nm</u> (fit) Layer # 2 = <u>SIO₂_JAW</u> Thickness # 2 = <u>100.93 nm</u> Layer # 1 = <u>INTR_JAW</u> Thickness # 1 = <u>1.00 nm</u> Substrate = <u>SI_JAW</u>
---	---

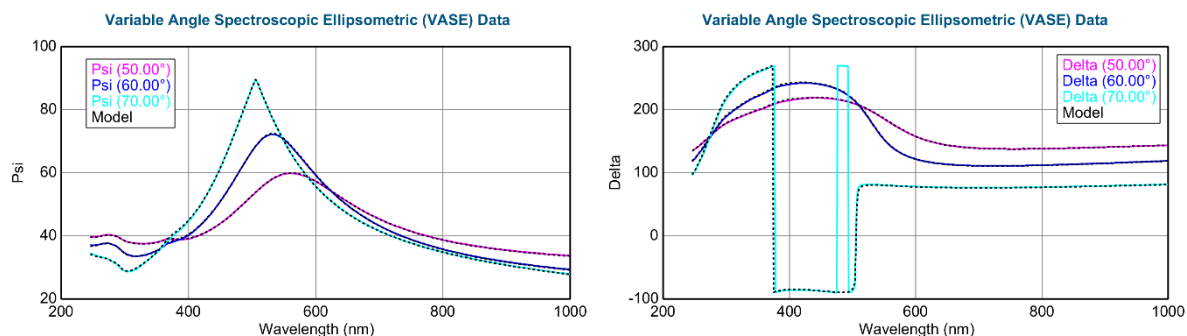


Figure S12 PDA 2 h deposition, fixed (tabulated) optical constants of PDA 6 h used in the model, leaving thickness as the only free parameter

Fit Results MSE = 45.250 Roughness = -0.47 ± 0.411 nm Thickness # 3 = 50.62 ± 0.038 nm Total Thickness = 153.05 ± 0.038 nm	Optical Model Roughness = <u>-0.47 nm</u> (fit) Layer # 3 = <u>6h PDA (Tabulated B-spline)</u> Thickness # 3 = <u>50.62 nm</u> (fit) Layer # 2 = <u>SIO₂_JAW</u> Thickness # 2 = <u>101.43 nm</u> Layer # 1 = <u>INTR_JAW</u> Thickness # 1 = <u>1.00 nm</u> Substrate = <u>SI_JAW</u>
---	---

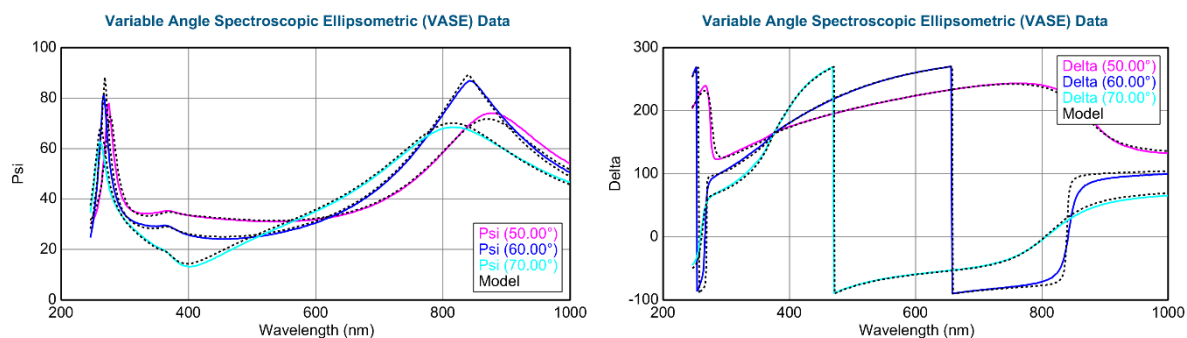


Figure S13 PDA 12 h deposition, fixed (tabulated) optical constants of PDA 6 h used in the model, leaving thickness as the only free parameter

S4. Sensitivity analysis for the B-spline function (PDA 6 h and 12 h): as discussed in the main article, optimizing the number of nodes of the B-spline function is crucial to avoid over-parametrization and correlation between the free parameters. Herein, we provide a detailed sensitivity analysis for the PDA films modelled with the B-spline function. **Figure S14** demonstrates the MSE as a function of number of nodes (left panel) as well the film thickness (right panel) for PDA 6 h sample. Herein, increasing the number of nodes has a minor effect on both MSE value and the film thickness. The former suggests that MSE value is not an appropriate parameter to decide on the minimum number of nodes. The later however suggests that thickness of the film is roughly around 22 nm regardless of the number of nodes (i.e., thickness is not sensitive to the number of nodes). **Figure S15**

shows the diagram of nodes (for the dielectric functions) for various numbers of nodes (4 to 19). Herein, one requires a minimum number of nodes so that the spline ϵ_2 (imaginary part of the dielectric function) curve goes through the free nodes (in the range of 1.2 – 5.3 eV), without showing small features in the dispersion (forcefitting, risk of overparameterization). Thus, **Figure S15** suggests that a total number of 6-7 nodes can provide a smooth spline ϵ_2 curve without overparameterization (see the plot for 10 nodes as an example of overparameterization). A similar deduction can be made from **Figure S16**, in which the n and k dispersions are plotted for different numbers of nodes. Accordingly, the overall shapes of n and k dispersions are independent of the number of nodes. Besides, the range of n and k are roughly 1.6-1.7 and 0-0.25 regardless of the number of nodes. Nevertheless, when the number of nodes is roughly larger than 6, extra features, i.e., wiggles in n and peaks in k , appear in the optical dispersions, which are unknown to be a physical feature of the sample or simply just due to overfitting. Hence, based on **Figure S14-S16**, we conclude that merely 6 nodes are enough in this case to obtain a reliable thickness value using the least number of free parameters in the model.

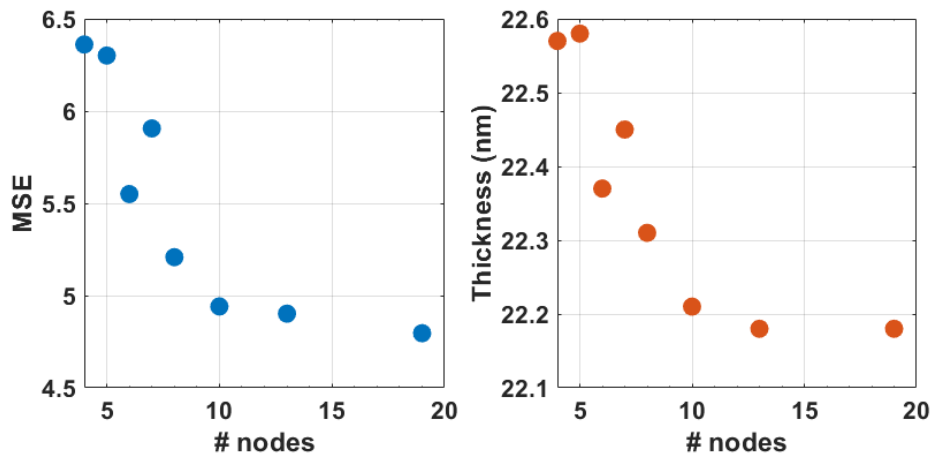


Figure S14 PDA 6 h deposition: sensitivity analysis for the number of nodes of the B-spline function (left) MSE vs. # nodes and (right) thickness vs. # nodes

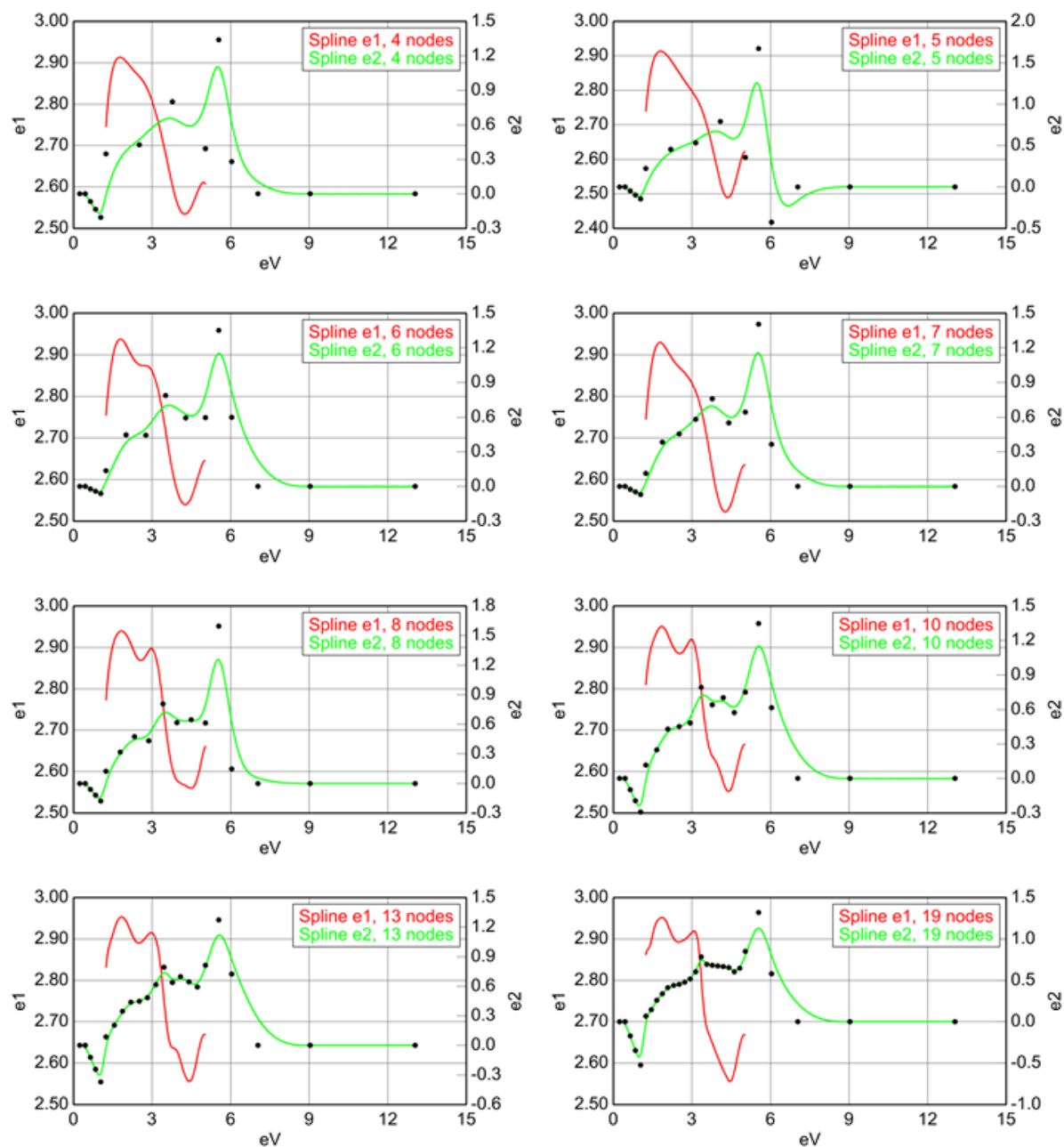


Figure S15 PDA 6 h deposition: sensitivity analysis for the number of nodes of the B-spline function; diagram of the nodes as a function of the number of nodes (4 to 19 nodes)

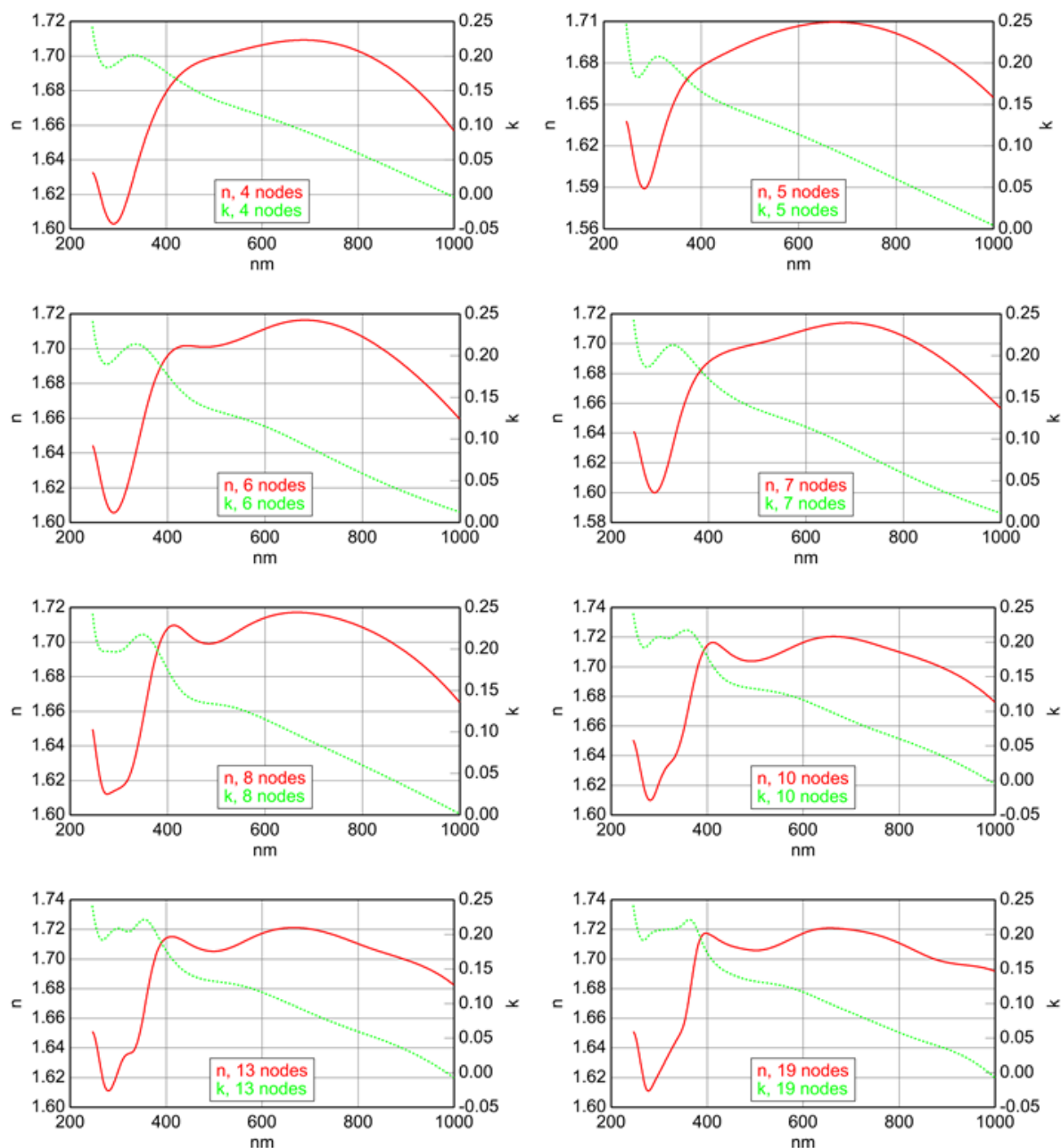
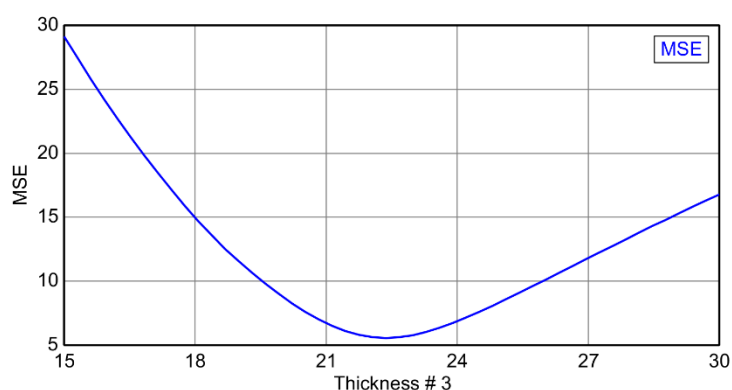


Figure S16 PDA 6 h deposition: sensitivity analysis for the number of nodes of the B-spline function; n and k dispersions as a function of the number of nodes (4 to 19 nodes)

Table S2 demonstrates the correlation matrix for the representative PDA 6 h sample. Herein, the larger the values (closer to 1) the more correlated the model parameters are. As a rule of thumb, a correlation value > 0.9 suggests that the two corresponding parameters are strongly correlated. Herein, none of the free parameters show strong correlation with each other. Noteworthy, the three outlier nodes of the KK-consistent B-spline, i.e., spline_e2(1.041), spline_e2(5.539), and spline_e2(6.039), do not show correlation with other parameters unlike what is typically observed. **Figure S17**, in which MSE is plotted against thickness, also suggests uniqueness of the estimated film thickness in the range of 15–30 nm. Finally, **Table S3** summarizes the modeling outcome for all studied PDA 6 h samples (15 measurement data) using 6 nodes. Herein, the thickness value shows a narrow standard deviation that suggests not only the uniformity of the film structure, but also that the modeling outcome is not model-dependent and is reliable.

Table S2 PDA 6 h deposition: correlation matrix for KK-consistent B-spline mode (6 nodes)

	Thickn ess # 3	E Inf	IR Amp	spline _e2(1. 041)	spline _e2(5. 539)	spline _e2(6. 039)	spline _e2(1. 241)	spline _e2(2. 000)	spline _e2(2. 760)	spline _e2(3. 520)	spline _e2(4. 280)	spline _e2(5. 039)
Thickness # 3	1.000	0.596	0.268	0.132	0.469	-0.718	0.203	-0.479	0.148	-0.611	-0.491	-0.430
E Inf	0.596	1.000	0.716	-0.196	0.811	-0.957	0.352	-0.340	0.012	-0.648	-0.212	-0.728
IR Amp	0.268	0.716	1.000	-0.712	0.436	-0.566	0.467	-0.255	0.077	-0.362	-0.095	-0.408
spline_e2(1.041)	0.132	-0.196	-0.712	1.000	-0.090	0.081	-0.587	0.322	-0.285	0.087	-0.140	0.101
spline_e2(5.539)	0.469	0.811	0.436	-0.090	1.000	-0.895	0.274	-0.340	0.136	-0.592	0.151	-0.897
spline_e2(6.039)	-0.718	-0.957	-0.566	0.081	-0.895	1.000	-0.318	0.413	-0.091	0.687	0.192	0.792
spline_e2(1.241)	0.203	0.352	0.467	-0.587	0.274	-0.318	1.000	-0.794	0.564	-0.408	0.044	-0.282
spline_e2(2.000)	-0.479	-0.340	-0.255	0.322	-0.340	0.413	-0.794	1.000	-0.763	0.611	0.046	0.351
spline_e2(2.760)	0.148	0.012	0.077	-0.285	0.136	-0.091	0.564	-0.763	1.000	-0.479	0.193	-0.180
spline_e2(3.520)	-0.611	-0.648	-0.362	0.087	-0.592	0.687	-0.408	0.611	-0.479	1.000	-0.090	0.632
spline_e2(4.280)	-0.491	-0.212	-0.095	-0.140	0.151	0.192	0.044	0.046	0.193	-0.090	1.000	-0.299
spline_e2(5.039)	-0.430	-0.728	-0.408	0.101	-0.897	0.792	-0.282	0.351	-0.180	0.632	-0.299	1.000

**Figure S17** PDA 6 h deposition: thickness uniqueness analysis for 6 nodes**Table S3** PDA 6 h deposition: summary of the modeling results

Sample no.	MSE	Thickness # 3 (nm)	E Inf	IR Amp
1	7.668	23.52	1.280	0.535
2	6.133	21.61	1.254	0.513
3	4.859	21.71	1.291	0.514
4	5.550	22.37	1.330	0.557
5	5.462	20.91	1.311	0.582
6	8.163	22.99	1.243	0.507
7	4.429	21.95	1.261	0.463
8	4.493	22.15	1.270	0.465
9	4.278	19.51	1.296	0.533
10	4.557	21.03	1.302	0.520
11	7.161	23.08	1.241	0.473
12	4.511	22.82	1.259	0.443
13	4.708	23.78	1.261	0.430
14	4.843	24.19	1.263	0.435
15	4.659	21.99	1.295	0.497
Average	5.43151	22.241	1.27713	0.49784
Std. Dev.	1.27015	1.224	0.02627	0.04545

The sensitivity analysis was also performed for the PDA 12 h sample. Similarly, it was found the number of nodes has little effect on MSE and estimated thickness, and 6 nodes were enough to obtain a smooth e2 spline function, as well as n and k dispersions. However, we herein have an additional free parameter, i.e., thickness of the roughness layer. Thus, we performed sensitivity analysis in terms of the correlation between the film thickness and the film roughness. **Figure S18** depicts the 2-parameter uniqueness chart where MSE is calculated for various combinations of thickness and roughness values. The areas indicated in red represent the smallest MSE values

(best match between the modelled and the experimental data). The left panel shows a larger range of values for thickness and roughness. Accordingly, a combination of thickness (~ 40 -50 nm) and roughness (~ 0 -20 nm) is the only combination that provides small MSE values. The right panel shows a higher resolution (smaller range of MSE values) chart for this combination. Accordingly, the modeling outcome (thickness ~ 45 nm and roughness ~ 10 nm) is unique and other thickness/roughness combinations yield excessively larger MSE values. Finally, **Table S4** summarizes the modeling outcome for all the studied PDA 12 h samples. Again, the thickness value shows a relatively narrow standard deviation that affirms reliable modeling outcome.

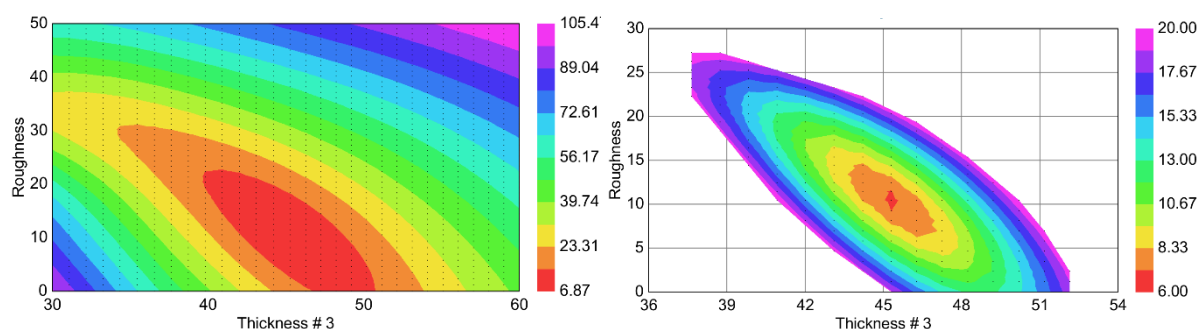


Figure S18 PDA 12 h deposition: thickness-roughness uniqueness analysis for 6 nodes (the panel on the right shows the chart with MSE values of 6-24)

Table S4 PDA 12 h deposition: summary of the modeling results

	MSE	Roughness (nm)	Thickness # 3 (nm)	E Inf	IR Amp
1	11.450	9.54	46.62	1.213	0.208
2	6.874	10.42	45.30	1.184	0.163
3	6.314	9.86	44.31	1.186	0.166
4	5.342	8.61	43.08	1.189	0.166
5	5.779	8.38	38.98	1.216	0.193
6	10.088	8.37	48.26	1.191	0.180
7	6.634	9.28	46.39	1.177	0.160
8	7.865	12.27	46.38	1.177	0.156
9	7.494	12.41	45.44	1.184	0.159
10	5.777	8.87	44.39	1.186	0.162
11	12.009	8.22	44.27	1.206	0.221
12	6.850	8.64	42.83	1.182	0.177
13	6.330	10.16	42.31	1.184	0.164
14	9.325	14.65	41.73	1.190	0.159
15	10.418	15.55	41.32	1.203	0.180
Average	7.90334	10.347	44.108	1.19104	0.17423
Std. Dev.	2.18922	2.331	2.433	0.01245	0.01938

S5. Roughness from Ellipsometry: we have here used the simplest approach (50:50 model) to implement a roughness layer into the optical model. As shown in **Figure S19**, a rough film is considered as a bilayer, i.e., a homogenous layer at the bottom and a layer comprising 50:50 mixture of material/void on top. The optical dispersions of the roughness layer are then described using an effective medium approximation (EMA) equation. The thickness of the EMA layer is then a “free” parameter in the model and is considered as the ellipsometry roughness. Thus, the optical constants of the material (when unknown, free parameters) vary in two layers, which may cause correlation between the parameters of the two layers as well as the modelled optical constants. In this study, we assessed merely if having a “roughness” layer can improve the quality of the modeling. Accordingly, it was found that for PDA films obtained by relatively long deposition times, having an EMA roughness layer improves the quality of the model. Nevertheless, a more accurate description of the PDA films roughness for ellipsometry modeling requires careful analysis of the roughness profiles of PDA films in different length scales and then obtaining the corresponding void profile in the vertical direction (Z axis). Such realistic profiles may then be used for the EMA model (instead of 50:50 assumption). Such analysis would be

more trustable if the optical constants of the material are known or at least a simple dispersion equation (e.g., transparent Cauchy equation) is required to model the optical behaviour. Considering the unknown and complex optical dispersion of PDA and its variable roughness in different length scales, determination of the correlation between the ellipsometry-AFM roughness values remains a challenge and needs further investigation.

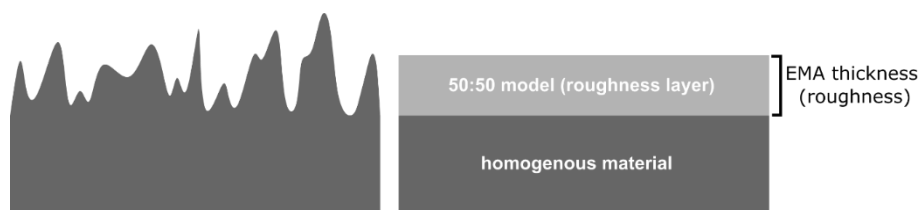


Figure S19 Ellipsometry roughness using 50:50 effective medium approximation (EMA)

S6. Optical dispersions of PDA films (2, 6, and 12 h): while spectroscopic ellipsometry cannot always be an accurate way of measuring the optical dispersions (when both thickness and optical dispersions of the material are unknown), it may provide an overall picture of the optical behaviour if the model is not overparameterized and the modeling outcome is unique (**Figure S20**). Regarding the PDA 2 h sample (left panel), the choice of model obviously affects the dispersion shape, but also the ranges of values (in particular n) are affected. In this case, since the film thickness is ≤ 10 nm, using a B-spline model is not favourable to estimate the film thickness due to the higher number of free parameters. Nevertheless, the B-spline model provides n and k dispersion shapes that are like those of 6 h and 12 h samples. Comparing the optical dispersions of all the samples (right panel), we can suggest that the overall shape of the dispersions (n relatively featureless at large wavelengths, decreasing in the UV range) is similar for all samples and could be the physical behaviour of PDA. However, the absolute values of the optical constants seem to depend on the deposition time (in particular n dispersion is shifted upwards with deposition time), which could be due to both the time-dependent physicochemical properties of the material and some degree of correlation between the model parameters.

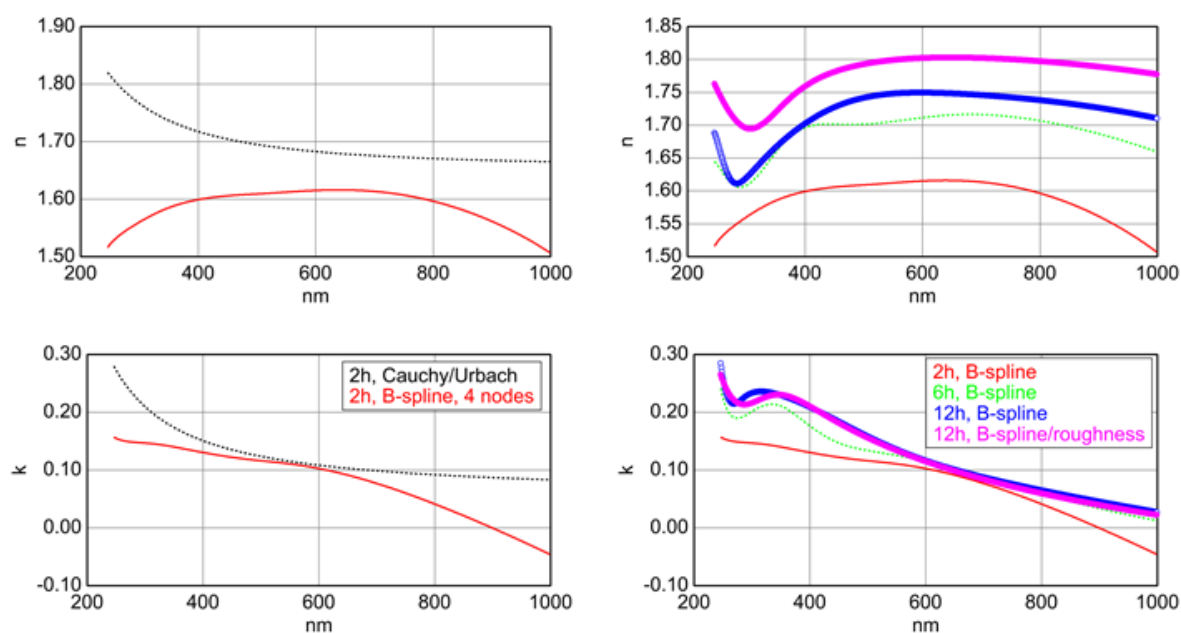


Figure S20 n (top row) and k (bottom row) dispersions obtained from the modeling of the ellipsometry data: (left) 2 h PDA sample modelled by Cauchy with the Urbach absorption term and KK-consistent B-spline with 4 nodes, (right) all samples modelled with KK-consistent B-spline without (2 h, 6 h, and 12 h PDA) or with roughness (12 h PDA) .

To see if we could more accurately estimate the optical dispersions of PDA using ellipsometry, we tried fixing the film thickness in the model, thus only having the B-spline parameters as the free model parameters. Herein, the average thickness values estimated from AFM were used. **Figure S21** displays the optical dispersions obtained from this modeling approach. The overall shape of the dispersions is similar to those in **Figure S20**, suggesting that the overall shape of the dispersions represent PDA optical behavior. Similarly, it is also found that n dispersion shows a shift to higher values with the deposition time, which can be an indication of the variable physicochemical/optical properties of PDA (considering that the thickness is fixed in the model). Unlike **Figure S20**, it is herein found that k values seem to be slightly dependent on the deposition time.

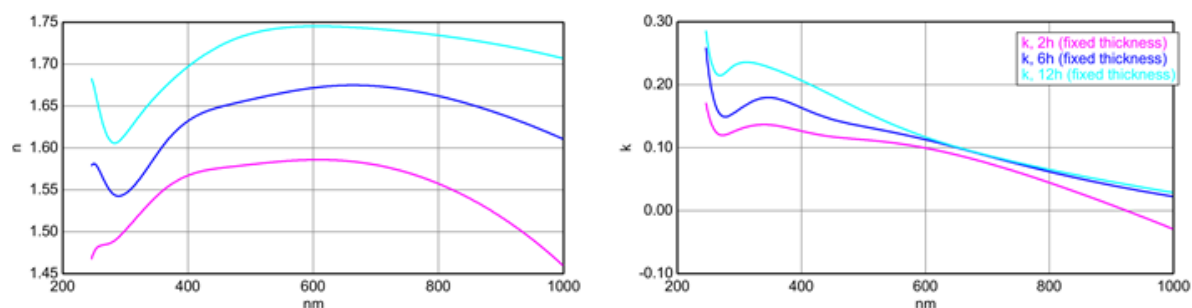


Figure S21 optical dispersions of PDA films obtained by B-spline model using fixed thickness values (from AFM)

S7. Step-by-step modeling approach for a PDA film obtained using the standard one-step deposition

procedure: As discussed in the main article, the PDA films studied herein were all obtained using a multi-step deposition method to minimize the surface roughness/thickness ratio of the films and thus improve the quality of the ellipsometry data. To test if the step-by-step modeling approach is valid for PDA films obtained through the standard one-step deposition, we herein prepared a PDA film by 24 h one-step deposition as a model sample for thick and rough PDA films.

Figure S22-S25 summarize the modeling outcome for the following step-by-step model construction: Cauchy relation (2 free parameters: PDA film thickness (layer # 3) and A of Cauchy), Cauchy with an Urbach absorption term (4 free parameters: PDA film thickness (layer # 3), A of Cauchy, amplitude and exponent of the Urbach relation), KK-consistent B-spline (9 free parameters: PDA film thickness (layer # 3), 6 nodes, 2 KK-relation parameters), and ultimately KK-consistent B-spline with a EMA roughness layer (10 free parameters: PDA film thickness (layer # 3), 6 nodes, 2 KK-relation parameters, thickness of the roughness layer). The KK-consistent B-spline function with a roughness layer can provide a satisfactory match with the experimental data suggesting applicability of the modeling approach for studying thick/rough PDA films. However, it should be noted that the excessive surface roughness/heterogeneity herein seem to promote some degree of correlation between the estimated thickness and roughness values.

Figure S26 depicts the 2-parameter thickness-roughness uniqueness chart. Herein, it can be seen that the mathematical model can yield two solutions that both satisfactorily match the experimental data (MSE \sim 25 nm): (i) a film with a thickness \sim 50-55 nm and roughness \sim 20-25 nm and (ii) a film with a thickness \sim 30-35 nm and roughness \sim 45-50 nm. While both solutions match the experimental data, in this case, one can safely choose the former modeling outcome as the second solution represents a layer with a roughness much larger than the film thickness. Regardless, this observation suggests that excessively rough and heterogeneous PDA films require more in-depth modeling and more importantly verification with another thickness/roughness analysis method, e.g., AFM imaging (**Figure S27**: representative AFM height image/height profile of a scratched 24 h one-step deposited PDA). The model parameters do not show any significant degree of correlation as shown in **Table S5**.

Fit Results

MSE = 176.220 (Out-Of-Spec)
Thickness # 3 = 45.95 ± 0.246 nm
 $A = 1.931 \pm 0.004978$
Total Thickness = 148.92 ± 0.246 nm

Optical Model

- Layer # 3 = Cauchy Thickness # 3 = 45.95 nm (fit)
 $A = 1.931$ (fit) $B = 0.01000$ $C = 0.0000$

+ Urbach Absorption Parameters

Layer # 2 = SIO2_JAW Thickness # 2 = 101.97 nm

Layer # 1 = INTR_JAW Thickness # 1 = 1.00 nm

Substrate = SI_JAW

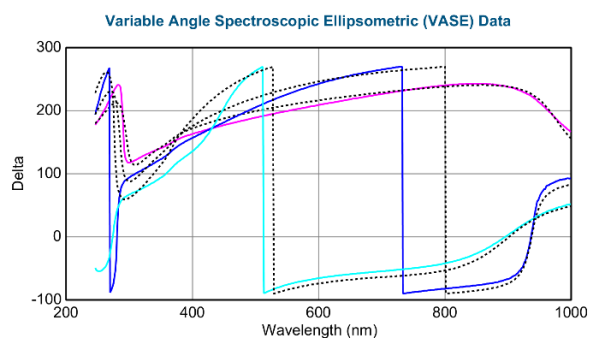
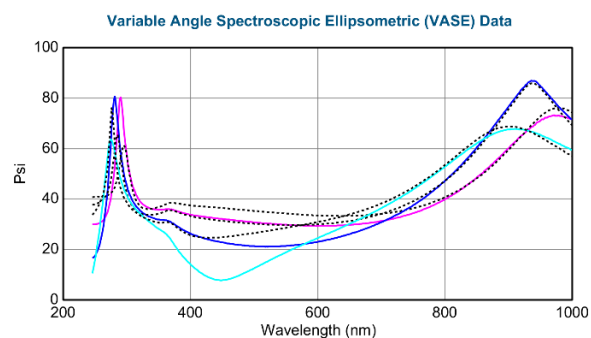


Figure S22 PDA 24 h one-step deposition, Cauchy model

Fit Results

MSE = 135.572 (Out-Of-Spec)
Thickness # 3 = 47.50 ± 0.191 nm
 $A = 1.897 \pm 0.003765$
 k Amplitude = 0.07846 ± 0.002397
Exponent = 0.688 ± 0.0215
Total Thickness = 150.47 ± 0.191 nm

Optical Model

- Layer # 3 = Cauchy Thickness # 3 = 47.50 nm (fit)
 $A = 1.897$ (fit) $B = 0.01000$ $C = 0.0000$

- Urbach Absorption Parameters

k Amplitude = 0.07846 (fit) Exponent = 0.688 (fit)
Band Edge = 400.0 nm

Layer # 2 = SIO2_JAW Thickness # 2 = 101.97 nm

Layer # 1 = INTR_JAW Thickness # 1 = 1.00 nm

Substrate = SI_JAW

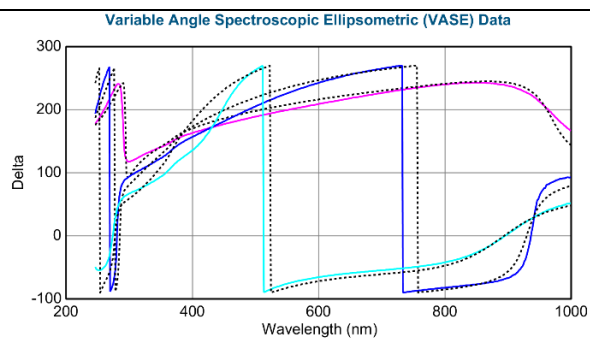
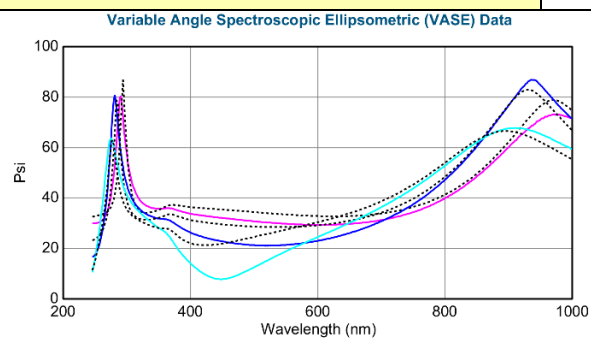


Figure S23 PDA 24 h one-step deposition, Cauchy with Urbach absorption model

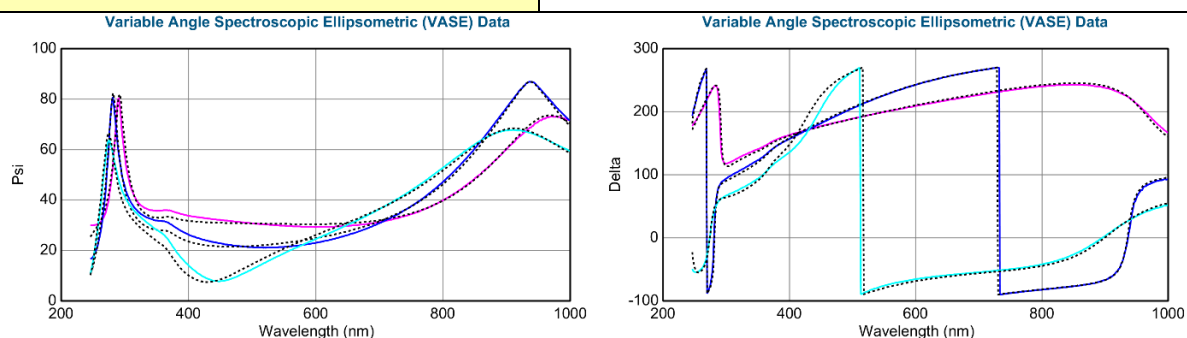
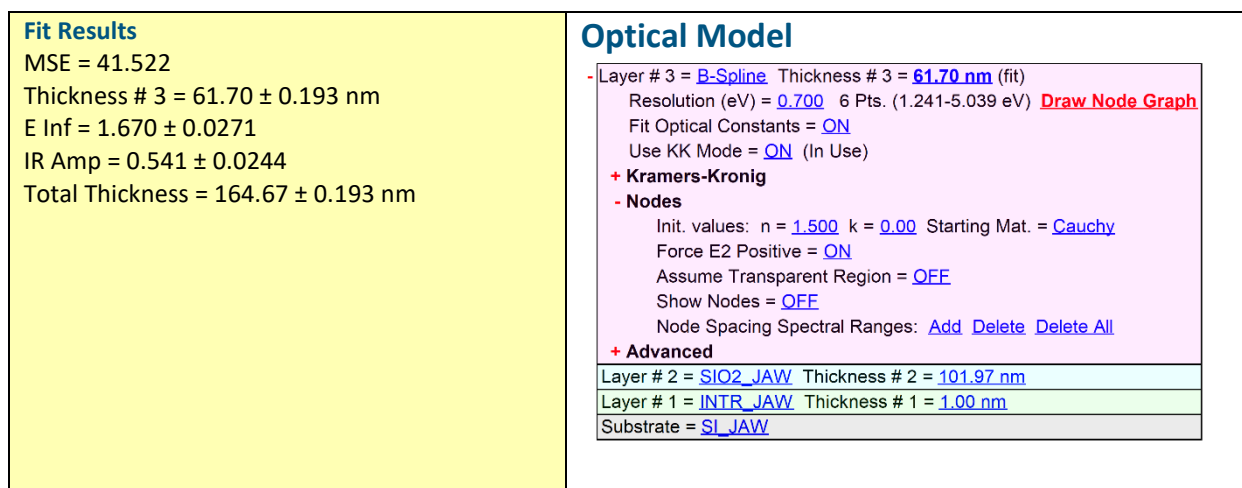


Figure S24 PDA 24 h one-step deposition, KK-consistent B-spline model

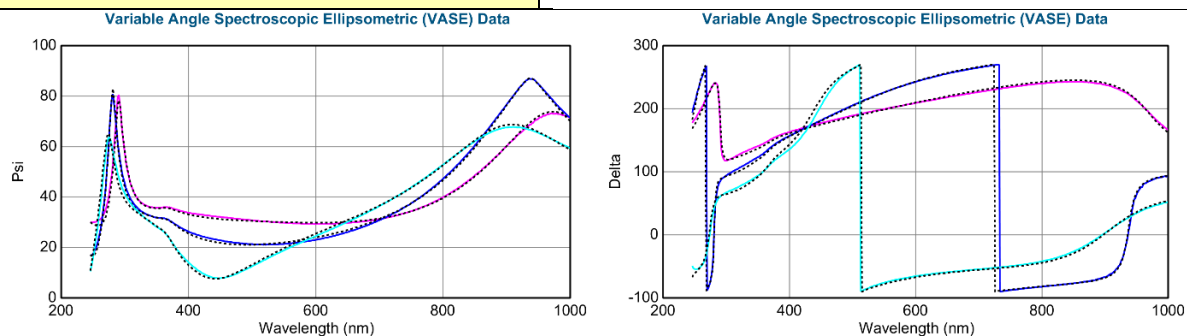
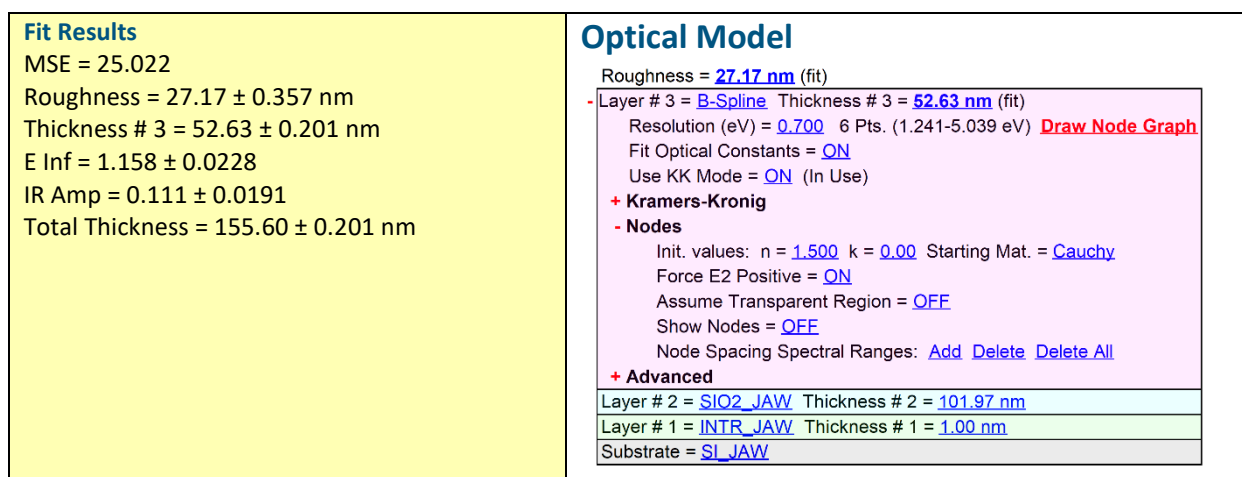


Figure S25 PDA 24 h one-step deposition, KK-consistent B-spline with roughness layer model

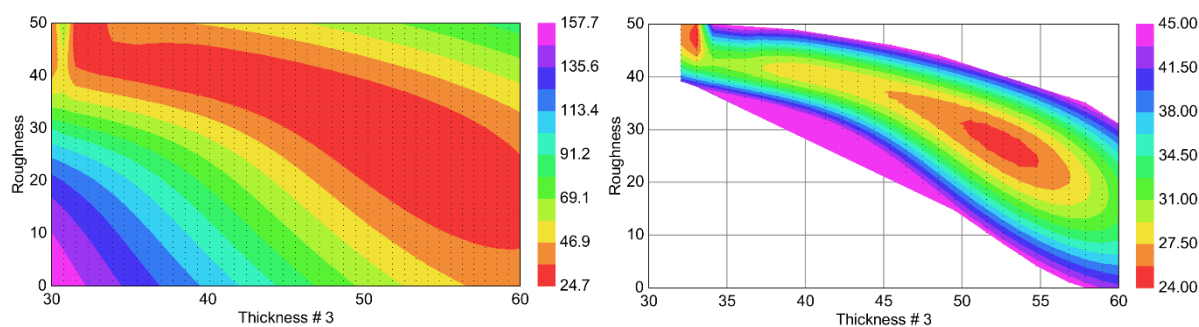


Figure S26 PDA 24 h one-pot deposition: thickness-roughness uniqueness analysis for 6 nodes, (the panel on the right shows the chart with MSE values of 24-45)

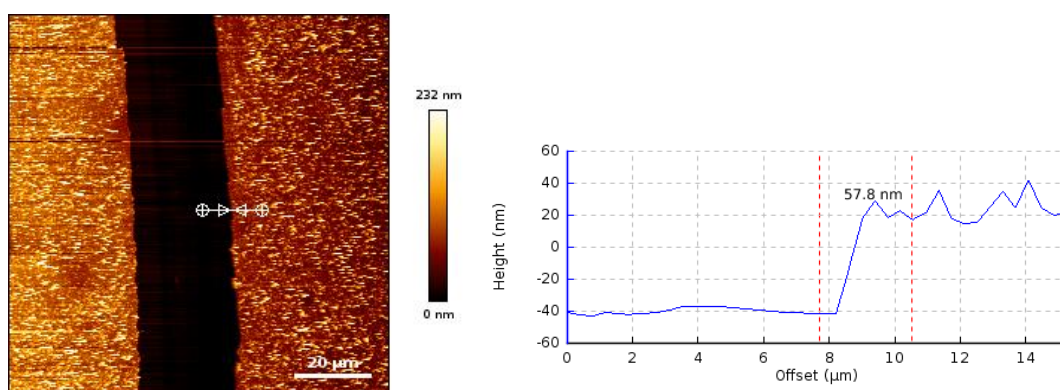


Figure S27 Representative AFM height image/profile of the scratched area of PDA 24 h one-step deposition, estimated thickness = 57.8 ± 4.3 nm estimated roughness (R_q) = 40.0 ± 8.5 nm.

Table S5 PDA 24 h one-step deposition: correlation matrix for KK-consistent B-spline with roughness model

	Roughness	Thickness # 3	E Inf	IR Amp	spline_e 2(1.041)	spline_e 2(5.539)	spline_e 2(6.039)	spline_e 2(1.241)	spline_e 2(2.000)	spline_e 2(2.760)	spline_e 2(3.520)	spline_e 2(4.280)	spline_e 2(5.039)
Roughness	1.000	-0.812	-0.571	-0.444	-0.085	-0.515	0.723	-0.148	0.143	0.324	-0.032	0.728	0.611
Thickness # 3	-0.812	1.000	0.477	0.237	0.302	0.630	-0.780	0.011	0.048	-0.540	0.085	-0.588	-0.754
E Inf	-0.571	0.477	1.000	0.784	-0.206	0.769	-0.893	0.411	-0.338	-0.119	-0.433	-0.227	-0.634
IR Amp	-0.444	0.237	0.784	1.000	-0.627	0.423	-0.567	0.699	-0.381	0.136	-0.279	-0.173	-0.381
spline_e 2(1.041)	-0.085	0.302	-0.206	-0.627	1.000	0.051	-0.041	-0.856	0.555	-0.489	0.251	-0.170	-0.107
spline_e 2(5.539)	-0.515	0.630	0.769	0.423	0.051	1.000	-0.911	0.193	-0.164	-0.235	-0.357	-0.083	-0.835
spline_e 2(6.039)	0.723	-0.780	-0.893	-0.567	-0.041	-0.911	1.000	-0.243	0.192	0.329	0.288	0.366	0.810
spline_e 2(1.241)	-0.148	0.011	0.411	0.699	-0.856	0.193	-0.243	1.000	-0.725	0.424	-0.317	0.045	-0.172
spline_e 2(2.000)	0.143	0.048	-0.338	-0.381	0.555	-0.164	0.192	-0.725	1.000	-0.592	0.434	-0.080	0.143
spline_e 2(2.760)	0.324	-0.540	-0.119	0.136	-0.489	-0.235	0.329	0.424	-0.592	1.000	-0.494	0.421	0.269
spline_e 2(3.520)	-0.032	0.085	-0.433	-0.279	0.251	-0.357	0.288	-0.317	0.434	-0.494	1.000	-0.504	0.369
spline_e 2(4.280)	0.728	-0.588	-0.227	-0.173	-0.170	-0.083	0.366	0.045	-0.080	0.421	-0.504	1.000	0.058
spline_e 2(5.039)	0.611	-0.754	-0.634	-0.381	-0.107	-0.835	0.810	-0.172	0.143	0.269	0.369	0.058	1.000

Table S6 summarizes the modeling outcome for all the studied 24 h one-pot PDA samples. Herein, the estimated film thickness shows relatively narrow standard deviation, suggesting reliability of the modeling procedure and output. However, the estimated roughness value (27.8 ± 8.9 nm) demonstrates a relatively larger standard deviation, which could be either due to heterogeneity of the PDA film surface or some degree of correlation between the roughness and other model parameters. According to AFM images, the film has a R_q roughness of 40.0 ± 8.5 nm. Thus, while the large standard deviation can be attributed to the heterogeneous surface structure, it appears that the estimated roughness from ellipsometry is relatively smaller than what is estimated by AFM. Interestingly, plotting the obtained n and k dispersions (**Figure S28**) for all 15 measurement data renders two types of dispersions: (i) a smaller population with relatively smaller roughness/MSE and (ii) a larger population with relatively larger roughness/MSE. The former group are characterized by optical dispersions that are more consistent, are closer to the range of values of optical constants of organic materials and show smoother dispersions. The optical dispersions of the latter group, however, demonstrate excessive sample-dependence, are relatively larger than the expected values for organic materials, and finally show various features in the dispersion (could suggest parameter correlation). This observation again suggests that PDA films, in particular those with excessive surface heterogeneity and roughness, need a careful optical modeling.

Table S6 PDA 24 h one-pot deposition: summary of the modeling results

	MSE	Roughness (nm)	Thickness # 3 (nm)	E Inf	IR Amp
1	34.092	33.74	54.88	1.236	0.212
2	31.116	32.55	52.95	1.107	0.117
3	26.670	26.33	55.95	1.066	0.0721
4	28.776	29.24	58.12	1.003	0.0408
5	42.483	37.71	53.29	1.006	0.193
6	25.022	27.17	52.63	1.158	0.111
7	17.452	18.53	54.69	1.145	0.119
8	15.778	15.52	55.52	1.144	0.123
9	14.703	13.22	57.10	1.144	0.125
10	20.716	17.55	57.87	1.110	0.100
11	37.197	35.70	51.95	1.104	0.166
12	31.736	32.89	53.91	1.068	0.0918
13	32.271	31.75	54.34	1.080	0.0993
14	38.549	35.68	54.45	0.904	0.0411
15	30.935	29.49	55.38	1.085	0.0873
Average	28.49971	27.805	54.869	1.09063	0.11325
Std. Dev.	8.41440	7.945	1.843	0.07841	0.04847

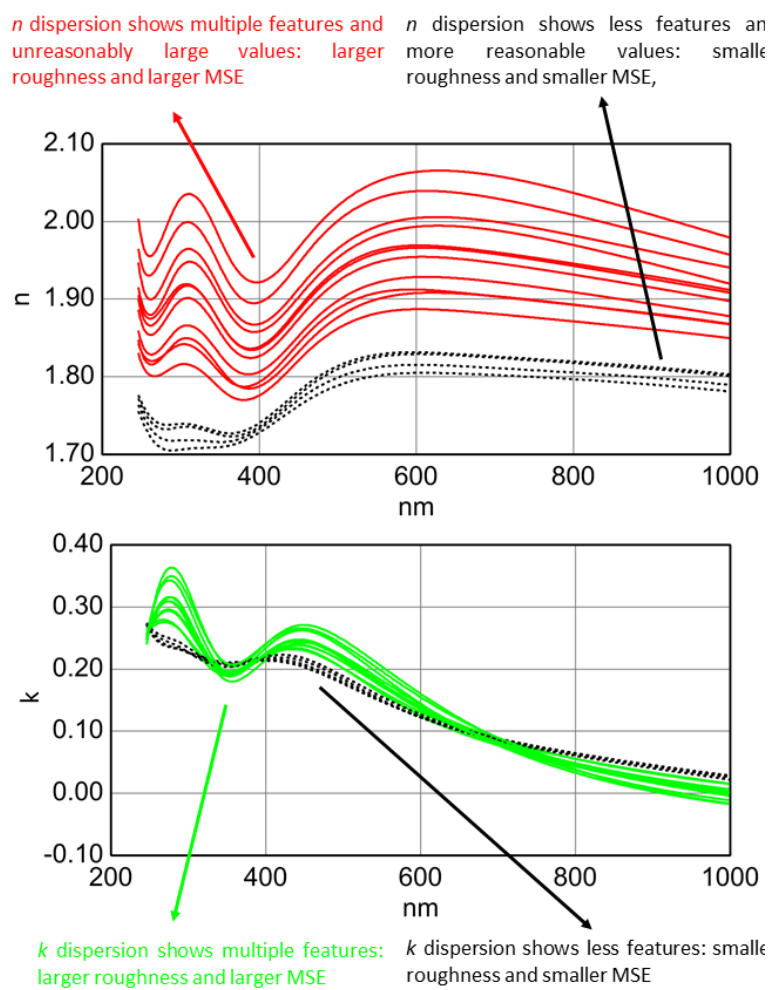


Figure S28 PDA 24 h one-step deposition: n and k dispersions obtained from the KK-consistent B-spline model with a roughness layer (15 samples)

Paper II

Reprinted with permission from Langmuir, submitted for publication.
Copyright [2022] American Chemical Society

This document is confidential and is proprietary to the American Chemical Society and its authors. Do not copy or disclose without written permission. If you have received this item in error, notify the sender and delete all copies.

**Dopamine-assisted Layer-By-Layer Deposition Providing
Coatings with Controlled Microstructure and
Physicochemical Properties**

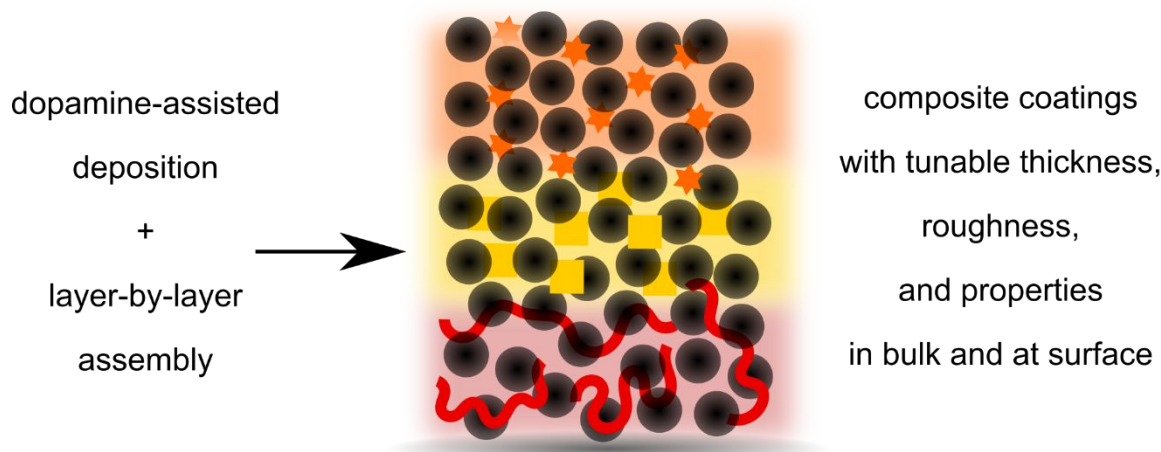
Journal:	<i>Langmuir</i>
Manuscript ID	la-2022-016895
Manuscript Type:	Article
Date Submitted by the Author:	28-Jun-2022
Complete List of Authors:	Qie, Runtian; Technical University of Denmark, Zafaroushan Moghaddam, Saeed; Danmarks Tekniske Universitet, Department of Chemistry Thormann, Esben; Danmarks Tekniske Universitet, Department of Chemistry

SCHOLARONE™
Manuscripts

Dopamine-assisted Layer-By-Layer Deposition Providing Coatings with Controlled Microstructure and Physicochemical Properties

Runtian Qie, Saeed Zajforoushan Moghaddam, Esben Thormann*

Department of Chemistry, Technical University of Denmark, 2800 Kgs. Lyngby, Denmark



Abstract. In this study, dopamine-assisted deposition combined with layer-by-layer assembly was investigated as an efficient method of preparing coatings with tunable microstructure and functional properties. Herein, one can first benefit from the versatile chemistry of dopamine allowing co-deposition of various functional materials, e.g., polymers, ions, and nanoparticles, within the coating. More importantly, the layer-by-layer approach allows tuning the coating thickness and surface morphology, as well as varying the chemical composition of the coating in the vertical direction.

Keywords: polydopamine, layer-by-layer assembly, coating, microstructure, physicochemical properties

1 Introduction

Since the first report, in 2007, on the formation of polydopamine (PDA) coatings through self-polymerization in aqueous solutions, it has developed into a promising coating method owing to its simplicity and versatility.^{1,2} Dopamine (DA) is a catecholamine that can be oxidized into dopamine-quinone, followed by intramolecular cyclization, oxidation to dopaminedochrome, formation of 5,6-dihydroxyindole (DHI), and further oxidation to 5,6-indolequinone (IDQ). These oligomers then undergo various covalent and non-covalent pathways self-assembling into supramolecular PDA structures in solution and at the surface.³⁻⁵ Due to the highly reactive nature of these intermediate compounds, DA can also be co-deposited with various materials including polymers,⁶⁻¹⁰ nanoparticles,^{6,11} and metal ions,¹²⁻¹⁴ whereby hybrid coatings with desired functionalities can be prepared. Despite the many benefits, preparing PDA-based coatings has challenges in controlling the coating growth and surface morphology. For example, the thickness of pure PDA coatings is usually limited to ~ 50-100 nm due to the consumption of DA in the solution.¹⁵⁻¹⁷ Moreover, the surface roughness of PDA coatings drastically increases with the deposition time due to aggregation, both in solution and at the surface.^{18,19}

More than a decade before the rise of studies on PDA coatings, the Layer-by-Layer (LbL) deposition method for the preparation of polyelectrolyte multilayer films was introduced as another versatile coating method. In the original approach, multilayer films are formed by alternating deposition of oppositely charged polyelectrolytes (electrostatically driven assembly), whereby the coating properties can be tuned by the choice of polymers, the number of depositions, and pH/ionic strength.^{20,21} Later, the LbL process has been extended to include not only polyelectrolytes but also combinations of polyelectrolytes, nanoparticles, and lipids.²²⁻²⁴ While other molecular interactions such as hydrogen bonding can also drive LbL assembly,^{25,26} the

1
2
3 electrostatically driven assembly is still the most effective and used approach. Thus, despite the
4 many advantages of the LbL method, the need for oppositely charged polymers is a limitation.
5
6

7
8 Considering the pros and cons of (i) DA-based deposition and (ii) LbL assembly of polyelectrolyte
9 multilayers, a natural next step is to combine these methods to gain better control of the hierarchal
10 structure of the coating, as one has in the LbL process, while benefiting from the compositional
11 tunability found in DA-based coatings. For pure PDA coatings, Ball et al. have reported a LbL
12 approach, where a surface repeatedly was immersed in a fresh DA solution.^{15,27} By doing so, they
13 were able to extend the coating thickness beyond what is typically obtained, but a natural thought
14 is that such a LbL approach should also affect the morphology of the PDA coatings. As the first
15 part of our study, we thus extended this investigation into a study on both the growth rate and the
16 surface morphology of PDA coatings fabricated with the LbL method. Few studies adopted a LbL
17 approach to form multilayers of PDA and polymers/nanoparticles.^{28–31} This method is generally
18 executed by alternate adsorption of polymers/nanoparticles and PDA, whereby PDA layers
19 practically work as a “glue” between the layers of polymers/nanoparticles. However, the LbL
20 approach has been rarely combined with the elegant co-deposition approach for the formation of
21 PDA-hybrid coatings. In the second part of our study, we thus investigated if co-deposition and
22 LbL methods together can provide better control of the growth of PDA/polymer hybrid coatings.
23 Specifically, we examined PDA-polyethyleneimine (PEI) hybrid films, where the assembly is
24 driven by covalent PDA-polymer interactions, and PDA-dextran hybrid films, where the assembly
25 is driven by noncovalent hydrogen bonding.
26
27
28
29
30
31
32
33
34
35
36
37
38
39
40
41
42
43
44
45
46
47
48
49

50 Besides the possibility for better control of the microstructure, the most promising perspective of
51 DA-assisted LbL deposition is the possibility of constructing hierarchically layered coatings by
52 sequential deposition of layers with different compositions and functionalities. For polyelectrolyte
53
54
55
56
57

multilayer films, this has for example been done by adding a specific initial layer to promote adhesion of the coating to the substrate,³² or by adding a specific top layer to tune the surface properties.³³ As the third part of this study, we thus prepared a multilayer coating through DA-assisted deposition of polymers, nanoparticles, and ions using the LbL approach. Herein, it was demonstrated that DA-assisted deposition combined with the LbL approach enable the preparation of diverse hierarchal structures with tunable properties in bulk and at the surface of the coating.

2 Experimental Section

2.1 Materials

DA hydrochloride and tris(hydroxymethyl)aminomethane (>99.9%), PEI (branched, Mw \approx 600), tetraethyl orthosilicate (TEOS), copper sulfate pentahydrate ($\text{CuSO}_4 \cdot 5\text{H}_2\text{O}$), dextran (Mw \sim 150000 from *Leuconostoc mesenteroides*), and sodium hydroxide were purchased from Sigma-Aldrich. Hydrochloric acid (HCl, 37%) was purchased from Fisher Scientific. Ultrapure water (Arium Pro UV water purification system) with a resistivity of 18.2 M Ω cm was used for all experiments.

2.2 PDA Coatings

Silicon wafers (WaferNet, San Jose, USA) were first rinsed with acetone, ethanol, and ultrapure water, then dried by a stream of compressed dry air. The wafers were next plasma cleaned (PDC-32G plasma cleaner, Harrick Plasma) using high power under a constant water vapor pressure of 500 mTorr for 30 s. The thickness of the silica layer was then measured by spectroscopic ellipsometry. DA was dissolved in Tris buffer solution (pH = 8.5, 50 mM) and the silicon wafers were immersed in the DA solution (2 mg mL⁻¹) and stirred at 250 rpm. To keep the individual sample surfaces fixed and vertically aligned, the wafers were mounted into a costume-made Teflon

holder (Supporting Information, S1). Coatings were deposited using the common one-step method or the LbL approach. In the former, the silicon wafers were immersed in the DA solution for a certain duration. Afterward, the silicon wafer was removed from the solution, rinsed with Tris buffer, sonicated in fresh Tris buffer for 1 min, and dried by compressed airflow. This cleaning procedure was repeated three times to ensure the removal of weakly attached PDA aggregates. In the LbL approach, the DA solution was exchanged with a fresh solution every 2 h. For instance, a total deposition time of 12 h comprises 6×2 h deposition steps. Between each deposition step, the samples were sonicated and dried as described above. Three replicas were prepared for each sample. Additionally, coatings were also obtained by 2×6 h depositions and a 12 h one-step deposition (Supporting Information, S2).

2.3 PDA-Dextran and PDA-PEI Coatings

A mixed solution of dextran (10 mg mL^{-1}) and DA (2 mg mL^{-1}) was prepared in Tris buffer. One-step and LbL deposition methods were then used to prepare PDA-dextran hybrid coatings. PDA-PEI hybrid coatings were deposited similarly using PEI and DA concentrations of 0.2 and 2 mg mL^{-1} , respectively.

2.4 PDA-based Hierarchical Coating

The LbL procedure consisted of five steps, where in each step a layer with specific composition was deposited. The silica wafer was immersed in DA (2 mg mL^{-1}), DA-PEI (2 and 0.2 mg mL^{-1}),¹⁸ (DA-TEOS 2 and 42 mg mL^{-1}),¹¹ DA-CuSO₄.5H₂O (2 and 0.3 mg mL^{-1}),³⁴ and DA-dextran (2 and 10 mg mL^{-1}),³⁵ respectively. Each deposition step was 2 h, and between the steps, the samples were sonicated and dried as described above.

2.5. Atomic Force Microscopy (AFM)

AFM (NanoWizard 3, JPK Instruments AG, Berlin, Germany) operating in tapping mode in air was used to obtain topographical images and to estimate the thickness of the coatings (scratching test). The topographical images were collected with a scan rate of 0.2 Hz, a pixel resolution of 128×128 , scan area of $10 \times 10 \mu\text{m}^2$, and a standard tapping mode cantilever (HQ: NSC5/AL BS, tip radius of 8 nm, $k = 40 \text{ N/m}$, Mikromasch, USA). For each sample, a total number of nine AFM height images (three randomly-selected areas on three replicas) were obtained. Root mean square roughness (R_q) was next calculated from the AFM images using the standard software of the instrument (JPK SPM Data Processing). To reduce the influence of error from the randomly chosen surface positions, the smallest and largest values of the roughness were eliminated, and the reported R_q values are thus the average of seven values for each sample. For the thickness evaluation, the coatings were carefully scratched using a tweezer and AFM images were collected over the scratched area (scan rate of 0.1 Hz).

2.6. Spectroscopic Ellipsometry

Spectroscopic ellipsometry (M-2000X, J.A. Woollam Co., Inc.) measurements were performed to assess the thickness and optical properties of the coatings. The ellipsometric ψ (amplitude ratio) and Δ (phase shift) were collected in air in the wavelength range of 245–1000 nm at 5 different angles of incidence (50, 55, 60, 65, 70°). For each sample, a total number of 15 measurements (five randomly-selected spots on three replicas) were conducted. Depending on the deposition time, different optical models were used to describe the optical behavior of the coatings,³⁶ namely Cauchy with Urbach absorption for short depositions, B-spline for intermediate depositions, and B-spline with roughness layer for long depositions (Supporting Information, S3)

2.7 X-ray photoelectron spectroscopy (XPS)

To analyse the chemical composition of the PDA-based coatings, angle-resolved XPS (Nexsa, Thermo Fisher Scientific, USA) measurements were performed with a monochromated Al K-alpha source (1486.6 eV) and a flood gun for charge compensation. For each sample, 3 randomly points were characterized and analyzed using Avantage software.

2.8 Zeta-potential

Zeta potential (SurPASS3, Anton Paar GmbH, Austria) measurements were conducted to evaluate the charging behavior of films. Two samples (2×1 cm) were mounted into the instrument flow cell separated by a 100 ± 5 μ m capillary channel. The solution (1 mM NaCl) was pumped through the capillary channel between the two samples, producing a linearly decreasing measurement pressure (600 to 400 mbar). The measurements were conducted in two pH conditions (3 and 9). To ensure the reliability of the data, the measurements were repeated five times in each condition.

3. Results

3.1 LbL Deposition of PDA

PDA coatings were constructed using the LbL approach to investigate how it can provide control of the growth rate and the morphology of the coatings. To do so, the substrate was immersed in a fresh DA solution for 2 h, rinsed to remove the loosely bound aggregates, and then immersed in a fresh DA solution. This cyclic process was repeated several times to obtain coatings of varying thicknesses. In Fig. 1a,b, the thickness of the coatings, obtained by ellipsometry, and the surface roughness, R_q , of the coatings, obtained by AFM, are directly compared to the values for PDA coatings obtained by the common one-step deposition method (i.e., DA solution is not exchanged with a fresh solution). For the one-step method, the coating thickness linearly grows for deposition times up to 12 h, after which it starts to flatten out. Such a decaying growth is in agreement with

the literature observations, which has been attributed to the consumption of DA and the formation of excessively large aggregates ($> \sim 50$ nm) in the aged solution.³⁷ The thickness of the PDA coatings obtained by the LbL method (for the same total deposition time) is however relatively larger, e.g., the average thickness from a one-step deposition for 24 h is ~ 50 nm, whereas 12×2 h LbL depositions yield a thickness of ~ 100 nm. In addition, a linear growth behavior is obtained when using the LbL approach, suggesting a roughly constant adsorbed amount through each deposition step.

Regarding surface morphology (Fig. 1b), in both methods, R_q is found to generally increase with the deposition time; however, surface aggregation is reduced by the LbL approach as shown in AFM images and corresponding height profiles (also see Supporting Information, S4). For instance, the coating obtained by 18 h one-step deposition contains surface aggregates of ~ 5 -200 nm height. The relatively large standard deviation of the calculated R_q herein can also suggest the heterogeneous nature of the surface. For 9×2 h LbL depositions, the size of the aggregated domains is found to be much smaller, i.e., ~ 5 -50 nm. The benefit of using the LbL approach on coating thickness/morphology can be better perceived from Fig. 1c, where the R_q -values are plotted against the coating thicknesses. Accordingly, the surface roughness increases exponentially with the coating thickness for the one-step method, whereas the LbL approach provides a moderate linear correlation.

3.2 LbL Co-deposition of PDA and Polymers

Dopamine-quinone oligomers can form various covalent (e.g., Schiff base and Michael addition) and non-covalent (e.g., hydrogen bonding and coordination) interactions with polymers, nanoparticles, and metal ions.⁸ Benefiting from this versatile chemistry, co-deposition of DA and

other materials, i.e., DA-assisted deposition, thus allows entrapping functional units within a PDA coating to yield desired bulk and surface properties. We herein investigated to what extent the LbL approach can provide control over the growth behavior and the surface morphology of PDA-polymer hybrid coatings. To do so, two model polymers, i.e., polyethyleneimine (PEI) and dextran, were selected, which represent covalent and non-covalent dopamine-assisted depositions.

PEI is a cationic polymer rich in amine groups that can form covalent (Schiff base and Michael addition) interactions with the quinone derivatives.^{18,38} In a mixed solution of DA and PEI, PDA-PEI aggregates grow with time and simultaneously adhere to the substrate, providing PDA-PEI hybrid coatings. PEI, by reacting with the quinone derivatives, interrupts PDA-PDA hydrogen bonds and π - π stacking interactions; thus, hindering excessive PDA aggregation. Therefore, PDA-PEI hybrid coatings in general are thinner with smoother surface morphologies, compared with PDA coatings.¹⁸ Herein, PDA-PEI hybrid coatings were prepared using one-step and LbL deposition methods (Fig. 2, top row). Using the one-step deposition method, a decaying growth rate is found, and the thickness reaches a plateau of ~ 12 nm after 10 h. The surface morphology of the coating is found to be relatively smooth (compared with PDA coatings), yet surface aggregates of ~ 5 -40 nm height are still present (for 12 h deposition). The LbL approach provides a linear growth behavior where the coating thickness reaches ~ 50 nm after 6×2 h depositions. The surface morphology herein is also found to be smoother, as the size of aggregates is reduced to ~ 5 -20 nm. The elemental composition (Table 1) of PDA-PEI coatings prepared by one-step and LbL depositions shows a rather similar C/N ratio for both coatings; thus, suggesting a rather similar chemical composition in both cases.

Dextran is a polysaccharide with a backbone rich in hydroxyl and ether groups that can form hydrogen bonds with DA oligomers.³⁵ Therefore, dextran can be incorporated into the coating by

non-covalent hydrogen bonding interactions. Similar to the case of PDA-PEI, it has been suggested that dextran also can prevent excessive aggregation of PDA by inhibiting the noncovalent assembly routes. PDA-dextran coatings were herein prepared by one-step and LbL deposition methods. For the one-step deposition method, rather linear growth is found where the coating thickness after 12 h reaches ~ 12 nm. The coating shows a relatively rough surface morphology where aggregates of ~ 5 -60 nm are observed. LbL deposition is found to both increase the film thickness, and significantly reduce the surface roughness, i.e., surface heights < 10 nm. The elemental composition of the two coatings is also found to be relatively similar according to the XPS analysis (Table 1).

In summary, our data demonstrate that the LbL approach allows preparing hybrid PDA-polymer coatings with enhanced thickness and reduced surface roughness. This approach is found effective for both cases of covalent and non-covalent co-depositions.

3.3 Hierarchically Layered Coating

The benefits of combining the dopamine-assisted deposition with the LbL approach are not limited to increased coating thickness and reduced surface aggregation. This combination enables vast possibilities to construct hierarchal composite coatings where the composition and physicochemical properties can be tuned in the Z-direction (perpendicular to the substrate). As a proof-of-concept, we herein constructed a model coating comprising five different layers by LbL deposition of (i) PDA, (ii) PDA-PEI, (iii) PDA-SiO₂, (iv) PDA-Cu²⁺, and (v) PDA-dextran. These different materials (polyelectrolyte, inorganic compound, metal ion, and uncharged polymer) associate with dopamine-quinone oligomers via different interactions (covalent bonds, hydrogen bonding, and coordination bonds). By constructing such a layer, we thus aimed to demonstrate the versatility of the proposed LbL approach.

Fig. 3 shows the physicochemical properties of the multilayer coating following each deposition step. Table 2 summarizes the elemental composition of the coating after each deposition step, which confirms the incorporation of the co-deposited units in each step. Clear variations in the properties of the coating are found after each deposition step, which affirms how each deposition step allows tuning the coating properties. Variations in the surface topography (Fig. 3b) are found after each deposition step. For instance, when the PDA-PEI layer is deposited (layer #2), rather smooth surface morphology is achieved. On the other hand, the PDA-SiO₂ layer produces a rather heterogeneous surface morphology due to PDA aggregates or the entrapped nanoparticles. Overall though, the final multilayer coating has a relatively smooth surface owing to the LbL approach. The combination of LbL and DA-assisted deposition herein thus allows modulating the surface roughness of composite coatings, e.g., through deposition of (i) an intrinsically smooth hybrid layer such as PDA-PEI or (ii) a shorter deposition of a desired hybrid layer, as the top layer. From the ellipsometry measurements (Supporting Information, Section S5), the optical constants of each deposited layer were also estimated (Fig. 3c,d). It should be noted that the values of *n* and *k* herein are not directly measured but obtained from a modeling analysis; hence, a certain degree of uncertainty in the absolute values and shape of the optical dispersions is inevitable. Yet, comparing the different layers with each other, variations in the optical constants are noticeable, which originates from different chemical compositions of the layers. For instance, the layer containing Cu²⁺ shows relatively larger values of *n* and *k*, while the next deposited layer including dextran has reduced values of *n* and *k*.

Surface charge is another parameter that showed large dependence on the deposited layers. We measured this parameter in both acidic and alkaline pH, to better see the effects of protonation/deprotonation of the incorporated ionizable groups (Fig. 3e). Starting from the bare

silica substrate, one can expect only minor deprotonation of the silanol groups at acidic pH and notable deprotonation towards higher pH, which is confirmed by a negative near-zero zeta potential at pH 3 and a large negative surface potential at pH 9. Having PDA deposited as the first layer, a more cationic surface at pH 3 and a more anionic surface at pH 9 are found due to the ionization of amine and carboxyl groups found in PDA particles. When the next layer containing PEI is deposited, the surface charge at pH 3 becomes significantly more positively charged due to the amine-rich and cationic nature of PEI. Deposition of the third layer, produced an overall shift to a more negatively charged surface charge values, resulting from the negatively charged groups on both DA and SiO₂. While the fourth layer with copper ions does not alter the surface charge notably, the last layer including dextran showed reduced surface charge (in magnitude) possibly due to the incorporation of uncharged dextran molecules. Aside from the general trends demonstrated here, the surface charge is a key parameter that greatly matters when dealing with adsorption, binding, or adhesion of charged molecules and particles to a surface; for instance, in designing anti-fouling coatings or cell-adhesive substrates. Herein, the ability to readily tune the surface charge of the coating using the LbL approach can provide great control of the surface interactions and properties.

Surface hydrophilicity (Fig. 3f) of the coating was also shown to greatly depend on each deposited layer. Silica being highly hydrophilic, showed an expected contact angle of $\sim 20^\circ$. PDA added as the first layer, made the surface more hydrophobic increasing the contact angle to $\sim 55^\circ$. In the same line, depending on the chemistry of the deposited units, the surface hydrophilicity of the coating was shown to be easily adjustable using the LbL approach. For instance, layers including hydrophilic units such as SiO₂ or dextran were shown to reduce the contact angle notably.

4. Summary and Conclusion

A combination of DA-assisted deposition with the LbL approach allows for constructing functional coatings with tunable microstructure and chemical composition. The versatile catechol chemistry herein enables the incorporation of various materials into the coating. On the other hand, the LbL approach allows extending the thickness of the coating, reducing the surface aggregation, and finally varying the composition and properties of the coating in the vertical direction as desired. Such “lego-like” construction provides infinite possibilities for constructing composite coatings where the chemistry and physicochemical properties can be tuned at the coating-substrate interface, within the coating bulk, and at the coating surface.

Acknowledgments

R.Q. acknowledges the scholarship from the China Scholarship Council

References

- (1) Lee, H.; Dellatore, S. M.; Miller, W. M.; Messersmith, P. B. Mussel-Inspired Surface Chemistry for Multifunctional Coatings. *Science* (80-.). **2007**, *318* (5849), 426–430. <https://doi.org/10.1126/science.1147241>.
- (2) Yang, H.-C.; Luo, J.; Lv, Y.; Shen, P.; Xu, Z.-K. Surface Engineering of Polymer Membranes via Mussel-Inspired Chemistry. *J. Memb. Sci.* **2015**, *483*, 42–59. <https://doi.org/10.1016/j.memsci.2015.02.027>.
- (3) Liu, R.; Fu, X.; Wang, C.; Dawson, G. Dopamine Surface Modification of Trititanate Nanotubes: Proposed In-Situ Structure Models. *Chemistry (Easton)*. **2016**, *22* (17), 6071–6074. <https://doi.org/10.1002/chem.201600075>.
- (4) Dreyer, D. R.; Miller, D. J.; Freeman, B. D.; Paul, D. R.; Bielawski, C. W. Elucidating the Structure of Poly(Dopamine). *Langmuir* **2012**, *28* (15), 6428–6435. <https://doi.org/10.1021/la204831b>.
- (5) Hong, S.; Wang, Y.; Park, S. Y.; Lee, H. Progressive Fuzzy Cation-Pi Assembly of Biological Catecholamines. *Sci Adv* **2018**, *4* (9), eaat7457. <https://doi.org/10.1126/sciadv.aat7457>.

- (6) Kang, S. M.; Hwang, N. S.; Yeom, J.; Park, S. Y.; Messersmith, P. B.; Choi, I. S.; Langer, R.; Anderson, D. G.; Lee, H. One-Step Multipurpose Surface Functionalization by Adhesive Catecholamine. *Adv. Funct. Mater.* **2012**, 22 (14), 2949–2955. <https://doi.org/10.1002/adfm.201200177>.
- (7) Yang, H. C.; Pi, J. K.; Liao, K. J.; Huang, H.; Wu, Q. Y.; Huang, X. J.; Xu, Z. K. Silica-Decorated Polypropylene Microfiltration Membranes with a Mussel-Inspired Intermediate Layer for Oil-in-Water Emulsion Separation. *ACS Appl Mater Interfaces* **2014**, 6 (15), 12566–12572. <https://doi.org/10.1021/am502490j>.
- (8) Qiu, W. Z.; Yang, H. C.; Xu, Z. K. Dopamine-Assisted Co-Deposition: An Emerging and Promising Strategy for Surface Modification. *Adv. Colloid Interface Sci.* **2018**, 256, 111–125. <https://doi.org/10.1016/j.cis.2018.04.011>.
- (9) Zhang, Y.; Thingholm, B.; Goldie, K. N.; Ogaki, R.; Stadler, B. Assembly of Poly(Dopamine) Films Mixed with a Nonionic Polymer. *Langmuir* **2012**, 28 (51), 17585–17592. <https://doi.org/10.1021/la304080c>.
- (10) Ma, M. Q.; Zhang, C.; Chen, T. T.; Yang, J.; Wang, J. J.; Ji, J.; Xu, Z. K. Bioinspired Polydopamine/Polyzwitterion Coatings for Underwater Anti-Oil and -Freezing Surfaces. *Langmuir* **2019**, 35 (5), 1895–1901. <https://doi.org/10.1021/acs.langmuir.8b02320>.
- (11) Ho, C. C.; Ding, S. J. Novel SiO₂/PDA Hybrid Coatings to Promote Osteoblast-like Cell Expression on Titanium Implants. *J Mater Chem B* **2015**, 3 (13), 2698–2707. <https://doi.org/10.1039/c4tb01841a>.
- (12) Son, H. Y.; Ryu, J. H.; Lee, H.; Nam, Y. S. Silver-Polydopamine Hybrid Coatings of Electrospun Poly(Vinyl Alcohol) Nanofibers. *Macromol. Mater. Eng.* **2013**, 298 (5), 547–554. <https://doi.org/10.1002/mame.201200231>.
- (13) Zhu, J.; Tsehay, M. T.; Wang, J.; Uliana, A.; Tian, M.; Yuan, S.; Li, J.; Zhang, Y.; Volodin, A.; Van der Bruggen, B. A Rapid Deposition of Polydopamine Coatings Induced by Iron (III) Chloride/Hydrogen Peroxide for Loose Nanofiltration. *J. Colloid Interface Sci.* **2018**, 523, 86–97. <https://doi.org/10.1016/j.jcis.2018.03.072>.
- (14) Wang, Z.; Zou, Y.; Li, Y.; Cheng, Y. Metal-Containing Polydopamine Nanomaterials: Catalysis, Energy,

- and Theranostics. *Small* **2020**, *16* (18), 1–21. <https://doi.org/10.1002/sml.201907042>.
- (15) Bernsmann, F.; Ball, V.; Addiego, F.; Ponche, A.; Michel, M.; Gracio, J. J.; Toniazzi, V.; Ruch, D. Dopamine-Melanin Film Deposition Depends on the Used Oxidant and Buffer Solution. *Langmuir* **2011**, *27* (6), 2819–2825. <https://doi.org/10.1021/la104981s>.
- (16) Ponzio, F.; Barthès, J.; Bour, J.; Michel, M.; Bertani, P.; Hemmerlé, J.; D’Ischia, M.; Ball, V. Oxidant Control of Polydopamine Surface Chemistry in Acids: A Mechanism-Based Entry to Superhydrophilic-Superoleophobic Coatings. *Chem. Mater.* **2016**, *28* (13), 4697–4705. <https://doi.org/10.1021/acs.chemmater.6b01587>.
- (17) Trzcińska, Z.; Bruggeman, M.; Ijakipour, H.; Hodges, N. J.; Bowen, J.; Stamboulis, A. Polydopamine Linking Substrate for AMPs: Characterisation and Stability on Ti6Al4V. *Materials (Basel)*. **2020**, *13* (17), 1–19. <https://doi.org/10.3390/MA13173714>.
- (18) Lv, Y.; Yang, S.-J.; Du, Y.; Hao-Cheng, Y.; Xu, Z.-K. Co-Deposition Kinetics of Polydopamine/Polyethyleneimine Coatings: Effects of Solution Composition and Substrate Surface. *Langmuir* **2018**. <https://doi.org/10.1021/acs.langmuir.8b02454>.
- (19) Ball, V.; Del Frari, D.; Toniazzi, V.; Ruch, D. Kinetics of Polydopamine Film Deposition as a Function of PH and Dopamine Concentration: Insights in the Polydopamine Deposition Mechanism. *J. Colloid Interface Sci.* **2012**, *386* (1), 366–372. <https://doi.org/10.1016/j.jcis.2012.07.030>.
- (20) Richardson, J. J.; Björnmalm, M.; Caruso, F. Technology-Driven Layer-by-Layer Assembly of Nanofilms. *Science (80-.)*. **2015**, *348* (6233). https://doi.org/10.1126/SCIENCE.AAA2491/ASSET/78DEDA0D-2838-49E5-B216-A308E79D1A7A/ASSETS/GRAPHIC/348_AAA2491_F3.JPEG.
- (21) Guzmán, E.; Rubio, R. G.; Ortega, F. A Closer Physico-Chemical Look to the Layer-by-Layer Electrostatic Self-Assembly of Polyelectrolyte Multilayers. *Adv. Colloid Interface Sci.* **2020**, *282*, 102197. <https://doi.org/10.1016/J.CIS.2020.102197>.
- (22) Richardson, J. J.; Cui, J.; Björnmalm, M.; Braunger, J. A.; Ejima, H.; Caruso, F. Innovation in Layer-by-Layer Assembly. *Chem. Rev.* **2016**, *116* (23), 14828–14867. <https://doi.org/10.1021/acs.chemrev.6b00627>.

- (23) Srivastava, S.; Kotov, N. A. Composite Layer-by-Layer (LBL) Assembly with Inorganic Nanoparticles and Nanowires. *Acc. Chem. Res.* **2008**, *41* (12), 1831–1841. <https://doi.org/10.1021/ar8001377>.
- (24) Heath, G. R.; Li, M.; Polignano, I. L.; Richens, J. L.; Catucci, G.; O'Shea, P.; Sadeghi, S. J.; Gilardi, G.; Butt, J. N.; Jeuken, L. J. C. Layer-by-Layer Assembly of Supported Lipid Bilayer Poly- L-Lysine Multilayers. *Biomacromolecules* **2016**, *17* (1), 324–335. <https://doi.org/10.1021/acs.biomac.5b01434>.
- (25) Kim, B.-S.; Park, S. W.; Hammond, P. T. Hydrogen-Bonding Layer-by-Layer-Assembled Biodegradable Polymeric Micelles as Drug Delivery Vehicles from Surfaces. *ACS Nano* **2008**, *2* (2), 386–392. <https://doi.org/10.1021/nn700408z>.
- (26) An, Q.; Huang, T.; Shi, F. Covalent Layer-by-Layer Films: Chemistry, Design, and Multidisciplinary Applications. *Chem. Soc. Rev.* **2018**, *47* (13), 5061–5098. <https://doi.org/10.1039/C7CS00406K>.
- (27) Bernsmann, F.; Ersen, O.; Voegel, J. C.; Jan, E.; Kotov, N. A.; Ball, V. Melanin-Containing Films: Growth from Dopamine Solutions versus Layer-by-Layer Deposition. *ChemPhysChem* **2010**, *11* (15), 3299–3305. <https://doi.org/10.1002/cphc.201000384>.
- (28) Ma, X.; Wu, G.; Dai, F.; Li, D.; Li, H.; Zhang, L.; Deng, H. Chitosan/Polydopamine Layer by Layer Self-Assembled Silk Fibroin Nanofibers for Biomedical Applications. *Carbohydr. Polym.* **2021**, *251*, 117058. <https://doi.org/10.1016/J.CARBPOL.2020.117058>.
- (29) Ou, J.; Wang, J.; Qiu, Y.; Liu, L.; Yang, S. Mechanical Property and Corrosion Resistance of Zirconia/Polydopamine Nanocomposite Multilayer Films Fabricated via a Novel Non-Electrostatic Layer-by-Layer Assembly Technique. *Surf. Interface Anal.* **2011**, *43* (4), 803–808. <https://doi.org/10.1002/SIA.3631>.
- (30) Xie, C.; Lu, X.; Wang, K.; Yuan, H.; Fang, L.; Zheng, X.; Chan, C.; Ren, F.; Zhao, C. Pulse Electrochemical Driven Rapid Layer-by-Layer Assembly of Polydopamine and Hydroxyapatite Nanofilms via Alternative Redox in Situ Synthesis for Bone Regeneration. *ACS Biomater. Sci. Eng.* **2016**, *2* (6), 920–928. https://doi.org/10.1021/ACSBIMATERIALS.6B00015/SUPPL_FILE/AB6B00015_SI_001.PDF.

- (31) Papananou, H.; Katsumata, R.; Neary, Z.; Goh, R.; Meng, X.; Limary, R.; Segalman, R. A. Dopamine-Mediated Polymer Coating Facilitates Area-Selective Atomic Layer Deposition. *ACS Appl. Polym. Mater.* **2021**, 3 (10), 4924–4931. <https://doi.org/10.1021/acsapm.1c00692>.
- (32) Follmann, H. D. M.; Naves, A. F.; Martins, A. F.; Félix, O.; Decher, G.; Muniz, E. C.; Silva, R. Advanced Fibroblast Proliferation Inhibition for Biocompatible Coating by Electrostatic Layer-by-Layer Assemblies of Heparin and Chitosan Derivatives. *J. Colloid Interface Sci.* **2016**, 474, 9–17. <https://doi.org/10.1016/J.JCIS.2016.04.008>.
- (33) Jiang, T.; Moghaddam, S. Z.; Thormann, E. A PH-Responsive Polyelectrolyte Multilayer Film with Tunable Interfacial Properties. *Polymer (Guildf)*. **2021**, 214, 123367. <https://doi.org/10.1016/j.polymer.2020.123367>.
- (34) Gao, R.; Zhang, L.; Hao, Y.; Cui, X.; Liu, D.; Zhang, M.; Tang, Y. One-Step Preparation of Magnetic Imprinted Nanoparticles Adopting Dopamine-Cupric Ion as a Co-Monomer for the Specific Recognition of Bovine Hemoglobin. *J. Sep. Sci.* **2015**, 38 (20), 3568–3574. <https://doi.org/10.1002/jssc.201500677>.
- (35) Liu, Y.; Chang, C. P.; Sun, T. Dopamine-Assisted Deposition of Dextran for Nonfouling Applications. *Langmuir* **2014**, 30 (11), 3118–3126. <https://doi.org/10.1021/la500006e>.
- (36) Qie, R.; Zajforoushan Moghaddam, S.; Thormann, E. Parameterization of the Optical Constants of Polydopamine Films for Spectroscopic Ellipsometry Studies. *Phys. Chem. Chem. Phys.* **2021**, 23 (9), 5516–5526. <https://doi.org/10.1039/d0cp04796a>.
- (37) Zhu, B.; Edmondson, S. Polydopamine-Melanin Initiators for Surface-Initiated ATRP. *Polymer (Guildf)*. **2011**, 52 (10), 2141–2149. <https://doi.org/10.1016/j.polymer.2011.03.027>.
- (38) Luo, R.; Wang, X.; Deng, J.; Zhang, H.; Maitz, M. F.; Yang, L.; Wang, J.; Huang, N.; Wang, Y. Dopamine-Assisted Deposition of Poly (Ethylene Imine) for Efficient Heparinization. *Colloids Surfaces B Biointerfaces* **2016**, 144, 90–98. <https://doi.org/10.1016/J.COLSURFB.2016.03.080>.

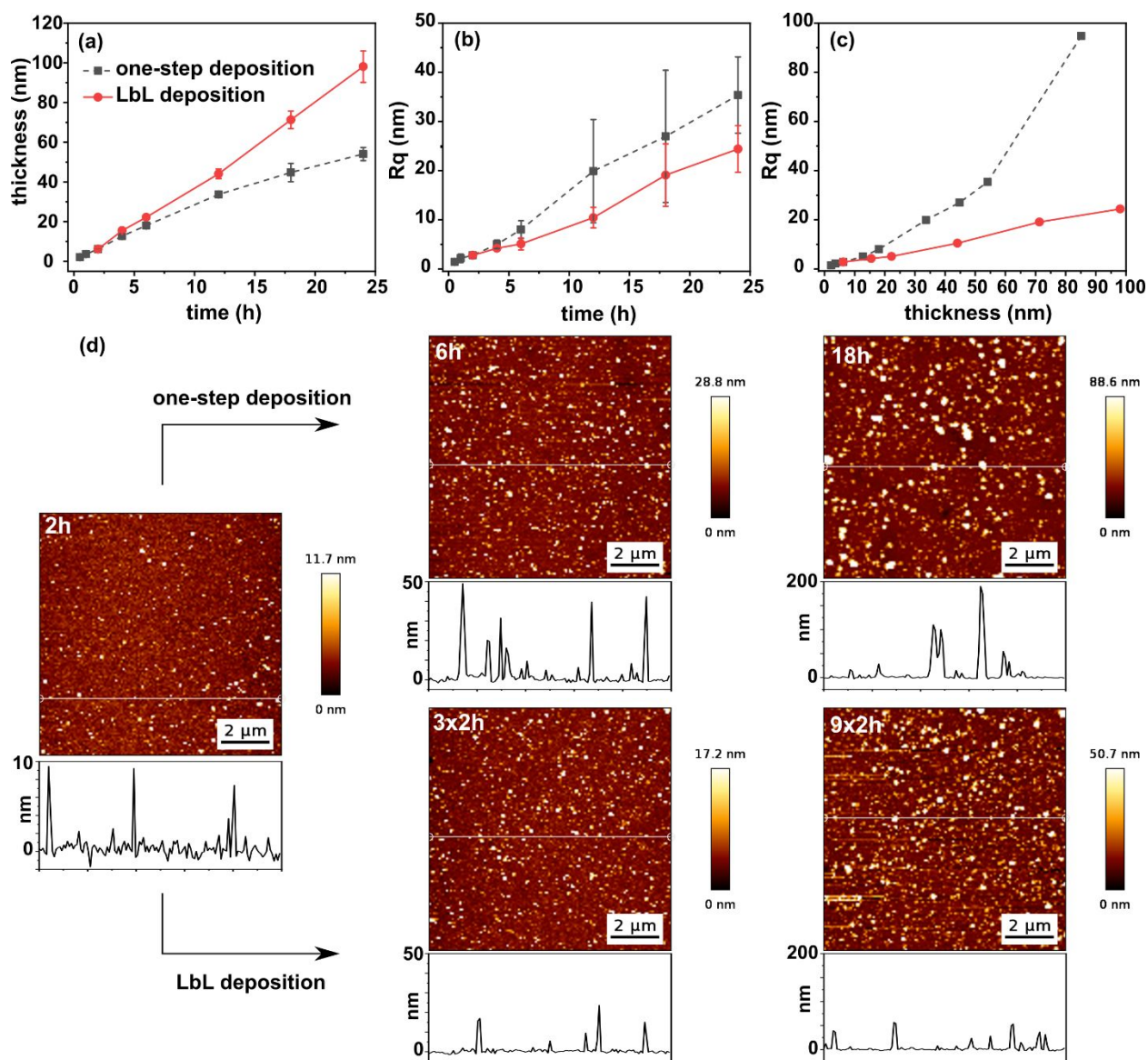


Fig. 1 PDA coatings obtained by one-step and LbL deposition methods: (a) ellipsometry thickness vs. deposition time ($n=15$). (b) Root-mean-square roughness (R_q) vs. deposition time ($n=7$) calculated over $10 \times 10 \mu\text{m}^2$ area. (c) R_q vs. ellipsometry thickness. (d) Representative AFM images and corresponding height profiles of PDA films.

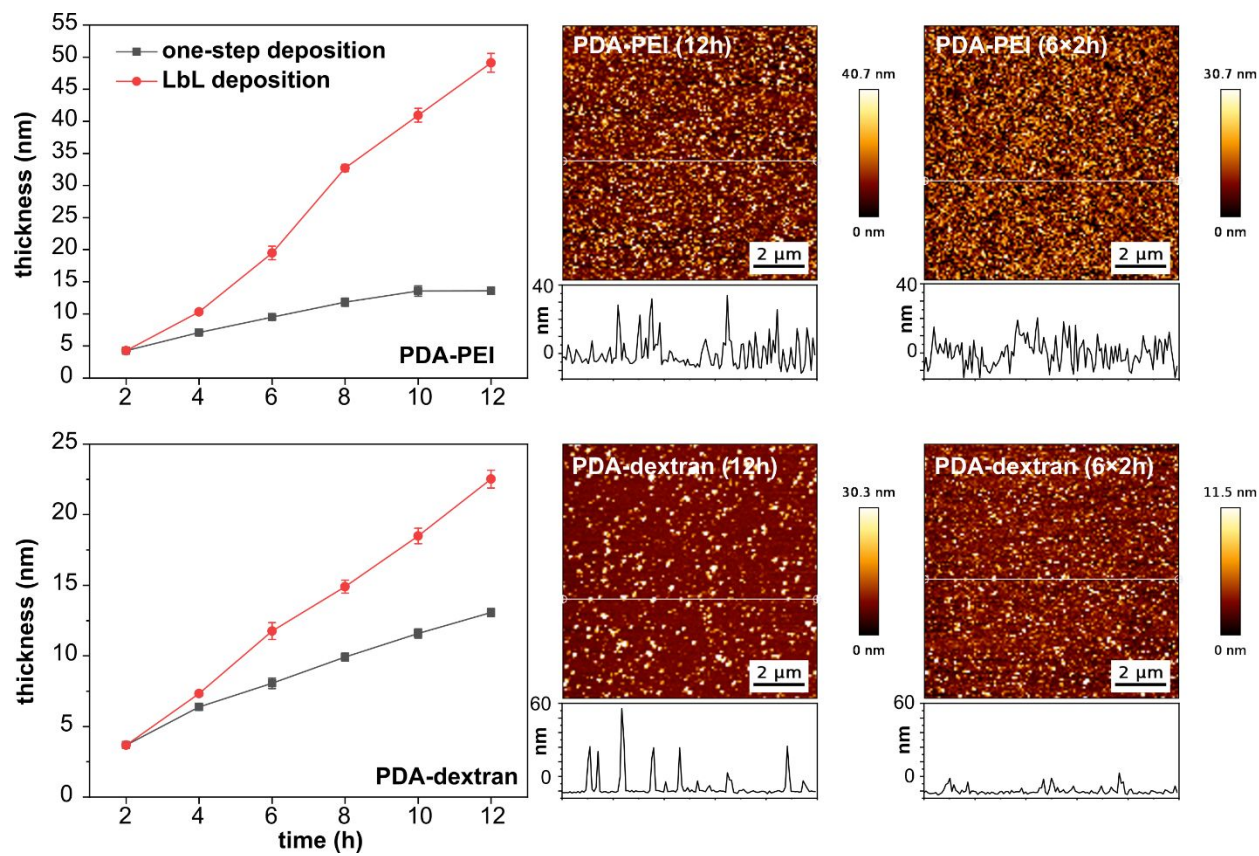


Fig. 2 PDA-polymer hybrid coatings obtained by one-step and LbL deposition methods: (top row) PDA-PEI coatings, (bottom row) PDA-dextran coatings.

Table 1 Elemental composition of hybrid PDA-polymer coatings obtained by one-step and LbL deposition methods

	C	N	O	Si	C/N
PDA/dextran (12 h)	65.7 ± 0.3	7.4 ± 0.3	25.5 ± 0.1	1.4 ± 0.1	8.9 ± 0.4
PDA/dextran (6×2 h)	68.9 ± 0.3	6.6 ± 0.2	24.5 ± 0.2	-	10.5 ± 0.4
PDA/PEI (12 h)	69.2 ± 0.3	14.8 ± 0.3	14.5 ± 0.2	1.5 ± 0	4.7 ± 0.1
PDA/PEI (6×2 h)	72.6 ± 0.4	14.4 ± 0.4	13.0 ± 0.1	-	5.1 ± 0.2

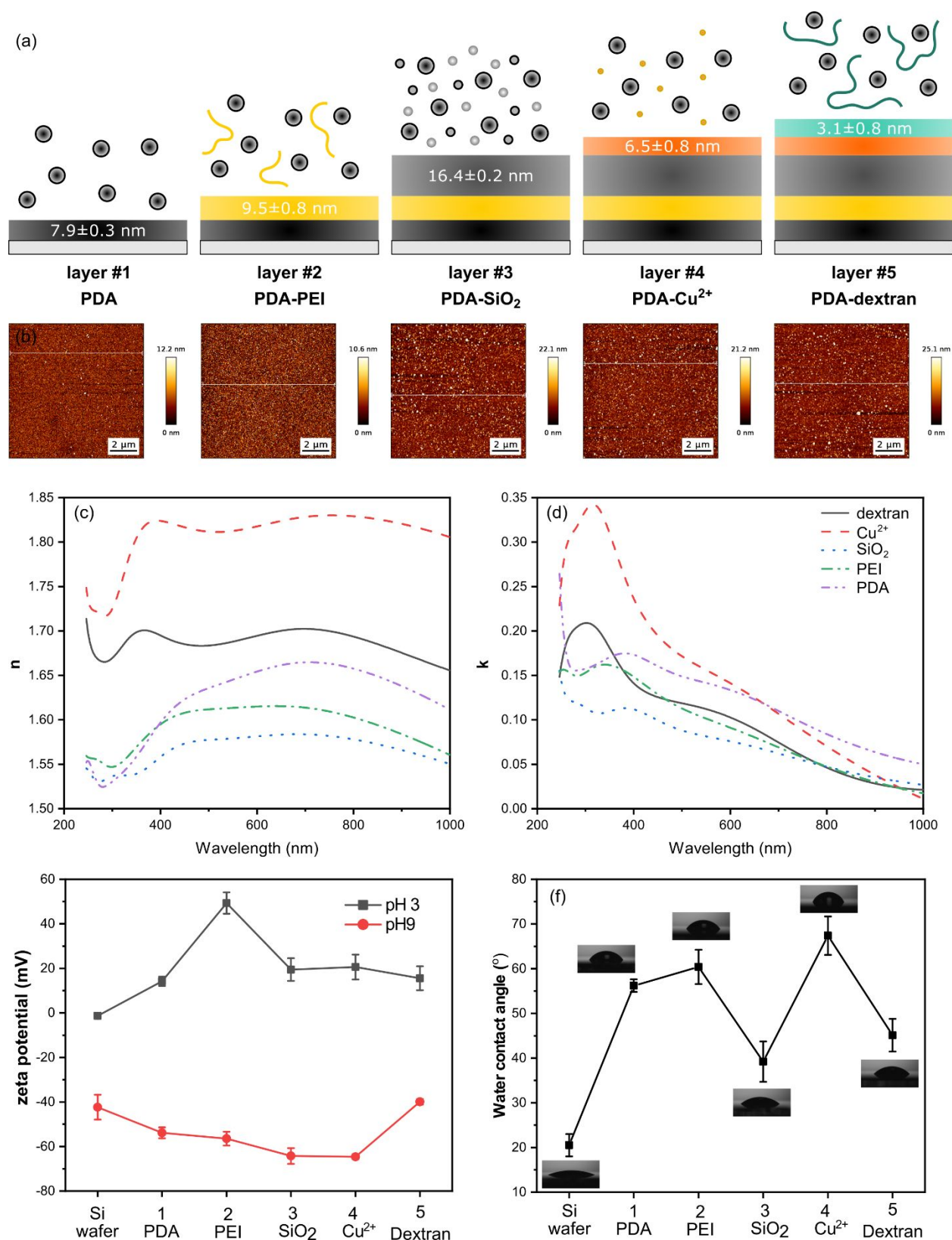


Fig. 3 Hierarchical multilayer coating obtained by LbL depositions (2 h) of DA, DA-PEI, DA-TEOS, DA-CuSO₄, and DA-dextran on a silica substrate; (a) schematic illustration of the multilayer structure and thickness of each layer calculated by ellipsometry (n=3), (b) representative AFM images of the multilayer coating after each deposition, (c)(d) modeled refractive index (n) and extinction coefficient of each layer from ellipsometry, (e) surface zeta potential after each deposition, (f) water contact angle after each deposition.

Table 2 Elemental composition for hierarchical multilayer coating after deposition of each layer

	C	N	O	Si	Cu	C/N	C/O
PDA	58.0 ± 1.8	7.5 ± 0.1	26.4 ± 0.9	8.1 ± 0.8		7.7 ± 0.3	2.2 ± 0.1
PDA-PEI	67.3 ± 0.4	13.2 ± 0.2	18.1 ± 0.2	1.4 ± 0.1		5.1 ± 0.1	3.7 ± 0.1
PDA-SiO ₂	38.3 ± 0.7	4.6 ± 0.2	41.7 ± 0.3	15.4 ± 0.5		8.3 ± 0.3	0.9 ± 0.1
PDA-Cu ²⁺	67.3 ± 0.1	8.2 ± 0.2	22.5 ± 0.1	1.4 ± 0.1	0.6 ± 0.1	8.2 ± 0.2	3.0 ± 0.1
PDA-dextran	68.7 ± 0.3	7.1 ± 0.3	24.2 ± 0.3			9.6 ± 0.4	2.8 ± 0.1

Supporting Information

Dopamine-assisted Layer-By-Layer Deposition Providing Coatings with Controlled Microstructure and Physicochemical Properties

*Runtian Qie, Saeed Zajforoushan Moghaddam, Esben Thormann**

Department of Chemistry, Technical University of Denmark, 2800 Kgs. Lyngby, Denmark

S1 Experimental Setup

To ensure the reproducibility of the coating properties, a custom-made Teflon holder (Fig. S1) was fabricated and used for immersing the samples in DA solutions. Herein, it was ensured that all the samples (center of the wafer) were kept at the same distance from the solution-air interface (~ 4 cm), also uniform stirring was achieved for all the samples.



Fig. S1 Teflon sample-holder used for the preparation of coatings

S2 12 h Single Deposition vs. 2 × 6 h LbL Depositions

As discussed, for each LbL deposition step, DA solution is exchanged with a fresh solution. Thus, aside from the number of depositions, the duration of each deposition may also affect the coating properties. To examine this point, we first prepared PDA coatings obtained from 2 × 6 h LbL depositions and 12 h single deposition. Herein, we compared the thickness and surface morphology of the coatings obtained from the two methods (Fig. S2, Table S1). Accordingly, no significant improvement in the thickness growth or reduction of the surface roughness was observed when using the LbL approach (via 6 h steps), in other words, the benefits of having “fresh” DA are not achieved when the duration of each step is relatively long. For this reason, all later samples were prepared using LbL depositions of 2 h duration, which showed to improve both the growth behavior and the surface morphology of the coatings.

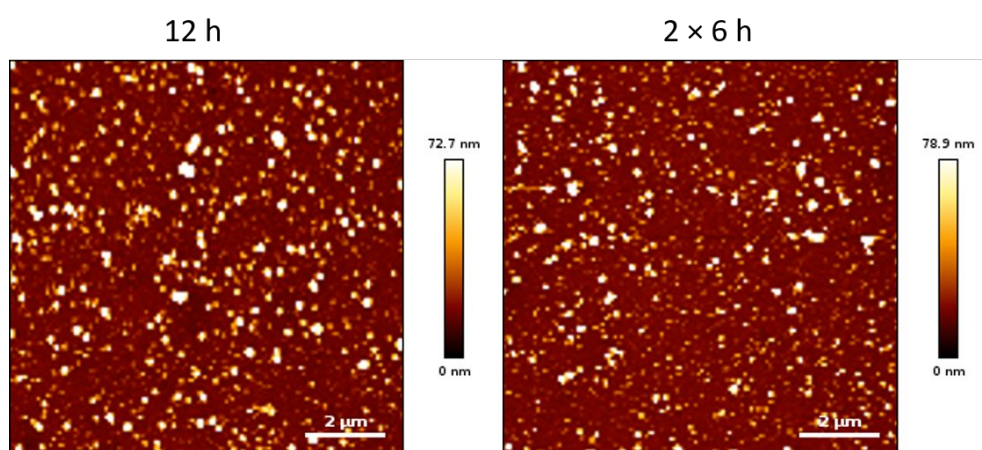


Fig. S2 Representative AFM images of PDA films on silicon wafer prepared by one-step (12 h) and LbL (2 × 6 h) deposition methods

Table S1 Thickness and Rq (Scan size, 10 × 10 μm²) comparison of PDA films on silicon substrates prepared by one-step (12 h) and LbL (2 × 6 h) deposition methods

	Thickness (nm)	Rq (nm)
12 h	33.2 ± 4.2	22.9 ± 11.4
2 × 6 h	34.2 ± 1.6	20.1 ± 5.3

S3 Ellipsometry Analysis: Optical Models

The complex light-absorbing behavior and growing surface roughness must be considered for modeling the optical properties and analyzing the ellipsometric thickness of PDA coatings. Herein, for samples prepared through different depositions times, we used a step-by-step modeling approach, starting from the simplest optical model, i.e., Cauchy for transparent films, and gradually increased the number of model variables, i.e., light absorption parameters, so a satisfactory fit between the experimental and modeled ellipsometric data was obtained without over-parametrization. On this basis, Cauchy with Urbach absorption term (deposition times ≤ 2 h), Kramers-Kronig-consistent B-spline ($2 \text{ h} < \text{deposition times} \leq 12 \text{ h}$), and Kramers-Kronig, consistent B-spline with roughness layer ($12 \text{ h} < \text{deposition times}$) were used for samples of different deposition times. Fig. S3-S5 show representative modeling data for PDA samples prepared through the LbL approach.

<p>Fit Results</p> <p>MSE = 8.048</p> <p>Thickness # 3 = $6.92 \pm 0.024 \text{ nm}$</p> <p>A = 1.658 ± 0.002135</p> <p>k Amplitude = 0.15371 ± 0.001110</p> <p>Exponent = 0.326 ± 0.008203</p> <p>Total Thickness = $108.78 \pm 0.024 \text{ nm}$</p>	<p>Optical Model</p> <ul style="list-style-type: none"> - Layer # 3 = <u>Cauchy</u> Thickness # 3 = <u>6.92 nm</u> (fit) A = <u>1.658</u> (fit) B = <u>0.01000</u> C = <u>0.0000</u> - Urbach Absorption Parameters k Amplitude = <u>0.15371</u> (fit) Exponent = <u>0.326</u> (fit) Band Edge = <u>400.0 nm</u> <table border="1"> <tr> <td>Layer # 2 = <u>SiO2_JAW</u></td> <td>Thickness # 2 = <u>100.86 nm</u></td> </tr> <tr> <td>Layer # 1 = <u>INTR_JAW</u></td> <td>Thickness # 1 = <u>1.00 nm</u></td> </tr> <tr> <td colspan="2">Substrate = <u>Si_JAW</u></td> </tr> </table>	Layer # 2 = <u>SiO2_JAW</u>	Thickness # 2 = <u>100.86 nm</u>	Layer # 1 = <u>INTR_JAW</u>	Thickness # 1 = <u>1.00 nm</u>	Substrate = <u>Si_JAW</u>	
Layer # 2 = <u>SiO2_JAW</u>	Thickness # 2 = <u>100.86 nm</u>						
Layer # 1 = <u>INTR_JAW</u>	Thickness # 1 = <u>1.00 nm</u>						
Substrate = <u>Si_JAW</u>							

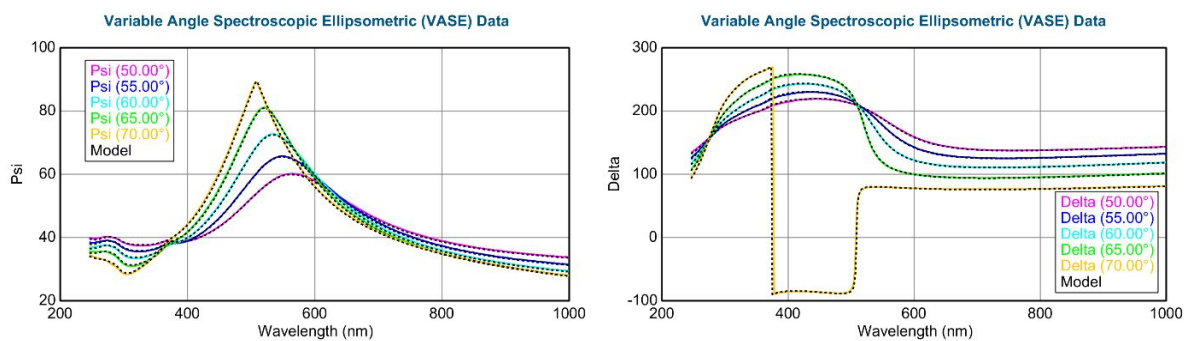


Fig. S3 Ellipsometry data of PDA film; 2 h (Cauchy with Urbach adsorption)

<p>Fit Results</p> <p>MSE = 7.668</p> <p>Thickness # 3 = 23.52 ± 0.047 nm</p> <p>E Inf = 1.280 ± 0.0135</p> <p>IR Amp = 0.535 ± 0.0145</p> <p>Total Thickness = 126.90 ± 0.047 nm</p>	<p>Optical Model</p> <ul style="list-style-type: none"> Layer # 3 = B-Spline Thickness # 3 = 23.52 nm (fit) <ul style="list-style-type: none"> Resolution (eV) = 0.700 6 Pts. (1.241-5.039 eV) Draw Node Graph Fit Optical Constants = ON Use KK Mode = ON (In Use) + Kramers-Kronig - Nodes <ul style="list-style-type: none"> Init. Values: n = 1.500 k = 0.00 Starting Mat. = Cauchy Force E2 Positive = ON Assume Transparent Region = OFF Show Nodes = OFF Node Spacing Spectral Ranges: Add Delete Delete All + Advanced <table border="1"> <tr> <td>Layer # 2 = SIO2_JAW</td> <td>Thickness # 2 = 102.38 nm</td> </tr> <tr> <td>Layer # 1 = INTR_JAW</td> <td>Thickness # 1 = 1.00 nm</td> </tr> <tr> <td colspan="2">Substrate = SI_JAW</td> </tr> </table>	Layer # 2 = SIO2_JAW	Thickness # 2 = 102.38 nm	Layer # 1 = INTR_JAW	Thickness # 1 = 1.00 nm	Substrate = SI_JAW	
Layer # 2 = SIO2_JAW	Thickness # 2 = 102.38 nm						
Layer # 1 = INTR_JAW	Thickness # 1 = 1.00 nm						
Substrate = SI_JAW							

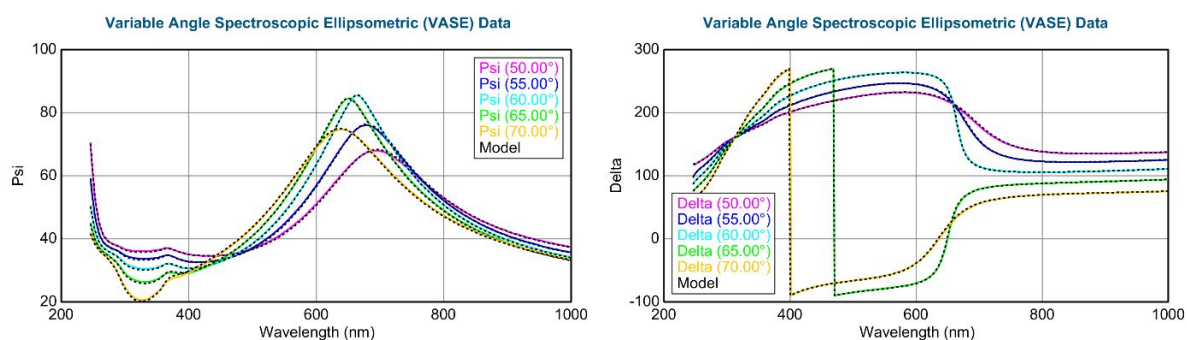


Fig. S4 Ellipsometry data of PDA film deposited; 3×2 h (B-spline)

<p>Fit Results</p> <p>MSE = 22.529</p> <p>Roughness = 20.45 ± 0.229 nm</p> <p>Thickness # 3 = 73.97 ± 0.126 nm</p> <p>E Inf = 1.028 ± 0.0159</p> <p>IR Amp = 0.0439 ± 0.0157</p> <p>Total Thickness = 174.33 ± 0.126 nm</p>	<p>Optical Model</p> <p>Roughness = <u>20.45 nm</u> (fit)</p> <p>- Layer # 3 = <u>B-Spline</u> Thickness # 3 = <u>73.97 nm</u> (fit)</p> <p>Resolution (eV) = <u>0.700</u> 6 Pts. (1.241-5.039 eV) Draw Node Graph</p> <p>Fit Optical Constants = <u>ON</u></p> <p>Use KK Mode = <u>ON</u> (In Use)</p> <p>+ Kramers-Kronig</p> <p>- Nodes</p> <p>Init. Values: n = <u>1.500</u> k = <u>0.00</u> Starting Mat. = <u>Cauchy</u></p> <p>Force E2 Positive = <u>ON</u></p> <p>Assume Transparent Region = <u>OFF</u></p> <p>Show Nodes = <u>OFF</u></p> <p>Node Spacing Spectral Ranges: Add Delete Delete All</p> <p>+ Advanced</p> <p>Layer # 2 = <u>SiO2_JAW</u> Thickness # 2 = <u>99.36 nm</u></p> <p>Layer # 1 = <u>INTR_JAW</u> Thickness # 1 = <u>1.00 nm</u></p> <p>Substrate = <u>SI_JAW</u></p>
---	---

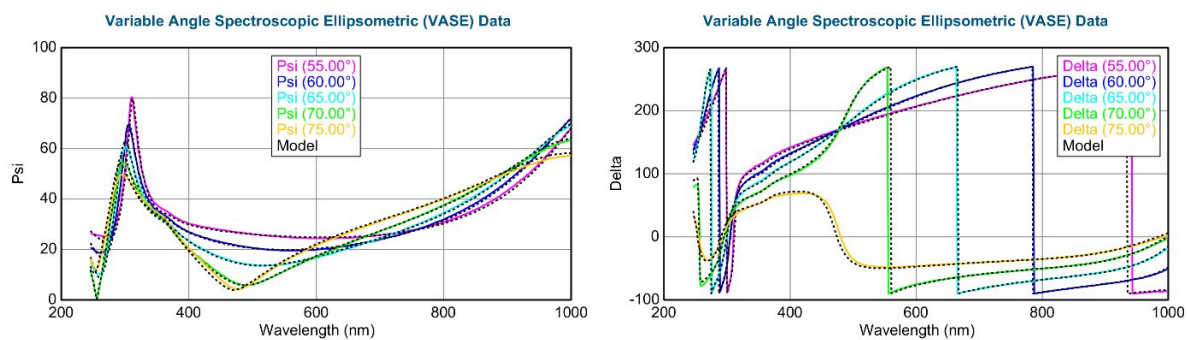


Fig. S5 Ellipsometry data of PDA film; 9×2 h (B-spline with roughness layer)

S4 Additional AFM Images

Fig. S6 illustrates the representative AFM height images for the PDA films obtained by single- and LbL deposition methods.

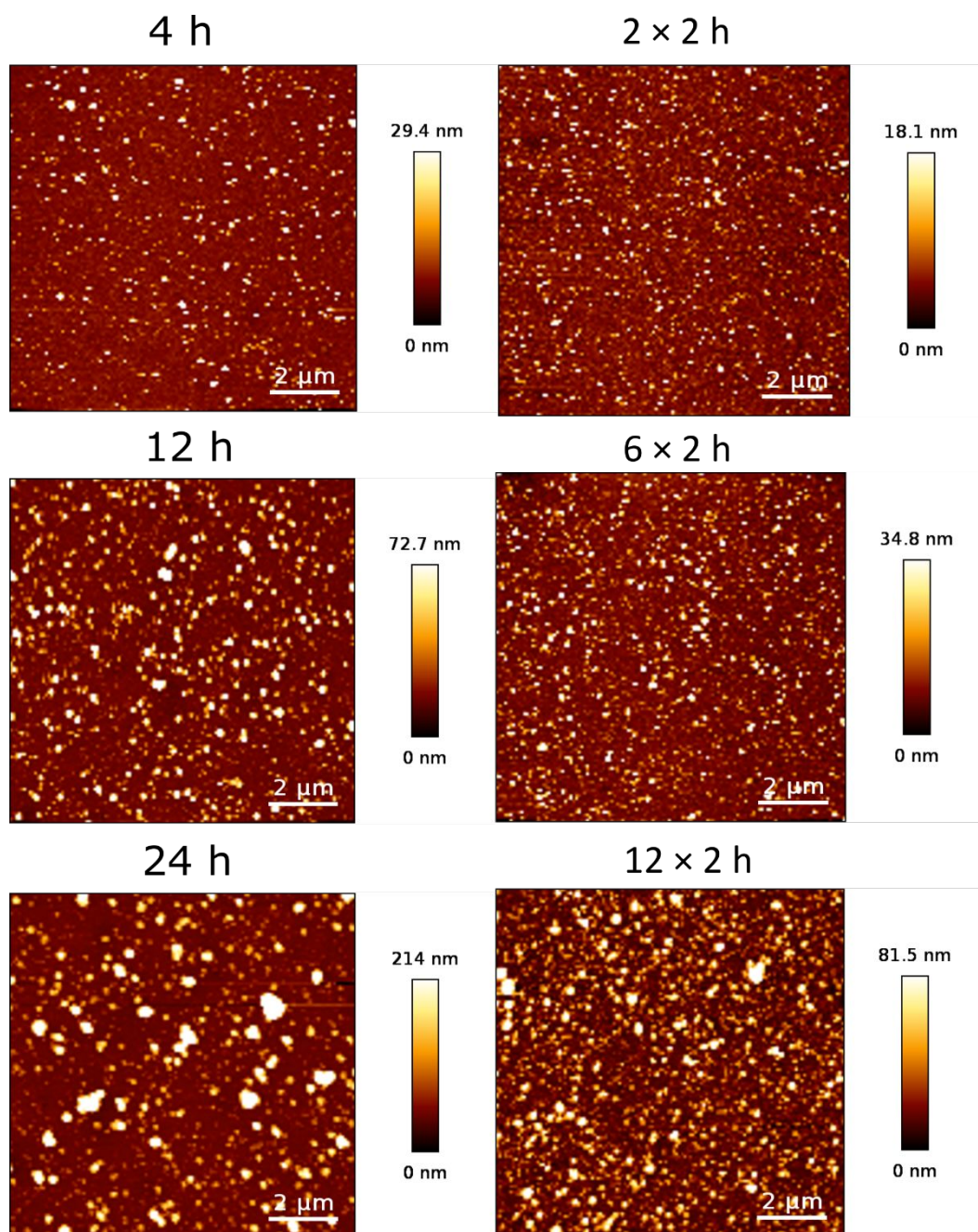


Fig. S6 Representative AFM images of PDA films prepared by one-step (left) and LbL deposition (right)

S5 Hierarchal Coating: Ellipsometry Analysis

Two different modeling approaches were conducted to analyze the ellipsometry data of the multilayer coating. The first approach was to simply have both thickness and optical constants (for each layer) as “free” model parameters. Thus, after each deposition, the experimental Ψ and Δ were collected, and a b-spline model (resolution 0.6 eV, KK-consistent, $\epsilon_2 > 0$, $n=1.7$, and $k=0.1$ as initial guess) with unknown optical constants and thickness (Fig. S7) was used. After modeling each layer, the parameters were then fixed in the model, the next layer was deposited, and a similar modeling procedure was repeated. Fig. S8 shows the optical dispersions of each layer obtained by this modeling approach.

Fit Results	Optical Model
MSE = 15.336	+ Layer # 7 = B-Spline-PDA with Dextran Thickness # 7 = 5.08 nm
Thickness # 7 = 5.08 ± 0.071 nm	+ Layer # 6 = B-Spline-PDA with Cu²⁺ Thickness # 6 = 6.72 nm
E Inf = 1.099 ± 0.0608	+ Layer # 5 = B-Spline-PDA with SiO₂ Thickness # 5 = 13.20 nm
IR Amp = 0.00 ± 0.0964	+ Layer # 4 = B-Spline-PDA with PEI Thickness # 4 = 11.44 nm
Total Thickness = 148.32 ± 0.071 nm	+ Layer # 3 = B-Spline-PDA Thickness # 3 = 9.80 nm
	Layer # 2 = SiO₂_JAW Thickness # 2 = 101.06 nm
	Layer # 1 = INTR_JAW Thickness # 1 = 1.00 nm
	Substrate = SI_JAW

Fig. S7 Optical modeling of the multilayer coating, using B-spline with both thickness and optical constants as free model parameters.

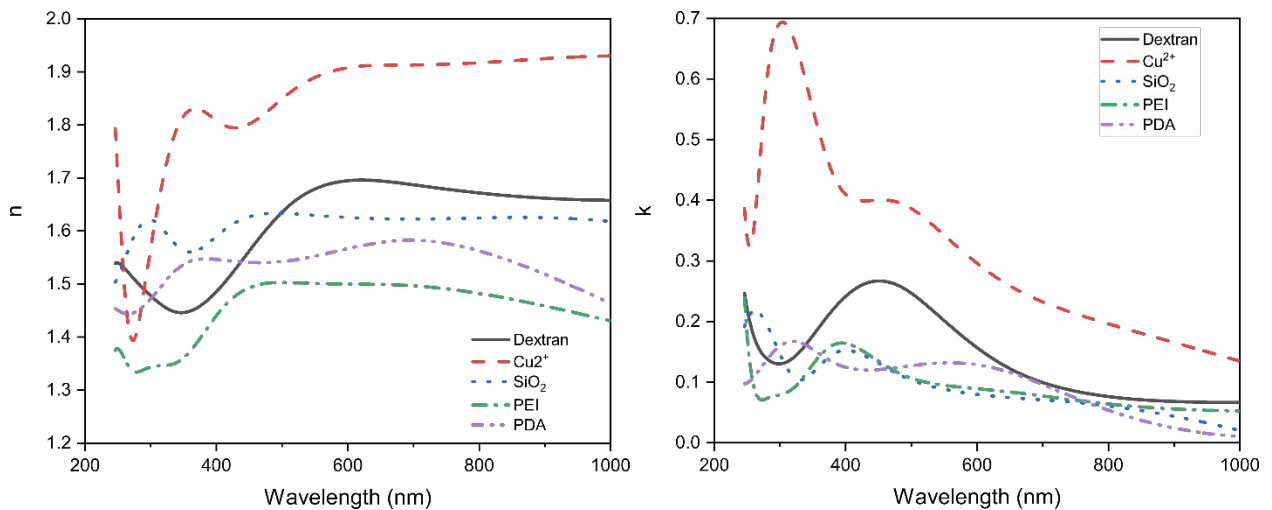


Fig. S8 Optical constants of the layers, obtained from the B-spline model with both thickness and optical constants as free model parameters

In the case of very thin layers (~ few nanometers thick), it is generally recommended to avoid having both optical constants and thickness as free model parameters, as overparametrization is possible. Therefore, for the next modeling approach, we first prepared five sets of coatings

(PDA, PDA-PEI, PDA-SiO₂, PDA-Cu²⁺, PDA-dextran) using 3×2h depositions. Then for each of these thick layers, a b-spline model (resolution 0.6 eV, KK-consistent, $\epsilon_2 > 0$, $n=1.7$, and $k=0.1$ as initial guess) with unknown optical constants and thickness was used. The optical constants were then obtained by modeling where (i) having thickness and optical constants as free model parameters, or (ii) using thickness estimated from AFM (Fig. S9) as an input so only having optical constants as free model parameters. In both routes, a quite similar modeling outcome was found, confirming the reliability of the obtained optical constants. Hereafter, the estimated optical constants for PDA, PDA-PEI, PDA-SiO₂, PDA-Cu²⁺, and PDA-dextran were used as input for the analysis of the multilayer coating data. Therefore, in this case (Fig. S10), fixed optical constants were used, and the thickness of each layer was the free model parameter.

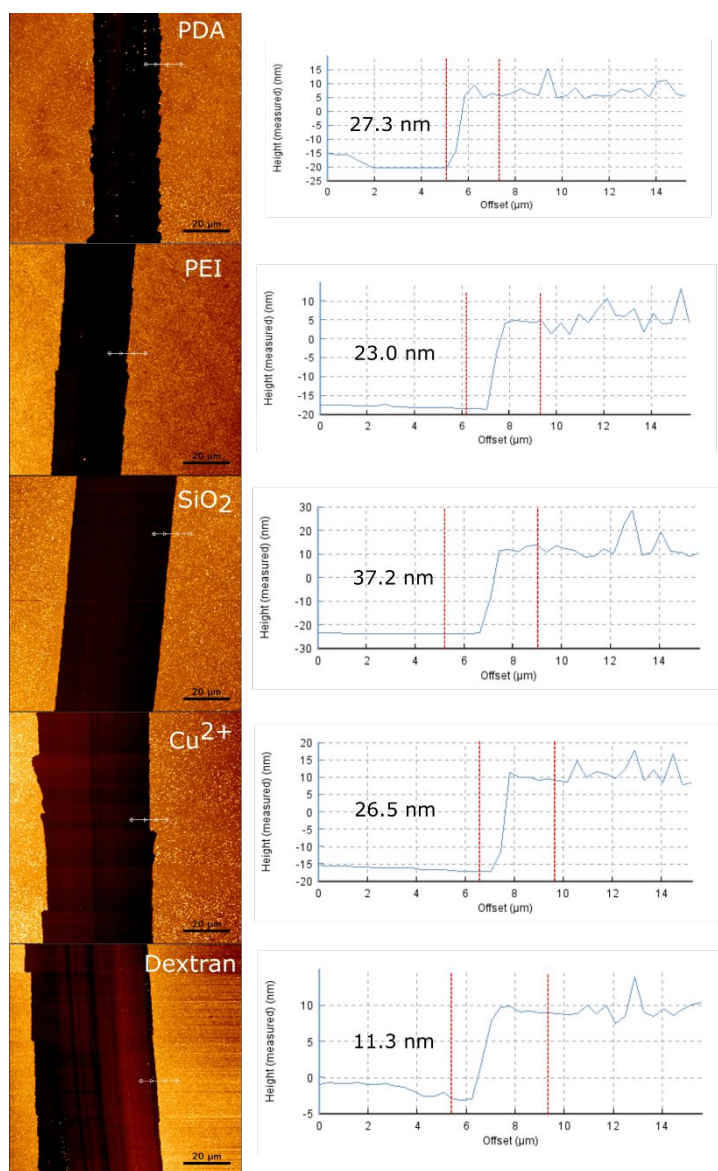


Fig. S9 Representative AFM height images/profiles of the scratched area of PDA, PDA/PEI, PDA/SiO₂, PDA/Cu²⁺, and PDA/dextran films obtained from a LbL deposition for 3 × 2 h.

<p>Fit Results</p> <p>MSE = 56.929</p> <p>Thickness # 7 = 3.76 ± 0.031 nm</p> <p>Total Thickness = 145.13 ± 0.031 nm</p>	<p>Optical Model</p> <table border="1"> <tr> <td>Layer # 7 = Tabulated B-spline-PDA with Dextran</td> <td>Thickness # 7 = 3.76 nm</td> </tr> <tr> <td>Layer # 6 = Tabulated B-spline-PDA with Cu2+</td> <td>Thickness # 6 = 7.43 nm</td> </tr> <tr> <td>Layer # 5 = Tabulated B-spline-PDA with SiO₂</td> <td>Thickness # 5 = 14.47 nm</td> </tr> <tr> <td>Layer # 4 = Tabulated B-spline-PDA with PEI</td> <td>Thickness # 4 = 9.03 nm</td> </tr> <tr> <td>Layer # 3 = Tabulated B-spline-PDA</td> <td>Thickness # 3 = 8.37 nm</td> </tr> <tr> <td>Layer # 2 = SiO₂_JAW</td> <td>Thickness # 2 = 101.06 nm</td> </tr> <tr> <td>Layer # 1 = INTR_JAW</td> <td>Thickness # 1 = 1.00 nm</td> </tr> <tr> <td>Substrate = SI_JAW</td> <td></td> </tr> </table>	Layer # 7 = Tabulated B-spline-PDA with Dextran	Thickness # 7 = 3.76 nm	Layer # 6 = Tabulated B-spline-PDA with Cu2+	Thickness # 6 = 7.43 nm	Layer # 5 = Tabulated B-spline-PDA with SiO₂	Thickness # 5 = 14.47 nm	Layer # 4 = Tabulated B-spline-PDA with PEI	Thickness # 4 = 9.03 nm	Layer # 3 = Tabulated B-spline-PDA	Thickness # 3 = 8.37 nm	Layer # 2 = SiO₂_JAW	Thickness # 2 = 101.06 nm	Layer # 1 = INTR_JAW	Thickness # 1 = 1.00 nm	Substrate = SI_JAW	
Layer # 7 = Tabulated B-spline-PDA with Dextran	Thickness # 7 = 3.76 nm																
Layer # 6 = Tabulated B-spline-PDA with Cu2+	Thickness # 6 = 7.43 nm																
Layer # 5 = Tabulated B-spline-PDA with SiO₂	Thickness # 5 = 14.47 nm																
Layer # 4 = Tabulated B-spline-PDA with PEI	Thickness # 4 = 9.03 nm																
Layer # 3 = Tabulated B-spline-PDA	Thickness # 3 = 8.37 nm																
Layer # 2 = SiO₂_JAW	Thickness # 2 = 101.06 nm																
Layer # 1 = INTR_JAW	Thickness # 1 = 1.00 nm																
Substrate = SI_JAW																	

Fig. S10 Representative AFM height images/profiles of the scratched area of PDA, PDA/PEI, PDA/SiO₂, PDA/Cu²⁺, and PDA/dextran films obtained from LbL deposition for 3×2 h.

Paper III

Making Protein-Based Adhesives Water Resistant: Role of Protein Water Solubility, Galloyl Modification, and Complexation

Saeed Zajforoushan Moghaddam,^{*,†} Runtian Qie,[†] and Esben Thormann^{*}



Cite This: *ACS Appl. Polym. Mater.* 2022, 4, 18–23



Read Online

ACCESS |



Metrics & More

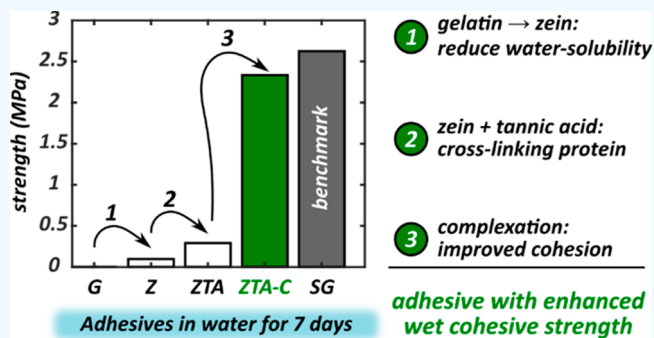


Article Recommendations



Supporting Information

ABSTRACT: There has been an ongoing interest in using proteins as more environmentally friendly substitutes for the existing synthetic adhesives. Poor water resistance is a particular shortcoming of protein-based adhesives, which negatively affects their outdoor functionality. In this study, we systematically investigated if water solubility of the protein, addition of a phenolic compound such as tannic acid, and protein–polyphenol complexation could improve the water resistance of protein-based adhesives. It was found that the synergetic effects of these parameters can yield commercial-level water resistance.



KEYWORDS: protein-based adhesive, biomimetic, water resistance, zein, tannic acid

Independence from petroleum resources and reducing the emission of harmful substances are the major incentives for replacing synthetic adhesives.¹ Biobased materials, e.g., proteins, are vastly investigated as potential substitutes; nevertheless, their “green” footprint rarely justifies their commercialization unless critical shortcomings of such adhesives are resolved.¹ As a major deficiency, protein-based adhesives demonstrate poor water resistance, meaning that the adhesive joint significantly weakens or often fails when exposed to humid or wet environments. Thus, prolonged outdoor durability becomes an issue.² The adsorbed water can induce various physical effects within an adhesive joint, i.e., swelling, plasticization, leaching of the adhesive components, and degradation of the substrate–adhesive interface.³ Hence, mechanisms by which water penetration/uptake within the adhesive is reduced may assist us in developing protein-based adhesives with enhanced water resistance.

Sticky marine creatures, e.g., mussels, have been sources of inspiration for designing adhesives with enhanced wet adhesive properties.^{4–6} The mussel adhesive comprises a complex mixture of several proteins that synergistically render strong underwater adhesion to various organic and inorganic surfaces (Scheme 1, top panel). Their signature amino acid, 3,4-dihydroxyphenyl-L-alanine (Dopa), regulates the interfacial adhesion and internal cohesion of the adhesive plaque through various catechol-mediated interactions such as hydrogen bonding, cation– π , and metal coordination.^{7,8} Moreover, the mussel foot proteins (mfps), in particular mfp-3s, are secreted under controlled pH through which liquid–liquid phase separation and coacervation occur.^{7,9–11} Coacervates, besides having low interfacial energies, show shear-thinning viscosities

that are smaller than those of uncondensed molecules at the same concentration, which thus assist surface wetting.^{7,12} Moreover, the intermolecular interactions within the protein complexes may serve as cross-linking moieties that assist water resistance.

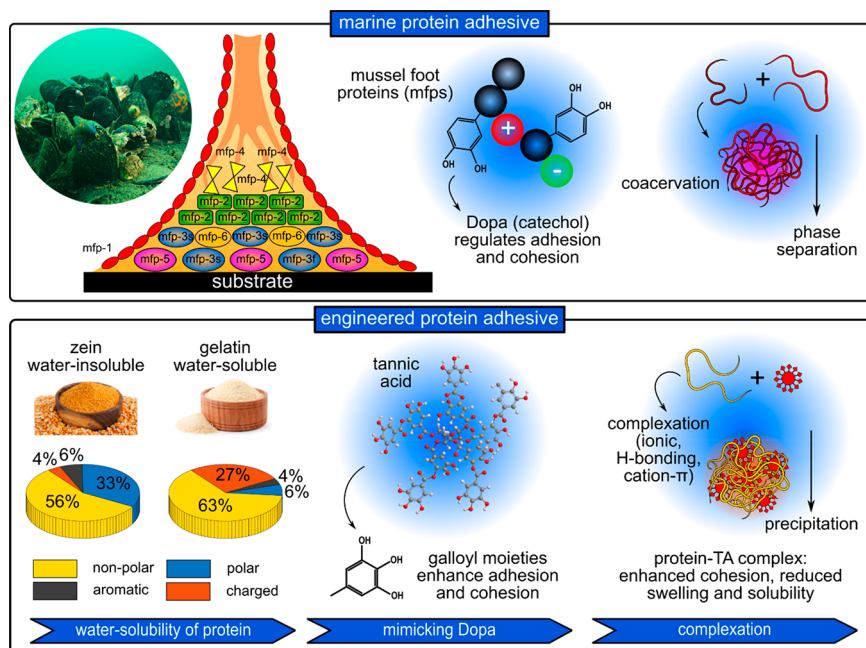
In this study, we systematically investigated the effects of three parameters, i.e., water solubility of the protein, adding a polyphenol, and protein–polyphenol complexation on the water resistance of protein-based adhesives (Scheme 1, bottom panel). The overall hypothesis herein is that water resistance of protein-based adhesives should be notably improved by mechanisms that hinder water penetration/uptake within the adhesive and thus prevent water-induced cohesive failure. By systematic investigation of these three parameters, we aim to achieve commercial-level water resistance (Loctite SuperGlue as the benchmark). Notably, we examined water resistance over short and long exposures to water, which is often neglected in the literature.^{13–16} By doing so, we studied how each parameter could contribute to short- and long-term water resistance and cohesive properties of the adhesive. Gelatin, as a water-soluble protein, and zein from maize, as a water-insoluble protein, were selected. The difference in water solubility arises from the different amino acid compositions of

Received: August 26, 2021

Accepted: December 9, 2021

Published: December 15, 2021



Scheme 1. (Top) Marine Adhesive^a and (Bottom) Engineered Protein Adhesive^b

^aThe mussel adhesive comprises several proteins, known as mussel foot proteins (mfps), each with a specific amino acid composition and position within the adhesive plaque. Mfps found at the interface, i.e., mfp-3 and mfp-5, are rich in Dopa, the catechol moiety of which enables wet adhesion to various substrates, as well as cohesion within the plaque. Besides, the secreted mfps, in particular mfp-3s, undergo coacervation and phase separation producing the adhesive plaque. ^bThree factors are investigated to enhance the water resistance of the engineered protein-based adhesive. Water-soluble gelatin from porcine skin and water-insoluble zein from maize were compared, galloyl-rich tannic acid was added to mimic Dopa (catechol) functionality mainly in terms of enhanced cohesion, and finally, protein–tannic acid complexation was examined.

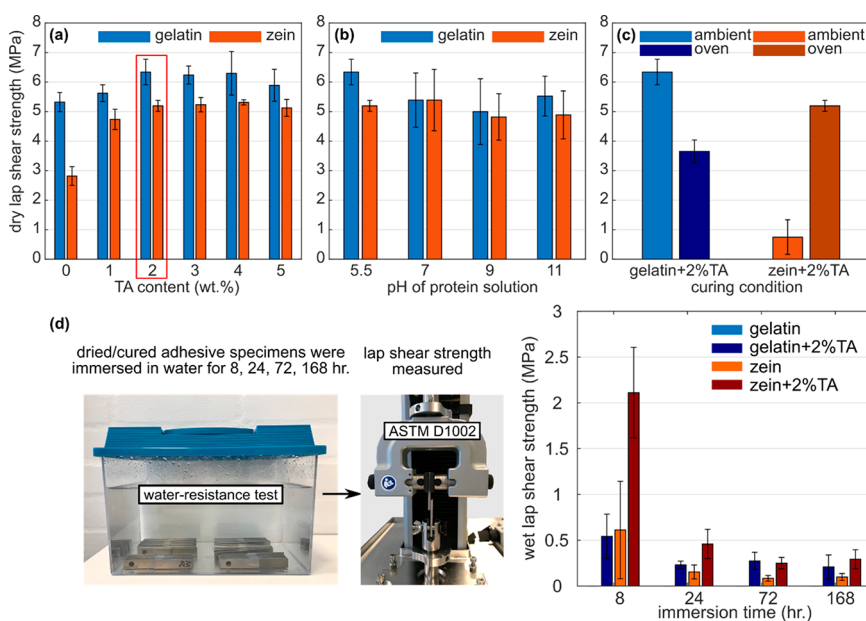


Figure 1. Gelatin- and zein-based adhesives (prepared by solution mixing) with and without tannic acid: (a) dry lap shear strength of zein and gelatin adhesives as a function of tannic acid content; adhesives with 2 wt % tannic acid were chosen for the next tests, (b) effect of pH of the protein solution on dry lap shear strength of zein and gelatin adhesives each containing 2 wt % tannic acid, (c) effect of curing condition (dried in ambient temperature for 48 h. or in the oven at 120° for 24 h) on dry lap shear strength of zein and gelatin adhesives each with 2 wt % tannic acid, and (d) water resistance (wet lap shear strength) of the adhesives tested as a function of immersion time ($n = 5$).

the two proteins (Scheme 1, bottom).¹⁷ Next, we investigated if marine-inspired adhesion mechanisms can enhance the water resistance of protein adhesives. From the various approaches to mimic the chemistry of Dopa,^{18–20} we chose tannic acid as a water-soluble plant phenolic that is rich in galloyl moieties, so

can mimic the interactions of the catechol group.²¹ Finally, we studied if incorporating tannic acid into the protein-based adhesive through complexation could further enhance the water resistance. Detailed information on experimental

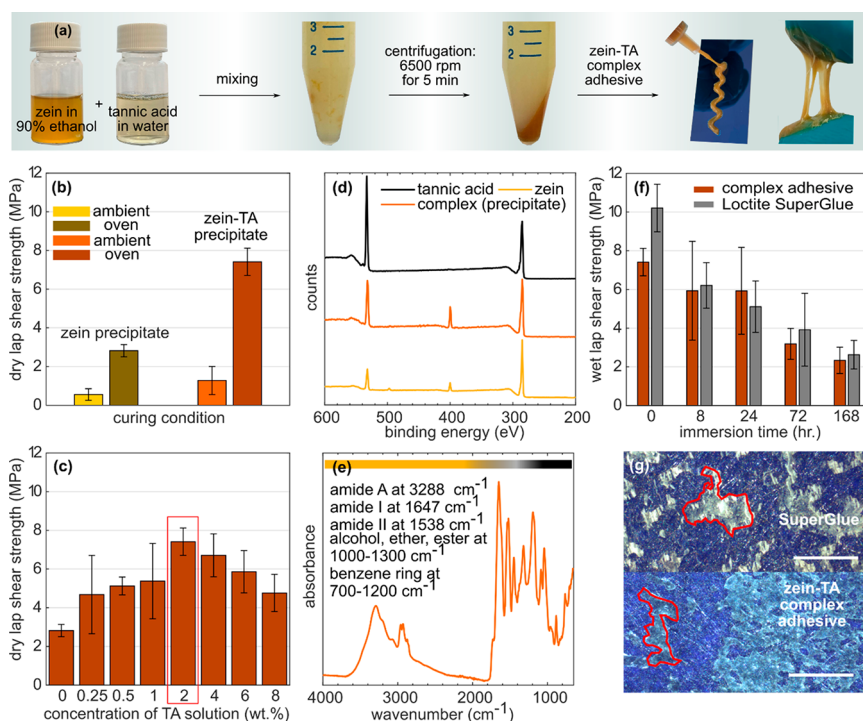


Figure 2. (a) Summary of the preparation route of zein–tannic acid complex adhesive, (b) effect of thermal curing on dry lap shear strength of complex zein adhesives with and without tannic acid, (c) effect of tannic acid concentration in the precursor solution on the dry lap shear strength of zein–tannic acid complex adhesives, (d) XPS spectra of zein, tannic acid, and zein–TA complex, (e) FTIR spectrum of the zein–TA complex, (f) dry and wet lap shear strength of the zein–tannic acid complex adhesive and Loctite SuperGlue ($n = 5$), and (g) polarized microscopy images of SuperGlue and the zein–TA complex adhesive after testing the shear strength. The adhesive residues are highlighted in red on the images, scale bars are 500 μm .

procedures is provided as Supporting Information (Section S1).

Figure 1 displays the lap shear strength of zein and gelatin adhesives (dry and wet), with and without tannic acid. Herein, tannic acid is dissolved together with the protein in the solvent (demineralized water for gelatin, 90% ethanol/water mixture for zein), and the final solution is used as the adhesive. Regarding pure protein adhesives, gelatin demonstrated a much larger lap shear strength, which can be attributed to the stronger mechanical properties of the protein film.^{22–25} The tannic acid content, in each case, was then optimized (Figure 1a). For both proteins, the dry adhesive shear strength increases by the addition of tannic acid up to a content of 2 wt %, after which a plateau is found. Tannic acid not only can promote the interfacial adhesion to aluminum through galloyl–substrate interactions (e.g., hydrogen bonding and metal coordination), it can also noncovalently (e.g., hydrogen bonding and cation– π) and covalently (amine–quinone reactions via Michael-type addition or Schiff base) cross-link the proteins and thus reinforce the cohesive properties. The overall effect of tannic acid (2 wt %) is more pronounced on zein (2.8 MPa \rightarrow 5.2 MPa) compared to gelatin (5.3 MPa \rightarrow 6.3 MPa). This observation can suggest that the effect of tannic acid on the cohesive properties (i.e., through cross-linking) of the adhesives is more crucial to the lap shear strength. Notably, we did not observe any significant correlation between the pH of the protein solution and the adhesives' lap shear strength (Figure 1b). In particular, Schmidt et al. have reported considerably larger adhesive strength (at least 4-fold) at pH 7 compared to other pH values, which was attributed to the presence of both nonoxidized and oxidized galloyl forms and

their effects on the interfacial adhesion and cohesion.¹³ Our observation herein though may suggest that tannic acid improves chiefly the cohesive properties of the adhesive through cross-linking, rather than tuning the interfacial adhesion. Drying/curing condition is another important factor that was optimized before testing the water resistance of adhesives. As shown in Figure 1c, the zein-based adhesive requires thermal curing to achieve a maximal lap shear strength, as previously reported.¹³ Thermal curing can produce both oxidative cross-linking of tannic acid,¹³ as well as self-cross-linking of zein.^{23,24} Both of these effects can enhance the mechanical and cohesive strength of the adhesive. Contrarily, thermal curing of the gelatin adhesive resulted in a reduction in the adhesive strength, which may be attributed to the formation of bubbles/foaming when the adhesive solvent evaporates.

Next, the water resistance of zein and gelatin adhesives, without and with 2 wt % tannic acid was examined by immersing the specimens in demineralized water for different times before testing the adhesive strength (Figure 1d). The pure gelatin adhesive demonstrated no water resistance, i.e., the adhesive joint broke apart after only 8 h immersion. Pure zein, in contrast, showed a relatively stronger water resistance, i.e., lap shear strength \sim 0.6 MPa after 8 h. immersion. The zein adhesive could also endure longer immersion times; nevertheless, the adhesive shear strength was significantly reduced. Water-insoluble zein, compared to gelatin, provides improved barrier properties against water penetration within the adhesive, which can thus impede cohesive failure. Such an effect appears to be efficient chiefly for short immersion times though. Therefore, while water insolubility of the protein can

assist water resistance, it cannot merely ensure prolonged durability of the adhesive joint.

Tannic acid was found to improve the water resistance of both protein adhesives. Gelatin–tannic acid adhesive maintained a lap shear strength ~ 0.5 MPa after 8 h immersion and could sustain the 1-week immersion. Zein–tannic acid adhesive also demonstrated improved adhesive shear strength compared to the pure zein adhesive. Nevertheless, the effect of tannic acid was more pronounced for short immersion times, whereas the protein adhesives with and without tannic acid performed nearly comparable when immersed in water for 1 week. Overall, our results suggest that tannic acid can improve the water resistance of protein adhesives, though the effect is more limited to short immersion times. Accordingly, it can be inferred that tannic acid improves water resistance mainly through cross-linking/cohesive reinforcement of the proteins, which is also supported by our water contact angle and swelling studies on zein and gelatin films (Supporting Information, Section S2).

Next, we investigated if protein–tannic acid complexation can enhance the water resistance of the adhesives. This means that the adhesive is prepared by mixing the solutions of protein and tannic acid, whereupon the adhesive (protein–tannic acid complex) is collected as a precipitated phase. Tannic acid can undergo complexation with different macromolecules through various interactions.^{26,27} The proximity of multiple hydroxyl groups assists deprotonation and thus renders tannic acid a partial negative charge that enables complexation with the basic residues on proteins.²⁶ The hydroxyl groups of the galloyl moieties are also able to form hydrogen bonds with the hydrogen bond accepting residues on the protein.²⁶ Finally, the galloyl units may also promote complexation through cation– π and hydrophobic interactions, as suggested for self-coacervation of like-charged mussel adhesive proteins.²⁸ Therefore, protein–tannic acid complexation is expected to provide multiple sources of cohesiveness, reduce water solubility/uptake of the adhesive, and thus enhance the water resistance. We examined this approach for both gelatin and zein proteins. The gelatin–tannic acid complex demonstrated limited wetting properties, which made it impractical to be applied onto the substrates at room temperature (probably due to the temperature responsiveness of gelatin), and thus was excluded from the adhesion testing.

Two approaches were examined to prepare the zein–tannic acid complex adhesives (Supporting Information, Section S3). It was found that precipitation of zein through decreasing the ethanol content of the solvent while simultaneously adding tannic acid (Figure 2a) provided an adhesive with favorable wetting properties and stronger dry bonding strength. Figure 2b shows the effect of the curing condition on the dry strength of the adhesives prepared through precipitation (complexation). For pure zein (precipitated by adding water, without tannic acid), thermal curing increased the dry lap shear strength from ~ 0.5 MPa to ~ 3.0 MPa. This indicates again that pure zein adhesive, when thermally treated, undergoes self-cross-linking and thus renders stronger cohesive strength. For zein–tannic acid complex (tannic acid solution added to zein solution), thermal curing has an even larger effect (~ 1.0 to ~ 7.5 MPa), which indicates that oxidative cross-linking of tannic acid has a significant contribution to the adhesive cohesive strength. It was also found that the concentration of tannic acid in the precursor solution (Figure 2c) affects the dry adhesive strength, which could be attributed to the differences

in the composition and physical properties of the complexes (Supporting Information, Section S3). The precipitated zein–tannic acid complex (made from 2 wt % tannic acid solution) was analyzed using XPS and FTIR (Figure 2d,e), confirming the presence of both zein and tannic acid. The XPS spectrum of the precipitate indicated traces of nitrogen, which affirms the presence of protein in the complex. The FTIR spectrum of the precipitate also demonstrated the characteristic peaks of amide bonds of the protein together with the benzene ring peaks of tannic acid. Considering the extremely low content of the basic amino acids in zein, i.e., one lysine, three arginine, and one histidine out of 240 units in total (for 19 kDa α -zein),²⁹ the main source of complexation between zein and tannic acid is speculated to be through hydrogen bonding (possibly through the amine moiety of 11 asparagine and 43 glutamine residues), as well as hydrophobic interactions (π – π interactions with phenylalanine and tyrosine residues).

Next, the water resistance of the complex adhesive was benchmarked against a commercial water-resistant adhesive (Figure 2f). As shown, the overall water resistance of the complex protein adhesive emulates the commercial adhesive. After 7 days of immersion in water, both zein–tannic acid complex adhesive and commercial SuperGlue demonstrated a wet lap shear strength of ~ 3.0 MPa. In both cases, as shown from microscopy images of the tested adhesive joints (Figure 2g), a combination of adhesive and cohesive failures was found. Regarding the protein adhesive, this observation suggests favorable wet interfacial adhesion as well as cohesiveness within the adhesive, so the adhesive did not fail solely cohesively or adhesively.

In conclusion, the results indicate that the combination of the three parameters studied herein can provide enhanced water resistance (for 1-week exposure to water) similar to that of a water-resistant commercial adhesive. Using a water-insoluble protein, such as zein, can reduce the water penetration (as well as the subsequent effects on the adhesive such as swelling, plasticization, and leaching) within the adhesive joint, which turned out to be effective but not efficient for prolonged durability. Adding a Dopa-mimetic compound, i.e., tannic acid, can strengthen the adhesive–substrate bonding but, more importantly, the cohesiveness of the adhesive joint when exposed to water (due to covalent and noncovalent cross-linking). Yet, this factor also did not provide long-term water resistance. Finally, the complexation of zein with tannic acid rendered an adhesive with the highest water resistance. Herein, we have synergetic contributions from protein water insolubility, galloyl-mediated adhesion and cohesion improvements, and superior wet-adhesive properties of the precipitated complex adhesive (larger dry matter content, favorable wetting properties, and enhanced cohesiveness due to zein–tannic acid interactions).

Overall, the zein–TA complex adhesive is a promising biobased adhesive for future studies. A few recent studies have revealed the potentials of zein adhesives,^{13,21,30} yet we suggest that further studies on zein complexation with an emphasis on adhesive water resistance are necessary. A deeper understanding of how different parameters such as the concentration of the components, solvent composition, and mixing ratios can affect the microstructure and physicochemical properties of the complex, followed by studies on how these properties correlate to the adhesive properties (viscosity, mechanical properties, bonding strength, and water resistance) can facilitate the

development of commercially competitive zein-based adhesives.

■ ASSOCIATED CONTENT

SI Supporting Information

The Supporting Information is available free of charge at <https://pubs.acs.org/doi/10.1021/acsapm.1c01089>.

Section S1, materials and methods, with a description of adhesives preparation procedures and testing methods; Section S2, water contact angle and swelling study of zein and gelatin films; Section S3, optimization of the adhesive strength of zein–tannic acid complex adhesive; and Section S4, significance test for water-resistance data (short and long exposures) (PDF)

■ AUTHOR INFORMATION

Corresponding Authors

Saeed Zajforoushan Moghaddam – Department of Chemistry, Technical University of Denmark, 2800 Kgs. Lyngby, Denmark; orcid.org/0000-0002-6536-7490; Email: saza@kemi.dtu.dk

Esben Thormann – Department of Chemistry, Technical University of Denmark, 2800 Kgs. Lyngby, Denmark; orcid.org/0000-0002-2364-3493; Email: esth@kemi.dtu.dk

Author

Runtian Qie – Department of Chemistry, Technical University of Denmark, 2800 Kgs. Lyngby, Denmark

Complete contact information is available at: <https://pubs.acs.org/doi/10.1021/acsapm.1c01089>

Author Contributions

†S.Z.M. and R.Q. have equally contributed to this study.

Notes

The authors declare no competing financial interest.

■ REFERENCES

- Heinrich, L. A. Future Opportunities for Bio-Based Adhesives - Advantages beyond Renewability. *Green Chem.* **2019**, *21* (8), 1866–1888.
- Frihart, C. R.; Lorenz, L. F. Protein Adhesives. In *Handbook of Adhesive Technology*, 3rd ed.; CRC Press: 2017; pp 145–176. DOI: [10.1201/9781315120942](https://doi.org/10.1201/9781315120942).
- Weitzenböck, J. R. *Adhesives in Marine Engineering*; 2012; DOI: [10.1533/9780857096159](https://doi.org/10.1533/9780857096159).
- Hofman, A. H.; van Hees, I. A.; Yang, J.; Kamperman, M. Bioinspired Underwater Adhesives by Using the Supramolecular Toolbox. *Adv. Mater.* **2018**, *30* (19), 1704640.
- Kord Forooshani, P.; Lee, B. P. Recent Approaches in Designing Bioadhesive Materials Inspired by Mussel Adhesive Protein. *J. Polym. Sci., Part A: Polym. Chem.* **2017**, *55* (1), 9–33.
- Wang, X.; Si, Y.; Zheng, K.; Guo, X.; Wang, J.; Xu, Y. Mussel-Inspired Tough Double Network Hydrogel As Transparent Adhesive. *ACS Appl. Polym. Mater.* **2019**, *1* (11), 2998–3007.
- Waite, J. H. Mussel Adhesion - Essential Footwork. *J. Exp. Biol.* **2017**, *220* (4), 517–530.
- Li, Y.; Cheng, J.; Delparastan, P.; Wang, H.; Sigg, S. J.; DeFrates, K. G.; Cao, Y.; Messersmith, P. B. Molecular Design Principles of Lysine-DOPA Wet Adhesion. *Nat. Commun.* **2020**, *11* (1), 3895.
- Petrone, L.; Kumar, A.; Sutanto, C. N.; Patil, N. J.; Kannan, S.; Palaniappan, A.; Amini, S.; Zappone, B.; Verma, C.; Miserez, A. Mussel Adhesion Is Dictated by Time-Regulated Secretion and Molecular Conformation of Mussel Adhesive Proteins. *Nat. Commun.* **2015**, *6* (1), 8737.
- Wei, W.; Tan, Y.; Martinez Rodriguez, N. R.; Yu, J.; Israelachvili, J. N.; Waite, J. H. A Mussel-Derived One Component Adhesive Coacervate. *Acta Biomater.* **2014**, *10* (4), 1663–1670.
- Priemel, T.; Degtyar, E.; Dean, M. N.; Harrington, M. J. Rapid Self-Assembly of Complex Biomolecular Architectures during Mussel Byssus Biofabrication. *Nat. Commun.* **2017**, *8* (1), 14539.
- Kim, S.; Huang, J.; Lee, Y.; Dutta, S.; Yoo, H. Y.; Jung, Y. M.; Jho, Y.; Zeng, H.; Hwang, D. S. Complexation and Coacervation of Like-Charged Polyelectrolytes Inspired by Mussels. *Proc. Natl. Acad. Sci. U. S. A.* **2016**, *113* (7), E847–E853.
- Schmidt, G.; Woods, J. T.; Fung, L. X. B.; Gilpin, C. J.; Hamaker, B. R.; Wilker, J. J. Strong Adhesives from Corn Protein and Tannic Acid. *Adv. Sustain. Syst.* **2019**, *3* (12), 1900077.
- Zhu, X.; Song, C.; Sun, X.; Wang, D.; Cai, D.; Wang, Z.; Chen, Y.; Chen, X. Improved Water Resistance of TA-Modified Soy Adhesive: Effect of Complexation. *Int. J. Adhes. Adhes.* **2021**, *108*, 102858.
- Ghahri, S.; Mohebbi, B.; Pizzi, A.; Mirshokraie, A.; Mansouri, H. R. Improving Water Resistance of Soy-Based Adhesive by Vegetable Tannin. *J. Polym. Environ.* **2018**, *26* (5), 1881–1890.
- Wang, X.; Zhu, J.; Liu, X.; Zhang, H. J.; Zhu, X. Novel Gelatin-Based Eco-Friendly Adhesive with a Hyperbranched Cross-Linked Structure. *Ind. Eng. Chem. Res.* **2020**, *59* (13), 5500–5511.
- Padua, G. W.; Guardiola, L. V. Microcapsules Produced from Zein. In *Microencapsulation and Microspheres for Food Applications*; Elsevier, 2015; pp 3–20; DOI: [10.1016/B978-0-12-800350-3.00002-9](https://doi.org/10.1016/B978-0-12-800350-3.00002-9).
- Liu, Y.; Cheong NG, S.; Yu, J.; Tsai, W.-B. Modification and Crosslinking of Gelatin-Based Biomaterials as Tissue Adhesives. *Colloids Surf., B* **2019**, *174*, 316–323.
- Mo, J.; Wang, F.; Xu, Z.; Feng, C.; Fang, Y.; Tang, X.; Shen, X. Characterization and Performance of Soybean Protein Modified by Tyrosinase. *Int. J. Adhes. Adhes.* **2019**, *92*, 111–118.
- Wang, Z.; Zhao, S.; Song, R.; Zhang, W.; Zhang, S.; Li, J. The Synergy between Natural Polyphenol-Inspired Catechol Moieties and Plant Protein-Derived Bio-Adhesive Enhances the Wet Bonding Strength. *Sci. Rep.* **2017**, *7* (1), 9664.
- Schmidt, G.; Hamaker, B. R.; Wilker, J. J. High Strength Adhesives from Catechol Cross-Linking of Zein Protein and Plant Phenolics. *Adv. Sustain. Syst.* **2018**, *2* (3), 1700159.
- Kosaraju, S. L.; Puvanenthiran, A.; Lillford, P. Naturally Crosslinked Gelatin Gels with Modified Material Properties. *Food Res. Int.* **2010**, *43* (10), 2385–2389.
- Sun, C.; Dai, L.; He, X.; Liu, F.; Yuan, F.; Gao, Y. Effect of Heat Treatment on Physical, Structural, Thermal and Morphological Characteristics of Zein in Ethanol-Water Solution. *Food Hydrocolloids* **2016**, *58*, 11–19.
- Bisharat, L.; Berardi, A.; Perinelli, D. R.; Bonacucina, G.; Casettari, L.; Cespi, M.; Alkhatib, H. S.; Palmieri, G. F. Aggregation of Zein in Aqueous Ethanol Dispersions: Effect on Cast Film Properties. *Int. J. Biol. Macromol.* **2018**, *106*, 360–368.
- Ku, K.; Song, K. B. Physical Properties of Nisin-Incorporated Gelatin and Corn Zein Films and Antimicrobial Activity against *Listeria Monocytogenes*. *J. Microbiol. Biotechnol.* **2007**, *17* (3), 520–523.
- Shutava, T.; Prouty, M.; Kommireddy, D.; Lvov, Y. PH Responsive Decomposable Layer-by-Layer Nanofilms and Capsules on the Basis of Tannic Acid. *Macromolecules* **2005**, *38* (7), 2850–2858.
- Lee, D.; Hwang, H.; Kim, J. S.; Park, J.; Youn, D.; Kim, D.; Hahn, J.; Seo, M.; Lee, H. VATA: A Poly(Vinyl Alcohol)- And Tannic Acid-Based Nontoxic Underwater Adhesive. *ACS Appl. Mater. Interfaces* **2020**, *12* (18), 20933–20941.
- Kim, H. J.; Yang, B.; Park, T. Y.; Lim, S.; Cha, H. J. Complex Coacervates Based on Recombinant Mussel Adhesive Proteins: Their Characterization and Applications. *Soft Matter* **2017**, *13* (42), 7704–7716.

- (29) Shukla, R.; Cheryan, M. Zein: The Industrial Protein from Corn. *Ind. Crops Prod.* **2001**, *13* (3), 171–192.
- (30) Wei, Y.; Yao, J.; Shao, Z.; Chen, X. Water-Resistant Zein-Based Adhesives. *ACS Sustainable Chem. Eng.* **2020**, *8* (20), 7668–7679.

Supporting Information

Making Protein-based Adhesives Water-resistant: Role of Protein Water-solubility, Galloyl Modification, and Complexation

Saeed Zajforoushan Moghaddam, Runtian Qie, and Esben Thormann**

*Department of Chemistry, Technical University of Denmark, 2800 Kgs. Lyngby,
Denmark*

Correspondence can be addressed to S. Z. M. (email: saza@kemi.dtu.dk) or E. T. (esth@kemi.dtu.dk).

S1 Experimental Section

Materials: Zein from maize, gelatin from porcine skin (gel strength ~175 g Bloom, Type A), tannic acid (ACS reagent), and ethanol absolute were purchased from Sigma Aldrich. Demineralized water was used in the preparation of all the samples. Whenever needed, the pH of the solutions was adjusted using 1M NaOH and HCl solutions.

Preparation of the adhesives: For pure gelatin adhesive (GTA-0), 5 g gelatin was dissolved in 20 g warm water (20 wt. % dry content, 65 °C) and gently stirred (to avoid bubbles) for 2 hr., yielding a light-yellow solution of mediocre viscosity. For gelatin–tannic acid formulation (GTA-2), first, 4.9 g gelatin was dissolved in 15 g lukewarm water for 1 hr., after which tannic acid solution (0.1 g dissolved in 5 gr water) was dropwise added to the gelatin solution and left stirring for 1 hr. The final solution had a light-brown color and was found to be slightly more viscous than the pure gelatin solution. **Curing:** the adhesive joints were dried at ambient temperature for 48 hr. Specimens were stored in a desiccator for 12 hr. before testing.

For pure zein adhesive (ZTA-0), 5 g zein powder was added to 6 g aqueous ethanol solution (90 v/v % ethanol) and mixed for 4 hr. using a vortex mixer, yielding a dark amber solution of high viscosity. For zein–tannic acid formulation (ZTA-2), first, 4.9 g zein was dissolved in 6 g aqueous ethanol for 2 hr., after which 0.1 g tannic acid powder was added to the mixture and mixed further for 2hr. The color and consistency of the adhesive were relatively similar to the pure zein adhesive. **Curing:** the adhesive joints were dried at ambient temperature for 1 hr., after which cured at 120 °C for 24 hr. Specimens were stored in a desiccator for 12 hr. before testing.

For zein–tannic acid complex adhesive, 5 g zein was dissolved in 75 g of 90% ethanol solution and stirred for 2 hr. 2 g tannic acid was dissolved in 98 g water and then mixed with zein solution in a 1:1.25 volume ratio in centrifuge tubes. The coacervate phase (dark orange color) was separated by centrifugation (6500 rpm, 5 min). **Curing:** the adhesive joints were dried at ambient temperature for 1 hr., after which cured at 120 °C for 24 hr. Specimens were stored in a desiccator for 12 hr. before testing.

Adhesive testing: single-lap shear test (Instron 345c, 2 kN load cell) was conducted according to modified ASTM D1002 standard. Single-lap aluminum joints were prepared with an overlap area of 1.2 cm × 1.2 cm. The aluminum substrates were polished and degreased before applying the adhesives (water contact angle before and after surface cleaning: 69° and 53°). To test water-resistance, the specimens were immersed in demineralized water for a certain duration (i.e., 8, 24, 72, and 168 hr.), after which the adhesive shear strength was immediately measured. For each experiment, five specimens were tested (n=5).

Chemical characterization: Fourier transform infrared (FTIR) spectroscopy (PerkinElmer, Spectrum 100) analysis was carried out on the zein, tannic acid, and zein–tannic acid precipitate (powder samples) over the wavenumber region of 600–4000 cm⁻¹. The elemental composition of the samples was examined by X-ray photoelectron spectroscopy (XPS, Nexsa, Thermo Fisher Scientific, USA) equipped with Al K α as the radiation source and data analysis was conducted using Advantage software.

S2 Water Contact Angle and Swelling Experiment

We compared the surface hydrophilicity and water uptake of zein and gelatin films, with and without tannic acid (corresponding to the adhesive samples discussed in Figure 1), the results of which are shown in Figure S1 and Table S1.

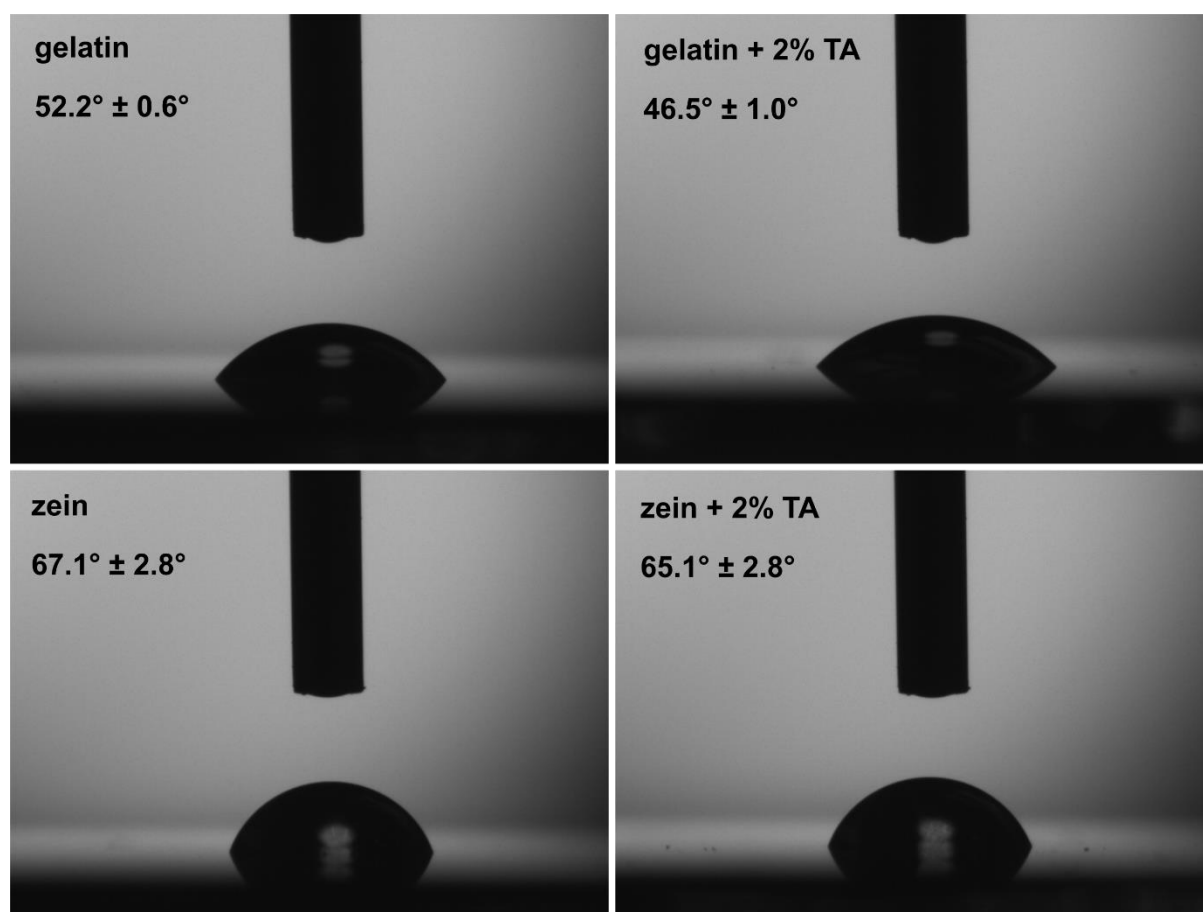


Figure S1 Water contact angle of zein and gelatin films with and without tannic acid (aqueous solutions were spin-coated on silica wafer to prepare the samples.)

As discussed in relation to Figure 1, adding tannic acid could improve the water-resistance of both zein and gelatin adhesives, specifically for short immersions. Herein, we conducted a water contact angle study to see if adding 2 wt.% tannic acid to zein and gelatin affects the surface hydrophilicity of the films. As shown in Figure 1, pure zein is more hydrophobic than pure gelatin as expected based on its more nonpolar and less charged amino acid composition. The addition of tannic acid to each

protein, however, did not affect the surface hydrophilicity in a significant manner. Indeed, a small decrement in the contact angles is observed that may suggest the presence of the hydroxyl groups of tannic acid at the film surface. Therefore, the improved water-resistance of the adhesives containing TA cannot be attributed to the variations in the surface hydrophilicity of the protein films.

To further test the interaction of the protein films with water, dried free-standing films of zein and gelatin, with and without tannic acid, were immersed in water for 24 hr. to see how much water they can adsorb, and how much of the films dissolve. As shown in Table S1, the water uptake data are in good agreement with the trends of water-resistance (Figure 1).

Table S1 Swelling data for zein and gelatin films, with and without tannic acid

sample	initial dry weight (mg)	hydrated weight (mg)	dried weight after swelling test (mg)
gelatin	67.6	x	x
	47.7	x	x
	75.3	x	x
gelatin + 2% TA	82.2	x	x
	76.3	x	x
	67.8	x	x
zein	54.5	139.3	49.5
	56.8	149.2	51.2
	58.2	153.9	51.3
zein + 2% TA	79.1	184.1	72.2
	82.2	174.3	74.6
	59.4	133.4	53.6

Pure gelatin films, after 24 hr. immersion in water, were mostly dissolved. Therefore, it was not possible to weigh the hydrated samples. Adding tannic acid to gelatin partly improved the stability of the films. Herein, the films were highly swollen but still disintegrated into pieces, so it was again not possible to weigh the hydrated samples.

But based on visual inspection, it could be inferred that adding tannic acid improved the stability of the film (due to cross-linking). Zein films, in contrast, showed excellent stability in water. Pure zein films showed an average swelling ratio of ~1.6 and undissolved matter content of ~90%. Adding tannic acid to zein cross-links the protein as confirmed by a reduced average swelling ratio of ~1.2, while the undissolved matter content remained nearly the same (~90%). Therefore, the overall water-resistance trends observed in Figure 1 can be mainly attributed to the cohesive properties of the hydrated protein films.

S3 Zein–Tannic Acid Complexation

Solubility of zein in aqueous ethanol solutions is represented by the ternary phase diagram in Figure S2.^{1,2} Accordingly, for a zein solution, decreasing the ethanol content should produce a phase transition from solution state to coacervation and precipitation.

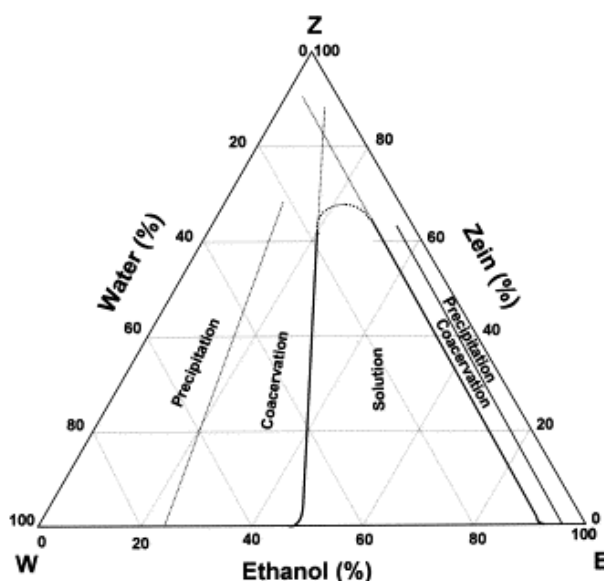


Figure S2 Ternary phase diagram for zein solubility in aqueous ethanol solutions (reprinted with permission from reference²)

We, accordingly, have examined two approaches for preparing the zein–tannic acid complex adhesives:

1. Both zein and tannic acid were dissolved in 90% aqueous ethanol solutions, whereupon the solutions were mixed, and the precipitated complex was collected using centrifugation. In this case, the precipitation is caused solely by zein and tannic acid interactions.
2. Zein was dissolved in 90% aqueous ethanol solution, whereas tannic acid was dissolved in demineralized water. The solutions were then mixed, so the final ethanol

content in the solvent will be ~40%. In this case, precipitation is caused by zein and tannic acid interactions, as well as the water-induced phase separation (precipitation) of zein when ethanol content is reduced from 90% to 40%.

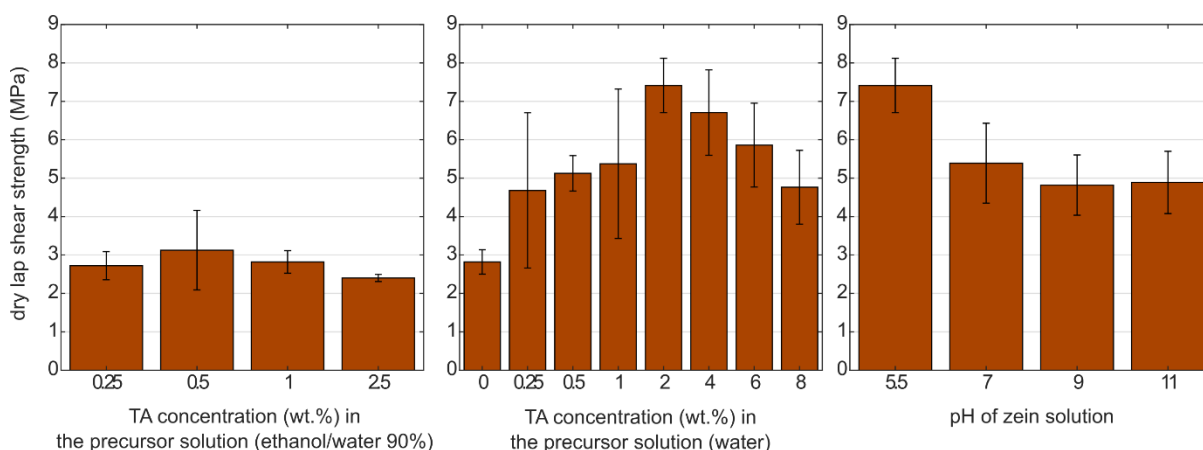


Figure S3 Dry adhesive shear strength of zein complex adhesives made from (left) zein and tannic both dissolved in 90% aqueous ethanol solutions (precipitation due to zein–tannic acid interactions), (middle) zein dissolved in 90% aqueous ethanol solution, and tannic acid dissolved in demineralized water (precipitation due to zein–tannic acid interactions as well as water-induced phase separation of zein); the concentration of tannic acid in the precursor solution was systematically varied to study the effect of zein/tannic ratio on the adhesive properties, (right) effect of pH of zein solution on dry lap shear adhesive of zein–tannic acid complex adhesive (made by mixing zein in ethanol/water 90% with 2 wt.% tannic acid in water).

Comparing the two precipitated systems, clear differences in the physical properties were observed. In particular, the former was found to be more “granular” and discontinuous, which was also less practical to be applied onto substrates as an adhesive. Conversely, the latter precipitate was more “glue-like”, uniform, and convenient to be applied onto substrates. Aside from the physical appearance, we also examined the adhesive properties of the two precipitates (Figure S3). In each case, the concentration of tannic acid was systematically varied to see if zein–tannic acid ratio has any impact on the adhesive strength. Regarding the first precipitate, a

dry lap shear strength of ~ 2.5 MPa was found, regardless of the zein–tannic acid ratio. The lower adhesive properties herein may be attributed to the unfavorable wetting properties of the precipitate. In contrast, the second precipitate adhesive demonstrated notably larger adhesive shear strength values that appeared to depend on zein–tannic acid ratio as well. The relatively larger adhesive strength herein may be attributed to the favorable wetting properties of the precipitate adhesive. Several factors can be responsible for the observed dependence of the adhesive strength to the zein/tannic acid ratio. First, the consistency of the precipitate significantly depended on the ratio of the components, where it was observed that higher tannic acid contents made the adhesive spreading/application less convenient (unfavorable wetting). Moreover, the composition of the precipitates was studied using XPS, the results of which are summarized in Table S2. Based on the detected nitrogen content, it appears that the amount of tannic acid in the complex increases with the ratio of tannic acid–zein, which can affect the interfacial adhesion and cohesive properties of the adhesives.

Table S2 XPS elemental composition of pure zein, pure tannic acid, and zein–tannic acid precipitates of various zein–tannic acid ratios (obtained using the second complexation approach)

	C	O	N
zein	80.34	13.02	6.64
0.25%	68.30	18.04	13.66
0.5%	69.73	18.53	11.74
1%	69.88	19.35	10.77
2%	68.15	20.22	11.63
4%	68.22	24.83	6.95
6%	67.43	25.17	7.40
8%	68.23	28.14	3.63
tannic acid	66.69	33.31	0

We also studied if the pH of zein solution can affect the lap shear strength of zein–tannic acid complex adhesive (Figure S3). It appears that pH may also affect the complexation and adhesive properties, in particular at lower pH values.

S4 Significance Test (paired-sample t-test) for Water-resistance Data

Four protein-based adhesives that showed water-resistance (did not fall apart after water immersion) were analyzed herein. Data for 8 hr. and 168 hr. immersions were selected as representative conditions for short-term and long-term exposures to water, respectively.

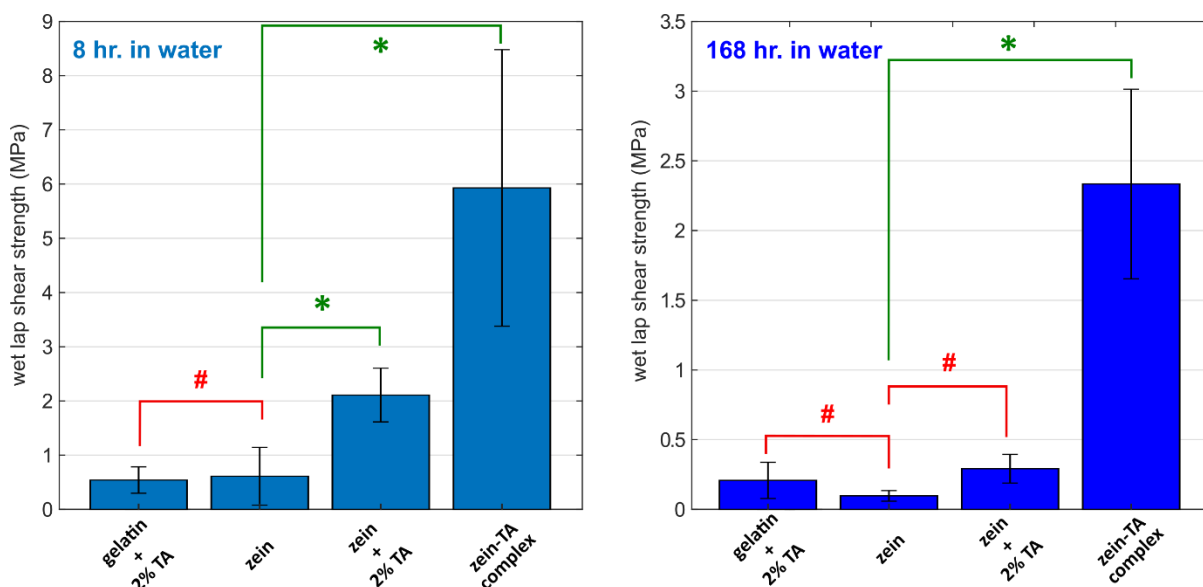


Figure S4 Wet lap shear strength data of protein-based adhesives studied herein; (left) 8 hr. immersion data representing short-term exposure to water, (right) 168 hr. immersion data representing long-term exposure to water. (paired-sample t-test: significance level 1%, # non-significant, *significant)

References

- (1) Shukla, R.; Cheryan, M. Zein: The Industrial Protein from Corn. *Ind. Crops Prod.* **2001**, *13* (3), 171–192.
[https://doi.org/10.1016/S0926-6690\(00\)00064-9](https://doi.org/10.1016/S0926-6690(00)00064-9).
- (2) Mosse, J. Monographie Sur Une Protéine Du Mais: La Zéine. *Ann. Physiol. Veg* **1961**, *3*, 105–139.

Paper IV



ChemComm

**A Self-Curable Underwater Adhesive Based on
Poly(Propylene Oxide) And Tannic Acid Coacervate**

Journal:	<i>ChemComm</i>
Manuscript ID	CC-COM-07-2022-003714
Article Type:	Communication

SCHOLARONE™
Manuscripts

COMMUNICATION

A Self-Curable Underwater Adhesive Based on Poly(Propylene Oxide) And Tannic Acid Coacervate

Runtian Qie, Saeed Zajforoushan Moghaddam, and Esben Thormann*

Received 00th January 20xx,
Accepted 00th January 20xx

DOI: 10.1039/x0xx00000x

Coacervation of the poly(propylene oxide) and tannic acid, driven by hydrogen bonding, renders a tacky viscous material that provides an underwater adhesion strength of ~ 350-550 KPa on aluminum substrates, also it can bond wet glass, metal, plastic, and porcelain. A curing functionality is achieved by designing a two-component system, using epoxidized PPO-TA coacervate as part A and aminated PPO as part B. Aside from underwater bonding, this adhesive can then cure underwater through amine-epoxide reactions providing a commercially competitive and waterproof bonding.

Marine organisms have been an inspiration for designing man-made adhesives with novel functionalities such as underwater or wet bonding.^{1–6} This biomimicry design is generally based on mimicking (i) the chemistry and (ii) the curing/complexation mechanisms of the marine adhesive proteins.^{7–10} One promising design approach is based on polymer-tannic acid coacervation/complexation. Here, one can benefit from the galloyl-rich structure of tannic acid (TA), which allows mimicking the interactions of the catechol group found in marine adhesives. Moreover, the adhesive, being in a coacervate phase, offers reduced solubility in water and favorable wetting properties. On this basis, coacervates of TA with several polymers, including poly(N-vinylpyrrolidone)¹¹, polyamidoamine-epichlorohydrin¹², poly(N-hydroxyethyl acrylamide)¹³, Pluronic¹⁴, poly(vinyl alcohol)¹⁵, poly(methyl vinyl ether-alt-maleic anhydride)¹⁶, and poly(2-ethyl-2-oxazoline)¹⁷ have been developed as underwater adhesives.

Commonly, such studies demonstrate the ability of the adhesive to bond surfaces underwater, by providing an instant tackiness. A natural consideration, though, is that an underwater adhesive not only should provide instant tackiness but also should undergo a curing/hardening reaction so a durable bonding can be obtained. Since such coacervate adhesives are often based on hydrogen bonding and ionic

interactions, they are not expected to cure and are thus unable to form a permanent and durable bonding.

In this study, we designed a novel underwater adhesive based on poly(propylene oxide) (PPO) and TA. This adhesive renders strong tackiness underwater, but more importantly cures underwater and provides a durable waterproof bonding. PPO is a non-toxic polyether with broad industrial uses in cosmetics, medicine, and food products. In low molecular weight forms, PPO is readily water-soluble at room temperature, which makes the preparation method much easier compared to other polymer-TA coacervate systems. Notably, PPO is commercially available with different end-group functionalities, including epoxidized and aminated derivatives, which allows for designing adhesives that can undergo covalent curing reactions (detailed experimental methods available as Supporting Information, S1).

PPO derivatives (i.e., with different MW and end groups) show a lower critical solution temperature (LCST) solubility behavior meaning that the solubility decreases with temperature.¹⁸ Considering this, we chose a low molecular weight PPO ($M_n \sim 400 \text{ g mol}^{-1}$) that can be readily dissolved in water. The adhesive is simply prepared by mixing aqueous solutions of dihydroxyl-terminated PPO and TA of the same concentrations in a 1:1 weight ratio. Upon mixing (Figure 1a), the solution instantly turns turbid/milky and is characterized by phase-separated droplets of the polymer-rich phase dispersed in the water-rich phase (i.e., coacervation). By centrifuging the mixture, two distinct phases are obtained, including a light orangish viscous and sticky precipitated material, which is the PPO-TA coacervate adhesive. The polyether backbone of PPO can form hydrogen bonds with the hydroxyl groups on tannic acid, which can herein promote the liquid-liquid phase separation. Considering that both PPO 400 g mol^{-1} and TA can be readily dissolved in water up to 40 wt.%, one can simply obtain a large amount of this adhesive all at once (Supporting Information, S2). Based on a preliminary examination, a 1:1 weight ratio between PPO and TA was found to be optimal, i.e., having one component in excess seems to weaken the underwater adhesion (Supporting Information, S3). The PPO-TA adhesive was found to provide instant underwater bonding

Department of Chemistry, Technical University of Denmark, 2800 Kgs. Lyngby, Denmark. E-mail: esth@kemi.dtu.dk

Electronic Supplementary Information (ESI) available: Materials and methods, effect of polymer concentration and molecular weight on adhesion, underwater adhesion test setup and method, demonstration of bonding different materials (video). See DOI: 10.1039/x0xx00000x†

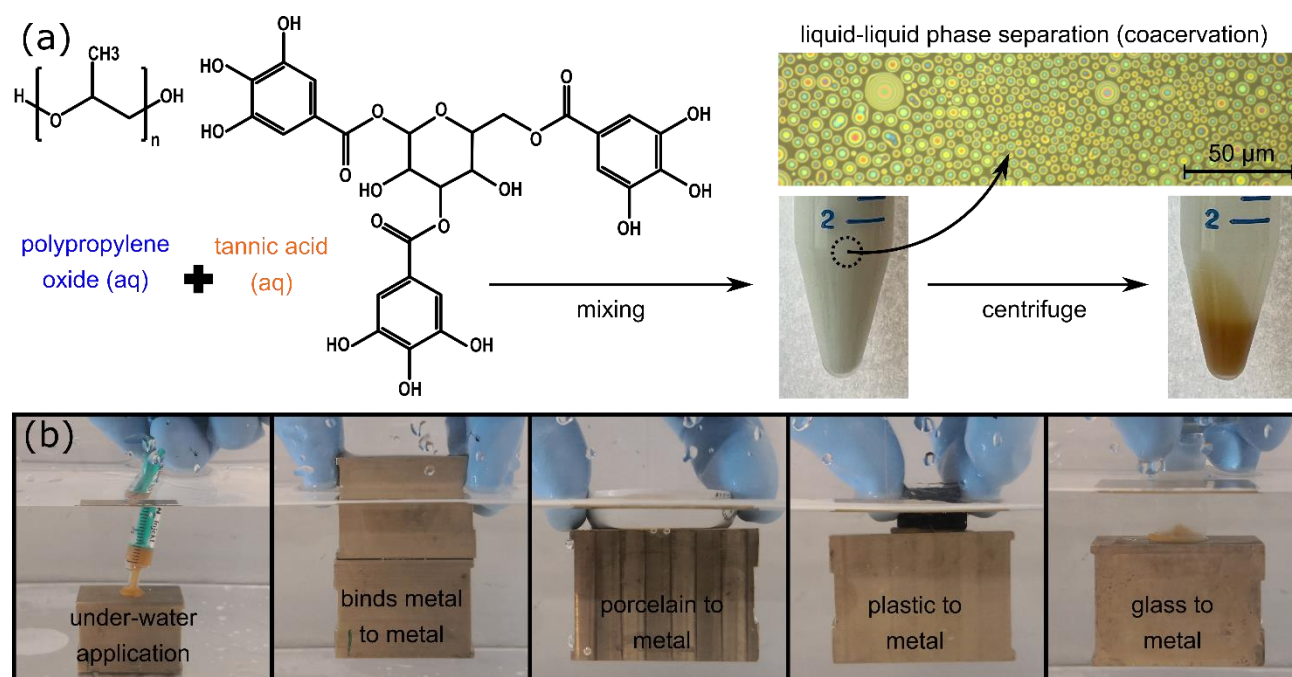


Fig. 1 Preparation and demonstration of the underwater adhesion of PPO-TA coacervate adhesive; upon mixing the aqueous solutions of PPO and TA coacervation occurs. The coacervate phase (i.e., underwater adhesive) can be collected by centrifugation. The coacervate adhesive is easily injectable underwater and can bond various organic and inorganic materials. Note: commercial tannic acid has 2-10 galloyl groups; herein, the structure with 3 galloyl groups is shown as an example.

between different materials including metal, glass, porcelain, and plastic (Figure 1b).

The hydrogen bonding between PPO and TA reduces water-solubility and provides enhanced cohesiveness, but it cannot ensure a durable and permanent bonding. To examine this, two sets of adhesion testing experiments were conducted. Instant underwater adhesion strength was quantified in tensile mode between aluminum substrates (Supporting Information, S4). In brief, the adhesive was applied onto a substrate, a second substrate was brought into contact and then retracted; providing a force-distance curve from which the underwater adhesion strength (maximum measured force through retraction) was obtained (Figure 2a). To test the long-term load-bearing performance, a standard lap shear test was conducted on the samples after being underwater for two days (Figure 2b). PPO-TA adhesive showed an underwater adhesion strength of ~ 350 kPa. However, as expected, the lap shear strength after two days of being in water was found to be zero. To address this issue, we utilized the versatile chemistry of PPO derivatives, in particular, by using the epoxide- and amine-terminated PPO derivatives.

In the first trial, diepoxide-terminated PPO ($M_n \sim 400$ g mol $^{-1}$) solution was mixed with tannic acid solution (1:1 ratio) to make a coacervate adhesive, where one could expect covalent bonding between the epoxide groups of PPO and the hydroxyl groups of TA. Herein, the underwater adhesion strength was found to be similar to dihydroxyl-terminated PPO adhesive. Nevertheless, no significant increment in the lap shear strength of the adhesive was found by using diepoxide-terminated PPO, which suggests insufficient covalent bonding between PPO and TA. Knowing that the reaction between epoxide and hydroxyl is catalyzed in alkaline conditions ($\text{pH} > 10$), we also tried bonding

samples in alkaline solution; however, quite a weak lap shear strength was again obtained. This observation suggests that either the reaction was inefficient or that the high pH dissolved the adhesive, i.e., tannic acid can become negatively charged at high pH and thus may leak out.

In the second trial, triamine-terminated PPO ($M_n \sim 400$ g mol $^{-1}$) solution was mixed with TA solution (1:1 weight ratio) to utilize the possible cross-linking interactions between amine and tannic acid in the oxidized form, i.e., quinone. However, the precipitate made by this method was found to be in the form of "a granular precipitate", not showing the fluid properties of a coacervate phase and thus not suitable as an underwater adhesive. This observation is most probably due to stronger interactions between amine and TA, which appear to produce a precipitated complex instead of a coacervate phase. Such interactions can be of both covalent (Schiff base and Michael addition) and non-covalent origins (hydrogen bonding and cation- π). Regardless, it is clear that the amine termini herein, compared with hydroxyl and epoxide end groups, can more strongly interact with TA.

In the final trial, we thus designed a two-component adhesive system. The first component was made based on the coacervation of diepoxide-terminated PPO and TA. This renders "part A" of the adhesive that provides overall glue-like consistency and underwater bonding ability; yet, it cannot cure on its own. To make this system curable, part A was then mixed with an optimized amount of triamine-terminated PPO (part B). Herein, the amine and epoxide groups are expected to react at room temperature. Also, the amine groups should provide strong interactions with TA. The combination of these reactions (Figure 2d) is thus expected to enable a curable underwater

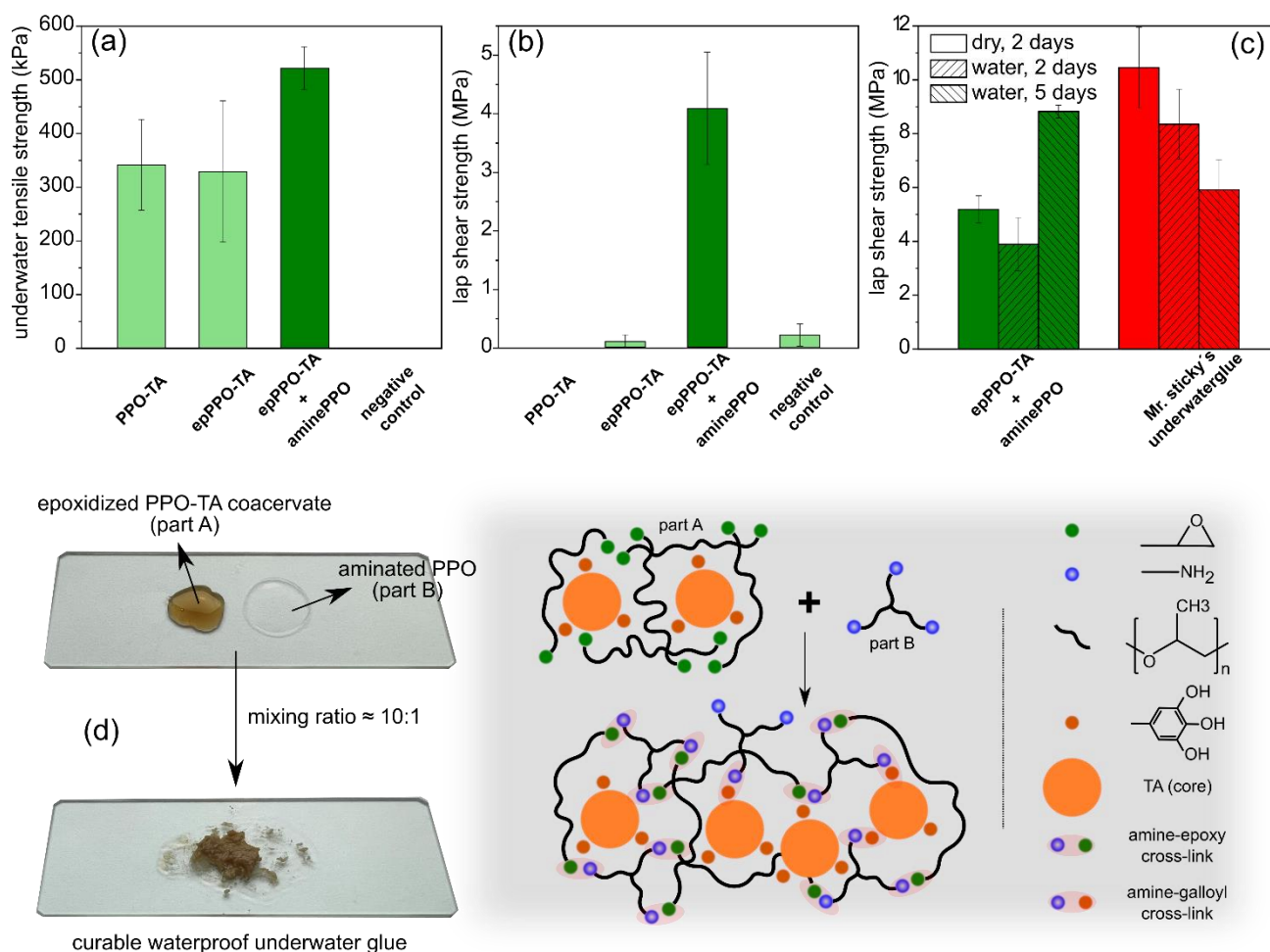


Fig. 2 Adhesive properties of hydroxyl-terminated PPO-TA coacervate, epoxide-terminated PPO-TA coacervate, two-component adhesive (epoxide-terminated PPO-TA coacervate + amine-terminated PPO), negative control (epoxide-terminated PPO + amine-terminated PPO), commercial benchmark (Mr. sticky's underwater adhesive); (a) underwater tensile strength, (b) lap shear strength after 2 days curing in water, (c) lap shear strength after 2 days curing in air, 2 and 7 days curing underwater, for two-component adhesive and the commercial benchmark, (d) preparation and schematic illustration of the two-component adhesive.

adhesive. By varying the amount of part B, It was found that a 10:1 ratio (part A-to-part B) provides an optimum cross-linking effect without sacrificing the underwater bonding feature. The two-component adhesive demonstrated an enhanced underwater adhesion strength (~ 500 kPa), which can be due to the higher cohesiveness of the system. More importantly, the two-component adhesive could cure underwater, i.e., a lap shear strength of ~ 4 -5 Mpa was obtained after being in the water for two days. Notably, we also tested a mixture of diepoxide-terminated PPO and triamine-terminated PPO as the negative control sample. Herein, despite the possible crosslinking of the polymers, no underwater bonding strength was found, also the lap shear strength was negligible. This observation suggests that the presence of TA in the adhesive, and its coacervation with PPO, is essential to both underwater bonding and crosslinking/curing.

Lastly, the two-component adhesive was benchmarked against a commercial underwater epoxy adhesive, i.e., Mr sticky's underwater glue. Herein (Figure 2c), the lap shear strength of the adhesives was compared for samples cured in air for two days, and samples cured in water for two and five

days. Overall, it can be concluded that the two-component adhesive shows commercial level lap shear strength in both dry and wet states. Notably, the commercial adhesive seems to weaken with the time being in water. On the other hand, our adhesive demonstrated an increased lap shear state after being in water for five days, which may be due to further cross-linking of the adhesive through galloyl (which may oxidize with time being in water) and the amine groups.

In summary, PPO-TA coacervation renders a tacky material with underwater bonding functionality. Like other coacervates driven by physical interactions (hydrogen bonding and ionic interactions), this coacervate can provide an instant tackiness underwater, but cannot produce a durable bond with load-bearing capacity. However, by using the coacervate of diepoxide-terminated PPO and TA as part A, and triamine-terminated PPO as part B (hardener), a curable, waterproof, underwater adhesive was obtained. Functionality aside, this adhesive also has favorable environmental and health aspects, such as being partly bio-based (i.e., TA content) and relatively safe (i.e., both TA and PPO are considered non-toxic). The environmental footprints of such an adhesive though can be

further minimized by using PPO derivatives obtained from renewable resources, also by substituting the short-chain amine hardener with water-soluble natural polyamines such as polylysine. Overall, the versatile chemistry of the components and the facile preparation methods herein allow designing various adhesive systems with desired functionalities suitable for applications in underwater/offshore operations.

R. Q. acknowledges a stipend from the China Scholarship Council (CSC).

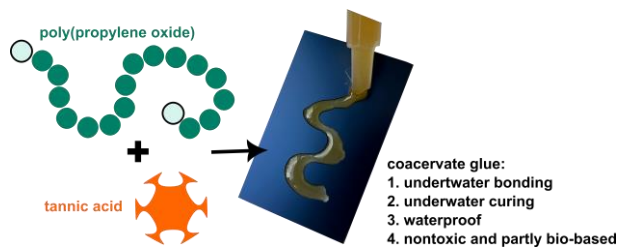
Conflicts of interest

There are no conflicts to declare.

Notes and references

- 1 X. Li, Y. Deng, J. Lai, G. Zhao and S. Dong, *J. Am. Chem. Soc.*, 2020, **142**, 5371–5379.
- 2 B. Cheng, J. Yu, T. Arisawa, K. Hayashi, J. J. Richardson, Y. Shibuta and H. Ejima, *Nat. Commun.* 2022 **131**, 2022, **13**, 1–9.
- 3 H. Fan and J. P. Gong, *Adv. Mater.*, 2021.
- 4 A. H. Hofman, I. A. van Hees, J. Yang and M. Kamperman, *Adv. Mater.*, 2018, **30**, 1704640.
- 5 X. Liu, J. Xu, X. Xie, Z. Ma, T. Zheng, L. Wu, B. Li and W. Li, *Chem. Commun.*, 2020, **56**, 11034–11037.
- 6 C. Zhang, B. Wu, Y. Zhou, F. Zhou, W. Liu and Z. Wang, *Chem. Soc. Rev.*, 2020, **49**, 3605–3637.
- 7 Q. Guo, J. Chen, J. Wang, H. Zeng and J. Yu, *Nanoscale*, 2020, **12**, 1307–1324.
- 8 P. Aich, J. An, B. Yang, Y. H. Ko, J. Kim, J. Murray, H. J. Cha, J. H. Roh, K. M. Park and K. Kim, *Chem. Commun.*, 2018, **54**, 12642–12645.
- 9 A. Li, Y. Mu, W. Jiang and X. Wan, *Chem. Commun.*, 2015, **51**, 9117–9120.
- 10 H. Birkedal, *Nat Chem*, 2017, **9**, 408–409.
- 11 H. G. Nam, M. G. Nam, P. J. Yoo and J. H. Kim, *Soft Matter*, 2019, **15**, 785–791.
- 12 Z. Wang, S. Zhang, S. Zhao, H. Kang, Z. Wang, C. Xia, Y. Yu and J. Li, *Chem. Eng. J.*, 2021, **404**, 127069.
- 13 D. Zhang, Z. Xu, H. Li, C. Fan, C. Cui, T. Wu, M. Xiao, Y. Yang, J. Yang and W. Liu, *Biomater. Sci.*, 2020, **8**, 1455–1463.
- 14 Q. Peng, Q. Wu, J. Chen, T. Wang, M. Wu, D. Yang, X. Peng, J. Liu, H. Zhang and H. Zeng, , DOI:10.1021/acsami.1c13744.
- 15 D. Lee, H. Hwang, J. S. Kim, J. Park, D. Youn, D. Kim, J. Hahn, M. Seo and H. Lee, *ACS Appl. Mater. Interfaces*, 2020, **12**, 20933–20941.
- 16 Y. Gao, X. Peng, Q. Wu, D. Yang, W. Wang, Q. Peng, T. Wang, J. Wang, J. Liu, H. Zhang and H. Zeng, *ACS Appl. Polym. Mater.*, 2022, **4**, 1836–1845.
- 17 Q. D. Dang, J. R. Moon, Y. S. Jeon and J. H. Kim, *J. Appl. Polym. Sci.*, 2020, **137**, 48285.
- 18 S. Z. Moghaddam and E. Thormann, *J. Colloid Interface Sci.*, 2016, **465**, 67–75.

A table of contents entry



A self-curable and waterproof underwater adhesive was developed based on poly(propylene oxide) and tannic acid coacervate.

Supporting information

**A Self-Curable Underwater Adhesive Based on Poly(Propylene Oxide) And Tannic
Acid Coacervate**

Runtian Qie, Saeed Zajforoushan Moghaddam, Esben Thormann*

Department of Chemistry, Technical University of Denmark, 2800 Kgs. Lyngby, Denmark

S1 Experimental Section

Materials: Poly(propylene oxide) (hydroxyl-terminated, PPO, $M_n \sim 425 \text{ g mol}^{-1}$) and poly(propylene oxide) diglycidyl ether ($M_n \sim 380 \text{ g mol}^{-1}$) were purchased from Sigma Aldrich. Triamine terminated poly(propylene oxide) ($M_n \sim 400 \text{ g mol}^{-1}$) was purchased from Alfa chemistry. Ultrapure water (Arium Pro UV water purification system) with a resistivity of $18.2 \text{ M}\Omega \text{ cm}^{-1}$ was used for all experiments.

Adhesives preparation: PPO-TA coacervate adhesives (for Figure 1) were prepared by mixing PPO (hydroxyl-terminated) and TA aqueous solutions at 4°C in a 1:1 weight ratio. The mixture was then centrifuged at 6500 rpm for 5 min to collect the PPO-TA coacervate phase. To make the curable adhesive, first, diepoxide-terminated PPO (5 wt. %) solution was mixed with TA solution (5 wt. %) in a 1:1 ratio at 4°C , whereby the coacervate phase was collected by centrifugation, labeled as “part A”. This coacervate adhesive was then mixed with triamine-terminated PPO (part B) in an optimized ratio of 10:1.

Testing: An underwater adhesion test (Instron 345c, 50 N load cell) was conducted on the aluminum surfaces in deionized water. The adhesive was applied using a syringe onto the bottom cylinder (diameter 2 cm) underwater, then the upper cylinder (diameter 1 cm) was lowered (vertical approach step) at a constant speed of 20 mm s^{-1} until contact was made (setpoint: 5, 10, 15 N), followed by a certain contact time (0.5, 1, 2, 5 min). Next, the upper cylinder was retracted at a speed of 1 mm s^{-1} , and a force vs. distance plot was collected. For each experiment, ten specimens were tested.

Lap shear test (Instron 345c, 2 kN load cell) was operated according to a modified ASTM D1002 standard. Adhesive joints were prepared on aluminum substrates ($12 \text{ mm} \times 50 \text{ mm}$) with an overlap area of $12 \text{ mm} \times 12 \text{ mm}$. The substrates were polished and cleaned with acetone before applying the adhesives. The adhered substrates were clamped and left at room temperature (2 days) or in water (2 and 7 days), and then the lap shear strength was measured. For each experiment, five specimens were tested.

S2 Demonstration of Scalability

Using the low molecular weight hydroxyl-terminated PPO (400 g mol^{-1}), one can easily dissolve up to 40 wt. % polymer in room temperature water. Mixing this solution in equal weight parts with 40 wt. % TA solution (Figure S1) provides a relatively large amount of the coacervate adhesive all at once.



Figure S1. coacervate of PPO-TA obtained after mixing and over-night standing of the PPO (40 wt. %, 25 g) and TA (40 wt. %, 25 g) aqueous solutions

S3 Different Mixing Ratios

PPO and TA solutions of varying concentrations (2.5-40 wt. %) were prepared and mixed in different combinations (Figure S2). First, no clear coacervation was observed when one component was significantly in excess. For instance, mixing PPO 40 wt. % with TA 2.5 wt. % and vice versa. In other cases, it was observed that a 1:1 weight ratio seems to provide the optimal adhesive properties (Table S1).

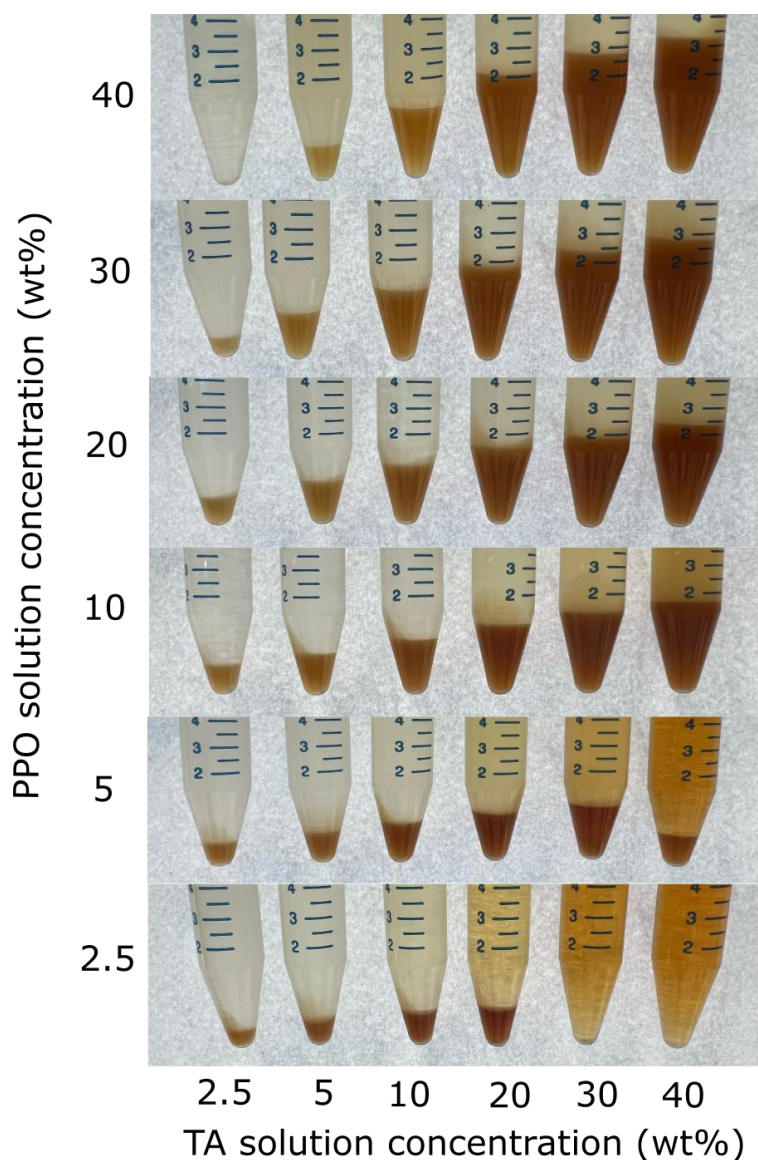


Figure S2. PPO-TA coacervation; different concentrations mixed in a 1:1 weight ratio

Table S1. underwater adhesion force (KPa) of PPO-TA coacervate adhesive; different concentrations mixed in a 1:1 weight ratio

	TA 2.5%	TA 5%	TA 10%	TA 20%	TA 30%	TA 40%
PPO 2.5%	218 ± 55					
PPO 5%		312 ± 84				
PPO 10%			264 ± 34	201 ± 45	237 ± 77	146 ± 41
PPO 20%			129 ± 15	228 ± 53	200 ± 25	
PPO 30%			167 ± 42	143 ± 22	234 ± 50	204 ± 38
PPO 40%				109 ± 24	189 ± 53	353 ± 36

S4 Underwater adhesion test

Figure S3 shows the custom-made setup used for measuring the underwater adhesion strength of the adhesives. Figure S4 shows a typical force-distance curve obtained from such a measurement. Herein, for one of the adhesives, the effect of contact time and contact pressure was partly investigated, to find out the appropriate testing parameters. Accordingly, a contact force of 10 N and a contact time of 1 min were selected for all the subsequent measurements.

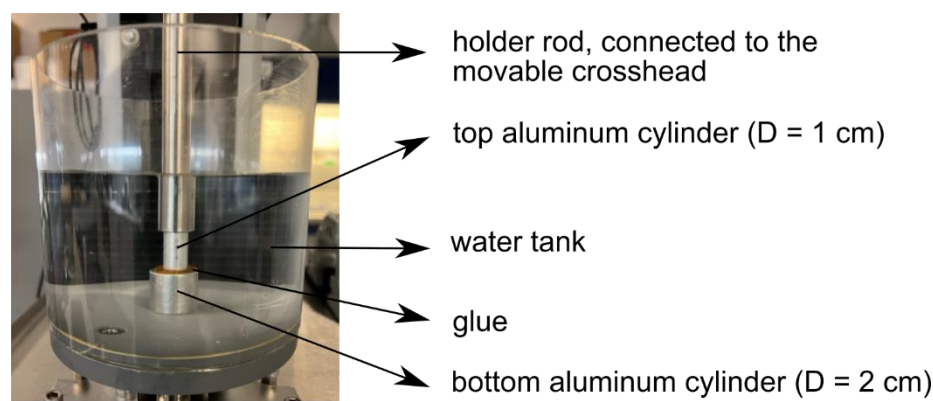


Figure S3 custom-made setup used for testing underwater adhesion

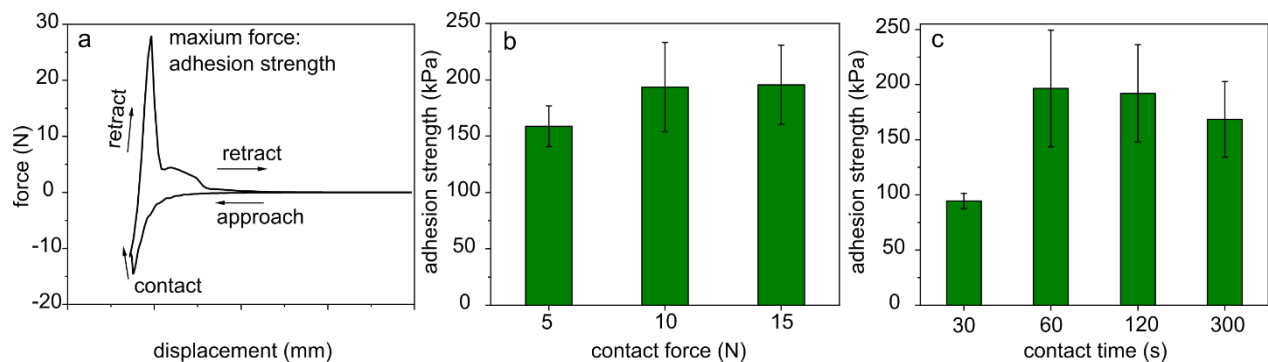


Figure S4 (a) typical force-distance curve, (b) effect of the variation in the contact force for a constant contact time of 60 s on underwater adhesion strength, (c) effect of variation in the contact time for a constant contact force of 10 N on underwater adhesion strength

S5 Effect of PPO MW

Hydroxyl-terminated PPO is commercially available in different molecular weights (~ 400 - 4000 g mol⁻¹). With increasing the MW, it was observed that the collected coacervate becomes significantly more viscous and less practical for surface application. In terms of adhesion strength, PPO with a molecular weight of 1000 g mol⁻¹ appears to provide the optimal adhesive strength. In this study though, PPO 400 g mol⁻¹ was used for all measurements considering its favorable solubility in water and the availability of PPO 400 g mol⁻¹ with epoxide and amine-terminations.

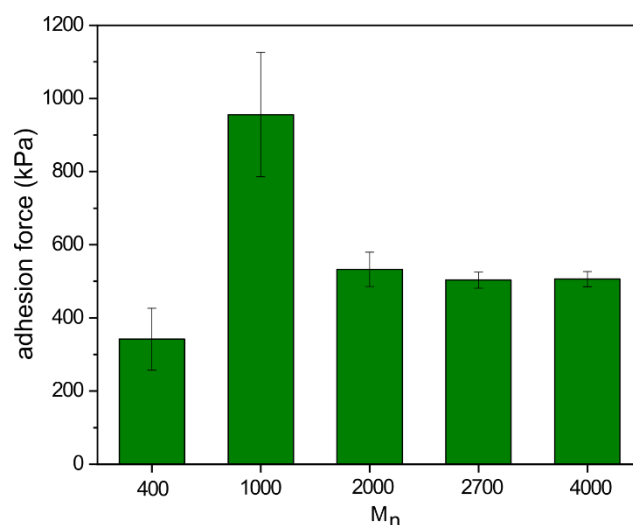


Figure S5 underwater adhesion force measured for PPO-TA coacervate adhesives of different molecular weights (400 - 4000 g mol⁻¹) of PPO